

Production and Characterization of Ytterbium
Monohydroxide (YbOH) for Next-Generation Parity and
Time-Reversal Violating Physics Searches

Thesis by
Nickolas Hovanec Pilgram

In Partial Fulfillment of the Requirements for the
Degree of
Doctor of Philosophy

CALIFORNIA INSTITUTE OF TECHNOLOGY
Pasadena, California

2023
Defended August 4, 2022

© 2023

Nickolas Hovanec Pilgram
ORCID: 0000-0002-5467-3783

All rights reserved except where otherwise noted

Acknowledgements

First, I would like to thank my advisor, Nick Hutzler. His guidance has been a critical component of my graduate work and has helped shape me into a much better scientist. As one of his first students, I have experienced first-hand what it takes to build and run a laboratory.

Additionally, I would like to thank Timothy Steimle, who has often acted as a second advisor to me. Much of the work described here was completed under his guidance and direction. It has been an honor and a privilege to learn the theory, techniques, and practices of molecular spectroscopy from one of the best.

Working with the members of the Hutzler Lab has been one of the true highlights of my time in graduate school and one of the things I will miss the most. Ashay Patel, Yi Zeng, Chandler Conn, Phelan Yu, and Yuiki Takahashi, even though I was the more senior student, I have learned a great deal from all of you. For that I am grateful. I want to especially acknowledge Arian Jadbabaie, with whom I worked to build the experiment from the ground up. Working with someone as brilliant and talented as Arian has been a privilege and has made me a better scientist.

I would also like to thank the other members of the PolyEDM collaboration, including students, postdocs, and P.I.s, for their advice and help. I would like to thank William Hargus for his mentorship and guidance. My work with him is what originally set me on the path to a PhD. I would like to thank my friend Robert Burns for always keeping me grounded. I would like to thank Eric and Kathie Oleson for welcoming me into their home and allowing me to write a significant portion of this dissertation at their kitchen counter.

Thank you to my family. I am so grateful and thankful for your continuous love and support. To my sister Jessica: your support and understanding has been critical in this journey. Though we are at separate universities, pursuing a PhD in physics at the same time as someone who knows me as well as, and only like, you do has been an immense blessing and privilege. To my parents Mark and Kathy Pilgram, thank you for teaching me the value of hard work and perseverance, for keeping me grounded, and for encouraging me to never settle. I owe much of who I am and what I have accomplished to you. I would also like to specifically thank my Mom, Kathy, for pushing me (even if somewhat motivated by her desire to keep me in Southern California) to apply to Caltech for graduate school, despite my doubts about getting

accepted. It turned out to be a life-changing decision.

Most of all, I want to thank my fiancée¹ Susannah. Susannah, thank you for supporting and putting up with me during my time in graduate school. Your support and encouragement has been critical; I could not have done this without you. This achievement is also yours. Of all the things I have accomplished and completed during my time at Caltech, the most important was meeting and proposing to you. Susannah, I love you and will always love you.

Last, and most importantly, I thank God for blessing me with the amazing opportunity to study a minute part of his creation, through which I have gained a greater appreciation for the beauty of His universe. I thank God for blessing me with the talents and abilities needed to complete this work. All of these blessings ultimately come through the grace and salvation He has provided to me through the sacrifice of His son, Jesus Christ, on the cross, for which I am eternally grateful. All glory and honor be to my Lord and savior Jesus Christ, who lives and reigns with God the Father and the Holy Spirit, one God, now and forever. Amen.

¹On and after August 13, 2022, Susannah will be my wife. If one is reading this after that date please mentally substitute fiancée with wife.

To God the Father, God the Son, and God the Holy Spirit, one God, now and forever.

“For what can be known about God is plain to them, because God has shown it to them. For his invisible attributes, namely, his eternal power and divine nature, have been clearly perceived, ever since the creation of the world, in the things that have been made.” Romans 1:19-20a ESV

Abstract

New sources of parity (P) and time-reversal (T) violating physics are motivated by several unanswered questions in fundamental physics, including the observed imbalance between matter and anti-matter in the universe. P,T-violating effects can induce permanent electric dipole moments (EDMs) in atoms and molecules, allowing them to act as sensitive probes of new physics. The linear, triatomic molecule ytterbium monohydroxide (YbOH) has emerged as a promising candidate for next-generation molecular EDM searches, because it possesses both an electronic structure amenable to optical cycling and parity doublets in the bending mode. These features enable laser cooling, highly polarizable science states, and internal comagnetometry which promises an order-of-magnitude improvement to current EDM sensitivities. Additionally, different isotopologues of YbOH offer sensitivity to different sources of P,T-violating physics: leptonic sources via a measurement of the electron's EDM in $^{174}\text{YbOH}$ and hadronic sources via a measurement of the nuclear magnetic quadrupole moment (NMQM) of the ^{173}Yb nucleus in $^{173}\text{YbOH}$. In this dissertation, I describe the design, construction, and optimization of a YbOH cryogenic buffer gas beam (CBGB) source, including the implementation of laser-enhanced chemical reactions for increased molecular production. Direct and frequency modulated (FM) absorption spectroscopy and laser-induced fluorescence measurements (LIF) were implemented in the CBGB source, and LIF and separated field pump/probe microwave optical double resonance spectroscopy was conducted in a supersonic molecular beam source. Additionally, laser-enhanced chemical reactions were utilized to develop a novel spectroscopic technique critical to the observation of the spectrum of the odd isotopologues. FM absorption spectroscopy in the CBGB source allowed the observation of the previously unobserved, weak $\tilde{A}^2\Pi_{1/2}(1, 0, 0) - \tilde{X}^2\Sigma^+(3, 0, 0)$, [17.68], and [17.64] vibronic bands. The $\tilde{X}^2\Sigma^+(0, 0, 0)$ ground state has been characterized at high precision and the $\tilde{A}^2\Pi_{1/2}(1, 0, 0) - \tilde{X}^2\Sigma^+(3, 0, 0)$ band of $^{174}\text{YbOH}$ and the $\tilde{A}^2\Pi_{1/2}(0, 0, 0) - \tilde{X}^2\Sigma^+(0, 0, 0)$ band of the odd $^{171,173}\text{YbOH}$ isotopologues have been characterized for the first time. This work provides much of the spectroscopic knowledge needed to implement next-generation P,T-violating physics searches in YbOH.

Published Content and Contributions

¹N. H. Pilgram, A. Jadbabaie, Y. Zeng, N. R. Hutzler, and T. C. Steimle, “Fine and hyperfine interactions in $^{171}\text{YbOH}$ and $^{173}\text{YbOH}$ ”, *The Journal of Chemical Physics* **154**, 244309 (2021).

N.H.P. designed and constructed significant portions of the experiment and led the absorption data collection, line assignment, analysis, and writing of the manuscript.

²A. Jadbabaie, N. H. Pilgram, J. Klos, S. Kotochigova, and N. R. Hutzler, “Enhanced molecular yield from a cryogenic buffer gas beam source via excited state chemistry”, *New Journal of Physics*, 022002 (2020).

N.H.P. designed and constructed portions of the experiment, collected and analyzed portions of the data, and participated in the preparation of the manuscript.

³S. Nakhate, T. C. Steimle, N. H. Pilgram, and N. R. Hutzler, “The pure rotational spectrum of YbOH ”, *Chemical Physics Letters* **715**, 105–108 (2019).

N.H.P participated in the data collection, analysis, and the writing of the manuscript.

Contents

Acknowledgements	iii
Abstract	vi
Published Content and Contributions	vii
Contents	vii
Chapter I: Introduction	1
1.1 The Baryon asymmetry and fundamental symmetry violation	1
1.2 T-violating electromagnetic moments	2
1.3 EDMs in molecules	5
1.4 YbOH for EDM measurements	11
1.5 Overview	12
Chapter II: Molecular Structure	14
2.1 Born–Oppenheimer approximation and separation of molecular wave- function	14
2.2 Electronic structure	16
2.3 Vibrational structure	19
2.4 Rotational structure	23
2.5 The effective Hamiltonian	24
2.6 Angular momentum coupling and Hund’s cases	28
2.7 Fine structure and parity doublets	31
2.8 Hyperfine structure	38
2.9 Molecular transitions	41
2.10 Overview of laser cooling molecules	44
2.11 Overview of YbOH	46
Chapter III: 4 Kelvin Cryogenic Buffer Gas Beam Source	49
3.1 Cryogenic buffer gas beams	49
3.2 4 K cryogenic buffer gas beam source	52
3.3 Diagnostics: Absorption and fluorescence	70
3.4 YbOH production	73
3.5 Testing cell with mesh aperture	76
Chapter IV: The Pure Rotational Spectrum of YbOH	86
4.1 Pump Probe Microwave Optical Double Resonance (PPMODR) spec- troscopy	86
4.2 Microwave spectrum of the $\tilde{X}^2\Sigma^+(0, 0, 0)$ state	87
4.3 Negative spin rotation parameter and perturbing states	91
Chapter V: Spectroscopy of Odd Isotopologues, $^{171,173}\text{YbOH}$	96
5.1 Laser-enhanced chemical reactions: Enhancement of YbOH production	96
5.2 Experimental setup for $^{171,173}\text{YbOH}$ spectroscopy	101
5.3 Novel spectroscopic technique utilizing laser-enhanced chemical re- actions	103

5.4	Observation of the $^{171,173}\text{YbOH}$ spectra	106
5.5	Analysis and discussion	110
Chapter VI: Frequency Modulation Spectroscopy of YbOH		127
6.1	Frequency modulation absorption spectroscopy: Theory	127
6.2	FM lineshapes and determining optimal modulation frequency	131
6.3	Modeling FM lineshapes	136
6.4	Experimental implementation of FM absorption in buffer gas cell	143
6.5	FM spectroscopy of $\tilde{A}^2\Pi_{1/2}(1, 0, 0) - \tilde{X}^2\Sigma^+(3, 0, 0)$ band of $^{174}\text{YbOH}$	147
6.6	FM spectroscopy of the [17.68] and [17.64] bands of $^{174}\text{YbOH}$	162
Chapter VII: Relevance of This Work to EDM Searches with YbOH		172
Appendix A: Measured YbOH Transitions		176
A.1	Pure rotational spectra of the $\tilde{X}^2\Sigma^+(0, 0, 0)$ state	177
A.2	$\tilde{A}^2\Pi_{1/2}(0, 0, 0) - \tilde{X}^2\Sigma^+(0, 0, 0)$ bands of $^{171,173}\text{YbOH}$	178
A.3	$\tilde{A}^2\Pi_{1/2}(100) - \tilde{X}^2\Sigma^+(300)$ FM spectroscopy	190
A.4	[17.68] and [17.64] bands of $^{174}\text{YbOH}$	197
Appendix B: Technical Drawings		204
B.1	Cryogenic buffer gas cell	204
B.2	50 K thermal shields	219
B.3	4 K thermal shields	227
B.4	Miscellaneous	236
Bibliography		241

Chapter 1

Introduction

1.1 The Baryon asymmetry and fundamental symmetry violation

The Standard Model of particle physics is one of the most successful scientific theories to date, surviving every challenge in the laboratory. Despite the standard model's success in describing the observable constituents of matter (quarks and leptons) and their interactions (through the electromagnetic, weak, and strong forces), it fails to provide a complete description for of the origin of these fundamental particles and forces. More specifically, the standard model fails to explain the large observed asymmetry between the amounts of matter and anti-matter in the universe. This observed asymmetry between matter and anti-matter is known as the Baryon asymmetry of the universe (BAU) [1, 2]. Sakharov noted that the BAU can occur if several conditions are met, including the violation of charge-parity (CP) symmetry¹ [2]. However, the magnitude of CP-violation in the standard model (generated by the flavor-changing weak interactions in the CKM matrix [3]) is too small to explain the BAU [4, 5]. New unobserved processes are then needed to explain this discrepancy.

There are three fundamental symmetries, charge (C), parity (P), and time reversal (T). Each of these symmetries can be represented as one of the following operations;

- Charge (C): the inversion of the electric charge of all particles ($+ \leftrightarrow -$). This is essentially converting all matter to anti-matter or vice versa.
- Parity (P): the inversion of all spatial coordinates ($x \rightarrow -x, y \rightarrow -y, z \rightarrow -z$).
- Time reversal (T): reversing time ($t \rightarrow -t$) or all momenta ($\vec{p} \rightarrow -\vec{p}$, $\vec{L} \rightarrow -\vec{L}$).

These operations are referred to as good symmetries if their application leaves the physics unchanged, e.g., the same set of equations correctly describe the physics both before and after the symmetry operation. The C, P, and T symmetries are all conserved (e.g., good symmetries) in classical and non-relativistic quantum theories; however, they are violated in the standard model (a relativistic quantum field theory)

¹The other conditions are charge (C) symmetry violation, baryon number violation, and a departure from thermal equilibrium.

[6–8]. While each of these symmetries are violated in the standard model, there are strong reasons to expect that their total combination, CPT, is conserved [9]. Therefore, under the CPT theorem, CP-violation is equivalent to T-violation and the two may be used interchangeably.

As described above, the standard model does not contain sufficient CP-violation (T-violation) to explain the BAU. Therefore, the existence of the BAU strongly suggests that additional sources of CP-violation beyond the standard model (BSM) exist. This additional CP-violation could manifest itself as new CP-violating particles or forces [10–12]. Detecting these new particles or forces could provide an explanation for the BAU. Additionally, many classes of theories which extend the standard model generically introduce new sources of CP-violation and are well motivated on other grounds besides the BAU [13].

1.2 T-violating electromagnetic moments

Electric dipole moments (EDMs)

Any fundamental (quark, electron, etc.) or composite (proton, neutron, nucleus, etc.) particle that possesses a permanent electric dipole moment violates both P and T symmetry. Consider any spin 1/2 particle, such as the electron. If the electron has a permanent electric dipole moment, \vec{d} , it must be aligned (or anti-aligned) with the electron's spin, \vec{S} , as this is the only internal vector which describes the particle. If the orientation of \vec{d} and \vec{S} is not fixed then the electron would have an additional degree of freedom. This additional degree of freedom would allow, according to the Pauli exclusion principle, for four electrons to occupy an atomic s orbital, which is not the case. Let us consider the case where \vec{S} and \vec{d} are aligned (the following argument also applies to the anti-aligned case). Now consider applying the P operator. Under a parity transformation, the electric dipole moment reverses direction ($\vec{d} \rightarrow -\vec{d}$) (an electric dipole moment represents a spatial charge separation) while the spin (the intrinsic angular momentum of the electron) remains unchanged. If \vec{S} and \vec{d} were originally aligned, a parity transformation would result in them being anti-aligned. As discussed above, the orientation of \vec{S} and \vec{d} must be fixed and, therefore, a parity transform will result in a different electron than we started with, one that cannot exist. Thus, the electron possessing a permanent electric dipole moment violates P. If we instead applied the T operator we would reverse the spin (an angular momentum) and \vec{d} would remain unchanged. Again, this results in a distinguishable electron and, therefore, the electron possessing a permanent electric dipole moment would violate T as well.

If the electron does have a permanent electric dipole moment (EDM), it is the result of T-violating (or CP-violating) physics. In the context of the standard model this arises through interaction of the electron with the quarks and the W boson. The lowest-order contribution to the electron's electric dipole moment (eEDM) then comes at third order (three-loop Feynman diagrams). However, it has been shown that all the three-loop diagrams cancel [14]. Therefore, the standard model contribution to the eEDM results from fourth- or higher-order interactions and is expected to be exceedingly small, $|d_e| \sim 10^{-44} e \cdot \text{cm}$ [15]. However, the existence of new T-violating BSM particles could also result in a non-zero eEDM. Interactions between the electron and the T-violating particle could result in a non-zero value of the eEDM. This is similar to the leading contributions to the electron's anomalous magnetic moment arising from one-loop interactions with the photon. One-loop Feynman diagrams which contribute to the anomalous magnetic moment of the electron and the eEDM (in the case of a super symmetric BSM model) are shown in Fig. 1.1 of Ref. [16].

Consider the case where a new particle F , of mass M_F exists, and couples to a standard model fermion, f , with CP-violating phase ϕ_{CPV} . Then at the l loop level, dimensional arguments indicate that the interaction with the new particle F will result in the standard model fermion f possessing an EDM, d_f , of magnitude [17]

$$d_f \sim eq_f \sin \phi_{CPV} \left(\frac{g^2}{16\pi^2} \right)^l \eta_{FV} \frac{m_f}{M_F^2}. \quad (1.1)$$

Where q_f and m_f are the charge and mass of the standard model fermion, g is a coupling constant, and η_{FV} is a possible enhancement factor from flavor violation. Eq. 1.1 indicates that the magnitude of the EDM is inversely proportional to the square of the new particles mass, M_F . Therefore, a measurement of (or limit on) the EDM of a standard model fermion, such as the electron, provides an indirect measurement (or bound) on the mass scale at which new T-violating BSM physics occurs.

Measurements of the eEDM are only sensitive to T-violating physics which couples to the electron. However, the same or other T-violating physics can also couple to hadrons. This can result in the quarks, the proton, the neutron, or nuclei possessing EDMs and other CP-violating observables. Experiments searching for these EDMs are complimentary to eEDM experiments as they probe T-violation in the hadronic sector, as opposed to leptonic sector. Experiments aiming to measure or improve

the limit on the proton [17, 18], neutron [19–23], and nuclear² [25–30] EDMs are currently underway. To date, no experimental measurements of a non-zero EDM of either a fundamental or composite particle have been made [17].

Nuclear magnetic quadrupole moments (NMQMs)

T-violating physics can result in permanent EDMs. However, EDMs are not the only permanent P,T-violating electromagnetic moment that can result from P,T-violating physics. Following an EDM the next-lowest order P,T-violating electromagnetic moment is a magnetic quadrupole moment (MQM). An MQM is a tensor quantity and therefore, can only exist in a particle or nucleus of spin $S \geq 1$. Since all the quarks and leptons, as well as the proton and neutron, have a spin of 1/2, they cannot have an MQM. However, many atomic nuclei have $S \geq 1$ and, therefore, can have a nuclear MQM (NMQM).

In a classical picture, an MQM looks like two oppositely circulating current loops separated by some distance d . This classical current configuration can also be realized by an orbiting EDM. Therefore, if a valence nucleon (proton or neutron) in a nucleus has an EDM, when it orbits the nuclear core it will create a NMQM [31]. In spherically shaped nuclei the NMQM is dominated by the contributions from the valence nucleons. However, in quadrupole deformed nuclei, a nucleus with an elliptically shaped mass distribution, $\sim A^{2/3}$ of the nucleons are in open shells and will contribute to the NMQM³, providing a large enhancement [32, 33]. In addition to contributions from the EDMs of the nucleons, an NMQM can also result from P,T-violating inter-nuclear forces, whose contributions can be one to two orders of magnitude larger than those from the nucleon EDMs [33]. Even though NMQMs are the result of a multitude of P,T-violating sources, they provide an indirect measurement of P,T-violating physics in the hadronic sector and compliment eEDM experiments. NMQM experiments also complement nuclear EDM searches since a measurement of both an NMQM and an nuclear EDM in several different systems will allow the exact source of the hadronic P,T-violating physics to be pinpointed. Currently, the only limit on an NMQM comes from measurements of the Cs atom [34].

²The experiments referenced here are aiming to measure nuclear Schiff moments, the residual nuclear EDM not screened by the electrons in an atom or molecule [24].

³Here A is the total number of nucleons in the nucleus.

1.3 EDMs in molecules

The goal of an EDM experiment is to measure an EDM or NMQM. Since NMQMs are more complicated than EDMs, we will first use an EDM measurement, specifically an eEDM measurement, as an example and address NMQM measurements afterward. If you place an electron with an EDM, \vec{d}_e , in an electric field $\vec{\mathcal{E}}$, the electric field will exert a torque on the EDM, $\vec{\tau} = \vec{d}_e \times \vec{\mathcal{E}}$. This torque will cause the EDM (and the spin of the electron) to precess at a frequency $\omega = d_e \mathcal{E} / \hbar$. After a precession time τ , the spin of the electron will have precessed through an angle $\phi = d_e \mathcal{E} \tau / \hbar$. A measurement of this precession angle can be used to determine the eEDM d_e . However, this experimental method with a fixed lab electric field has one problem: if the electron is placed in a constant electric field it will be accelerated away, completely preventing the spin precession measurement from occurring⁴.

To circumvent this problem we can instead examine the interaction of the eEDM with the internal electric field of an atom or molecule, $\vec{\mathcal{E}}_{int}$. Ostensibly, performing EDM measurements in neutral atomic or molecular systems presents issues as well. One of these issues was addressed by Schiff [35]. Schiff noted that when a neutral system, such as an atom or molecule, is placed in a constant electric field, it is not accelerated. Therefore, all the charged components of the atom or molecule (nuclei and electrons) must organize in a way so that the net electric field they experience is zero. In this case the electron must experience an average internal electric field of zero, and so the expectation value of the eEDM interaction is zero, $\langle -\vec{d}_e \cdot \vec{\mathcal{E}}_{int} \rangle = 0$. While this is true for non-relativistic systems, when relativistic effects are considered it results in a nonzero expectation value for the eEDM interaction, $\langle -\vec{d}_e \cdot \vec{\mathcal{E}}_{int} \rangle \neq 0$ [36, 37]. Sanders showed [38] that these relativistic effects not only give nonzero expectation values for the eEDM interaction but also enhance it. In this case, $-\vec{d}_e \cdot \vec{\mathcal{E}}_{int} = -d_e \mathcal{E}_{eff} \vec{S} \cdot \hat{n}$ where \hat{n} is the unit vector along the internuclear axis and $\mathcal{E}_{eff} = \langle \vec{d}_e \cdot \vec{\mathcal{E}}_{int} \rangle / \langle \vec{d}_e \rangle \sim 10 - 100$ GV/cm is the effective internal electric field. These extremely large effective internal electric fields ($\sim 10^6$ times larger than the maximum electric field that can be created in a laboratory) make molecules very sensitive systems for EDM measurements.

Since the internal electric field results from relativistic effects, it is maximized when the electron is accelerated to high relativistic speeds. This occurs in atoms or molecular states with a large overlap of the electron's wavefunction and the nucleus,

⁴You could circumvent this problem by doing the experiment in a storage ring. However, performing the experiment with an atomic or molecular system provides many advantageous features as we shall see.

meaning states with large s- and p-like content. Additionally, the internal electric field scales with the atomic number roughly as Z^3 [36], making heavy atoms or molecules containing heavy atoms extremely sensitive to EDM measurements.

The eEDM interaction in an atom or molecule is described by the P,T-violating effective atomic/molecular Hamiltonian

$$\hat{H}_d = -\vec{d}_e \cdot \vec{\mathcal{E}}_{eff}, \quad (1.2)$$

where $\vec{\mathcal{E}}_{eff} = \mathcal{E}_{eff} \hat{n}$, and \hat{n} is the internuclear axis. In the absence of external fields, the total atomic or molecular Hamiltonian is rotationally symmetric and, therefore, the expectation value of the parity-odd vector quantity $\langle \vec{\mathcal{E}}_{eff} \rangle = 0$. If an external electric field, $\vec{\mathcal{E}}_{ext}$, is applied, it breaks the rotational symmetry and polarizes or orients the atoms or molecules in the lab frame by mixing states of opposite parity. In this case, $\langle \vec{\mathcal{E}}_{eff} \rangle \neq 0$ and is now proportional to the degree to which the atom or molecule is polarized, thus $\langle \vec{\mathcal{E}}_{eff} \rangle \propto P$ where $0 \leq P < 1$ is the polarization. The expectation value of the internal electric field takes its maximum value when the atom or molecule is fully polarized, maximizing the eEDM sensitivity. The atom or molecule is fully polarized when the external electric field completely mixes the opposite parity states. This occurs when the energy of the interaction of external field with the atom's or molecule's CP-conserving dipole moment, \vec{D} , is much larger than the energy separation of the opposite parity states (ΔE), $\vec{D} \cdot \vec{\mathcal{E}}_{ext} \gg \Delta E$.

In order to estimate the magnitude of electric field needed to fully polarize the atom or molecule (and maximize the eEDM sensitivity) we can make the approximation⁵, $P \sim \vec{D} \cdot \vec{\mathcal{E}}_{ext} / \Delta E$. The atom or molecule is fully polarized when $P \sim 1$, which corresponds to an electric field of $|\vec{\mathcal{E}}_{ext}| \sim \Delta E / |\vec{D}|$. For atoms, the closest states of opposite parity are electronic states which are separated by $\sim 10 - 100$ THz. If we make the justified assumption that the atomic (or molecular) dipole moment is about one atomic unit $|\vec{D}| \sim ea_0$, then we need an electric field of $\mathcal{E}_{ext} \sim 1,000 - 10,000$ kV/cm to fully polarize the atom. This is challenging since the largest electric field that can be created in vacuum over reasonably large volumes in the laboratory⁶ is ~ 100 kV/cm. At these fields, an atom would only have a polarization of $P \sim 10^{-3}$, which would only project a very small fraction of \mathcal{E}_{eff} for the EDM

⁵This approximation is good in the low-polarization limit, $P \ll 1$, but becomes less accurate as the polarization increases. However, it is still helpful for making order of magnitude estimates. An analytic expression for the polarization of a two-level system can be found in Sec. 2.1 of Ref [39].

⁶Above this threshold, arcing between the materials creating the electric field occurs preventing higher fields from being realized. However, careful engineering can result in fields as high as 500 kV/cm [40] though with many design constraints.

measurement. Diatomic molecules, however, have opposite parity rotational states which are typically separated by $\sim 1 - 100$ GHz. Therefore, a diatomic molecule can be fully polarized with a field of $\mathcal{E}_{ext} \sim 10 - 100$ kV/cm. Since molecules can be fully polarized, they are ~ 1000 times more sensitive to EDMs compared to atoms. Finally, certain diatomic molecules and generally all polyatomic molecules have parity doublets, closely spaced states of opposite parity. These parity doublets are generally separated by $\lesssim 100$ MHz and therefore allow the molecule to be fully polarized in fields of $\mathcal{E}_{ext} \lesssim 100$ V/cm. These parity doublets will be discussed in more detail later in this section.

Finally, I would like to note that the quantity $\vec{\mathcal{E}}_{eff}$, known as the effective internal electric field, is a parameter which describes how sensitive a molecular state is to energy shifts from an EDM. Dimensionally, $\vec{\mathcal{E}}_{eff}$ takes on the units of an electric field and even though it is not physically observable, treating it as an electric field provides good intuition⁷. The NMQM interaction in a molecule is parameterized by a similar parameter W_M . W_M is similar to \mathcal{E}_{eff} as it describes the sensitivity of a molecular state to an NMQM, is proportional to the degree to which the molecule is polarized, and is enhanced by relativistic effects [33]. Therefore, the discussion above is also applicable to NMQM measurements as well.

Measuring EDM energy shifts

When performing an EDM measurement, we want to fully polarize the molecules with an external electric field so that $\langle \hat{H}_d \rangle = \langle -\vec{d}_e \cdot \vec{\mathcal{E}}_{eff} \rangle \neq 0$ and \mathcal{E}_{eff} is maximized. In this case, the eEDM interaction results in the following energy shift

$$E_d = -\vec{d}_e \cdot \vec{\mathcal{E}}_{eff} = -d_e \mathcal{E}_{eff} \vec{S} \cdot \hat{n} = -d_e \mathcal{E}_{eff} \Sigma, \quad (1.3)$$

where Σ is the projection of \vec{S} on the internuclear axis \hat{n} . When fully polarized, \hat{n} is aligned or anti-aligned with the external electric field (which defines the lab z-axis). If we consider preparing a superposition of two states with opposite eEDM shifts (e.g., opposite values of Σ so that $\langle \psi_1 | \hat{H}_d | \psi_1 \rangle = -\langle \psi_2 | \hat{H}_d | \psi_2 \rangle$), then the eEDM interaction will cause the states to precess at a frequency of

$$\omega_d = -2d_e \mathcal{E}_{eff} \Sigma. \quad (1.4)$$

This precession frequency can be measured experimentally. Upon reversal of the internal electric field $\vec{\mathcal{E}}_{eff}$ the precession frequency will reverse. The key experimental signature that distinguishes the energy shift of an eEDM from other energy

⁷Additionally, $\vec{\mathcal{E}}_{eff}$ behaves like an electric field in the effective Hamiltonian describing the molecular energy shifts which result from an eEDM.

shifts in the molecule is a change of the measured precession frequency correlated with the reversal of the effective internal electric field, $\vec{\mathcal{E}}_{eff}$.

One way to reverse $\vec{\mathcal{E}}_{eff}$ is to reverse the external electric field \mathcal{E}_{ext} . However, reversals of laboratory electric fields are imperfect and can result in systematic errors. However, in molecules with parity doublets, the internal electric field can be reversed spectroscopically, e.g., by changing quantum states. As previously mentioned parity doublets are closely spaced opposite parity states. They result when a molecule has a non-zero projection of angular momentum on the internuclear axis (or symmetry axis for nonlinear polyatomic molecules). In diatomic molecules this can only result from a non-zero projection of the electronic angular momentum on the internuclear axis (Λ), called lambda-doublets. In polyatomic molecules the angular momentum projection can come from the ligand degrees of freedom, such as angular momentum associated with bending modes (l and l -doublets) or rotation about the symmetry axis. Bending angular momentum and l -doublets are discussed in more detail in Section 2.3, while the details of non-linear molecules are beyond the scope of this dissertation and will not be discussed further. For the following discussion we will use the quantum number K to denote the projection of angular momentum on the internuclear axis⁸. For any angular momentum with a non-zero projection on the inter nuclear axis, the projection can take one of two values $|+K\rangle$ and $|-K\rangle$. These correspond to opposite alignments on the internuclear axis. In free field, the eigenstates must be rotationally symmetric (no directionality) so the eigenstates are equal superpositions of the two, creating two states of opposite parity

$$|\pm\rangle = \frac{1}{\sqrt{2}} (|K\rangle \pm |-K\rangle), \quad (1.5)$$

where $|+\rangle$ is the state of positive parity and $|-\rangle$ is the state of negative parity. These states are nominally degenerate; however, the rotation of the molecule breaks this degeneracy, resulting in the parity doublets. As previously mentioned these doublets allow the molecule to be fully polarized in relatively small electric fields. When fully polarized the parity doublets are fully mixed, resulting in the following quantum states

$$|\psi_{\pm}\rangle = \frac{1}{\sqrt{2}} (|+\rangle \pm |-\rangle) = |\pm K\rangle. \quad (1.6)$$

The $|+K\rangle$ state corresponds to the molecule internuclear axis, and $\vec{\mathcal{E}}_{eff}$, being aligned to the lab electric field $\vec{\mathcal{E}}_{ext}$, and $|-K\rangle$ corresponds to the molecule

⁸In linear molecules $K = \Lambda + l$. In the following discussion one can replace K with Λ or l .

internuclear axis, and $\vec{\mathcal{E}}_{eff}$, anti-aligned with the lab electric field $\vec{\mathcal{E}}_{ext}$. If the experiment is first performed in $|+K\rangle$, spectroscopically switching to the $|-K\rangle$ state will reverse $\vec{\mathcal{E}}_{eff}$ without changing $\vec{\mathcal{E}}_{ext}$. This internal field reversal is not subject to the same systematics as reversing the external laboratory field. Pairs of states which allow the spectroscopic reversal of $\vec{\mathcal{E}}_{eff}$ are often referred to as internal comagnetometer states.

Internal comagnetometers allow the rejection of critical systematic errors associated with lab electric field reversals. The two experiments which set the most stringent limits on the value of the eEDM rely on internal comagnetometers to reach their exceptional sensitivities [41, 42]. Therefore, it is desirable, if not critical, that future molecular EDM experiments utilize these internal comagnetometer states as well.

Now we will examine the NMQM energy shifts in a molecule and their experimental signature. The effects of a NMQM on the energy levels of a molecule are described by the effective P,T-violating MQM Hamiltonian [33]:

$$\hat{H}_{MQM} = -\frac{W_M M}{2I(2I-1)} \mathbf{S} \hat{\mathbf{T}} \hat{n}, \quad (1.7)$$

where M is the magnitude of the NMQM, S is the spin of the electron, I is the magnitude of the spin of the nucleus, and $\hat{\mathbf{T}}$ is a second-rank tensor⁹ which relates the NMQM shift to the orientation of the nuclear spin. As mentioned before, W_M is a coupling constant which describes the sensitivity of a molecular state to the NMQM interaction. W_M behaves similarly to \mathcal{E}_{eff} , so that the expectation value of \hat{H}_{MQM} is maximized when the molecule is fully polarized and switches sign when the internal comagnetometer state is switched or the external lab field is reversed. The energy shift resulting from \hat{H}_{MQM} is dependent on the projection of the nuclear spin on the lab z-axis, I_z (when the molecule is fully polarized this is equivalent to the projection on the internuclear axis). When the projection of the nuclear spin is maximized, $I_z = I$, the NMQM energy shift is [33]

$$E_{MQM}(I_z = I) = -\frac{1}{3} M W_M \Sigma. \quad (1.8)$$

If you compare Eq. 1.8 to Eq. 1.3 you can see that the energy shifts behave in the same way (just differing by a factor of 1/3) with a direct correspondence between d_e and M and \mathcal{E}_{int} and W_M . Therefore, a NMQM experiment is performed in the

⁹In Eq. 1.7, \mathbf{S} and \hat{n} are first rank tensors (vectors). The product of these two first rank tensors with the second rank tensor, $\hat{\mathbf{T}}$, results in a scalar, $\mathbf{S} \hat{\mathbf{T}} \hat{n} = \sum_{i,j} S_i T_{i,j} n_j$.

same way as the eEDM experiment; preparing a superposition of two states with opposite NMQM shifts and measuring the precession frequency

$$\omega_{MQM}(I_z = I) = -\frac{2}{3}MW_M\Sigma. \quad (1.9)$$

Again the experimental signature of an NMQM is the change in the precession frequency with a reversal of W_M . Lastly, the background in an NMQM experiment will include effects from a possible eEDM. However, eEDM shifts are constant with respect to I_z while the NMQM energy shifts will depend on the value of I_z . If the precession frequency is measured in states with different projections of I_z then the NMQM shift can be isolated from the eEDM shift.

Improving EDM sensitivity

Here I will briefly examine the sensitivity of EDM measurements in the context of how they can be improved. Again, I will use the eEDM as an example. Since eEDM and NMQM measurements are performed using the same spin precession method, everything discussed regarding an eEDM can be applied to the NMQM. The current best limit on the eEDM is $|d_e| < 1.1 \times 10^{-29} e \cdot \text{cm}$ [41]. This limit was set by the ACME collaboration using a molecular beam of ThO molecules. Experiments aimed at improving this limit are currently underway [43–46]. For an eEDM measurement the ultimate shot noise limit is set by [47]

$$\delta d_e = \frac{\hbar}{2\mathcal{E}_{eff}\tau\sqrt{N}}, \quad (1.10)$$

where τ is the coherence time (spin precession time) and N is the total number of molecules. Increasing sensitivity is accomplished by decreasing δd_e . Therefore, next-generation eEDM experiments want to maximize \mathcal{E}_{eff} , τ , and N . As discussed before, \mathcal{E}_{eff} (or W_M) is maximized by performing the EDM experiment with a heavy polar molecule. The ACME experiment was able to produce large numbers of molecules using a cryogenic buffer gas source; however, the coherence time is limited by the beam transit to $\sim 1 - 10$ ms. Therefore, gains in sensitivity can be made by increasing the coherence time. This can be accomplished by performing the experiment with a laser cooled and trapped molecular sample as opposed to a molecular beam.

In the past decade not only has the laser cooling and trapping of molecules been accomplished but the field has also seen tremendous progress. Multiple species, both diatomic [48–52] and polyatomic [53–56] molecules have been laser cooled. Several

of these species have been magneto-optically trapped [57–60] and some loaded into conservative traps [61–66]. A brief overview of molecular laser cooling is provided in Section 2.10. Performing an EDM measurement with a laser cooled and trapped sample can increase the coherence time, and therefore the EDM sensitivity, by orders of magnitude [67].

Upgrades to current EDM experiments [44, 68] are projected to improve EDM sensitivity by an order of magnitude (10^{-30} e cm) in the next few years (by 2024). Experiments utilizing the laser cooling and trapping of molecules [43] are projected to provide an additional order of magnitude improvement in EDM sensitivity (10^{-31} e cm) in the next ~ 5 years (2027). For more details on improvements to EDM sensitivity see Ref. [17], particularly Fig. 5.

1.4 YbOH for EDM measurements

Based on the discussions in this chapter, an ideal molecule with which to perform an eEDM or NMQM experiment will meet the following criteria:

- Contain a heavy atom (large Z): $\mathcal{E}_{eff} \propto Z^3$ and $W_M \propto Z^2$ so this will provide large \mathcal{E}_{eff} , W_M .
- Have a science state comprised of valence electron orbitals derived from the atomic s orbitals of the heavy atom: Due to relativistic effects, \mathcal{E}_{eff} and W_M are larger in states where the valence electron has a large overlap with the heavy nucleus.
- Have a science state with parity doublets: Allows the molecule to be fully polarized in small fields and provides systematic error rejection via internal comagnetometer states.
- The molecule can be produced in a cryogenic buffer gas source: This allows the production of a large number of molecules.
- Can be laser cooled: Will allow very large coherence times.
- In the case of an NMQM measurement, the heavy nucleus should have a spin of $S \geq 1$ and a large quadrupole deformation.

The linear triatomic molecule ytterbium monohydroxide (YbOH) meets all of the above criteria (as I will describe below) and is therefore an excellent molecule with which to develop next-generation EDM experiments. First, the Yb atom is heavy,

$Z = 70$, and the ground $\tilde{X}^2\Sigma^+$ electronic state is largely comprised of $6s\sigma$ molecular orbitals (correlated to the Yb^+ $6s$ orbital)¹⁰. This provides large \mathcal{E}_{eff} and W_M which have been calculated to be $\mathcal{E}_{eff} = 23.4$ GV/cm [69] and $W_M = -1.067 \times 10^{33}$ Hz/(e cm²) [70] in the ground $\tilde{X}^2\Sigma$ state¹¹. Second, the excited bending mode of the $\tilde{X}^2\Sigma^+$ state has parity doublets, in the form of l -doubles, due to the angular momentum associated with the bending motion. These l -doublets are expected to be split by ~ 10 MHz [67] and will provide full polarization and internal comagnetometers. Third, YbOH is chemically and electronically similar to the alkaline earth fluorides and hydroxides (CaF , SrF , SrOH , etc.) which were produced in a cryogenic buffer gas source prior to the work described in this dissertation [71]. Fourth, YbOH has an electronic structure that is amenable to laser cooling [67] and similar to SrOH which was laser cooled prior to the start of this work [53]. Finally, Yb has multiple isotopologues. The most abundant isotope, ^{174}Yb , has a nuclear spin of $S = 0$, making $^{174}\text{YbOH}$ ideal for eEDM searches. The ^{173}Yb nucleus has a spin of $S = 5/2$ and a large quadrupole deformation making $^{173}\text{YbOH}$ ideal for NMQM searches.

1.5 Overview

The work described in this dissertation is focused on the production and spectroscopic characterization of YbOH for the development of eEDM and NMQM searches. The work related to the eEDM search is part of the PolyEDM collaboration which aims to perform a next-generation eEDM experiment with a laser cooled and trapped sample of polyatomic molecules. The NMQM experiment aims to perform the first NMQM measurement in a molecular system using a cold molecular beam of YbOH . Following generations of the NMQM experiment will aim to increase sensitivity by adding laser cooling. The work described here lays much of the groundwork for these experiments.

This dissertation is organized in the following way. Ch. 2 provides an overview of molecular structure and spectroscopy. Ch. 3 describes the design, construction, and testing of our 4 K cryogenic buffer gas beam source. Ch. 4 presents the pure rotational spectroscopy of the $\tilde{X}^2\Sigma^+(0, 0, 0)$ state of $^{174}\text{YbOH}$. Ch. 5 presents the spectroscopy of the $\tilde{A}^2\Pi_{1/2}(0, 0, 0) - \tilde{X}^2\Sigma^+(0, 0, 0)$ band of the odd isotopologues, $^{171,173}\text{YbOH}$, as well as a novel spectroscopic technique based on laser-enhanced

¹⁰The hyperfine measurements of the odd isotopologues of YbOH , described in this dissertation indicate, that the $\tilde{X}^2\Sigma^+$ state is $\sim 54\%$ $6s\sigma$.

¹¹The hyperfine measurements of the odd isotopologues of YbOH described in this dissertation provided experimental confirmation of the computational methods used to calculate these values.

chemical reactions. Ch. 6 describes the implementation of frequency modulated absorption spectroscopy in the cryogenic buffer gas source and the measurement of the $\tilde{A}^2\Pi_{1/2}(1, 0, 0) - \tilde{X}^2\Sigma^+(3, 0, 0)$, [17.68], and [17.64] bands of $^{174}\text{YbOH}$. Finally, Ch. 7 provides an overview of the relevance of this work to the eEDM and NMQM experiments and the ongoing and future work that the work of this dissertation has enabled.

Chapter 2

Molecular Structure

In this chapter I describe the general molecular structure of linear molecules with a single valence electron which is applicable for describing the quantum mechanical structure of YbOH. Though the goal is to describe YbOH, the molecular structure described here is general and applicable to many diatomic and linear polyatomic molecules with doublet (spin = 1/2) electronic states. In addition to YbOH (and YbF) all alkaline earth metal (AEM) fluoride and and some alkaline earth metal hydroxide molecules are described by this molecular classification. These molecules are extremely relevant in the context of atomic, molecular, optical physics as several of the AEM fluorides and hydroxides have been laser cooled [48, 49, 52–55] and trapped [57, 59–65], and several of these molecules are highly sensitive to new physics [43, 67]. The various isotopologues of YbOH themselves have structures amenable to laser cooling and (as discussed in Ch. 1) are highly sensitive probes for measuring either an eEDM, NMQM [67], or NSD-PV [72].

2.1 Born–Oppenheimer approximation and separation of molecular wavefunction

The quantum mechanical structure of a molecule is determined by solving the time-independent Schrödinger equation

$$\hat{H}_{tot}\Psi = E\Psi, \quad (2.1)$$

where \hat{H}_{tot} is the total electrostatic Hamiltonian of the molecular system, Ψ is the molecular wavefunction describing a quantum state, and E is the energy of the state Ψ . \hat{H}_{tot} describes the total energy of the molecular system, both kinetic and potential and is given by [73, 74],

$$\hat{H}_{tot} = \hat{T}_e + \hat{T}_n + \hat{V}_{e,e} + \hat{V}_{e,n} + \hat{V}_{n,n}. \quad (2.2)$$

The terms in \hat{H}_{tot} are as follows:

- the kinetic energy of the electrons of mass m

$$\hat{T}_e = -\frac{\hbar^2}{2m} \sum_{i=1}^{N_e} \nabla_i^2; \quad (2.3)$$

- the kinetic energy of the nuclei, each of mass M_j

$$\hat{T}_n = -\frac{\hbar^2}{2} \sum_{j=1}^{N_n} \frac{1}{M_j} \nabla_j^2; \quad (2.4)$$

- the repulsive electrostatic potential between the electrons, located at r_i

$$\hat{V}_{e,e} = \frac{e^2}{4\pi\epsilon_0} \sum_{i' < i}^{N_e} \sum_{i=1}^{N_e} \frac{1}{|r_i - r_{i'}|}; \quad (2.5)$$

- the attractive electrostatic potential between the electrons, located at r_i , and the nuclei, each of charge Z_j and located at R_j

$$\hat{V}_{e,n} = -\frac{e^2}{4\pi\epsilon_0} \sum_{i=1}^{N_e} \sum_{j=1}^{N_n} \frac{Z_j}{|r_i - R_j|}; \quad (2.6)$$

- the repulsive electrostatic potential between the nuclei

$$\hat{V}_{n,n} = \frac{e^2}{4\pi\epsilon_0} \sum_{j' < j}^{N_n} \sum_{j=1}^{N_n} \frac{1}{|R_j - R_{j'}|}. \quad (2.7)$$

This Hamiltonian does not include the electronic and nuclear spin degrees of freedom. The interactions arising from these degrees of freedom are generally treated as perturbations to the electrostatic Hamiltonian and are discussed in detail in sections 2.7 and 2.8.

The Hamiltonian given in Eq. 2.2 can't be solved exactly, so numerical methods and well-justified approximations are needed [73]. One such simplification is the Born-Oppenheimer (BO) approximation [73, 75]. This approximation relies on the fact that the much lighter electrons move significantly faster than the heavier nuclei and therefore the electrons can rapidly adjust to any change in the nuclear configuration. In this case, the nuclear motion can be treated as a perturbation to the electronic Hamiltonian,

$$\hat{H}_e = \hat{H}_{tot} - \hat{T}_n = \hat{T}_e + \hat{V}_{e,e} + \hat{V}_{e,n} + \hat{V}_{n,n}. \quad (2.8)$$

In this approximation, the electron configuration for a fixed nuclear configuration, R_0 , can be determined. In the BO approximation, the motions of the nuclei, both vibrations and rotations, do not couple to the electrons so that the molecular wavefunction can be factored into two separate parts,

$$\Psi_{tot} \approx \psi_e(r, R)\chi_n(R). \quad (2.9)$$

The electronic wavefunction, $\psi_e(r, R)$, describes the motion and positions of the electrons and depends on the electron, r , and nuclear, R , coordinates while the nuclear wavefunction, $\chi_n(R)$, describes the motion of the nuclei and only depends on the nuclear coordinates, R . The electronic wavefunction is a solution to the electronic Schrödinger equation,

$$\hat{H}_e\psi_e(r, R) = E_e(R)\psi_e(r, R), \quad (2.10)$$

which can be solved for a fixed nuclear configuration, R_0 . Plugging Eq. 2.8 and 2.9 into Eq. 2.1 gives [73],

$$(E_e(R) + \hat{T}_n)\chi_n(R) = E\chi_n(R), \quad (2.11)$$

where $E = E_e + E_n$ and E_n is the energy from the nuclear motion. Eq. 2.11 indicates the energy of a given configuration of the electrons, $E_e(R)$, determines the potential in which the nuclei move.

Finally, if we work in a molecule fixed frame which rotates with the molecule we can further separate the vibrational and rotational parts of the nuclear wavefunction, $\chi_n = \psi_v\psi_R$ [73]. This allows the total molecular wavefunction to be expressed as,

$$\Psi = \psi_e\psi_v\psi_R. \quad (2.12)$$

This is especially useful since the energies associated with the electronic states, nuclear vibration, and nuclear rotation are generally orders of magnitude different ($E_e > E_v > E_R$). We can therefore view each electronic state as having its own manifold of vibrational states and each of these vibrational (vibronic) states as having its own manifold of rotational states.

2.2 Electronic structure

Potential energy surface and molecular geometry

The electronic states of the molecule, $\psi_{e,i}(R)$, are determined by solving Eq.2.10. Each electronic state, $\psi_{e,i}(R)$ has an associated energy, $E_{e,i}(R)$ which depends on the nuclear configuration. The functional dependence of $E_{e,i}(R)$ on the nuclear coordinates determines the potential energy surface (PES) for the electronic state. If the PES has a minimum, the electronic state is bound; if not, then the state

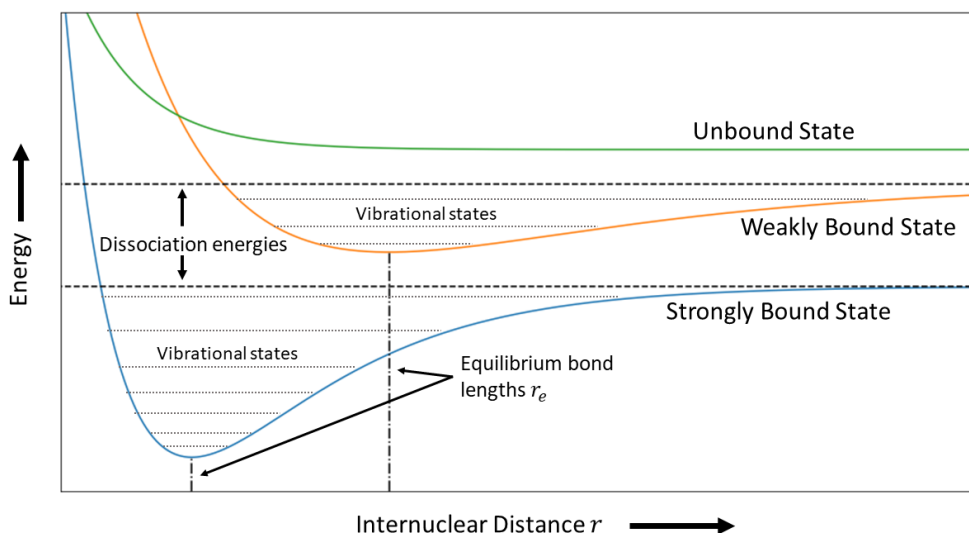


Figure 2.1: Example one-dimensional potential energy surfaces (PESs) as a function of internuclear distance r . The solid colored lines provide examples of a strongly bound, weakly bound, and an unbound PES. Dashed horizontal lines indicate the dissociation energies of the bound states. Vertical dot-dashed lines mark the minima of the PESs and give the equilibrium bond distances for each electronic state. Also shown are the vibrational states, the dotted horizontal lines, for each bound PES.

is unbound and no molecule forms, or it dissociates. If the electronic state is bound the nuclear configuration which minimizes the PES, R_0 , gives the equilibrium molecular geometry (bond lengths and angles). If the PES has multiple minima then each minimum corresponds to a different stable, or pseudo-stable, geometry; each of these geometries is a separate isomer (same set of atoms in different configuration). Each electronic state of the molecule has its own associated PES and therefore its own equilibrium geometry. Examples of weakly bound, strongly bound, and unbound one-dimensional PESs (for a diatomic molecule) are shown in Fig. 2.1.

Molecular orbitals and ligand field theory

Atoms bond to form molecules to lower the total energy of the combined system. The bonds are made via the occupation of bonding molecular orbitals (MOs). Though these bonding orbitals (and non-bonding MOs as well) can be very delocalized, it can still be helpful to think of them in the more localized atomic orbital (AO) basis. Consider the case of a Yb (or an alkaline-earth metal Mg, Ca, Sr, etc.) bonding to the halogen F (or other halogen or pseudo-halogen Cl, OH, etc.). The F has two filled and one half-filled atomic p-orbitals while the Yb has a filled s-orbital. The

Yb and the F bond by filling a bonding orbital which is comprised of some linear combination of the Yb and F AOs. In this case, a simple intuitive picture is that the bonding orbital is comprised of the linear combination of the half-filled F p-orbital and the Yb s-orbital. This bonding MO is completely filled, one electron from the F and one from the Yb, resulting in a lowered total energy. Since the total number of available orbitals stays the same, the combination of the two atomic orbitals (the Yb s orbital and F p orbital) results in two molecular orbitals, the bonding orbital and another antibonding orbital. The other Yb s-electron resides in this antibonding orbital. The more covalent the bond, the more delocalized the MOs become, and the AO basis becomes an increasingly non-intuitive description as the MOs are comprised of more AOs. However, more ionic bonds result in more localized MOs and therefore viewing the MOs in the AO basis is quite useful.

In the case of an Yb bonded to F or OH, the bond is very ionic and results in a bonding orbital fairly localized around the F atom or OH radical. The picture then looks like the F or OH grabbing one of the valence s electrons from the Yb and leaving the other localized on the metal. In this case the valence electron is centered on the Yb metal 2+ ion (Yb^{2+}) which is ionically bonded to the negatively charged F^- or OH^- . With the localized valence electron on the metal, the electronic structure of the molecule can then be well described by ligand field theory [76–78]. Ligand field theory treats the electric field, called the ligand field (LF) in this case, from the negatively charged halogen or pseudo-halogen as a perturbation to the states of the atomic metal ion M^{2+} ($\text{M}=\text{Yb}$ in the example above). The Hamiltonian for the valence electron is then [76, 79],

$$\hat{H}_{\text{valence}} = \hat{H}^0 + \hat{H}' = \hat{H}_{\text{M}^{2+}} + \hat{H}_{\text{LF}}. \quad (2.13)$$

The LF perturbs the AOs of the metal ion in multiple ways. First, the energies of the AOs are shifted by the LF. Second, the LF breaks the degeneracy between AOs which have different angular momentum projections (m_l) on the bonding axis, via the Stark effect. Last, the LF mixes AOs with the same m_l to form the MOs. In this case the valence MOs can be well described by linear combinations of a small number of AOs.

Labeling of electronic states

Atomic single-electron states are labeled by lower case letters corresponding to the electron's orbital angular momentum; s,p,d, and f for angular momenta of 0 , $1\hbar$, $2\hbar$, and $3\hbar$ respectively. Multi-electron atomic states are labeled with capital letters

corresponding to the total electron angular momenta; S, P, D, F, etc, with the capital letters corresponding to the same angular momentum as the lower case ones. In linear molecules, the molecular bond breaks the spherical symmetry of the system so that only the projection of the orbital angular momentum on the molecular axis, Λ , is relevant. Lower case Greek letters ($\sigma, \pi, \delta, \phi$) and capital Greek letters ($\Sigma, \Pi, \Delta, \Phi$) correspond to single electron and total electronic angular momenta projections of $0, 1\hbar, 2\hbar$, and $3\hbar$ respectively.

Atomic electronic states are denoted by the term symbols $^{2S+1}L_J$ where S is the total electron spin, L is the total electronic angular momentum (S, P, D, F, etc.), and J is the total angular momentum, $J = L + S$. The term symbols for molecular electronic states follow a similar convention where each electronic state is denoted by the term symbol $^{2S+1}\Lambda_\Omega$ where S again is the total electron spin, Λ is the projection of the total electronic angular momentum on the internuclear axis ($\Sigma, \Pi, \Delta, \Phi$ for $\Lambda = 0, 1\hbar, 2\hbar, 3\hbar$), and $\Omega = \Lambda + \Sigma$ which is the projection of the total electronic angular momentum J_e along the internuclear axis. Here, Σ denotes the projection of the total electron spin on the internuclear axis (not to be confused with the term symbol of Σ for an electronic state with $\Lambda = 1$). Oftentimes one can think of molecular Σ states (e.g., $^2\Sigma_{1/2}$ states) as being similar to atomic S states (e.g., $^2S_{1/2}$ states) and similarly for molecular Π , and Δ states and atomic P and D states.

2.3 Vibrational structure

Each electronic state has a ladder of vibrational states. The vibrational energies and wavefunctions are given by solving the vibrational Schrödinger equation, $\hat{H}_v\psi_v = (\hat{T}_n + \hat{V}_n)\psi_v = E_v\psi_v$, where \hat{V}_n is the PES given by solving Eq. 2.10 and \hat{T}_n is the kinetic energy of the nuclei. If the amplitude of the vibrations is small, such that the nuclei do not move far from the equilibrium position, the PES can be approximated as a harmonic potential¹. Working in the normal coordinate system the vibrational Hamiltonian can then be expressed² as a sum of $3N_n - 5$ harmonic

¹More accurate potentials which better describe the actual PES can also be used. One example is the Morse potential for which exact analytical solutions to the Schrödinger equation are known [80].

²Linear molecules have $3N_n - 5$ vibrational degrees of freedom. All molecules have $3N_n$ degrees of freedom but in the linear case there are 3 degrees of freedom for translation and only 2 for rotation, leaving $3N_n - 5$ vibrational degrees of freedom. Linear molecules only have 2 rotational degrees of freedom because they are symmetric about their internuclear axis. Non-linear molecules are not limited in this manner and have 3 rotational degrees of freedom.

oscillator Hamiltonians [81],

$$\hat{H}_v = \sum_{i=1}^{3N_n-5} \left(-\frac{\hbar^2}{2} \frac{\partial^2}{\partial Q_i^2} + \frac{1}{2} \omega_i^2 Q_i^2 \right), \quad (2.14)$$

where Q_i are the $3N_n - 5$ normal coordinates and ω_i are the vibrational frequencies of each normal mode. In this normal coordinate system the vibrational Schrödinger equation factors into $3N_n - 5$ independent single quantum harmonic oscillator equations allowing each of the $3N_n - 5$ normal vibrational modes of the molecule to be treated separately. The solution to the quantum harmonic oscillator is known and the total vibrational wavefunction of the molecule is given by the product of the individual vibrational wavefunctions of each normal mode,

$$\psi_v = \prod_{i=1}^{3N_n-5} \psi_{v,i}(Q_i). \quad (2.15)$$

The total vibrational energy is then given by the sum of the energy of each normal mode,

$$E_v = \sum_{i=1}^{3N_n-5} E_i = \sum_{i=1}^{3N_n-5} \hbar \omega_i \left(v_i + \frac{d_i}{2} \right), \quad (2.16)$$

where d_i is the degeneracy of the vibrational mode.

In reality the vibrational potential is not perfectly harmonic and anharmonic terms must be added, which becomes especially important when dealing with larger vibrations. These anharmonic terms mix the wavefunctions of the different normal modes so that the resulting eigenstates are linear combinations of the harmonic wavefunctions. The energies of the vibrational states are then given by [82],

$$\begin{aligned} \frac{E_v}{\hbar} = & \sum_{i=1}^{3N_n-5} \omega_i \left(v_i + \frac{d_i}{2} \right) \\ & + \sum_{i=1}^{3N_n-5} \sum_{k \geq i} x_{ik} \left(v_i + \frac{d_i}{2} \right) \left(v_k + \frac{d_k}{2} \right) + \sum_{i=1}^{3N_n-5} \sum_{k \geq i} x_{ik} g_{ik} l_i l_k, \end{aligned} \quad (2.17)$$

where x_{ik} and $g_{i,k}$ are the anharmonicity constants and l_i and l_k are the angular momentum of the degenerate bending vibrations.

Bending modes in linear polyatomic molecules

In linear polyatomic molecules there are two types of vibrational modes: stretching modes and bending modes. For example, the linear triatomic molecule YbOH has three vibrational modes: two stretching modes, the Yb-O and O-H stretch, and

one bending mode, the molecule bending so the angle between the Yb-O and O-H bonds is smaller than 180° . Unlike stretching modes, bending modes are doubly degenerate, one mode bending in the x,z-plane and the other in the y,z-plane (here the z-axis is the internuclear axis). In this case, the Hamiltonian for the bending vibrations can be represented as that of a two-dimensional harmonic oscillator instead of two separate one-dimensional oscillators with the same normal frequency [83, 84],

$$\hat{H}_{bend} = -\frac{\hbar^2}{2} \left(\frac{\partial^2}{\partial Q_x^2} + \frac{\partial^2}{\partial Q_y^2} \right) + \frac{1}{2} \omega_{bend}^2 (Q_x^2 + Q_y^2). \quad (2.18)$$

If the two-dimensional oscillator is solved in polar planar coordinates ($Q_x = r \cos(\phi)$ and $Q_y = r \sin(\phi)$, where r is bending amplitude and ϕ bending angle), the wavefunctions take the form $\psi_{bend}(r, \phi) = \psi(r) \exp(il\phi)$ where l must take integer values [83]. Plugging this solution into the bending Schrödinger equation ($\hat{H}_{bend}\psi_{bend} = E_{bend}\psi_{bend}$) and integrating over ϕ results in a one-dimensional Schrödinger equation with an effective potential,

$$V_{bend,eff} = \frac{\hbar\omega_{bend}}{2} \left(r^2 + \frac{l^2}{r^2} \right). \quad (2.19)$$

This effective potential corresponds to a harmonic oscillator with an angular momentum barrier due to the rotation of the bent molecule about the internuclear axis. The projection of this rotational angular momentum along the internuclear axis is given by $\hbar l$. This bending angular momentum must take on values of $l = \nu, \nu - 2, \nu - 4, \dots, -\nu$, where ν is the quanta of the bending vibration. Additionally, the solutions to Eq. 2.19, $\psi(r)$, with $l \geq 1$ take on values of zero ($\psi(r) = 0$) at $r = 0$ [83]. Therefore, when there is bending angular momentum due to rotation, $l \geq 1$, the molecule never assumes a linear configuration, $r \neq 0$, and instead resembles a bent molecule rotating about the “former” internuclear axis.

A more intuitive classical picture of the bending modes and their associated angular momentum can be gained by returning to the picture of degenerate bending motions in the separate x,z and y,z-planes. Since these modes are degenerate any linear combination of them is also a solution. If these two x and y bends are combined with a 90° phase difference it corresponds to a “bent” molecule orbiting around the “former” internuclear axis. This orbiting nuclei has an associated angular momentum which must be quantized along the internuclear axis in integer units of \hbar .

The states with opposite values of l (the parity eigenstates are actually the linear combinations $\frac{1}{\sqrt{2}} (|+l\rangle \pm |-l\rangle)$) are nominally degenerate. However, this degener-

acy is broken by the end-over-end rotation of the molecule (Coriolis interactions). This is described in more detail in Section 2.7. The degeneracy between bending states of the same bending quanta, ν_{bend} , but different values of l , is broken by anharmonic terms in the vibrational Hamiltonian.

Due to the additional angular momentum from the bending vibrations, it is convention to label bending vibronic states by the combination of the total electronic and vibrational angular momentum, $K = \Lambda + l$. Then vibronic states are denoted by the term symbol $^{2S+1}K_P$ where $P = \Lambda + \Sigma + l$ is now the projection of the total angular momentum J on the internuclear axis. Capital Greek letters are still used to denote the values of K ($\Sigma, \Pi, \Delta, \Phi$ for $K = 0, 1\hbar, 2\hbar, 3\hbar$). The degeneracy between the states of different K in the same electronic state are broken by vibronic perturbations. Note that this can often lead to confusion as a molecule can be in a $^2\Pi$ vibronic state while in a $^2\Sigma$ electronic state. This is the case for the lowest bending mode of the ground electronic state of YbOH.

Vibronic Interactions: The Renner-Teller effect

So far we have assumed that the motion of the nuclei, e.g., vibrations, does not affect the electronic configuration of the molecule. This approximation is good for molecules in electronic states with $\Lambda = 0$ or for stretching vibrations; however, it breaks down for degenerate electronic states with bending vibrations. Electronic states with non-zero projections of orbital angular momentum, $\Lambda \geq 1$, are degenerate due to the cylindrical symmetry of the linear molecule. When the molecule begins to bend, the cylindrical symmetry is broken and the bending induces an electric dipole moment which perturbs the electronic structure and mixes electronic states. This creates a coupling between the orbital and vibrational angular momenta, Λ and l , and breaks the degeneracy of the electronic state. This coupling is called the Renner-Teller effect and it can be included as a perturbation with the following Hamiltonian [85],

$$\hat{H}_{RT}/hc = V_{11} \left(Q_+ e^{-i\theta} + Q_- e^{i\theta} \right) + V_{22} \left(Q_+^2 e^{-2i\theta} + Q_-^2 e^{2i\theta} \right) + O \left(Q_{\pm}^3 \right), \quad (2.20)$$

where Q_{\pm} are the bending vibrational angular momentum raising and lowering operators (see Ref. [84, 85] for the matrix elements), θ is the electron azimuthal angle, $e^{\pm i\theta}$ acts as a raising and lowering operator for Λ , and V_{11} and V_{22} quantify the strength of the coupling. The first term in \hat{H}_{RT} mixes states with $\Delta\nu_{bend} = \pm 1$, $\Delta l = \pm 1$, $\Delta\Lambda = \mp 1$, and $\Delta K = 0$ while the second term mixes states with $\Delta\nu_{bend} = \pm 2$, $\Delta l = \pm 2$, $\Delta\Lambda = \mp 2$, and $\Delta K = 0$. \hat{H}_{RT} acts to mix neighboring electronic states

with the same value of K . For example, in a Π state \hat{H}_{RT} mixes in neighboring Σ and Δ electronic states.

For Π electronic states, an effective Hamiltonian which encompasses the effects of the Renner-Teller interaction but only operates within the manifold of the Π electronic state can be derived [84],

$$\hat{H}_{RT,\Pi}/hc = \frac{1}{2}\epsilon\omega_2 \left(q_+^2 e^{-2i\theta} + q_-^2 e^{2i\theta} \right) + g_K (G_z + L_z) L_z, \quad (2.21)$$

where ω_2 is the frequency of the bending vibration, $q_{\pm} = \sqrt{\frac{hc\omega_2}{\hbar^2\mu_2}} Q_{\pm}$ (μ_2 is the reduced mass of the bending vibration), and $G_{l,z}$ and L_z are the projections of the vibrational and electron orbital angular momentum, G_l^3 and L , along the internuclear axis. The parameters $\epsilon\omega_2$ and g_K are what are spectroscopically determined, and their relation the the parameters in Eq. 2.20 are [84]:

$$\epsilon\omega_2 = \epsilon^{(1)}\omega_2 + \epsilon^{(2)}\omega_2 \quad (2.22)$$

$$\epsilon^{(1)}\omega_2 = \left(\frac{\hbar}{hc} \right)^2 \omega_2^{-1} \langle \eta | V'_{22} | \eta' \rangle \quad (2.23)$$

$$\epsilon^{(2)}\omega_2 = -\frac{1}{2} \left(\frac{\hbar}{hc} \right)^2 \omega_2^{-1} \sum_{\Sigma \text{ states}} (-1)^s |\langle \eta | V'_{11} e^{i\theta} | \eta \rangle|^2 \frac{1 + (hc\omega_2/\Delta E)^2}{\Delta E} \quad (2.24)$$

$$g_k = \frac{\hbar^2}{4hc} \sum_{\eta'} (-1)^p \frac{|\langle \eta | V'_{11} | \eta' \rangle|^2}{(\Delta E)^2}. \quad (2.25)$$

In the above equations $V'_{ii} = 2V_{ii}/(\mu_2)^{i/2}$, η and η' refer to the Π or Σ and Δ states respectively, s is even or odd with respect to Σ^+ and Σ^- states respectively, $\Delta E = E_0(\eta', \Lambda') - E_0(\eta, \Lambda)$ is the energy difference between the zero-order electronic states, and p is even or odd for Σ and Δ states respectively. More detailed descriptions of the Renner-Teller effect can be found in [84–88].

2.4 Rotational structure

The rotational structure of diatomic and linear molecules can be obtained by considering the molecule as a rigid rotor. In the case of a linear molecule, the molecule can only rotate about a single axis,⁴ corresponding to end-over-end rotation of the

³The angular momentum associated with bending vibrations is traditionally denoted by G in the literature but here we use G_l to avoid confusion with the intermediate quantum number $G = S + I$ in the Hund's case $b_{\beta S}$ coupling scheme which deals with strong hyperfine couplings (see section 2.6).

⁴A linear molecule has two moments of inertia of equal magnitude which correspond to rotations about axes perpendicular to the internuclear axis and each other. The cylindrical symmetry of the molecule makes these axes indistinguishable such that there is only one distinct rotation, end-over-end motion. A linear molecule can not rotate about its axis of symmetry since the moment of inertia along this axis is zero.

molecule. The rotational Hamiltonian, \hat{H}_R , is the kinetic energy due to the angular momentum of this rotation. The energies and wavefunctions of the rotational states are found by solving the Schrödinger equation for a quantum rigid rotor [81],

$$\hat{H}_R \psi_R = \frac{\hbar^2}{2I} \mathbf{J}^2 \psi_R = E_R \psi_R, \quad (2.26)$$

where \mathbf{J} is the angular momentum of the rotation and I is the moment of inertia of the molecule about the rotational axis ($I = \sum_i m_i r_i^2$ where the sum is over all nuclei of mass m_i , and r_i is the distance from the center of mass). The solution to Eq. 2.26 in spherical coordinates are the spherical harmonics [81],

$$\psi_R = Y_J^M(\theta, \phi) = |J, M\rangle, \quad (2.27)$$

where here l is the angular momentum of the quantum state (J in the equation above) and m is the projection of J along the z-axis (the internuclear axis). The energies of the rotational states are [81],

$$E_R = \frac{\hbar^2}{2I} J(J+1) = BJ(J+1). \quad (2.28)$$

Here we have introduced the rotational constant, B , such that the rotational levels are separated by $BJ(J+1)$. Since B depends on the moment of inertia of the molecule, measurements of the rotational constant can allow the bond distances in the molecule to be determined. Additionally, since changing molecular isotopologues changes both the center of mass and the masses of the nuclei, the rotational constant differs between different isotopologues of the same molecule and scales as $1/I$.

2.5 The effective Hamiltonian

The BO approximation has allowed the separation of the molecular wavefunction into electronic, vibrational, and rotational parts. This is especially useful since the energies associated with these different interactions are orders of magnitude different; $\sim 10^4$ - 10^5 cm^{-1} for electronic states, $\sim 10^2$ - 10^3 cm^{-1} for vibrational states, and $\sim 10^{-1}$ - 1 cm^{-1} for rotational states. High-resolution molecular spectra can resolve spectral features separated by 10-100 MHz (much less than the rotational energy scale, noting that $1 \text{ cm}^{-1} \sim 30 \text{ GHz}$) and therefore interactions with energy scales equivalent or less than the rotational energies are relevant. Additionally, to adequately describe the energy levels of a molecule to the level needed to perform precision measurements and laser cooling, the fine and hyperfine structure of molecule must be included. Therefore, most of the relevant molecular interactions

occur at energy scales less than or equal to the rotational energy. When studying these interactions, it is often most convenient to construct an effective Hamiltonian, \hat{H}_{eff} , that only operates in the subspace of a single vibronic state. This can be accomplished by considering all interactions with energy scales smaller than the vibrational energy as perturbations⁵. The total Hamiltonian can then be written as [89],

$$\hat{H}_{tot} = \hat{H}_0 + \lambda \hat{H}_1. \quad (2.29)$$

H_0 is the zeroth-order Hamiltonian that includes the electronic and vibrational Hamiltonians such that

$$\hat{H}_0|\eta, i\rangle^0 = E_\eta^0|\eta, i\rangle^0, \quad (2.30)$$

where $E_\eta^0 = E_e + E_v$ is the energy of the vibronic state and $|\eta, i\rangle^0$ is the zeroth-order eigenfunction of the vibronic state. η denotes all the quantum numbers that describe the vibronic state (which is a solution to Eq. 2.30) and i describes all the degenerate quantum numbers for the state $|\eta\rangle^0$ (the rotational, electronic spin and nuclear spin degrees of freedom). What we are interested in determining are the eigenstates of the total Hamiltonian, $|\eta, k\rangle$,

$$\hat{H}_{tot}|\eta, k\rangle = (E_\eta^0 + E_{\eta,k})|\eta, k\rangle. \quad (2.31)$$

Here $|\eta, k\rangle$ are a linear combination of the zero-order eigenfunctions,

$$|\eta, k\rangle = \sum_{\eta', i} c_{\eta', i}^k |\eta', i\rangle^0. \quad (2.32)$$

We want to derive an effective Hamiltonian that only operates in the subspace of a single vibronic state, $|\eta\rangle^0$ and returns the correct eigenvalues given by the total Hamiltonian. Therefore, the effective Hamiltonian will satisfy the following eigenvalue equation,

$$\hat{H}_{eff}(\eta) \sum_i d_{\eta, i}^k |\eta, i\rangle^0 = (E_\eta^0 + E_{\eta, k}) \sum_i d_{\eta, i}^k |\eta, i\rangle^0. \quad (2.33)$$

If we define a projection operator

$$P_\eta = \sum_i |\eta, i\rangle^0 \langle \eta, i|^0, \quad (2.34)$$

⁵This section summarizes the derivation of H_{eff} given in ch. 7.2 of Ref. [89], to which the reader is referred for more details.

which projects a state $|\eta', k\rangle$ into the vibronic subspace $|\eta\rangle^0$, such that $P_\eta|\eta, k\rangle = \sum_i c_{\eta,i}^k |\eta, i\rangle^0$, and the opposite of the projection operator,

$$U = \sum_k \sum_i b_{\eta,j}^k |\eta, k\rangle \langle \eta, j|^0, \quad (2.35)$$

such that $U \sum_i c_{\eta,i}^k |\eta, i\rangle^0 = |\eta, k\rangle$, then it can be shown [89]

$$\hat{H}_{eff}(\eta) = \hat{H}_0 + \lambda P_\eta \hat{H}_1 P_\eta + \lambda^2 P_\eta \hat{H}_1 \frac{Q_\eta}{a} \hat{H}_1 P_\eta + \mathcal{O}(\lambda^3) \quad (2.36)$$

up to second order in λ (see Ref. [89] Eq. 7.43 for higher-order terms). Here

$$\frac{Q_\eta}{a^r} = \sum_{\eta' \neq \eta} \sum_i \frac{|\eta', i\rangle^0 \langle \eta', i|^0}{E_\eta - E_{\eta'}}. \quad (2.37)$$

In Eq. 2.36 the zeroth-order term gives the zero-order energies for the vibronic state and is a diagonal matrix with the values of the vibronic energy $E_e + E_v$ on the diagonal. The higher-order terms project the effects of the perturbing Hamiltonian, \hat{H}_1 , into the vibronic subspace, at different orders in perturbation theory, while preserving its effects on determining the correct eigenvalues of \hat{H}_{tot} . The effects of terms in \hat{H}_1 that are off diagonal in η (mix different vibronic states) are included in parameters in the effective Hamiltonian.

To illustrate this we can derive the effective rotational Hamiltonian for a single electronic state. The rotational Hamiltonian is

$$\hat{H}_R = B\mathbf{R}^2 = B(\mathbf{N} - \mathbf{L})^2 = B(\mathbf{N}^2 - N_z^2 + \mathbf{L}^2 - L_z^2 - N_+L_- - N_-L_+), \quad (2.38)$$

where \mathbf{R} is the angular momentum of the en-over-end rotation of the molecule (\mathbf{J} was used in Section 2.4 to better match the literature). As can be seen above, the operator \mathbf{R}^2 has terms off diagonal with respect to the electronic state (the N_+L_- and N_-L_+ terms) and therefore the rotational Hamiltonian has been expressed in terms of $\mathbf{N} = \mathbf{R} + \mathbf{L}$ ⁶, the total angular momentum minus spin. \mathbf{N}^2 is diagonal with respect to each vibronic state and, therefore, is considered by some to be the more natural

⁶This formulation of \mathbf{N} is for a non-bending state, for a bending state $\mathbf{N} + \mathbf{R} + \mathbf{L} + \mathbf{G}_l$. The extra terms added by the addition of the bending angular momentum which are off diagonal with respect to the vibronic state can be treated in the same way as those off diagonal with respect to the electronic state and will only add additional terms in the definition of the effective rotational constant (see the definition below).

way to frame the rotational Hamiltonian⁷. The $\mathbf{L}^2 - L_z^2$ term is diagonal in the vibronic state and can be neglected as it simply adds to the zero-order Hamiltonian as a constant energy offset.

We can now derive the form of the effective rotational Hamiltonian which operates in the subspace of a single vibronic state $|\eta\rangle$ by setting $\hat{H}_1 = \hat{H}_R$ in Eq. 2.36. To first order we have

$$\begin{aligned}\hat{H}_{R,eff}^{(1)} &= P_\eta \hat{H}_R P_\eta \\ &= |\eta\rangle\langle\eta| B(\mathbf{N}^2 - N_z^2 - N_+L_- - N_-L_+) |\eta\rangle\langle\eta| = B^{(1)}(\mathbf{N}^2 - N_z^2)\end{aligned}\quad (2.39)$$

where

$$B^{(1)} = \langle\eta|B|\eta\rangle. \quad (2.40)$$

Note above that we have dropped the i quantum numbers in kets since they define the basis we are projecting into, and we used the fact that for any operator \hat{O} that is diagonal in the space of vibronic states (e.g., $\langle\eta|\mathbf{O}|\eta'\rangle = \delta_{\eta,\eta'}\lambda_O$) $P_\eta \hat{O} P_\eta = \hat{O}$. The second-order term in $\hat{H}_{R,eff}$ is

$$\begin{aligned}\hat{H}_{R,eff}^{(2)} &= P_\eta \hat{H}_R \frac{Q_\eta}{a} \hat{H}_R P_\eta \\ &= |\eta\rangle \sum_{\eta' \neq \eta} \frac{\langle\eta| - B(N_+L_- + N_-L_+) |\eta'\rangle \langle\eta'| - B(N_+L_- + N_-L_+) |\eta\rangle}{E_\eta - E_{\eta'}} \langle\eta|,\end{aligned}\quad (2.41)$$

where we have not included the diagonal terms in $|\eta\rangle$ as they are equal to zero. For each value of η' in Eq. 2.41, there are four terms, $\langle\eta| - BN_\pm L_\mp |\eta'\rangle \langle\eta| - BN_\pm L_\mp |\eta'\rangle$ and $\langle\eta| - BN_\pm L_\mp |\eta'\rangle \langle\eta| - BN_\mp L_\pm |\eta'\rangle$. Noting that N_\pm is diagonal in $|\eta\rangle$ and $|\eta'\rangle$ and that only the terms with opposite L raising and lowering operators are non-zero we get

$$\hat{H}_{R,eff}^{(2)} = \sum_{\eta' \neq \eta} \frac{\langle\eta|BL_\mp |\eta'\rangle \langle\eta'|BL_\pm |\eta\rangle}{E_\eta - E_{\eta'}} N_\pm N_\mp = B^{(2)}(N_x^2 + N_y^2) = B^{(2)}(\mathbf{N}^2 - N_z^2) \quad (2.42)$$

⁷Describing the rotational Hamiltonian in terms of \mathbf{R}^2 is known as the \mathbf{R}^2 formalism while describing the rotational Hamiltonian in terms of \mathbf{N} is known as the \mathbf{N}^2 formalism. As to which formalism is more appropriate is up for debate. The \mathbf{R}^2 formalism more accurately models the end-over-end rotation (\mathbf{R} is the angular momentum of the end-over-end rotation) but requires evaluating matrix elements involving \mathbf{L} . The \mathbf{N}^2 formalism avoids the matrix elements involving \mathbf{L} but since the rotational Hamiltonian is described by \mathbf{N}^2 it does not represent the end-over-end rotation as accurately as the \mathbf{R}^2 formalism. Either formalism will accurately represent and model the rotational spectra. Which formalism is used is generally only important if you are trying to reproduce the calculated rotational energy levels. For a more detailed discussion see Ref. [90]

where

$$B^{(2)} = \sum_{\eta' \neq \eta} \frac{\langle \eta | BL_{\mp} | \eta' \rangle \langle \eta' | BL_{\pm} | \eta \rangle}{E_{\eta} - E_{\eta'}}. \quad (2.43)$$

Notice that $\hat{H}_{R,eff}^{(2)}$ has the same form as $\hat{H}_{R,eff}^{(1)}$ so we can write

$$\hat{H}_{R,eff} = B_{eff}(\mathbf{N}^2 - N_z^2) \quad (2.44)$$

with

$$B_{eff} = B^{(1)} + B^{(2)}. \quad (2.45)$$

We have constructed an effective Hamiltonian, $\hat{H}_{R,eff}$, which operates only within the vibronic subspace $|\eta\rangle$ that incorporates all the effects of the total Hamiltonian \hat{H}_R . The first-order term, $B^{(1)}$, incorporates the effects of \hat{H}_R that operate only within $|\eta\rangle$ (e.g., the end-over-end rotation) while the second-order term, $B^{(2)}$, incorporates the effects of \hat{H}_R mixing different vibronic states and projects them into the $|\eta\rangle$ subspace. Higher-order terms can be included in \hat{H}_{eff} and will include higher-order mixings of vibronic states, however the effects of higher-order terms have a smaller and smaller effect on the eigenvalues of \hat{H}_{eff} and therefore can be neglected.

The operator N_z^2 gives a value of $\Lambda^2 + l^2$ in any vibronic state. Therefore, the term $B_{eff}N_z^2$ provides a constant offset to the initial energy of the vibronic state. Therefore, the effective rotational Hamiltonian can be expressed as,

$$\hat{H}_{R,eff} = B_{eff}\mathbf{N}^2. \quad (2.46)$$

The beauty of the effective Hamiltonian approach lies in the fact the energy levels of a vibronic state can be computed without diagonalizing the full Hamiltonian of the molecule. Therefore, to predict the spectrum for a single vibronic band, the energies and wavefunctions of each state can be calculated separately and then the transitions between each set of states computed. If you fit a measured spectrum to the calculated one, the parameters in the effective Hamiltonian can be determined. These parameters provide insight into each molecular state as well as other excited states in the molecule (through higher-order contributions to these parameters, such as $B^{(2)}$). In addition to rotation, fine and hyperfine terms are also included in the effective Hamiltonian, and the terms relevant for modeling YbOH and other molecules in doublet states are given in Sections 2.7 and 2.8.

2.6 Angular momentum coupling and Hund's cases

When diagonalizing an effective Hamiltonian it is often best to choose a basis (the i quantum numbers in $|\eta, i\rangle^0$) in which \hat{H}_{eff} is most diagonal. While \hat{H}_{eff} can be

diagonalized in any basis, choosing the one in which \hat{H}_{eff} is most diagonal will result in the eigenfunctions of \hat{H}_{eff} having a large overlap with the basis functions, $|\eta, i\rangle^0$. The eigenfunctions closely resembling the basis function allow one to develop a good intuition for what the eigenstates look like in terms of the basis functions. The basis in which \hat{H}_{eff} is most diagonal is determined by the relative strength of the interactions in \hat{H}_{eff} and how these interactions couple the angular momentum in the molecule. These angular momentum couplings are described by Hund's coupling cases [89]. There are five Hund's coupling cases but we will only describe the first two, as the molecular states of YbOH are best described by these two cases. First we will describe the coupling cases in the absence of hyperfine structure (no nuclear spins) and then introduce the coupling cases in the presence of hyperfine structure. The relevant angular momenta and their projections on the internuclear axis \hat{n} , in the absence of nuclear spins, are shown in Table 2.1.

Hund's case (a)

For Hund's case (a) to provide a good description of the molecular state, two conditions must be met. First, the electron orbital angular momentum is strongly coupled to the internuclear axis and, second, that the electron spin \mathbf{S} is strongly coupled to \mathbf{L} via spin orbit coupling (spin orbit coupling is discussed in Section 2.7). In this case \mathbf{L} and \mathbf{S} precess rapidly about the internuclear axis so that their projections on the internuclear axis, Λ and Σ respectively, are well defined [89]. The quantum number $\Omega = \Lambda + \Sigma$ is also well defined. Additionally, if the molecule is in a bending state, Ω couples to the bending angular momentum \mathbf{G}_l to give the quantum number $P = \Omega + l$. P (or Ω if $l = 0$) couples to the end-over-end rotation \mathbf{R} to give the total angular momentum \mathbf{J} . The basis vectors for Hund's case (a) are

$$|\eta, \Lambda; \nu_{bend}, l; S, \Sigma; J, \Omega, M_J\rangle = |\eta, \Lambda\rangle|\nu_{bend}, l\rangle|S, \Sigma\rangle|J, \Omega, M_J\rangle, \quad (2.47)$$

where here η again refers to all the quantum numbers specifying the vibronic state defining the space in which \hat{H}_{eff} operates. M_J is the projection of the total angular momentum \mathbf{J} onto the laboratory z-axis. In the absence of external electric or magnetic fields, the different M_J states are $(2J + 1)$ -fold degenerate. The right side of Eq. 2.47 is included to indicate that this basis vector is an uncoupled basis where the kets can be separated. Hund's case (a) is generally relevant for vibronic states with non-zero projections of \mathbf{L} on the internuclear axis ($\Lambda \geq 0$)⁸.

⁸The more technical definition for when Hund's case (a) is relevant is that the spin orbit interaction is much larger than the rotation, $A\Lambda \gg BJ$.

Table 2.1: Relevant molecular angular momenta, in the absence of nuclear spins, and their projections on the internuclear axis \hat{n} [89, 91].

Angular Momentum	Projection on \hat{n}	Description
\mathbf{L}	Λ	total electron orbital angular momentum
\mathbf{S}	Σ	total electron spin angular momentum
\mathbf{G}_l	l	bending angular momentum
\mathbf{R}		rotational angular momentum (end-over-end)
$\mathbf{N} = \mathbf{R} + \mathbf{L} + \mathbf{G}_l$ ^a	$K = \Lambda + l$	total angular momentum minus spin
$\mathbf{J} = \mathbf{N} + \mathbf{S}$	$P = K + \Sigma$	total angular momentum
$\mathbf{J}_e = \mathbf{L} + \mathbf{S}$	$\Omega = \Lambda + \Sigma$ ^b	total electronic angular momentum

^a Also given by $\mathbf{N} = \mathbf{J} - \mathbf{S}$.

^b In diatomic molecules and linear molecules with no bending vibrations Ω is the projection of the total angular momentum \mathbf{J} . The quantum number P is not used in this case since $P = \Omega$.

Hund's case (b)

In the situation where there is little or no spin orbit coupling (e.g., $\Lambda = 0$), the spin is decoupled from the internuclear axis and Hund's case (b) provides a good description of the molecular state [89]. Since the spin is decoupled from the internuclear axis, \mathbf{N} , the total angular momentum minus spin, and its projection, $K = \Lambda + l$, are good quantum numbers. Additionally, Σ and Ω are not well defined. The electron spin, \mathbf{S} , will then couple to the nuclear rotation, \mathbf{N} (via spin rotation discussed in Section 2.7), to give the total angular momentum \mathbf{J} . The basis vectors for Hund's case (b) are

$$|\eta, \Lambda; \nu_{bend}, l; N, K, S, J, M_J\rangle. \quad (2.48)$$

Hund's case (b) provides a good description for molecular states with $\Lambda = 0$ or the rare case where the energy scale of the spin orbit coupling is smaller than the rotation [89].

Angular momentum coupling with nuclear spins

If one or more nuclei in the molecule has a non-zero spin, \mathbf{I} , the nuclear spin will couple to the other angular momenta present in the molecule. Here we describe two special cases of coupling schemes involving the nuclear spin. The first is Hund's case ($a_{\beta J}$). Just as in Hund's case (a), in Hund's case ($a_{\beta J}$) \mathbf{L} and \mathbf{S} are coupled to the internuclear axis so that Λ , Σ , Ω , and P are well defined and P couples to \mathbf{R} to give \mathbf{J} . Hyperfine interactions (discussed in Section 2.8) couple the nuclear spin to \mathbf{J} to give the total angular momentum⁹ $\mathbf{F} = \mathbf{J} + \mathbf{I}$. The basis vectors for Hund's case ($a_{\beta J}$) are

$$|\eta, \Lambda; \nu_{bend}, l; S, \Sigma; J, \Omega, I, F, M_F\rangle. \quad (2.49)$$

Hund's case ($a_{\beta J}$) is a good description of molecular states with $\Lambda \geq 1$ and spin orbit coupling.

In the absence of spin orbit coupling ($\Lambda = 0$) and when the hyperfine interactions are strong, Hund's case ($b_{\beta S}$) provides a good description of the molecular state. As in Hund's case (b) the electron spin is decoupled from the internuclear axis; however, now the strong hyperfine interactions cause the electron spin, \mathbf{S} to couple to the nuclear spin \mathbf{I} before coupling to the rotation \mathbf{N} . The coupling of \mathbf{S} to \mathbf{I} gives the intermediate quantum number $\mathbf{G} = \mathbf{S} + \mathbf{I}$ which then couples to the rotation to give the total angular momentum¹⁰ \mathbf{F} . The basis vectors for Hund's case ($b_{\beta S}$) are

$$|\eta, \Lambda; \nu_{bend}, l; S, I, G, N, K, F, M_F\rangle. \quad (2.50)$$

Hund's case ($b_{\beta S}$) is a good description of molecular states with $\Lambda = 0$ and hyperfine interactions whose energy scales are larger than the rotational energy scale.

2.7 Fine structure and parity doublets

Now that we have introduced the various basis sets defined by the Hund's cases we can look at the various terms in the effective Hamiltonian. In addition to

⁹If the molecule contains more than one nuclear spin, following the coupling of \mathbf{J} to the first nuclear spin \mathbf{I}_1 , denoted \mathbf{F}_1 in this case, the intermediate quantum number \mathbf{F}_i will sequentially couple to each nuclear spin, \mathbf{I}_{i+1} , to give the final total angular momentum \mathbf{F} .

¹⁰If there is another nuclear spin with which the hyperfine interactions are smaller, \mathbf{G} will first couple to \mathbf{N} to give \mathbf{F}_1 before coupling with the other nuclear spins to give the total angular momentum \mathbf{F} .

the molecular rotation, the other terms in the effective Hamiltonian generally fall into two classes: fine and hyperfine structure. This section will cover the fine structure terms which describe the interactions of the the electron spin with the other angular momenta (not including the nuclear spins) in the molecule. The effective Hamiltonian for the fine structure of the molecule is given by

$$\hat{H}_{FS} = \hat{H}_{SO} + \hat{H}_{SR} + \hat{H}_{\Lambda D} + \hat{H}_{lD} + \hat{H}_{CD}. \quad (2.51)$$

The terms in \hat{H}_{FS} are as follows; spin orbit, spin rotation, Λ doubling, l doubling, and centrifugal distortions. We will discuss each term in more detail below¹¹.

Spin orbit

The spin orbit interaction results from the coupling of the magnetic moment of the electron with the magnetic field seen by the electron as it moves through the Coulomb field of the nucleus. This causes the electron spin \mathbf{S} to couple to the orbital angular momentum of the electron, \mathbf{L} . Therefore, $\hat{H}_{SO} \propto \mathbf{L} \cdot \mathbf{S} = L_z S_z + \frac{1}{2}(L_+ S_- + L_- S_+)$ which has terms which mix electronic states that must be dealt with in a manner similar to how we dealt with the off-diagonal terms in the rotational Hamiltonian (see Ref. [89] for a derivation of the effective spin orbit Hamiltonian to second order). The effective spin orbit Hamiltonian takes the form [89]

$$\hat{H}_{SO} = A L_z S_z, \quad (2.52)$$

where $A = A^{(1)} + A^{(2)}$ and $A^{(1)}$ accounts for the first-order terms and $A^{(2)}$ accounts for the second-order terms that result from the mixing of electronic states. Definitions of $A^{(1)}$ and $A^{(2)}$ can be found in Eq. 7.109 and 7.120 in Ref. [89].

The effects of the spin orbit interaction can be seen by looking at the diagonal matrix elements of \hat{H}_{SO} in a case (a) basis,

$$\langle \eta, \Lambda; \nu_{bend}, l; S, \Sigma; J, \Omega, M_J | A L_z S_z | \eta, \Lambda; \nu_{bend}, l; S, \Sigma; J, \Omega, M_J \rangle = A \Lambda \Sigma. \quad (2.53)$$

\hat{H}_{SO} shifts the energy of each state by $A \Lambda \Sigma$. Consider a ${}^2\Pi$ electronic state where $\Lambda = \pm 1$, $\Sigma = \pm 1/2$, and $\Omega = \pm 1/2, \pm 3/2$. If Λ and Σ are aligned ($\Omega = \pm 3/2$) then $\Lambda \Sigma = 1/2$ and the state is shifted up by $A/2$. If Λ and Σ are anti-aligned ($\Omega = \pm 1/2$) then $\Lambda \Sigma = -1/2$ and the state is shifted down by $A/2$. This results in the separation of $\Omega = 1/2$ and $\Omega = 3/2$ components of a ${}^2\Pi$ state by A . This separation of the

¹¹We have not included the spin-spin interaction \hat{H}_{SS} in the fine structure Hamiltonian as it is only non-zero for states with $\mathbf{S} \geq 1$ and we are constraining our discussion to doublet molecular states ($\mathbf{S} = 1/2$).

different Ω components of an electronic state is known as spin orbit splitting. Note that for an electronic state with $\Lambda = 0$, the spin orbit interaction is not relevant as $\hat{H}_{SO} = 0$. At a fundamental level, the spin orbit interaction is a relativistic effect and therefore its strength increases with increasing atomic number. For molecules containing heavy nuclei, the spin orbit splitting can become so large the different spin orbit components are treated as separate electronic states. This is the case in YbOH.

Spin rotation

The spin rotation interaction accounts for the interaction of the electron's spin with the rotation of the molecule, \mathbf{N} . The rotation of a linear molecule will generate a magnetic field (the nuclei are charged and therefore their rotation will generate a current) which will interact with the magnetic moment of the electron. The effective Hamiltonian for the spin rotation interaction for a molecule of any symmetry is given in Equation (2.3.29) and (2.3.30) in [85], where the strength of the spin rotation coupling is parameterized by the tensor $T^k(\epsilon)$. $T^k(\epsilon)$ describes the coupling of the spin to the molecule's three-dimensional rotation (similar to how the moment of inertia tensor describes the rotation of a rigid body in three-dimensional space). For an axially symmetric molecule $T^k(\epsilon)$ has only three non-zero elements, the diagonal elements ϵ_{xx} , ϵ_{yy} , and ϵ_{zz} (again similar to how the moment of inertia tensor for an axially symmetric body is diagonal), and the spin rotation Hamiltonian is reduced to

$$\hat{H}_{SR} = (\epsilon_{xx} + \epsilon_{yy})(\mathbf{N} \cdot \mathbf{S} - N_z S_z) + 2\epsilon_{zz} N_z S_z = \gamma(\mathbf{N} \cdot \mathbf{S} - N_z S_z) + \gamma' N_z S_z. \quad (2.54)$$

For an axially symmetric molecule $\epsilon_{xx} = \epsilon_{yy} = \gamma/2$, where γ is the spin rotation parameter and $\gamma' = 2\epsilon_{zz}$ is the parameter describing the coupling of spin to rotation about the axis of symmetry. \hat{H}_{SR} has different effects in bending and non-bending states so we will examine each separately.

Spin rotation in linear vibrational states ($l = 0$)

For a diatomic molecule or a linear molecule in a state with $l = 0$, rotation about the internuclear axis is not possible, resulting in $\gamma' = 2\epsilon_{zz} = 0$. Therefore only end-over-end rotation is possible and results in rotational angular momentum perpendicular to the internuclear axis such that $N_z = 0$. Taking this into account, the effective Hamiltonian for the spin rotation interaction in a linear state with $l = 0$ reduces to

¹² [89]

$$\hat{H}_{SR} = \gamma \mathbf{N} \cdot \mathbf{S}. \quad (2.55)$$

In a given rotational level, \mathbf{N} , the spin rotation interaction given in Eq. 2.55 lifts the degeneracy between states with different values of \mathbf{J} ($\mathbf{J} = \mathbf{N} + \mathbf{S}$ and $\mathbf{J} = \mathbf{N} - \mathbf{S}$) so that they are separated by an energy of $\gamma(1/2 + \mathbf{N})$. This splitting is known as spin rotation splitting.

As with other parameters in the effective Hamiltonian, the spin rotation parameter can have contributions from first- and higher-order terms, $\gamma = \gamma^{(1)} + \gamma^{(2)} + \mathcal{O}(3)$. The first-order contribution, $\gamma^{(1)}$, comes directly from the coupling of the electron's spin to the magnetic moment of the rotating nuclei. However, the contribution of $\gamma^{(1)}$ to γ is very small due to the very small magnetic moment generated by the orbiting nuclei. Therefore, the spin rotation parameter is dominated by the second-order contributions given by $\gamma^{(2)}$. The second-order contributions arise from interactions of the off diagonal terms in the rotation and spin orbit Hamiltonians which, when projected into the vibronic subspace, result in an effective operator of the form $\mathbf{N} \cdot \mathbf{S}$. The second-order contributions to the spin rotation parameter are given by [89]

$$\gamma^{(2)} = -2 \sum_{\eta'} \left[\frac{\langle \eta, \Lambda, \Sigma | BL_- | \eta', \Lambda + 1, \Sigma \rangle \langle \eta', \Lambda + 1, \Sigma | \hat{H}_{SO} | \eta, \Lambda, \Sigma + 1 \rangle}{(E_\eta - E_{\eta'}) \langle S, \Sigma | S_- | S, \Sigma + 1 \rangle} + \frac{\langle \eta, \Lambda, \Sigma | \hat{H}_{SO} | \eta', \Lambda - 1, \Sigma + 1 \rangle \langle \eta', \Lambda - 1, \Sigma + 1 | BL_- | \eta, \Lambda, \Sigma + 1 \rangle}{(E_\eta - E_{\eta'}) \langle S, \Sigma | S_- | S, \Sigma + 1 \rangle} \right]. \quad (2.56)$$

$\gamma^{(2)}$ results from the combination of the rotation and spin rotation mixing in other electronic states with $\Lambda' = \Lambda \pm 1$ and therefore measurements of γ can provide information about other electronic states in the molecule. The effects of excited electronic states on the value of γ in the $\tilde{X}^2\Sigma^+$ state of YbOH are discussed in more detail in Section 4.3 and 6.5.

Spin rotation in bending states ($l \geq 1$)

If the molecule is in an excited bending state with $l \geq 1$, then $N_z \neq 0$ and the molecule “rotates” about the interuclear axis due to the bending angular momentum. This rotation about the internuclear axis also results in $\gamma' = 2\epsilon_{zz} \neq 0$. In this case, the operator form of \hat{H}_{SR} given in Eq. 2.55 does not correctly account for the rotation

¹²While using the functional form $\hat{H}_{SR} = \gamma \mathbf{N} \cdot \mathbf{S}$ for the spin rotation interaction is correct for diatomic molecules and linear molecules in states with $\nu_{bend} = 0$, since $N_z S_z$ component of $\mathbf{N} \cdot \mathbf{S}$ is zero, it is incorrect for states with $l > 0$ since $N_z = l \neq 0$, and the form of the spin rotation Hamiltonian given in Eq. 2.54 must be used.

about the internuclear axis and Eq. 2.54 must be used. The form of Eq. 2.54 is easily understood. For the value of γ to be consistent with the linear definition (describing the coupling of \mathbf{S} to the end-over-end rotation), the contribution from the bending angular momentum, $N_z S_z$ must be subtracted. However, this bending angular momentum will also couple to \mathbf{S} and is accounted for by the second γ' term. For states with $l \geq 1$, the spin rotation interaction still creates an energy splitting between the $\mathbf{J} = \mathbf{N} \pm \mathbf{S}$ states, but now the spin rotation splitting is given by [91]

$$\Delta_{SR} = \frac{(2N+1)(N(N+1)-l^2)}{2N(N+1)}\gamma + \frac{(2N+1)l^2}{N(N+1)}\gamma'. \quad (2.57)$$

The first-order contribution to γ' is very small, again due to the small magnetic moment generated by the rotating nuclei. Therefore, for the γ' term in Eq. 2.54 to make any significant contribution to the effective Hamiltonian, the second-order contributions to γ' must be significant.

Parity doubling

In the absence of external electromagnetic fields, \hat{H}_{eff} conserves parity and therefore the eigenstates of \hat{H}_{eff} have well-defined parity. These states are given by taking the sum and difference of the states with opposite projections of each angular momentum

$$|J, +\rangle = |\eta, \Lambda; \nu_{bend}, l; S, \Sigma, J, P\rangle + (-1)^{J-S} |\eta, -\Lambda; \nu_{bend}, -l; S, -\Sigma, J, P\rangle, \quad (2.58)$$

$$|J, -\rangle = |\eta, \Lambda; \nu_{bend}, l; S, \Sigma, J, P\rangle - (-1)^{J-S} |\eta, -\Lambda; \nu_{bend}, -l; S, -\Sigma, J, P\rangle. \quad (2.59)$$

In the non-rotating molecule, the opposite parity states $\frac{1}{\sqrt{2}}(|\Lambda\rangle \pm |-\Lambda\rangle)$ and $\frac{1}{\sqrt{2}}(|l\rangle \pm |-l\rangle)$, are degenerate. However, the rotation of the molecule lifts this degeneracy and gives rise to parity doublets. An intuitive explanation of the origin of parity doubling can be found in Appendix A.4 of [47]. More technically, these parity doublets are generated by second-order interactions in the effective Hamiltonian. If we expand the rotational Hamiltonian $\hat{H}_R = B\mathbf{N}^2 = B(\mathbf{J} - \mathbf{L} - \mathbf{G}_l - \mathbf{S})^2$, we find cross terms of the form $B\mathbf{J} \cdot \mathbf{L}$ and $B\mathbf{J} \cdot \mathbf{G}_l$. These terms are known as the Coriolis terms and are responsible for parity doubling.

Λ doubling

The lifting of the degeneracy between the states $\frac{1}{2}(|\Lambda\rangle \pm |-\Lambda\rangle)$ is known as Lambda-doubling (Λ -doubling). As mentioned above, Λ -doubling arises at second order in the effective Hamiltonian. More specifically, it is the result of a combination of off diagonal terms from the spin orbit and rotational Hamiltonians

which connect states with $|\pm\Lambda\rangle$ to states with $|\mp\Lambda\rangle$ through the mixing with other electronic states [89]. The effective Λ -doubling Hamiltonian is given by ¹³

$$\hat{H}_{\Lambda D} = -\frac{1}{2}q(J_+^2 e^{-2i\theta} + J_-^2 e^{2i\theta}) + \frac{1}{2}(p + 2q)(J_+ S_+ e^{-2i\theta} + J_- S_- e^{2i\theta}), \quad (2.60)$$

where θ is the electron azimuthal angle and $e^{\pm i\theta}$ acts as a raising and lowering operator for Λ so that $\langle\Lambda = \pm 1|e^{\pm 2i\theta}|\Lambda = \mp 1\rangle = -1$, and p and q quantify the strength of the interaction due to the mixing with other electronic states. p results from the mixing with other electronic states due to the combination of the spin orbit and rotational Hamiltonians, while q results solely from mixing with other electronic states due to the rotational Hamiltonian. The expressions for p and q to second order can be found in Eq. (7.142) and (7.143) of [89].

***l*-doubling**

The lifting of the degeneracy between the states $\frac{1}{2}(|l\rangle \pm |-l\rangle)$ is known as *l*-doubling. *l*-doubling arises in a similar fashion to Λ -doubling with the only difference being that the terms involve bending angular momentum \mathbf{G}_l instead of the electronic orbital angular momentum \mathbf{L} . Therefore, *l*-doubling also only arises at second and higher orders in the effective Hamiltonian that cause mixing with other bending vibrational states. This is due to the combination of terms in the rotational Hamiltonian and the analogous spin orbit interaction for the bending angular momentum, $\mathbf{G}_l \cdot \mathbf{S}$ ¹⁴, which connect states with $|\pm l\rangle$ to states with $|\mp l\rangle$. The effective Hamiltonian for *l*-doubling is given by¹⁵ [84, 87]

$$\hat{H}_l D = -\frac{1}{2}q_{v2}(J_+^2 e^{-2i\phi} + J_-^2 e^{2i\phi}) + \frac{1}{2}(p_{v2} + 2q_{v2})(J_+ S_+ e^{-2i\phi} + J_- S_- e^{2i\phi}), \quad (2.61)$$

where $\langle l = \pm 1|e^{\pm 2i\phi}|l = \mp 1\rangle = +1$ and p_{v2} and q_{v2} quantify the mixing with other bending states and ultimately the strength of the *l*-doubling interaction. p_{v2} and q_{v2} are directly analogous to their counterparts in the Λ -doubling Hamiltonian.

Centrifugal distortions

So far we have treated the rotation of the molecule as that of a rigid rotor. However, the molecule is not a rigid rotor, and as the molecule rotates, the nuclei will experience a centrifugal force that will cause the nuclei to separate, increasing the effective

¹³We have omitted the term $(1/2)(o + p + q)(S_+^2 e^{-2i\theta} + S_-^2 e^{2i\theta})$ since it is only non-zero for states with $\mathbf{S} \geq 1$.

¹⁴This interaction is accounted for in the effective Hamiltonian by the γ' term in \hat{H}_{SR} in Eq. 2.54.

¹⁵Just as with Λ -doubling we have again dropped the term proportional to $(S_+^2 e^{-2i\phi} + S_-^2 e^{2i\phi})$ since it is only non-zero for states with $\mathbf{S} \geq 1$.

bond length. This increase in the bond length will increase the moment of inertia for the rotation and therefore decrease the effective rotational constant [81]. This effective bond lengthening will increase with increasing molecular rotation \mathbf{J} . The effect of these centrifugal forces on the rotational Hamiltonian is called centrifugal distortion. The effective Hamiltonian for centrifugal distortion is given by [89, 92]

$$\hat{H}_{CD} = -D\mathbf{N}^2\mathbf{N}^2 = -D\mathbf{N}^4, \quad (2.62)$$

where D is the centrifugal distortion parameter. The effect of \hat{H}_{CD} is to change the energy of the rotational levels such that

$$E_R = BJ(J+1) - D(J(J+1))^2 = (B - DJ(J+1))J(J+1), \quad (2.63)$$

so that there is a corrected rotational constant of $B - DJ(J+1)$. The magnitude of D is generally several orders of magnitude smaller than B so that the effects of centrifugal distortions on the energies of lower rotational states are negligible. However, the inclusion of \hat{H}_{CD} in the effective Hamiltonian is needed to accurately describe higher rotational states. Higher-order terms can also be added to account for higher-order corrections [81].

Centrifugal distortions also impact the other interactions in the effective Hamiltonian as well. Take spin rotation for example. If centrifugal distortions change the energy of the molecular rotations then they will change how the spin couples to that rotation in a manner that scales with the rotational quantum number \mathbf{J} . This centrifugal interaction between the spin rotation and the rotation is described by the spin rotation centrifugal distortion effective Hamiltonian [93]

$$\hat{H}_{SRCD} = \frac{1}{2}\gamma_D[\mathbf{N} \cdot \mathbf{S}, \mathbf{N}^2]_+, \quad (2.64)$$

where γ_D is the spin rotation centrifugal distortion parameter and $[A, B]_+ = AB + BA$, is the anticommutator. In general, any interaction described by a term in the effective Hamiltonian will have corrections due to centrifugal distortions. For an interaction described by an effective Hamiltonian of the form $\hat{H}_{\hat{O}} = \alpha\hat{O}$, the corresponding effective Hamiltonian for the centrifugal corrections is given by

$$\hat{H}_{\hat{O}CD} = \frac{1}{2}\alpha_D[\hat{O}, \mathbf{N}^2]_+, \quad (2.65)$$

where α_D is the centrifugal correction to the parameter α . In this manner, the centrifugal correction to the spin orbit (paramaterized by A_D) can be obtained by substituting $\hat{O} = L_z S_z$ in Eq. 2.65. Other interactions such as Λ -doubling can be

accounted for as well. Oftentimes, and especially for low-rotational states, these corrections will not make any significant or measurable changes to the energy levels, and they do not need to be included in the effective Hamiltonian.

2.8 Hyperfine structure

If the molecule contains one or more nuclei with non-zero nuclear spin, \mathbf{I} , hyperfine interactions will be present. The hyperfine interactions describe the magnetic and electronic interactions of the nuclear, electric, and magnetic moments with other angular momenta present in the molecule. Here we will only consider the interactions due to the nuclear magnetic dipole and nuclear electric quadrupole moments. The effects of hyperfine interactions are generally much smaller than those resulting from the fine structure, and therefore it is usually only necessary to include the first-order contributions to the effective Hamiltonian. These are the only contributions we will discuss here.

Magnetic dipole terms

The magnetic dipole terms describe the magnetic interactions between the magnetic dipole of the nucleus and the other magnetic moments in the molecule. Several of these interactions arise from interactions between the spin of the electron and the spin of the nucleus. These nuclear-electron spin-spin interactions are characterized by three terms in the effective Hamiltonian: the Fermi contact, dipole-dipole coupling, and the parity-dependent dipole-dipole terms. The effective Hamiltonian for the Fermi contact interaction is [89, 94]

$$\hat{H}_{b_F} = b_F \mathbf{I} \cdot \mathbf{S}, \quad (2.66)$$

where b_F is the Fermi contact parameter and is defined as [89, 94]

$$b_F = \frac{\mu_0}{4\pi h} \frac{8\pi}{3\Sigma} g_e g_N \mu_B \mu_N \langle \eta, \Lambda; S, \Sigma | \sum_i \mathbf{s}_i \delta(r) | \eta, \Lambda; S, \Sigma \rangle. \quad (2.67)$$

In Eq. 2.67, μ_0 is the vacuum permeability, g_e and g_N are the electron and nuclear g-factors, μ_B and μ_N are the Bohr and nuclear magneton, \mathbf{s}_i is the spin angular momentum of the i th electron, $\delta(r)$ is the Dirac delta function, r and θ (not used in Eq. 2.67 but will be used below) are polar coordinates, and the sum runs over all unpaired electrons. The Fermi contact interaction describes the magnetic contact interaction between the electron and nuclear spins arising from the overlap of the electron wavefunction with the nucleus (the $\delta(r)$ in Eq. 2.67). Therefore, measurements of the Fermi contact parameter provide information about how much

overlap the electron wavefunction has with the nucleus. Comparison of determined b_F values to atomic b_F values can provide experimental information on the atomic orbital composition of the MO.

The second magnetic dipole interaction is referred to as the anisotropic dipole-dipole interaction and describes the magnetic dipole-dipole interaction between the electron and nuclear magnetic dipole moments. The effective Hamiltonian for the dipole-dipole interaction is [89, 94]

$$\hat{H}_c = \frac{1}{3}c(3I_zS_z - \mathbf{I} \cdot \mathbf{S}), \quad (2.68)$$

where c is the dipole-dipole coupling parameter and is defined as

$$c = \frac{\mu_0}{4\pi h} \frac{3}{2\Sigma} g_e g_N \mu_B \mu_N \langle \eta, \Lambda; S, \Sigma | \sum_i \mathbf{s}_i \frac{(3\cos^2\theta_i - 1)}{r_i^3} | \eta, \Lambda; S\Sigma \rangle. \quad (2.69)$$

c is again dependent on the valence electron's wavefunction and therefore measurements of it can provide information about the valence MOs.

In Eq. 2.68 and 2.69, we only considered the terms from the magnetic dipole-dipole interaction which were diagonal in Λ . There are also terms off-diagonal in Λ , specifically those which connect states of $|\Lambda = \pm 1\rangle$ to states with $|\Lambda = \mp 1\rangle$ ¹⁶. These off-diagonal terms provide a hyperfine contribution to the Λ -doubling so that one component of a Λ -doublet obtains a different hyperfine shift than the other. Therefore, if the state in question has a non-zero value of Λ , the parity-dependent hyperfine interaction must be included. The effective Hamiltonian for this interaction is given by [89, 94]

$$\hat{H}_d = \frac{1}{2}d(S_+I_-e^{-2i\phi} + S_-I_+e^{2i\phi}), \quad (2.70)$$

where d is the parity-dependent hyperfine parameter and is given by

$$d = \frac{\mu_0}{4\pi h} \frac{3}{2} \frac{g_e g_N \mu_B \mu_N}{\sqrt{S(S+1) - \Sigma(\Sigma+1)}} \langle \eta, \Lambda = -1; S, \Sigma + 1 | \sum_i \mathbf{s}_i^+ \frac{(\sin^2\theta_i e^{-2i\phi_i})}{r_i^3} | \eta, \Lambda = +1; S, \Sigma \rangle \quad (2.71)$$

where \mathbf{s}_i^+ is the spin-raising operator for a single electron and ϕ_i is the azimuthal angle for the i th electron.

¹⁶There are also terms which change Λ by 1 and therefore would mix electronic state. These effects would only show up at second-order in the effective Hamiltonian and provide energy shifts much below any measurable limit so they are generally not included. These second order terms only become measurable when there are nearly degenerate electronic states [94].

Finally, if the molecular state has $\Lambda \geq 1$, there will be an additional magnetic hyperfine interaction describing the magnetic dipole interaction between the nuclear spin and the magnetic moment generated by the orbiting electron. This is analogous to the spin orbit interaction. The effective Hamiltonian for the nuclear spin orbit interaction to first order¹⁷ is given by [94]

$$\hat{H}_a = aI_zL_z, \quad (2.72)$$

where a is the nuclear spin orbit parameter and is given by

$$a = \frac{\mu_0}{4\pi\hbar} g_e g_N \mu_B \mu_N \frac{1}{\Lambda} \langle \eta, \Lambda; S, \Sigma | \sum_i \frac{l_{zi}}{r_i^3} | \eta, \Lambda; S, \Sigma \rangle. \quad (2.73)$$

In the above equation l_{zi} is the z-component of the single electron angular momentum operator of the i th electron. Note in the above discussion we have assumed that there is only one nucleus with non-zero spin. If the molecule contains multiple nuclei with non-zero spin then the above interactions with each nucleus must be accounted for separately. Therefore, if the molecule has j nuclei, the total magnetic dipole hyperfine effective Hamiltonian is give by¹⁸

$$\hat{H}_{\text{dipole HFS}} = \sum_j \hat{H}_{a_j} + \hat{H}_{b_{Fj}} + \hat{H}_{c_j} + \hat{H}_{d_j}. \quad (2.74)$$

Electric Quadrupole terms

If a nucleus has a nuclear spin of $\mathbf{I} \geq 1$ then the nucleus could have an observable quadrupole moment, a non-spherical distribution of mass and charge so that the nucleus resembles an ellipsoid. This non-spherical charge distribution will result in the nucleus having an electric quadrupole moment. This electric quadrupole moment will interact with the electric field gradient created between the positively charged nucleus and the negatively charged electrons. This will lead to different orientations of the quadrupole deformed nucleus in the electric field gradient having different energies. Since the orientation of the nucleus is given by the orientation of the nuclear spin, this will result in an interaction that is dependent on both the nuclear spin orientation and the magnitude of the electric field gradient. The effective Hamiltonian that describes this electric quadrupole interaction is [89]

$$\hat{H}_{EQ0} = e^2 Q q_0 \frac{(3I_z - \mathbf{I}^2)}{4I(2I - 1)}, \quad (2.75)$$

¹⁷Technically $\hat{H}_a = a\mathbf{I} \cdot \mathbf{L}$ but, just as with the spin orbit interaction, the effective operator is given by only the elements diagonal in $\eta, I_z L_z$.

¹⁸We have not included the nuclear spin rotation (analogous to fine structure spin rotation) terms in the effective dipole hyperfine Hamiltonian as they are not relevant for describing the structure of YbOH. The nuclear spin rotation effective Hamiltonian is $\hat{H}_{NSR} = C_I \mathbf{I} \cdot \mathbf{J}$.

where e is the charge of the electron and Q is the quadrupole moment of the nucleus. q_0 is the expectation value of the electric field gradient over the electronic wavefunction

$$q_0 = -2\langle\eta, \Lambda|T_{q=0}^2(\nabla E)|\eta, \Lambda\rangle = \frac{-1}{4\pi\epsilon_0 h}\langle\eta, \Lambda|\sum_i \frac{(3\cos^2\theta_i - 1)}{r_i^3}|\eta, \Lambda\rangle, \quad (2.76)$$

where ϵ_0 is the electric constant, $T_{q=0}^2(\nabla E)$ is the $q = 0$ component of the second-rank spherical tensor describing the electric field gradient¹⁹, and the sum over i is now taken over all electrons.

In Eq. 2.75 we have only included terms diagonal in Λ ; however, the electric quadrupole interaction also has terms off diagonal in Λ . As with the dipolar interactions, the terms which mix states with $\Delta\Lambda = \pm 1$ will cause electronic states to mix and will only become relevant at higher order. These terms are not included in the effective Hamiltonian. The off diagonal terms which connect states with $\Delta\Lambda = \pm 2$ are included in the non-axial electric quadrupole effective Hamiltonian

$$\hat{H}_{EQ2} = -e^2 Q q_2 \frac{(e^{-2i\theta} I_+^2 + e^{2i\theta} I_-^2)}{4I(2I - 1)}. \quad (2.77)$$

q_2 is the non-axial electric quadrupole coupling parameter and is determined by the non-diagonal effects of the electric field gradient

$$q_2 = -2\sqrt{6} \sum_{q=\pm 2} \langle\eta, \Lambda = \pm 1|T_q^2(\nabla E)|\eta, \Lambda = \mp 1\rangle, \quad (2.78)$$

where now the $T_{q=\pm 2}^2(\nabla E)$ are the $q = \pm 2$ components of the second-rank spherical tensor describing the electric field gradient. \hat{H}_{EQ2} has the selection rules $\Delta\Sigma = 0$ and $\Delta\Lambda = 2$ and therefore will only connect states with $\Delta\Omega = 2$. Therefore, in a ${}^2\Pi$ state, \hat{H}_{EQ2} will only connect states from different spin orbit components, the $\Omega = 1/2$ and $\Omega = 3/2$ states.

2.9 Molecular transitions

It is not possible to directly observe the energy levels of a molecule but only the transitions between two molecular states. These transitions are driven by the interaction of electromagnetic radiation (photons) and the molecule. These photons can directly interact with either the electrons to cause the electron to change states or the dipole moment of the molecule itself. The former induces rovibronic transitions

¹⁹An overview of spherical tensors including their relation to the Cartesian operators can be found in Ch. 5 of Ref. [89].

(a transitions between different rovibronic states) while the latter induces rotational transitions within a single vibronic state. By observing either the absorption or emission of photons when these transitions are driven, we can determine the transition frequencies and ultimately the energies of the states involved. In addition to providing a means to observe and measure molecules, molecular transitions can also be utilized to control and manipulate molecules (laser cooling, coherent state preparation, etc.).

We are interested in understanding electric dipole transitions ²⁰, how the electric dipole operator (first term in the multipole expansion of the electric field of the laser or microwaves) connects two different molecular states. For two given molecular states, the transition intensity or strength is given by the expectation value of the electric dipole operator, $\hat{\mu}$, between the two states

$$I = |\langle \alpha | \hat{\mu} | \beta \rangle|^2. \quad (2.79)$$

Here α and β describe all the quantum numbers of the ground and excited states.

Vibrational transitions

If we only consider vibronic transitions (e.g., the laser is broad enough that transitions from many rotational/fine/hyperfine states are excited at once so that the rotational, fine and hyperfine structure is unresolved) then the intensity is given by [81]

$$I_{vibronic} = |\langle \eta'', v'' | \hat{\mu} | \eta', v' \rangle|^2 = |\langle v'' | v' \rangle \langle \eta'' | \hat{\mu} | \eta' \rangle|^2 = q_{v'',v'} |\mu_{\eta'',\eta'}|^2, \quad (2.80)$$

where here we use η and v to describe the electronic vibrational wavefunctions respectively, and we have used the spectroscopic notation of the double prime and prime referring to the ground and excited states respectively. In Eq. 2.80 we have used the fact $\hat{\mu}$ does not operate on the vibrational coordinates. $q_{v'',v'}$ is known as the Frank Condon factor (FCF) which is the overlap integral of the vibrational wavefunctions

$$q_{v'',v'} = |\langle v'' | v' \rangle|^2 = \left| \int \psi_{v''} \psi_{v'}^* d\tau \right|^2. \quad (2.81)$$

If the electronic PES is known for both the ground and excited states, $q_{v'',v'}$ can be easily calculated. $\mu_{\eta'',\eta'}$ is the transition dipole moment (TDM) and is dependent on the specific nature of the electronic wavefunctions. While it is possible to calculate

²⁰There are also magnetic dipole, electric quadrupole, and higher-order transitions, however they are largely suppressed compared to electric dipole transitions and, for the transitions of interest here, are not discussed.

the TDM using numerical methods, it is often a measured quantity. For the set of different vibrational transitions between two electronic states, $\mu_{\eta'',\eta'}$ is constant and the relative transition intensities are only dependent on the FCFs.

Following excitation to an excited state $|\eta', \nu'\rangle$ the molecule will decay back down to the ground state (or some other lower state). The probability that the molecule will decay to a given vibrational state $|\eta'', \nu''\rangle$ is given by the vibrational branching ratio [91]

$$b_{\nu' \rightarrow \nu''} = \frac{q_{\nu'',\nu'} \omega_{\nu'',\nu'}^3}{\sum_{\nu''} q_{\nu'',\nu'} \omega_{\nu'',\nu'}^3}, \quad (2.82)$$

where $\omega_{\nu'',\nu'}$ is the frequency of the transitions from $|\eta'', \nu''\rangle$ to $|\eta', \nu'\rangle$. Therefore the probability of a vibrational decay is dependent on the FCF. This fact becomes important when laser cooling molecules.

Vibrational selection rules

Whether or not a vibrational transition is allowed is determined by $q_{\nu'',\nu'}$. From Eq. 2.81 we know that $q_{\nu'',\nu'} = 0$ if the product $\psi_{\nu''} \psi_{\nu'}^*$ is odd with respect to the origin of the coordinate system. This occurs when one of the wavefunctions is even and the other is odd. For a linear molecule, all stretching mode wavefunctions are even with respect to the origin and therefore nothing inherently prevents vibrational transitions between different stretching modes. However, for bending vibrations the situation is different. All bending wavefunctions with odd values of l are odd while even values of l are even. This results in the following vibrational selection rules for linear molecules: $\Delta l = 0$ and therefore $\Delta \nu_{bend} = 0, \pm 2, \pm 4, \dots$ More intuitively, this can be thought of in the following way. Since the photon only interacts with the valence electron's charge or the molecule's dipole moment, it can not cause a change in the bending angular momentum (similar to how a photon can't change the spin), and $\Delta l = 0$. For a more rigorous description of vibrational selection rules with respect to the molecular symmetry, see Ref. [81, 82].

It is important to note that forbidden $\Delta l \neq 0$ transitions do occur and are due to mixing from vibronic perturbations such as the Renner-Teller effect. For example consider the case of a ${}^2\Sigma^+(v_{bend} = 1) \rightarrow {}^2\Pi_{1/2}(v_{bend} = 0)$ transition which is normally forbidden. Vibronic and spin orbit interactions can mix the ${}^2\Pi_{1/2}(v_{bend} = 0)$ state with the bending mode of an excited Σ^- state so that the true wavefunction of the ${}^2\Pi_{1/2}(v_{bend} = 0)$ state is now $\psi = |{}^2\Pi_{1/2}(v_{bend}=0)\rangle + \epsilon |{}^2\Sigma^-(v_{bend} = 1)\rangle$. The ${}^2\Sigma^+(v_{bend} = 1) \rightarrow {}^2\Sigma^-(v_{bend} = 1)$ transition is not forbidden which will now

allow the ${}^2\Sigma^+(v_{bend} = 1) \rightarrow {}^2\Pi_{1/2}(v_{bend} = 0)$ to occur via intensity borrowing. A thorough calculation and measurement of this “forbidden” vibrational branching for CaOH, SrOH, and YbOH was done in Ref. [95].

Rotational and rovibronic transitions

If the rotational, fine, and hyperfine structure are resolved, then the transition intensity will also depend on the specifics of the rotational/fine/hyperfine states involved. Taking this into account, the transition intensity is given by

$$I_{rovibronic} = |\langle \eta'', v'', \kappa'' | \hat{\mu} | \eta', v', \kappa' \rangle|^2 = q_{v'',v} |\mu_{\eta'',\eta'}|^2 S_{\kappa'',\kappa'} \quad (2.83)$$

where $S_{\kappa'',\kappa'}$ is the Hönl-London factor and κ denotes the quantum numbers which describe the rotational/fine/hyperfine state. In a case (a) basis $|\eta, v, \kappa\rangle = |\eta, \Lambda; v, l; S, \Sigma; J, P\rangle$. In reality the state $|\eta, \kappa\rangle$ will be some linear combination of the basis functions which will be determined by diagonalizing \hat{H}_{eff} and therefore the values of $S_{\kappa'',\kappa'}$ will depend on the specifics of the effective Hamiltonian.

Rotational and rovibronic transitions have the following selection rules for the total angular momentum and parity; $\Delta J = 0, \pm 1$ ($\Delta F = 0, \pm 1$ when there is hyperfine structure), and parity $+$ \leftrightarrow $-$ [96]. There are also the following approximately good selection rules; $\Delta S = 0$, $\Delta \Sigma = 0$, $\Delta \Lambda = \Delta \Omega = 0, \pm 1$. The value of ΔJ is used to label different rotational branches. $\Delta J = -1$ transitions form the P branch, $\Delta J = 0$ transitions form the Q branch, and $\Delta J = +1$ transitions form the R branch.

More specifically, each transition is labeled with the following branch designation, ${}^{\Delta N} \Delta J_{F'_i, F''_i}(N'')$ where $\Delta N = O, P, Q, R, S$ for $\Delta N = -2, -1, 0, 1, 2$ and $\Delta J = P, Q, R$ for $-1, 0, 1$. Here F_i does not refer to the angular momentum \mathbf{F} but denotes the spin orbit and spin rotation components of the ground and excited states. For a ${}^2\Sigma^+ \rightarrow {}^2\Pi$ transitions $F'_i = 1$ or 2 if the transition is to the $\Omega = 1/2$ or $3/2$ spin orbit components respectively and $F''_i = 1$ or 2 if the transitions comes from the $J = N + 1/2$ or $J = N - 1/2$ spin rotation components respectively [97]. An example of a ${}^2\Sigma^+ \rightarrow {}^2\Pi$ transitions with the branch designations is shown in Fig. 2.2.

2.10 Overview of laser cooling molecules

Now that we have introduced general molecular structure we will take a slight aside to give a brief overview of laser cooling molecules. For a more thorough and complete discussion of molecular laser cooling and trapping see [98, 99].

Laser cooling of atoms and molecules is accomplished by utilizing the interaction of the atom or molecule with laser light to exert forces on the atom or molecule. When a laser's frequency is resonant with an atomic or molecular transition, the atom or molecule will absorb a photon and transition to an excited state. This absorption will provide a momentum kick of $\hbar k$ in the direction of the laser propagation. The atom or molecule will then decay from the excited state emitting a photon. This process of photon absorption and emission is known as photon scattering. Upon decay, the emitted photon has no preferred propagation direction. Therefore, after many photon scatters, the momentum transfer from each photon emission will cancel, on average, resulting in each photon scatter providing an average momentum kick of $\hbar k$ in the direction of the laser propagation. Therefore, if an atom or molecule of mass m moves with velocity v then the atom or molecule can be brought to a stop after $N_{stop} = mv/\hbar k$ photon scatters. In general, to laser cool and trap an atom or molecule, about 10,000 photon scatters are needed. This repeated process of photon absorption and emission is referred to a photon cycling.

In order to actually cool and trap an atom or molecule, it must contain a closed cycling transition so that thousands to millions of photons can be scattered. By closed, we mean that upon excitation, the atom or molecule will not decay to a state unaddressed by the laser and stop scattering photons. While finding closed cycling transitions in certain atoms is fairly easy, it is much more difficult in molecules due to the addition of vibrational and rotational branching. The strict angular momentum and parity selection rules for rotational transitions can be utilized to provide rotational closure [100]. For a $^2\Sigma^+ \rightarrow ^2\Pi_{1/2}$ transition, this is accomplished by driving transitions from the negative parity $N = 1$ state to the even parity $J = 1/2$ state (the $^P Q_{12}(1)$ and $^P P_{11}(1)$ transitions in Fig. 2.2). The angular momentum and parity selection rules enforce that a $J = 1/2$ positive parity state can only decay to $J = 1/2, 3/2$ negative parity states. There are no $J = 3/2$ negative parity states in a $^2\Sigma^+$ electronic state so the molecule will always decay back to the original $N = 1$, $J = 1/2, 3/2$ states, providing rotational closure.

The lack of strict selection rules for vibrational transitions makes addressing vibrational branching much more difficult. From Eq. 2.82 we know that the vibrational branching is proportional to the FCF. Therefore, if we choose a molecule with diagonal FCFs ($q_{v'',v'} \approx 1$ for $v'' = v'$), then the branching to higher vibrational modes not addressed by the cooling lasers will be small. In this case only a small, experimentally feasible, number of repumping laser will be needed to optically

pump the population in these higher vibrational states back into the cooling cycle. Diagonal FCFs are achieved when the vibrational wavefunctions of the ground and excited state are very similar, which occurs when the ground and excited state PESs are almost nearly identical. This occurs when the valence electron involved in the optical cycling is decoupled from the bonding electrons. As discussed in Section 2.2, this is the case for molecules formed by the bonding of alkaline earth or alkaline earth-like metals to halogens or pseudo-halogens, but it occurs in other cases as well [50, 101–104]. To date, several diatomic [48–52] and polyatomic [53–56] molecules have been laser cooled several of which have been trapped as well [57–60].

2.11 Overview of YbOH

Finally, we conclude this chapter with a brief overview of our molecule of choice, ytterbium monohydroxide (YbOH). Prior to the development of experiments to search for a NMQM and eEDM in YbOH, a single spectroscopic study of YbOH had been performed using a high-temperature sample [105]. This study found that YbOH is indeed similar to the alkaline earth hydroxides (CaOH and SrOH), a linear molecule with a ground $\tilde{X}^2\Sigma^+$ electronic state and a first excited $\tilde{A}^2\Pi_{1/2}$ state. Here we have introduced the spectroscopic notation where the ground state is denoted by an \tilde{X} and all other excited states are denoted by capital letters in alphabetical order, first excited is \tilde{A} , second excited is \tilde{B} , etc.²¹ Additionally, this study confirmed that YbOH has a very large spin orbit splitting in the $\tilde{A}^2\Pi$ state, $A = 1350 \text{ cm}^{-1}$, so that the $\tilde{A}^2\Pi_{1/2}$ and $\tilde{A}^2\Pi_{3/2}$ states are separated by 1350 cm^{-1} . In this case the $\tilde{A}^2\Pi_{1/2}$ and $\tilde{A}^2\Pi_{3/2}$ states are considered to be separate electronic states rather than different spin orbit components of the same electronic state. This original study did contain an error which resulted in an incorrect value for the spin rotation parameter. The correct value of the spin rotation parameter was determined as part of the work described in this dissertation, and resulted in a reanalysis of the high-temperature study [106]. The state ordering (not to scale) of the first few rotational levels of the $\tilde{X}^2\Sigma^+(0, 0, 0)$ and $\tilde{A}^2\Pi_{1/2}(0, 0, 0)$ states of YbOH is presented in Fig. 2.2.

YbOH is a linear triatomic molecule and will have three vibrational modes: Yb-O stretch denoted ν_1 , Yb-O-H bend denoted ν_2 , and O-H stretch denoted ν_3 . Vibrational states are indicated in parentheses (ν_1, ν_2, ν_3) following the electronic state designations. Similar to CaOH and SrOH, the strong ionic bond between the Yb and OH provides very diagonal FCFs making YbOH amenable to laser cooling.

²¹Sometimes the state labeling is out of order when lower excited states are experimentally observed after higher-lying excited states.

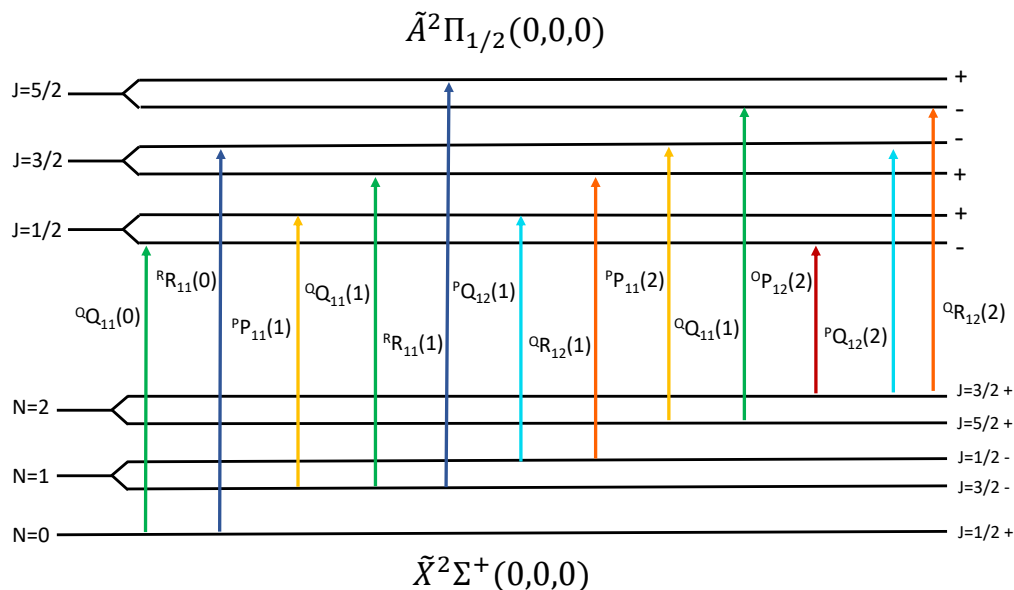


Figure 2.2: Example of the rotational transitions of the $\tilde{A}^2\Pi_{1/2}(0,0,0) - \tilde{X}^2\Sigma^+(0,0,0)$ band of YbOH. The transitions shown here are typical for a ${}^2\Pi_{1/2} - {}^2\Sigma^+$ band. The spacing between the molecular states is not to scale. The state ordering of the rotational and fine structure components of the $\tilde{A}^2\Pi_{1/2}(0,0,0)$ and $\tilde{X}^2\Sigma^+(0,0,0)$ states is representative of YbOH. The negative value of γ in the $\tilde{X}^2\Sigma^+(0,0,0)$ state results in the $J = N - S$ state residing higher in energy than the $J = N + S$ state. Similarly, the negative value of the $(p + 2q)$ parameter in the $\tilde{A}^2\Pi_{1/2}(0,0,0)$ state reverses the ordering of the parity components compared to similar alkaline earth metal fluorides and hydroxides. One or more transitions from each of the six branches typical for a ${}^2\Pi_{1/2} - {}^2\Sigma^+$ band are shown and labeled. All transition labels are to the left of the arrow designating the transition except the $\overset{O}{R}_{12}(2)$ line, which is to the right. The six different branches are color coded: $\overset{O}{P}_{12}$ red, $\overset{O}{Q}_{11}$ green, $\overset{P}{P}_{11}$ yellow, $\overset{P}{Q}_{12}$ light blue, $\overset{O}{R}_{12}$ orange, and $\overset{R}{R}_{11}$ dark blue. The branch designations are described in the text.

The vibrational branching ratios of YbOH have been measured to high precision [107]. The vibrational branching from the $\tilde{A}^2\Pi_{1/2}(0,0,0)$ state (for branching ratios $\geq 0.01\%$) are presented in Fig. 2.3. In addition to diagonal FCFs, the bending mode of the ground electronic state, $\tilde{X}^2\Sigma^+(0,1,0)$, will have parity doublets due to the l -doubling. This parity doubling can be used for internal comagnetometry and, therefore, the $\tilde{X}^2\Sigma^+(0,1,0)$ state will act as the science state for both the NMQM and eEDM measurements.

Finally, Yb has seven naturally occurring isotopes with moderate abundances: ${}^{168}\text{Yb}$ (0.1%), ${}^{170}\text{Yb}$ (3.0%), ${}^{171}\text{Yb}$ (14.3%), ${}^{172}\text{Yb}$ (21.8%), ${}^{173}\text{Yb}$ (16.1%), ${}^{174}\text{Yb}$ (31.8%), and ${}^{176}\text{Yb}$ (12.8%). The even isotopes of Yb have no nuclear spin so

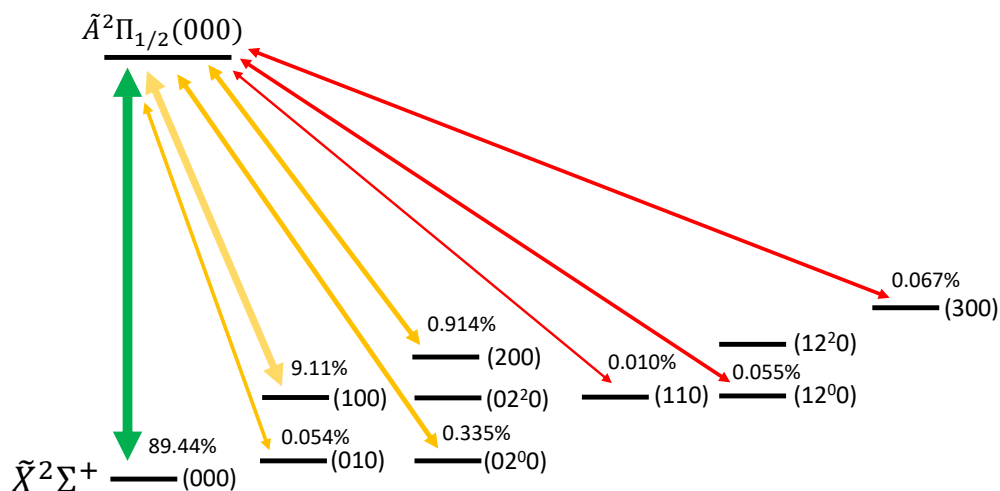


Figure 2.3: Vibrational branching of the $\tilde{A}^2\Pi_{1/2}(0,0,0)$ state of YbOH. Only known branching ratios $\geq 0.01\%$ are presented and were taken from Ref. [107].

the only hyperfine interactions in the even isotopologues of YbOH result from the nuclear spin of the H ($I_H = 1/2$). However, the odd isotopes do have nuclear spins of $I_{171Yb} = 1/2$ and $I_{173Yb} = 5/2$ which result in strong hyperfine interaction in the odd isotopologues. Additionally, the ^{173}Yb nucleus is quadrupole deformed and has an electric quadrupole moment resulting in electric quadrupole hyperfine interactions. The focus of the work described in this dissertation is the production of YbOH and the characterization of the ground and several excited electronic and vibrational states of the even ($^{174}\text{YbOH}$) and odd ($^{171,173}\text{YbOH}$) isotopologues. These measurements are essential for the implementation of laser cooling, spin precession, and EDM measurements in YbOH.

Chapter 3

4 Kelvin Cryogenic Buffer Gas Beam Source

In order to study and ultimately perform measurements of P,T-violation with YbOH, we must first produce it. YbOH is a free radical (molecule with an unpaired valence electron) and is not chemically stable. Therefore, we must use production methods that will avoid the loss of YbOH through chemical reactions. Furthermore, at room temperature a sample of molecules will typically occupy thousands of different rotational and vibrational states so we must also cool the molecules to cryogenic temperatures where the thermal distribution of molecules is spread over only a few rotational levels. We accomplish the production and cooling of the molecules with cryogenic buffer gas cooling and ultimately extract the molecules to form a cryogenic buffer gas beam (CBGB). In this chapter I provide a brief review of CBGBs (more complete and thorough reviews and studies can be found in [108–112]) and a description of our 4 K CBGB source, including the design, construction, and characterization.

3.1 Cryogenic buffer gas beams

Cryogenic buffer gas cooling

At the heart of any CBGB source is buffer gas cooling. Buffer gas cooling utilizes elastic collisions with a cold, inert buffer gas, typically helium or neon, to cool the molecular species of interest. In practice this is accomplished inside of a cryogenic buffer gas cell: a small volume, typically 10-50 cm³, which is cooled to cryogenic temperatures, typically 1-10 K¹. The buffer gas cell is filled with the buffer gas, in our case Helium, which is thermalized to the cell temperature through collisions with the cell walls. The molecular species of interest can be introduced into the cell via laser ablation, capillary filling, or other methods [108]. Following the introduction of the molecular species, collisions with the cold buffer gas will quickly cool the rotational, and translational degrees of freedom of the molecules to near that of the buffer gas².

¹These temperature are typical for a helium buffer gas, neon sources run hotter ~ 20 K.

²The vibrational quenching collisional cross section for buffer gas collisions is typically much smaller than the rotational quenching cross section [71] and therefore buffer gas cooling may not efficiently cool the vibrational degrees of freedom resulting in an athermal vibrational population. It is known that this athermal vibrational population also occurs in supersonic molecular beam sources.

Buffer gas cooling relies on collisions, and therefore, is a generic method that can be applied to almost any molecule. More importantly, the buffer gas is inert which makes this technique especially attractive for free radicals such as YbOH. Buffer gas cooling will result in a molecular sample cooled to a few Kelvin where the molecules will occupy only a few tens of internal states, an ideal starting point for both spectroscopy and experiments requiring specific quantum state control (e.g. laser cooling or parity violation searches). Buffer gas cooling has been used to cool atoms and small [109] and large molecules [113].

Cryogenic buffer gas beam properties

A cryogenic buffer gas molecular beam can be formed by putting an aperture, typically 1-5 mm, in the cell and applying an constant buffer gas flow, typically 1-100 SCCM³. The buffer gas flow into the cell must equal the flow out of the aperture and therefore the buffer gas density in the cell is dependent on both the buffer gas flow and the size of the aperture [108]:

$$n_b \approx \frac{4f_b}{A_{ap}\bar{v}_{0,b}}, \quad (3.1)$$

where f_b is the buffer gas inlet flow, A_{ap} is the area of the aperture, and $\bar{v}_{0,b}$ is the mean thermal velocity of the buffer gas. The higher this density, the more collisions per unit time which results in quicker thermalization.

Not only will the collisions with the buffer gas cool the molecules but it will entrain them into the buffer gas flow and extract them from the cell to form a molecular beam with high extraction efficiency [108, 114]. The extraction of the molecules follows an exponential decay with a time scale given by [108]

$$\tau_{extract} = \frac{4V_{cell}}{\bar{v}_{0,b}A_{ap}} \quad (3.2)$$

where V_{cell} is the cell volume. This extraction time needs to be slower than the thermalization time, so that the molecules can be cooled before they are extracted, but quicker than the time it takes for the molecules to diffuse to the cell walls.

Buffer gas beams are often operated in an intermediate regime where the buffer gas density is high enough that there are a significant number of collisions such that the gas flow cannot be described by molecular flow (e.g. effusive beam) but not high enough (or dense enough) to be described by hydrodynamics either. The

³SCCM or standard cubic centimeters per minute is a standard unit of gas flow. 1 SCCM is equivalent to $\sim 4.5 \times 10^{17}$ atoms per second.

output velocity of the CBGB is highly sensitive to how close to the effusive or hydrodynamic regimes the CBGB operates. We can quantify this using a quantity called the Reynolds number, Re . In the case of a CBGB it is most important to consider the Reynolds number at the aperture, where it is approximately equal to twice the number of collisions that occur within an aperture diameter away from the aperture [108]. Since Re is proportional to the number of collisions near the aperture, it directly tells indicates in which regime the buffer gas source is operating. In terms of the CBGB properties, the Reynolds number is given by

$$Re \approx \frac{8\sqrt{2}f_b\sigma_{bb}}{d_{ap}\bar{v}_{0,b}}, \quad (3.3)$$

where σ_{bb} is the buffer gas-buffer gas collision cross section, and d_{ap} is the diameter of the aperture.

In the effusive regime, $Re \lesssim 1$ there are almost no collisions near the aperture and the flow is molecular. Since there are not many collisions, the buffer gas and molecules randomly wander out of the aperture while diffusing around at their thermal velocity. In this case the beam's forward velocity, v_{beam} (here we refer to the velocity of the species of interest not the buffer gas) is given by

$$v_{beam} \approx 1.2\bar{v}_{0,s}, \quad (3.4)$$

where $\bar{v}_{0,s}$ is the mean thermal velocity of the species of interest.

In the low end of the intermediate regime, $1 \lesssim Re \lesssim 10$, there are now collisions with the buffer gas near the aperture. These collisions will speed up the beam. In this regime, the beam's forward velocity can be approximated by

$$v_{beam} \approx 1.2\bar{v}_{0,s} + 0.6\bar{v}_{0,b}Re\frac{m_b}{m_s}, \quad (3.5)$$

where m_b and m_s are the mass of the buffer gas and molecular species of interest respectively. As Re gets higher there are more collisions near the aperture which will cause additional boosting of the beam velocity. At very high Re , $Re \gtrsim 100$, the buffer gas flow is almost fully hydrodynamic and results in a fully boosted beam with a forward velocity of

$$v_{beam} \approx 1.4\bar{v}_{0,b}. \quad (3.6)$$

For intermediate Re higher than that described by Eq. 3.5 but lower than the fully hydrodynamic regime, $10 \lesssim Re \lesssim 100$, the CBGB forward beam velocity is better described by

$$v_{beam} \approx 1.4\bar{v}_{0,b}\sqrt{1 - Re^{-4/5}}. \quad (3.7)$$

Notice that the beam velocity given in Eq. 3.7 saturates to the fully hydrodynamic value. CBGB sources are most often operated in the intermediate regime, $1 \lesssim Re \lesssim 100$ where the forward beam velocity is best described by Eq. 3.5 and 3.7.

It is often advantageous to produce the slowest molecular beam possible. This is especially true for laser cooling as slower beams will make slowing and stopping the molecular beam easier. Many techniques have been used to accomplish this, including second stage cells and cooling the buffer gas cell to colder temperatures [111]. These techniques were not used in this work so they will not be discussed further.

3.2 4 K cryogenic buffer gas beam source

At the center of what will become the NMQM experiment is the 4 K CBGB source. A description of this source is provided here, including the design principles and lessons learned. Much of this system was custom designed and fabricated. Many of the spectroscopic measurements detailed in this dissertation were measured using this 4 K CBGB source.

To cool to cryogenic temperatures we utilized a Cryomech PT415 pulse tube refrigerator, referred to as the pulse tube. The pulse tube has two stages, the first stage cooling to ~ 40 K, referred to as the 50 K stage, and the second which cools to ~ 3.5 K, referred to as the 4 K stage. The pulse tube, and all other cryogenic components, are mounted in a custom aluminum 14.5 inch x 14.5 inch x 24.5 inch rectangular vacuum chamber, referred to as the 300 K chamber. This chamber has removable side, top, and bottom plates. The vacuum seals between the plates and the chamber are made using Viton o-rings. All o-ring seals in the 4 K CBGB source are made with Viton o-rings; Buna is avoided due to higher outgassing rates.

When the pulse tube is mounted directly to the top of the 300 K chamber, the 4 K stage of the pulse tube rests near the bottom of the chamber. In order to maximize the usable space and provide a beam output near the center of the 300 K chamber, the pulse tube was mounted higher in the 300 K chamber. This was accomplished by mounting the pulse tube to a custom 2.0-inch-thick octagon-shaped collar which was in turn mounted to a custom 8.0-inch-diameter 7.315-inch-long nipple. This nipple was mounted to the top of the 300 K chamber (a drawing of the octagon-shaped collar and custom nipple can be found in Appendix B). The octagon-shaped collar was used to adapt the mounting pattern of the pulse tube to that of the 300 K chamber's top plate, which is the same mounting pattern used for the custom nipple.

All vacuum seals were made with Viton o-rings. When the pulse tube is mounted to the custom nipple, the 50 K stage resides inside the nipple. An adaptor was made to address this issue and is described in Section 3.2. A three dimensional CAD drawing of the full 4 K CBGB assembly (excluding the buffer gas cell) is shown in Fig. 3.1, including the mounting of the pulse tube using the octagon collar and custom nipple.

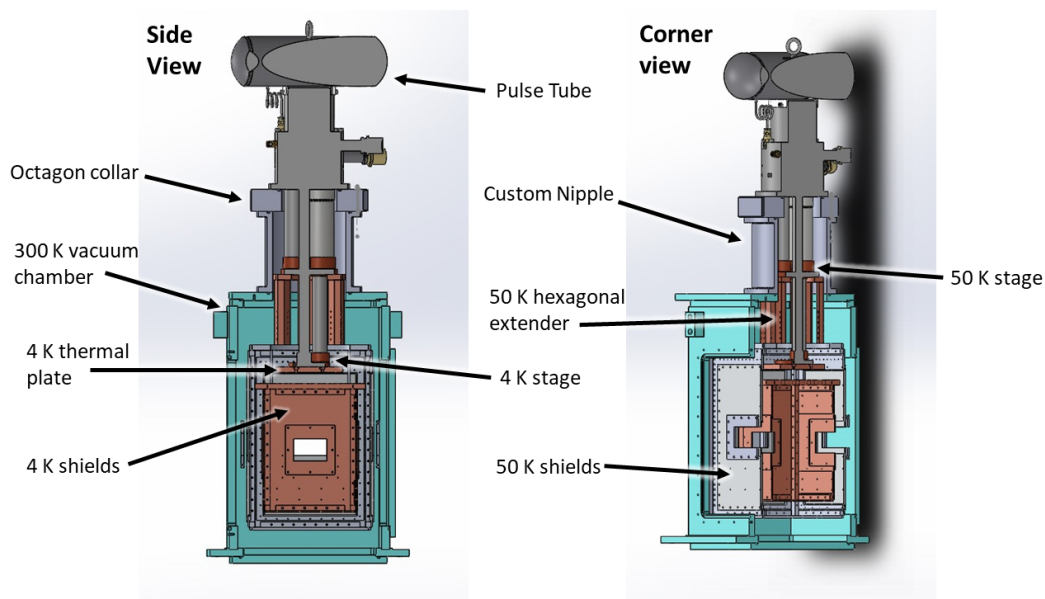


Figure 3.1: Three-dimensional CAD drawing of the full 4 K CBGB assembly. Both a side view and angled corner view are shown. For both views a cut was taken down the center of the assembly so that the interior can be clearly seen. For the corner view, one of the 300 K side plates is removed to show the side face of the 50 K shields. All labeled components are described in detail in the text. The buffer gas cell and its mounting structure are not shown.

Radiation shields

The inner walls of the 300 K chamber will radiate 300 K blackbody radiation (BBR) into the inside of the chamber. Mounting the cryogenic buffer gas cell directly inside of the 300 K chamber, with no thermal shielding, will expose the cell to this large 300 K BBR heat load and prevent the cell from cooling down to 4 K. In order to reduce the heat load on the cell it is surrounded with nested 50 K and 4 K radiation shields (connected to the 50 K and 4 K stages of the pulse tube respectively). In this configuration only the 50 K shields are exposed to the 300 K BBR while the 4 K shields are exposed to 50 K BBR and the cell is exposed to 4 K BBR. The lower 4 K heat load on the cell results in a lower operating temperature. It is important

to note that while the 4 K shields reduce the BBR heat load, their existence does not significantly lower the temperature of the cell, as the cell and the 4 K shields are cooled by the same stage of the pulse tube. The 4 K shields, however, act as a cold surface on which the cryopumping charcoal sorbs (to be discussed later) can be mounted. With these shields, the 4 K CBGB source is essentially a cell mounted in a 4 K box, mounted in a 50 K box, mounted in 300 K box.

Finally, it is important to note that all mechanical and thermal connections were made using brass screws and Belleville spring washers. The brass screws provide the best match (for non-custom fasteners) for the thermal contraction of both aluminum and copper (the materials used for the 50 K and 4 K shields). This prevents thermal contraction of the metals from making the contacts between different parts less tight and reducing thermal conduction needed for cooling. The Belleville washers prevent thermal contact from being lost during cool-down. These conical washers act as springs when compressed and will keep the face to face connection of two parts tight even when thermal contraction occurs. Lastly, the surfaces between parts where good thermal contact is needed are coated with a thin layer of Apiezon N thermal grease to increase thermal conduction.

50 K shields

All of the 50 K shields were fabricated using Aluminum 6061. Aluminum 6061 was chosen due to the thermal properties at 50 K, cost, and ease of machining. Drawings for all of the 50 K shield components can be found in Appendix B. The 50 K shields form an approximately 11 inch x 11 inch x 16 inch box.

The 50 K top plate is 0.5 inches thick and has a 7.5-inch-diameter hole in the center for the pulse tube to pass through. There are 4 additional 1.0 inch diameter holes (on the corners of a 8.5 inch x 8.5 inch square) for gas lines and electrical wires to be fed through. The rest of the surface of the plate is covered by a grid of 10-32 tapped holes (to be used for mounting the 50 K stage to the pulse tube or other components to the 50 K stage) separated by 0.5 inches in both dimensions. The 50 K top plate is suspended from the top⁴ of the 300 K chamber by four stainless steel threaded rods⁵. The 50 K top plate rests on a pair of locked nuts threaded onto these threaded

⁴The threaded rods are screwed directly into the top plate of the 300 K chamber and are not vented. Technically, this creates trapped volumes which are typically avoided in vacuum chambers. However, since the 50 K and 4 K surfaces act as gigantic cryopumps, and we will be purposefully flowing helium into the chamber, the gas load from these trapped volumes is negligible.

⁵Stainless steel threaded rods were used since stainless steel has relatively poor thermal conduc-

rods, this allows the height of the 50 K stage to be adjusted. These rods can be seen in Fig. 3.4 and 3.5.

The 50 K bottom plate is 0.25 inches thick and has a grid of 10-32 tapped holes. A temperature diode is attached to the bottom plate for monitoring the temperature of the 50 K stage. The 50 K top and bottom plates are connected by 0.5 inch x 0.5 inch x 16.0 inch rectangular connecting bars (vertical connecting bars). The bars have tapped holes in the center of the ends, which are used to fasten to the top and bottom plates. The sides of the connecting bars have a single line of 10-32 tapped holes (thru all), separated by 1.0 inch and offset by 0.5 inches on adjacent sides to prevent the holes from intersecting. These holes are used for fastening the side plates. Additional connecting bars (horizontal connecting bars) are mounted to the inner sides of the top and bottom plates to provide additional points for fastening the side plates. The frame of the 50 K shields, comprised of the connecting bars and the top and bottom plates, can be seen in Fig. 3.2a. Note that in the original design the nuts on which the top plate rests contact the vertical connecting bars. The sides of the connecting bars had to be filed down to prevent this.

The 11 inch x 16 inch side plates are too large to fit through the side of the 300 K chamber so they were separated into two separate plates. First is the larger (50 K side flange) 11 inch x 16 inch plate with a 8.5 inch x 13.0 inch rectangular hole offset 0.5 inches below the center. The second plate (50 K side cover plate) is 9.5 inch x 14.0 inch plate which is attached to the 50 K side flange to cover the rectangular hole. The smaller plate fits through the side flange in the 300 K chamber allowing the inside of the 50 K stage to be accessed through the side flange of the 300 K chamber. Access to the 4 K shields with the 300 K front plate and 50 K front side cover plate removed is shown in Fig. 3.3. Both side plates are 0.25 inches thick. It is important to note that in the original design the mounting screws extruded too far out from the surface of the smaller side plates preventing the 300 K from fitting over these screw heads so that the chamber could not be dropped without removing the smaller 50 K side plates. This was fixed by trimming down the edges of the smaller 50 K side plates by 0.125 inches so that they sit 0.125 inches closer to the 50 K side flange.

The side cover plates on the sides parallel to the beam direction have a 2 inch x 4 inch rectangular hole for a window. The windows are mounted using 0.25 inch

tivity at 4 K and 50 K. Therefore, these rods will not create a thermal short between the 50 K and 300 K stages. The heat transfer from the 300 K stage to the 50 K stage through these rods was calculated and found to be negligible.

thick rectangular window flanges and indium wire is placed between the window and both the side cover plate and window flange. Rectangular borosilicate glass windows are used. The front side cover plate (in front of the front of the cell) has a 3/8 in diameter hole counter bored on the outer face such that the hole is diverging in the beam propagation direction. A side view of the fully assembled 50 K shields is shown in Fig. 3.2b.

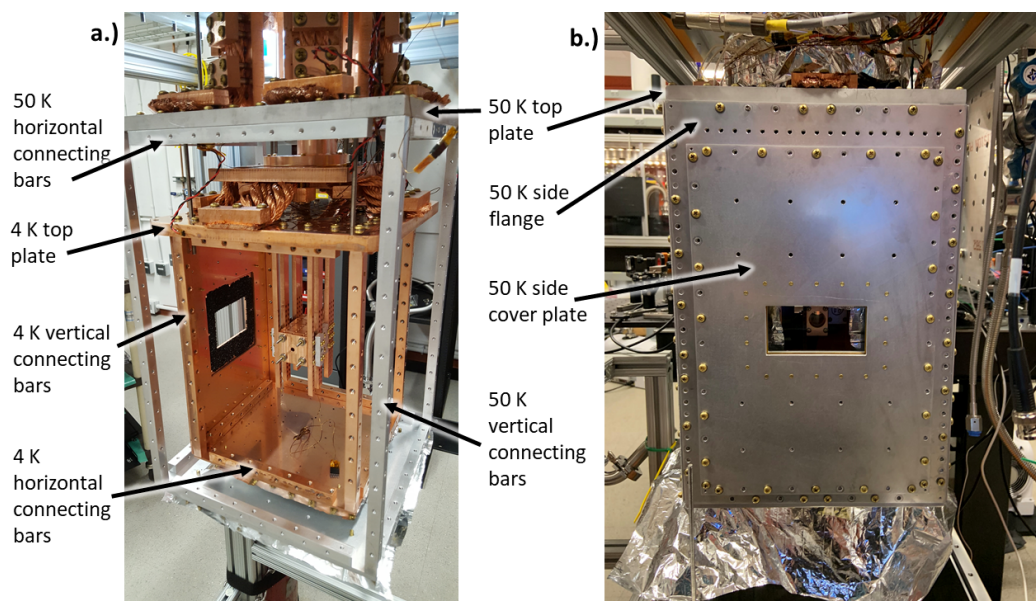


Figure 3.2: Frames of the 50 K and 4 K shields and assembled 50 K shields. Detailed description of the labeled parts is given in the text. **a.)** Outer silver (Aluminum 6061) and inner orange (Copper C10100) parts are the 50 K and 4 K frames respectively. The frames consist of the top and bottom plates connected by the vertical connecting bars. The horizontal connecting bars are also shown. The 50 K and 4 K bottom plates are not labeled. One side plate of the 4 K shields is installed, the black region around the window hole is activated charcoal, or sorb, used for cryopumping. The first generation of the buffer gas cell is mounted inside the 4 K frame. The completed copper braid connections of the 50 K and 4 K shields to the respective stages of the pulse tube are visible at the top of each frame, though not labeled. **b.)** Side view of fully assembled 50 K shields. The window is mounted on the inside of the 50 K side plate so that the window mounting flange is not seen.

4 K shields

All of the 4 K shields were fabricated using high purity Copper 101, specifically alloy⁶ C10100. Copper 101 was chosen as it provides the best thermal conduction

⁶"Copper 101" or "Copper C101" is not a defined alloy, and different vendors unfortunately use this to mean either C10100 or C11000, the latter of which is more commonly known as C110. In

at 4 K. The 4 K shields form a 8.2 inch x 8.2 inch x 11 inch box. The design of the 4 K shields is nearly the same as that of the 50 K shields. As with the 50 K shields, the 4 K top and bottom plates are connected with vertical connecting bars and the side plates are fastened to the sides of these bars as well as to horizontal connecting bars mounted to the inside of the top and bottom plates (shown in Fig. 3.2). The 4 K top plate is 0.5 inches thick and is oversized to 10 inches x 10 inches so that it hangs over the sides of the 4 K shields⁷. This provides more room for connections with the 4 K stage of the pulse tube to be made. As with the 50 K shields, there are four 1.0 inch diameter holes for gas lines and electrical wires to be passed through. The 4 K top plate is suspended by threaded rods attached to the 50 K top plate, shown in Fig. 3.5. The 4 K top plate also has a grid of tapped holes for mounting. However, due to the soft and gummy nature of copper, all tapped holes for the 4 K stage have stainless steel helicoil inserts to prevent damage to the threads from repeated fastening and unfastening.

The 4 K bottom and side plates are all 0.125 inches thick. Each side plate has a 4.5 inch x 4.5 inch square hole in the center. This hole is covered by a blank plate in the back of the shield (behind the cell) and by plates with a 2 inch x 3 inch window hole on the sides. In contrast to the 50 K shields, these window holes are left open and not covered by a window. In the front of the 4 K shield the square hole is covered by a plate with a 0.25-inch-diameter hole used to skim and collimate the CBGB after it leaves the cell and before it leaves the CBGB source. As with the 50 K collimator, the 0.25-inch hole has a conical counter bore on the front. In order to improve beam quality, this collimator was eventually replaced by a skimmer. This is discussed in more detail in Section 3.2. The inner walls of the 4 K shields are coated with activated charcoal (sorb), shown in Fig. 3.2, 3.13, and 3.14. These sorbs drastically increase the cryopumping capacity of the CBGB, allowing the background Helium to be efficiently pumped away. However, the sorbs eventually fill up and have to be periodically emptied by heating up the 4 K stage to ~12-15 K and letting the desorbed Helium be mechanically pumped away. A side and front view of the fully assembled 4 K shields is shown in Fig. 3.3. Drawings of all of the components of the 4 K shields can be found in Appendix B.

this dissertation I will use Copper 101 to refer to C10100.

⁷The corners of the 4 K top plate had to be filed off as they contacted the 50 K shields.

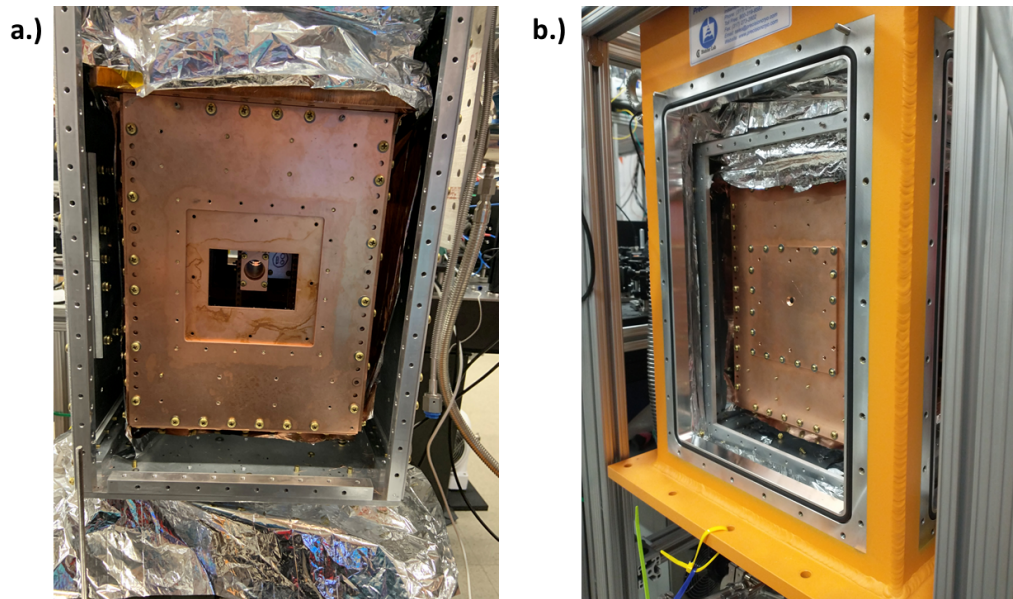


Figure 3.3: Fully assembled 4 K shields. **a.)** Side view of the 4 K shields. Here the 4 K shields are in the assembled 50 K shields with the 50 K side flange and 50 K side cover plate removed. **b.)** Front view of assembled 4 K shields. Here the 4 K collimator can be seen. This is where the CBGB passes out of the source and into the beam region. This view is shown with the 300 K side plate and 50 K side cover plate removed, illustrating how the design allows the internal portion of the CBGB source to be accessed with minimal disassembly.

Thermal connections with pulse tube refrigerator

While the top plate of the 4 K shields sits right below the 4 K stage of the pulse tube, allowing easy connections, the 50 K stage of the pulse tube resides inside of the custom nipple, above the top plate of the 300 K chamber. In order to thermally anchor the 50 K shields to the 50 K stage, a thermally conductive surface must extend down through the custom nipple from the 50 K stage to near the 50 K top plate. This is accomplished with what we call the 50 K hexagonal extender. The 50 K hexagonal extender is comprised of seven parts, all fabricated from Copper 101. Again, all tapped holes have stainless steel helicoil thread inserts installed. The first piece is the 50 K hexagonal thermal plate, which is a 0.5-inch-thick hexagonal shaped plate which attaches directly to the 50 K stage of the pulse tube. The top of six 2.0 inch x 5.86 inch x 0.5 inch bars (50 K extender bars) is attached directly to the 50 K hexagonal thermal plate so that they hang vertically down to provide thermal contact with the 50 K top plate. The assembled 50 K hexagonal extender mounted to the pulse tube (before the pulse tube was mounted in the custom nipple) is shown in Fig. 3.4. Where the 50 K hexagonal extender sits with relation to the 50

K top plate when the pulse tube is mounted with the custom nipple is shown in Fig. 3.5, and its position in the full assembly is shown in the three-dimensional CAD drawing in Fig. 3.1. Drawings of the parts of the 50 K hexagonal extender can be found in Appendix B.

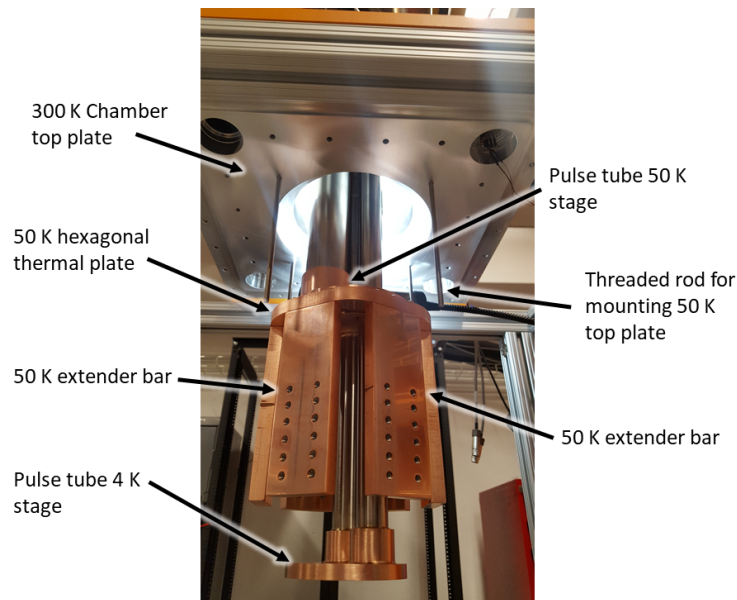


Figure 3.4: 50 K hexagonal extender. Detailed descriptions of the labeled parts are given in the text. Here, the mounting of the 50 K hexagonal extender to the 50 K stage of the pulse tube is shown. This was before the pulse tube was mounted with the custom nipple. In the final configuration the 50 K stage and the top of the 50 K hexagonal extender reside in the custom nipple above the 300 K top plate.

Even though the 4 K stage sits just above the 4 K top plate, an adaptor plate (4 K thermal plate) to make thermal connections was used. The uses of the 4 K thermal plate were twofold: first, to provide more surface area with which thermal connections could be made and second, to prevent direct damage to the threaded holes on the 4 K stage of the pulse tube. The 4 K thermal plate was fabricated from Copper 101 and all tapped holes have stainless steel helicoil thread inserts installed. The plate is 6.0 inches x 6.0 inches and 0.5 inches thick. A drawing of the 4 K thermal plate can be found in Appendix B. Where the 4 K thermal plate sits with respect to the 50 K and 4 K top plates is shown in Fig. 3.5 (this can also be seen in the CAD drawing in Fig. 3.1).

When thermally anchoring the shields to the pulse tube, it is important that the connections provide good thermal contact but are not mechanically rigid. The pulse tube refrigerator can be easily bent, and made inoperable, when small or moderate

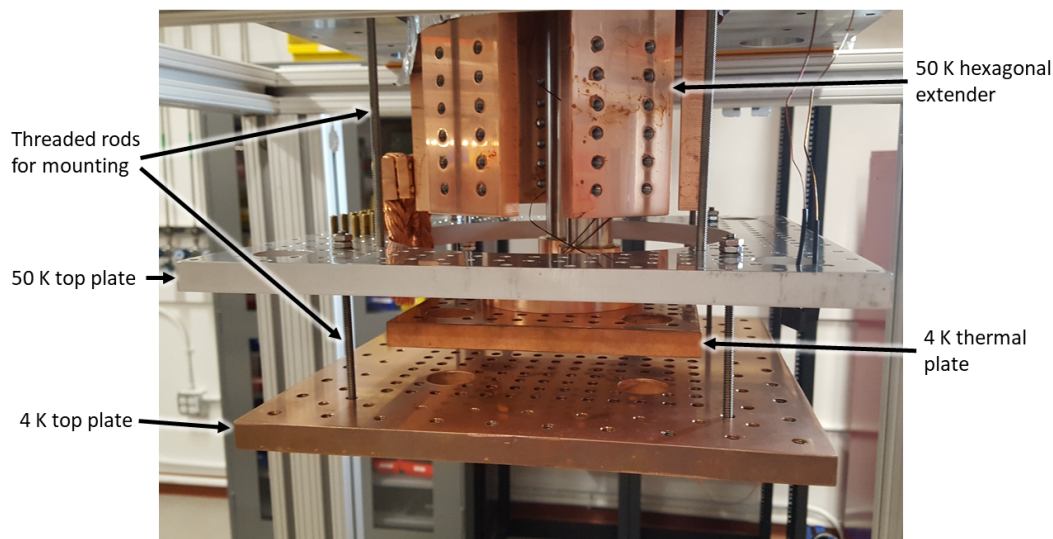


Figure 3.5: Relative positions of the 4 K top plate, 50 K top plate, 4 K thermal plate, and 50 K hexagonal extender. Detailed descriptions of the labeled parts are given in the text. The 300 K top plate (not labeled) is at the top of the image. This was before the thermal connections between the 4 K thermal plate/50 k hexagonal extender and the 4 K/50 K shields were made. The stainless steel threaded rods from which the 50 K and 4 K top plates are suspended can be seen.

amounts of torque are applied to it. When assembling or disassembling the radiation shields, torques that could damage the pulse tube can be both purposefully and inadvertently applied. Therefore, thermally conductive yet mechanically non-rigid connections between the radiation shields and the pulse tube are needed to protect the pulse tube from damage. These connections were accomplished using Copper 101 braided wire⁸.

The thermal connections between the radiation shields and the pulse tube were made by compressing the Copper braid between either the 4 K top plate, 50 K top plate, 4 K thermal plate, or the 50 K hexagonal extender and a small 0.5-inch-thick Copper 101 bar. We refer to these thermal connections as heat links. The Copper bars are compressed down with brass screws and bellville washers. The heat links between the 50 K top plate and the 50 K hexagonal extender are shown in Fig. 3.6a. The heat links between 4 K top plate and the 4 K thermal plate are shown in Fig. 3.6b. A full view of the completed heat link connections can also be seen in Fig. 3.2a. When making the thermal heat link connections, the copper bars must be fully fastened

⁸Cooner Wire, NER 7710836 B-OFE (Bare OFE C101001 copper braided wire, 2/0 braid, 7x7x108/36 strands).

down and then left for approximately a day before being re-tightened to allow the copper braid to compress fully. If the copper bars are not re-tightened then the heat links may not provide adequate thermal connection.

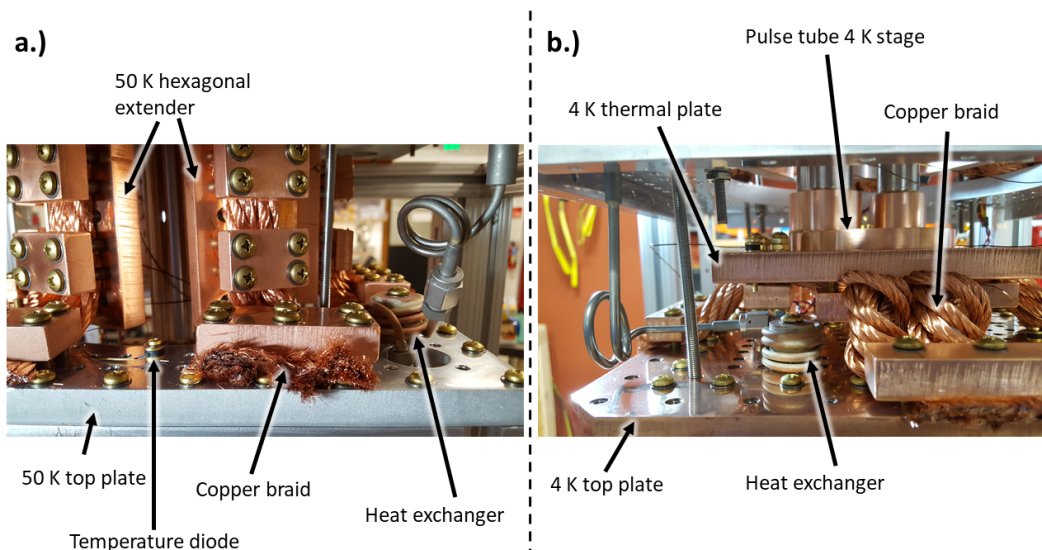


Figure 3.6: Heat link thermal connections between the radiation shields and the pulse tube stages. **a.)** Heat links between the 50 K top plate and the 50 K hexagonal extender. The thermal connection is provided by compressing the copper braid with 0.5-inch-thick copper bars. The position of a temperature diode on the 50 K top plate is indicated. Also indicated is the 50 K heat exchanger used for cooling the Helium to 50 K before it reached the 4 K stage. **b.)** Heat links between the 4 K top plate and the 4 K thermal plate. These connections are also made by compressing the copper braid with 0.5 inch copper bars. The 4 K heat exchanger is shown, which cools the Helium to 4 K before it reaches the buffer gas cell.

Buffer gas cell

The internal volume of the buffer gas cell is a 0.5-inch-diameter cylinder, which can vary in length. The variable length is achieved using a modular design which allows different portions of the cell to be swapped out, added, or removed. This allows the cell length, available optical access, cell aperture, or gas inlet to be changed at any time without requiring a new cell to be fabricated. All cell parts are fabricated from Copper 101 and all tapped holes have stainless steel helicoil thread inserts. The modular cell pieces are created by machining a 0.5-inch-diameter cylindrical hole through the center of at 1.5 inch x 1.5 inch copper bar of varying lengths. All cell pieces have four 4-40 clearance holes on the corners of a 1.0 inch x 1.0 inch square and parallel to the boar of the cell. These 4-40 holes are used to connect the cell

pieces.

The body of the cell is formed by two different types of modular cell pieces. First are blank cell pieces which are comprised of the 0.5-inch hole that forms the cell. All sides of the blank pieces have a grid of 4-40 tapped holes. The blank sections provide surface area with which thermal and mechanical connections can be made. The blank cell pieces vary in length from 0.25 inches to 1.0 inch in 0.25-inch increments. A 0.5-inch blank cell piece is shown in Fig. 3.7a.

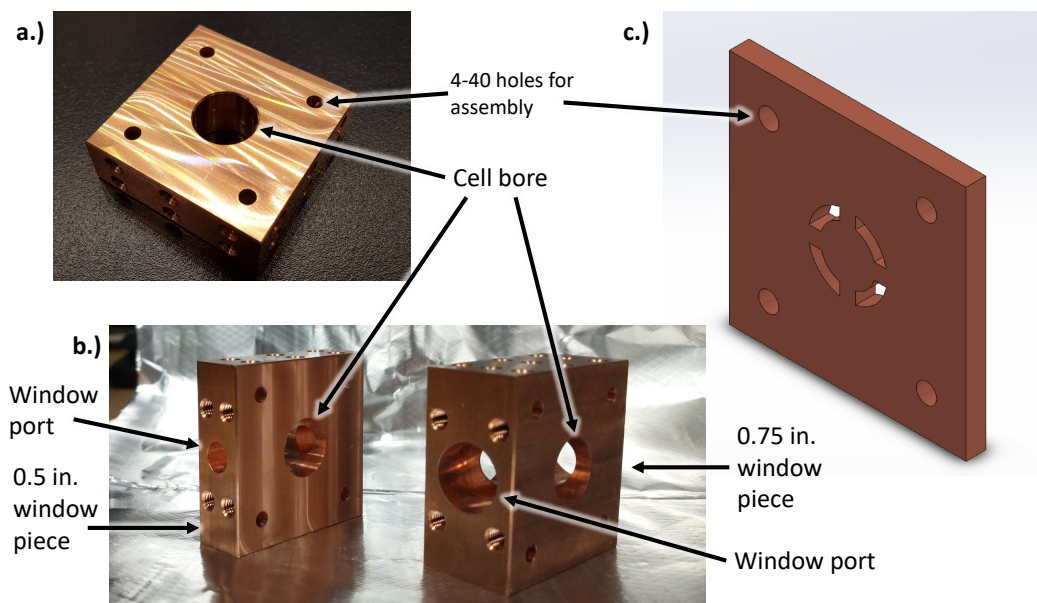


Figure 3.7: Various cell pieces used to form a modular buffer gas cell. **a.)** 0.5-inch blank cell piece. The cell bore and the 4-40 through holes used for assembling the cell are labeled. The grid of mounting holes can be seen on the side of the piece. The surface is machined copper; the lines are due to lighting in the photograph. **b.)** 0.5-inch and 0.75-inch window pieces. The cell bore and the window ports are labeled. The tapped holes surrounding the window port are used for mounting the window. **c.)** Three-dimensional CAD drawing of the diffuser plate. The helium enters the cell 0.125 inches before this plate on the center line of the plate. The arc-shaped slots function to push the helium flow towards the outside of the cell so that the helium is more evenly distributed over the cell volume.

The second type of cell piece is a window cell piece. Compared to the blank cell pieces, the window cell pieces have an additional cylindrical hole cut perpendicular to the cell bore and completely through the entire piece (referred to as the window port). Window cell pieces come in three lengths, 0.5 inch, 0.75 inch, and 1.0 inch. The diameter of the window ports are 0.25 inch, 0.5 inch, and 0.75 inch for the 0.5-inch, 0.75-inch, and 1.0-inch window pieces respectively. Four tapped holes are

also added parallel to the window port for mounting windows to the cell. Examples of a 0.5-inch and 0.75-inch window pieces are shown in Fig. 3.7b.

A window flange is used to fasten a window to the cell. Before the window is compressed between the flange and the side of the window cell piece, both the side of the window cell and the flange are coated in several layers of kapton tape. Borosilicate glass windows were used. Mounted windows can be seen in Fig. 3.8. The window cell pieces provide optical access to the interior of the cell for laser ablation, cell diagnostics, or spectroscopy.

The section of the cell used for laser ablation has the window extended from the side of the window cell piece by a snorkel. This allows the window through which the ablation laser passes to be further removed from the ablation targets to prevent it from becoming coated with ablation products. The snorkel is made by brazing two flanges to the ends of a copper tube. The snorkel is shown in Fig. 3.8d. Even though the snorkel helps the ablation window from becoming coated it does not prevent it completely, and the ablation window (and other windows) need to be changed periodically. Opposite the snorkel the targets are mounted to the cell in place of a window. This is accomplished by attaching the targets to a blank window flange (target plate) with stycast epoxy before attaching the flange to the cell. Initially we used Aluminum 6061 for the target plates but have switched to Copper 101 for better thermal conduction.

The helium is introduced into the cell through the gas inlet. The gas inlet is made by brazing a 0.125-inch Copper 101 tube to a blank 0.25-inch cell piece which has a 0.125-inch hole instead of the normal 0.5-inch cell bore. The back of a gas inlet plate is shown in Fig. 3.8c. Though it was not initially used, a diffuser plate was added to the back of the cell. This plate has arc-shaped slots cut in it which act to disperse the helium flow more evenly throughout the cell volume. A CAD drawing of the diffuser plate is shown in Fig. 3.7c. The diffuser plate is separated from the gas inlet by a 0.125-inch blank cell piece.

Unless otherwise stated the cell aperture is a 5-mm-diameter circular hole. The aperture plate is made by cutting a 5-mm-diameter hole in the center of a 0.25-inch blank cell piece (no 0.5-inch hole was cut in this piece). A 0.5-inch-diameter pocket is then milled down approximately 0.1875 inches so that the aperture is only 1/16th of an inch thick. The aperture can be seen in Fig. 3.8a.

The cell is assembled by stacking the desired cell pieces on 4-40 threaded stainless

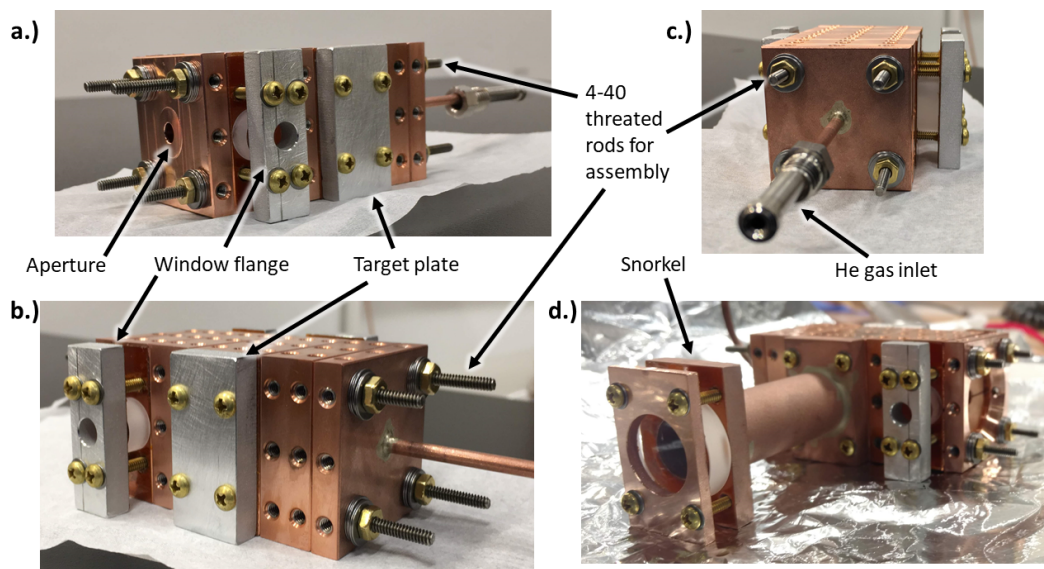


Figure 3.8: Buffer gas cells assemblies **a.)** Front/side view of first buffer gas cell assembly. The aperture, window flange, and target plate are labeled. The 4-40 threaded rods used to assemble the cell are visible and labeled. **b.)** Back/side view of first cell assembly. A window flange, target plate and 4-40 threaded rods are labeled as in **a.** **c.)** Back view of the first buffer gas cell assembly. This shows the back of the gas inlet plate. The helium gas inlet tube with which the helium is introduced into the cell is labeled. Also labeled are the 4-40 threaded rods used for assembly. **d.)** Side view of later buffer gas cell assembly which has a mesh aperture (see Section 3.5). Here the snorkel used to separate the ablation window from the cell is shown.

steel rods and compressing them together with nuts and stacked bellville washers. The first cell assembly, shown in Fig. 3.8a, b, and c, was comprised of (in order): gas inlet, 0.5-inch blank, 0.75-inch window piece for ablation, 0.5-inch blank, 0.5-inch window piece for diagnostics, and 0.25-inch aperture. Note that this original cell assembly did not have a snorkel, though it was added soon after. The cell assembly has varied over time. The current cell assembly is comprised of: gas inlet, 0.125-inch blank, diffuser plate, 0.5-inch blank, 1.0-inch window piece for ablation (with snorkel), 0.5-inch blank, 0.5-inch window piece for diagnostics/spectroscopy, and 0.25-inch aperture plate. Drawings for all cell pieces can be found in Appendix B.

Mounting the buffer gas cell

The buffer gas cell is mounted to the inside of the 4 K top plate. This is accomplished with a system of mounting bars. First two 0.5 inch x 0.5 inch copper 101 bars (plate-to-bar mounts) are attached to the inside of the 4 K top plate. These plate-to-bar mounts have a pattern of 4-40 tapped holes on the side (with helicoil inserts) which the cell mounting bars are attached to. The cell mounting bars are 8.0 inches long, 0.25 inches thick, and vary from 0.25 to 1.0 inches wide (in 0.25-inch increments). These cell mounting bars are attached to the sides of the blank cell pieces with 4-40 brass screws and bellville washers. A thin layer of Apiezon N thermal grease is also used. We later replaced all the cell mounting bars with 0.5 inch thick mounting bars for better thermal conduction so that the cell would operate at a lower temperature. Two mounted cells are shown in Fig. 3.9. Drawings of the plate-to-bar mounts and the 0.25-inch-wide cell mounting bars can be found in Appendix B.

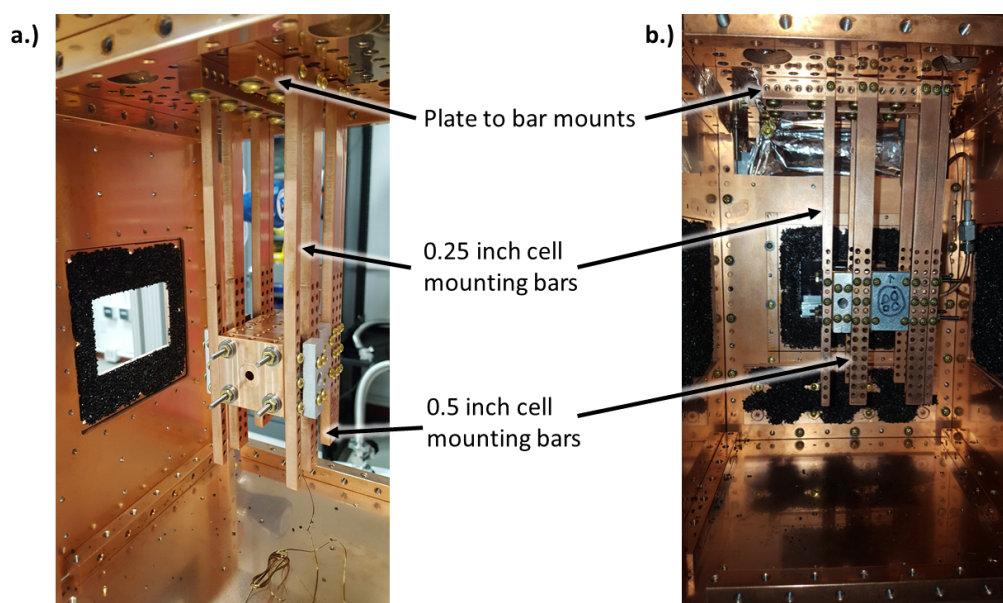


Figure 3.9: Mounted buffer gas cells **a.)** Front view of first buffer gas cell configuration mounted in the CBGB source. The plate-to-bar mounts and cell mounting bars are labeled. **b.)** Side view of a later buffer gas cell configuration mounted in the CBGB source. The plate-to-bar mounts and cell mounting bars are labeled.

Helium gas manifold

The helium is introduced into the buffer gas cell through the helium gas manifold. A piping and instrumentation diagram of the helium gas manifold is shown in Fig.

3.10. The helium is sourced from a gas cylinder and the pressure is stepped down and regulated with a pressure regulator. Following the pressure regulator, is a mass flow controller (MFC), with a range of 0-10 SCCM, which controls the flow of helium provided to the cell. There is a hand valve⁹ after the MFC which allows the helium gas manifold to be isolated from the CBGB source. After this hand valve, the helium enters the 300 K vacuum chamber through a fluid feedthrough. Before reaching the buffer gas cell the helium passes through a 50 K and 4 K heat exchanger which are thermally anchored to the 50 K and 4 K top plates respectively. These heat exchangers cool the helium to 50 K and then 4 K before it reaches the buffer gas cell. This reduces the heat load on the cell and makes the buffer gas cooling more efficient. The heat exchangers are made by coiling copper 101 tube around a copper 101 rod and brazing the outside of the tubing to the rod. The 50 K and 4 K heat exchangers are shown in Fig. 3.6a and Fig. 3.6b respectively.

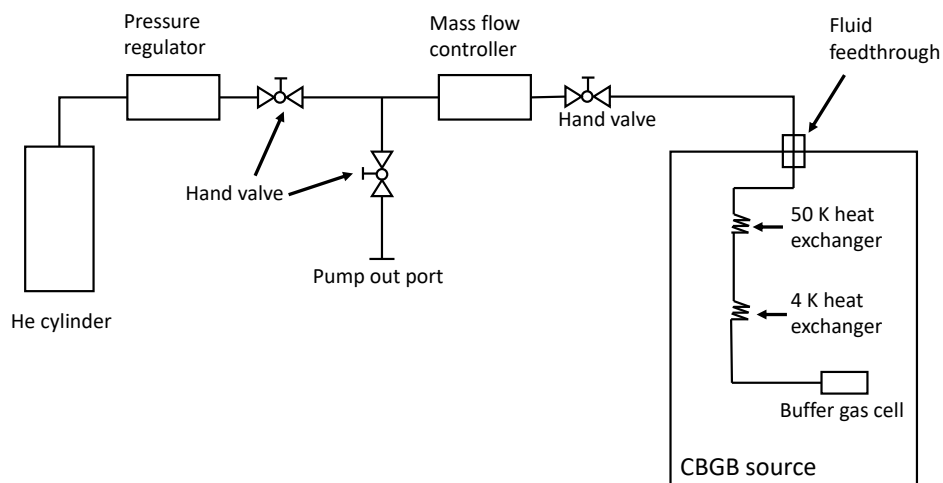


Figure 3.10: Helium gas manifold. The helium is provided by the He cylinder and the pressure in the manifold is regulated by a pressure regulator. The helium flow rate is controlled by the mass flow controller. The 50 K and 4 K heat exchangers cool the helium before it reaches the buffer gas cell. The pump out port is used to pump out or leak check the gas manifold.

After the pressure regulator, all connections are made using Swagelok VCR metal face seal gaskets and fittings and all of the components are "all metal." Prior to the 50 K heat exchanger and between the 50 K and 4 K heat exchangers, stainless steel

⁹Swagelok SS4BKV31 bellows sealed valve.

tubing is used. Stainless steel tubing has relatively poor thermal conductivity and will not create a significant thermal short between the 300 K chamber and the 50 K top plate or the 50 K and 4K top plates. After the 4 K heat exchanger only copper 101 tubing is used.

Beam extension and vacuum system

After the buffer gas beam is skimmed and collimated by the skimmers in the front of the 4 K and 50 K shields, it exits the CBGB source through a KF 50 port in the 300 K chamber and enters a room-temperature vacuum region called the beam extension. Except for a custom ordered 10-way KF 50 cross, the beam extension is comprised of off the shelf KF and CF vacuum components. Again, all o-ring seals are made using only viton o-rings. A manually operated gate valve is attached directly to the KF 50 port of the 300 K vacuum chamber. This gate valve allows the beam extension to be isolated from the CBGB source. The beam extension region allows optical access to the CBGB with which beam diagnostics or spectroscopic measurements can be made or state preparation or spin precession tests performed. In the final NMQM experiment, the beam extension will connect to or be replaced by the NMQM science chamber in which the NMQM measurement will be performed.

Originally, the custom 10-way KF 50 cross followed the gate valve and provided optical access. More recently, a 6-way KF 50 cross was inserted between the gate valve and the 10-way cross to provide a second region with optical access. AR-coated KF 40 windows (from AccuGlass) are attached to the KF crosses via KF 40 nipples and adaptors. More recently, the two windows on the 10-way cross (which provide laser access perpendicular to the CBGB) have been replaced by custom Brewster angle windows. The entire interior surface of all KF components (both crosses, all nipples, and all adaptors) is coated with air-brushed Alion MH2200 black paint to reduce laser scatter. A light pipe is attached to the top port of the 10-way cross for light collection and a metal mirror was recently mounted below the light pipe to reflect downward emitted molecular fluorescence back into the light pipe. A KF 50 window is mounted on the top port of the 6-way cross for light collection.

Vacuum pumping for both the CBGB source and the beam extension is provided by the combination of an Agilent IDP 10 dry scroll pump and a Agilent TwisTorr 84FS Turbo pump. A piping and instrumentation diagram of the vacuum system for the CBGB source and beam extension is shown in Fig. 3.11. Only dry, oil-free pumps

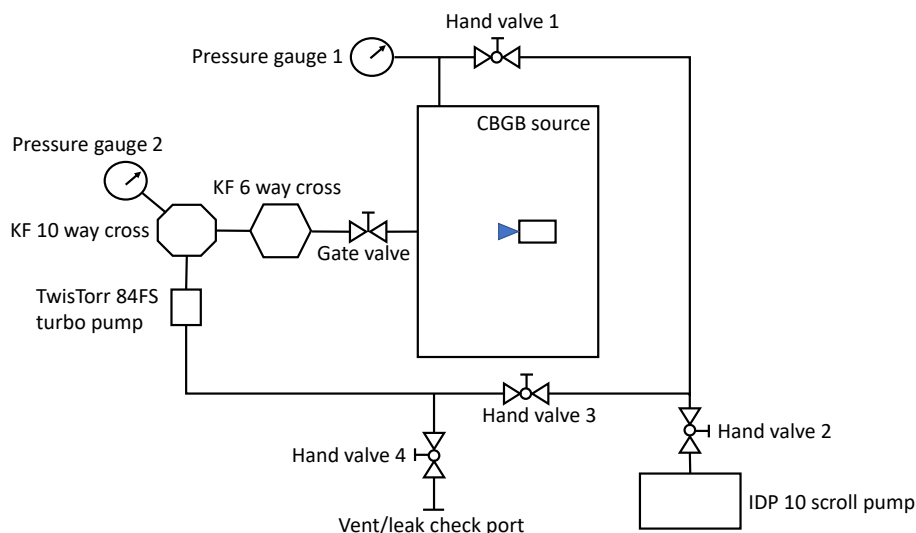


Figure 3.11: Diagram of vacuum system for the CBGB source and beam extension. Pumping is provided by the combination of the TwisTorr 84FS turbo pump and IDP 10 scroll pump. The turbo pump is always backed by the scroll pump when operated. Under normal operating conditions hand valves 2 and 3 and the gate valve are open and all others are closed, so the system is pumped by the turbo pump through the beam extension. Closing the gate valve and hand valve 3 while opening hand valve 1 isolates the beam extension from the CBGB source. Hand valve 2 allows the scroll pump to be isolated when leak checking, and hand valve 4 isolates the vent/leak checking port.

are used on the system. Oil lubricated pumps can back-flow oil into the system which would contaminate the CBGB source, especially the activated charcoal sorbs, and destroy the cryopumping capacity. The turbo pump is mounted to the bottom of the 10-way cross and provides the pumping for the beam extension. The turbo pump is backed by the scroll pump. The scroll pump also provides vacuum pumping for the CBGB source when the beam extension is isolated. Pressure gauges are mounted directly to both the CBGB source (an Instrutech convectron) and the 10-way cross (a MKS multi-ion gague). When operating with both the CBGB source and beam extension under vacuum hand valve 1 (see Fig. 3.11) is closed so that the system is pumped through the beam extension. When this valve was not closed we observed ice formation in the source due to back flow through the IDP-10 scroll pump. Further upgrades to the vacuum system have been made and are discussed in Section 3.2 below.

Background gas issues and solutions

While optimizing the CBGB source to perform spectroscopy of weak YbOH bands, we observed that the magnitude of the laser induced fluorescence (LIF) signal decreased with increasing buffer gas flow. This indicated that we had a buildup of background gas in our system that was attenuating the molecular beam. The background gas buildup could be occurring in any or all of the following regions; in the 4 K shields, in the space between the 4 K and 50 K shields or 50 K shields and 300K chamber, or in the beam extension. We solved the issue by increasing both the mechanical and cryopumping capacity of the system.

Mechanical pumping capacity was increased with the addition of two turbo pumps. A diagram of the upgraded vacuum system is shown in Fig. 3.12. A large TwisTorr 304FS turbo pump was added to the bottom of the 6-way KF 50 cross. This drastically increased the pumping capacity in the beam extension and acted to keep background gas from collecting in the 6-way cross. In order to increase the pumping rate near the CBGB output and near the space between the radiation shields and the 300 K chamber, an additional TwisTorr 74FS turbo pump was added to the front plate of the 300 K chamber. This turbo pump was mounted directly above the beam output. Manual valves are placed in the system so that this 74FS turbo pump can pump on the CBGB source even when the beam extension is isolated and open to atmosphere. All turbo pumps are backed by the same IDP 10 scroll pump.

The cryopumping capacity of the CBGB source was increased with the addition of more activated charcoal sorbs. The additional sorbs were added in the form of vertical sorb plates, 0.125-inch-thick copper 101 plates coated with activated charcoal on both sides. These vertical sorb plates are mounted to the sides of square copper bars (sorb bars) which are mounted to the inside of the 4 K bottom plate. The vertical sorb plates and mounting bars are shown in Fig. 3.14. Drawings of the vertical sorb plates and sorb bars can be found in Appendix B.

When making the upgrades, we discovered that the sorb on the 4 K skimmer plate had become coated with debris, shown in Fig. 3.13. This prompted the replacement of the 4 K skimmer plate with a conical skimmer. The conical skimmer is shown in Fig. 3.14b. The conical skimmer acts to both skim the beam and reflect any background gas away from the output of the buffer gas cell.

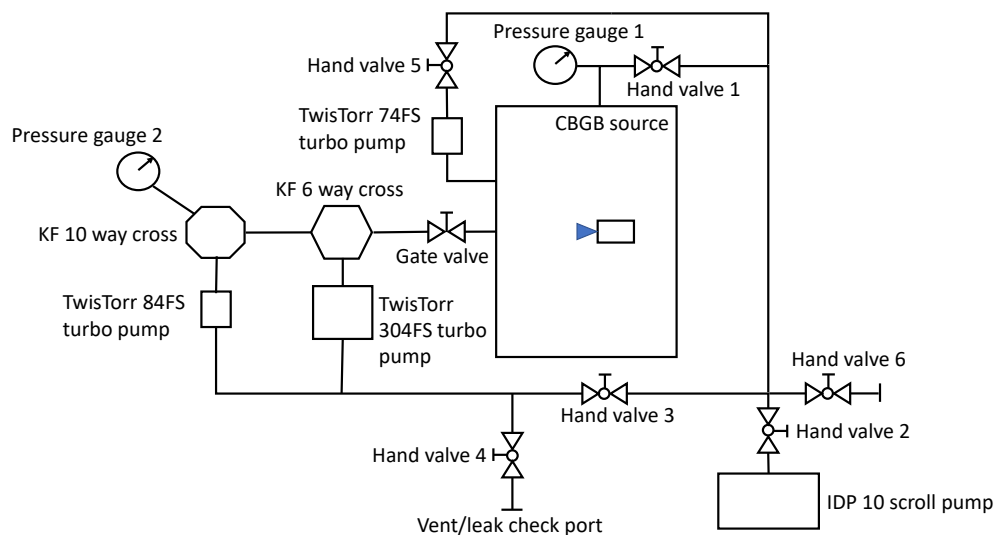


Figure 3.12: Diagram of upgraded vacuum system for CBGB source and beam extension. Pumping capacity was increased by adding a TwisTorr 304 FS and TwisTorr 74 FS turbo pumps. All turbo pumps are backed by the same IDP 10 scroll pump. Under normal operating conditions hand valves 2, 3, and 5 and the gate valve are open while all other valves are closed. Compared to the vacuum system in Fig. 3.11, the CBGB source is now pumped both through the beam extension and directly by the 74FS turbo pump. The beam extension also has additional pumping from the 304 FS turbo pump. Closing the gate valve and hand valve 3 isolates the beam extension from the CBGB source while still pumping the CBGB source with the 74FS turbo pump. Closing hand valve 5 and opening hand valve 1 will pump the CBGB source with the IDP 10 directly, bypassing the 74 FS turbo pump. Hand valves 2 and 4 operate just as they did in Fig. 3.11. An additional vent/leak check port was added (not labeled), isolated by hand valve 6, so that the CBGB source and the beam extension can be leak checked separately.

3.3 Diagnostics: Absorption and fluorescence

All beam diagnostics and spectroscopic measurements are performed via either absorption or laser-induced fluorescence (LIF). We perform absorption measurements in and in front of the buffer gas cell and LIF measurements in the beam extension. Laser beam attenuation due to absorption is measured with a photodiode while LIF is measured with a photomultiplier tube (PMT). A simple diagram showing the optical paths with respect to the CBGB source and beam extension is shown in Fig. 3.15. The ablation laser path is shown as well.

When a laser beam passes through a gas of molecules or atoms, the molecules or atoms will absorb photons from the laser if the laser frequency is resonant with a

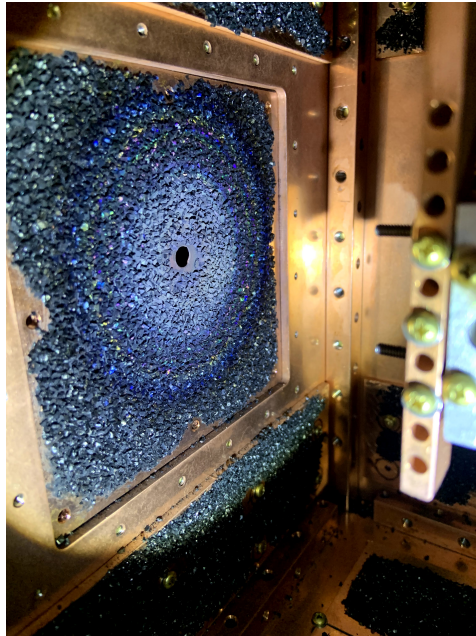


Figure 3.13: Debris in activated charcoal sorb of 4 K skimmer plate.

transition in the atom or molecule. This will cause the intensity, or power, of the laser beam to be attenuated. In the limit of low intensity (e.g., saturation < 1), this attenuation is given by the Beer-Lambert law [115],

$$P_T = P_0 e^{-\sigma(\omega)n(t)l}, \quad (3.8)$$

where P_T is the transmitted power, P_0 is initial power incident on the molecular/atomic cloud, $\sigma(\omega)$ is the absorption cross section, $n(t)$ is the number density of molecules/atoms per unit area, and l is the interaction length of the laser with the molecular/atomic cloud. The absorption cross section, $\sigma(\omega)$, depends on the frequency of the laser and this frequency dependence is the absorption line shape. The number density of molecules/atoms per unit area, $n(t)$, is dependent on time due to the pulsed nature of the CBGB source. By measuring P_0 and P_T , we can determine the optical depth (OD)

$$OD(\omega, t) = \ln \frac{P_0}{P_T} = \sigma(\omega)n(t)l, \quad (3.9)$$

and the integrated OD

$$OD_{int}(\omega) = \int OD(t)dt = \sigma(\omega)l \int n(t)dt. \quad (3.10)$$

Measuring the frequency dependence of OD_{int} results in a measurement of the absorption spectrum of the molecules/atoms. The total number of molecules/atoms

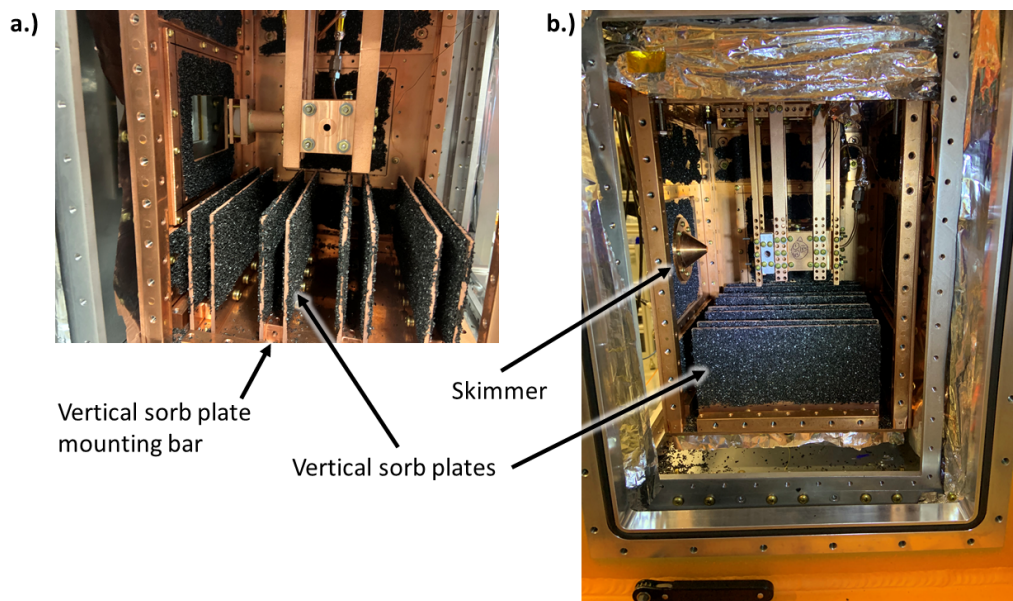


Figure 3.14: Vertical sorb plates and conical skimmer. **a.)** Front view of vertical sorb plates. The vertical sorb plates and the mounting bars are indicated. **b.)** Side views of vertical sorb plates and the conical skimmer, both are indicated.

that interact with the laser for a given amount of time, dt , is $dN = An(t)vdt$, where A is the cross sectional area of the laser beam and v is the velocity of the molecular beam. Integrating gives $N_{tot} = Av \int n(t)dt$. Using Eq. 3.10 results in the total number of molecules/atoms as a function of the integrated OD,

$$N_{tot} = \frac{Av}{\sigma(\omega)l} OD_{int}. \quad (3.11)$$

Therefore, a measurement of the integrated OD can also be used to determine the total number of molecules/atoms interacting with the laser beam.

After absorbing a photon and transitioning to an excited state, the molecule or atom will soon, typically after nanoseconds to microseconds, decay emitting a photon. This laser-induced fluorescence (LIF) can be detected using a PMT. The magnitude of the LIF is proportional to the number of molecules/atoms that absorb a photon initially, $\sigma(\omega)$, and, therefore, measuring the frequency dependence of the LIF provides a measurement of the spectrum of the molecule or atom. Additionally, LIF can be used to measure the Doppler shift of molecular or atomic transitions due to the velocity of the molecular/atomic CBGB. This provides accurate measurements of the CBGB velocity and velocity distribution. When dealing with molecules, the decay can occur to multiple vibrational states (see Section 2.9) and filters can be used to obtain background free detection of off-diagonal transitions.

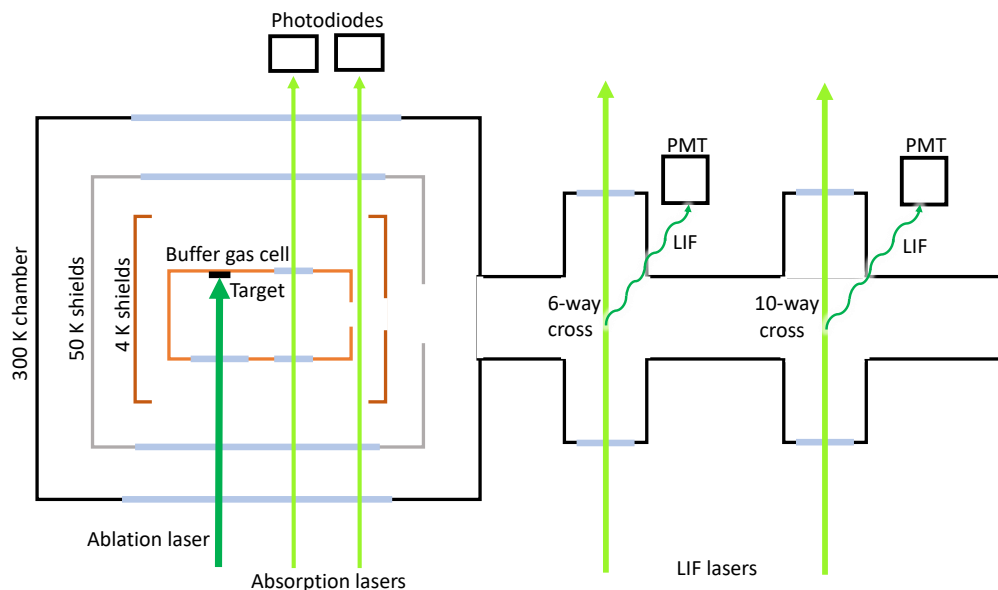


Figure 3.15: Simple diagram of the optical setup (not to scale). Absorption lasers pass through the 300 K chamber, the 50 K shields, and the 4 K shields before being detected by photodiodes. The in-cell beam passes through the buffer gas cell while the in-front-of-cell probe passes in front of the cell aperture. LIF detection beams pass through the 6-way or 10-way KF 50- crosses. LIF is detected by PMTs mounted above the 6-way or 10-way crosses. The ablation laser and target are shown as well.

3.4 YbOH production

Laser Ablation

YbOH molecules (and Yb atoms) are produced in the buffer gas cell via laser ablation. This is accomplished by focusing a doubled, pulsed Nd:YAG laser (532 nm)¹⁰ onto a pressed powder target (Yb foil for the case of Yb atoms). The high-intensity laser light vaporizes the surface of the target and forms a plasma. YbOH molecules are formed in the plasma and then cooled via collisions with the buffer gas. We typically ablate with pulse energies in the range of 10-50 mJ/pulse (most often operating near 30 mJ/pulse) and repetition rates from 4-10 Hz. A lens is used to focus the ablation laser, with the focal point overlapping with the target location. We find that angling this lens can improve the molecular yield from the ablation. Exact positioning and angling of the lens is done in situ while monitoring the in cell absorption signals.

¹⁰Early in the experiment we utilized a Continuum Minilight laser for ablation but switched to a Big Sky Nd:YAG laser and have not switched back.

Target production and testing

Homemade pressed powder targets are used for YbOH production. The targets are made by mixing various ratios of Yb powder with other powdered compounds which contain oxygen and hydrogen. The target-making procedure is as follows¹¹. First the powdered compounds (the Yb powder and other compounds containing oxygen and hydrogen, such as $\text{Yb}(\text{OH})_3$) are mixed and ground with a mortar and pestle until they pass through a 230 mesh sieve. The powder mixture is then combined with 4% polyethylene glycol (PEG8000, often referred to simply as PEG) by weight, which acts as a binder. Several targets containing $\text{Te}(\text{OH})_6$ used KF as a binder instead of PEG¹². The mixture is then pressed in an 8-mm die at ~ 10 MPa for ~ 15 minutes. The dye components are coated in dry-moly lubricant prior to pressing. A summary of the targets made and tested during the work described in this dissertation is given in Table 3.1.

The quality of a target is assessed using two metrics: overall yield, and how fast (number of ablation shots) the YbOH production decreases or decays. These quantities are measured using in-cell absorption spectroscopy. The integrated OD is proportional to the total number of molecules created in each pulse, therefore monitoring the OD as a function of number of ablation shots provides a measurement of the total yield and the decay. Tests comparing the integrated OD vs number of ablation shots for three targets (Stoichiometric Yb to $\text{Yb}(\text{OH})_3$ + 4%PEG, 0.17 $\text{Te}(\text{OH})_6$ to 3 Yb to 1.83 KF, and 0.25 $\text{Te}(\text{OH})_6$ to 3 Yb to 1.75 KF) were conducted at various YAG ablation energies. For all YAG energies tested, the stoichiometric Yb + $\text{Yb}(\text{OH})_3$ target had a significantly higher yield for the first few hundred ablation shots. However, the YbOH yield (integrated OD) from the stoichiometric Yb + $\text{Yb}(\text{OH})_3$ target decayed significantly over the first several hundred ablation shots, sometimes decaying to values near that of the $\text{Te}(\text{OH})_6$ + Yb+ KF targets. In contrast to the stoichiometric Yb + $\text{Yb}(\text{OH})_3$ target the yield from the two $\text{Te}(\text{OH})_6$ + Yb+ KF targets decayed at a much slower rate, essentially providing relatively constant integrated ODs over the range of ablation shot numbers tested.

When operating the CBGB source decay in the YbOH signals is compensated for by adjusting the ablation laser so that it hits a fresh spot on the target, reviving the signal. The consistency and lack of decay from the $\text{Te}(\text{OH})_6$ + Yb+ KF targets prompted us to use the $\text{Te}(\text{OH})_6$ + Yb+ KF targets tested here in spectroscopic

¹¹This target-making procedure was taught to us by Elizebeth West.

¹²These targets were made in coordination with Richard Mawhorter and Graceson Aufderheide.

Table 3.1: Summary of YbOH targets.

Target composition	Mixture ratio
Yb(OH) ₃	Yb(OH) ₃ + 4%PEG
Yb + Yb(OH) ₃	Stoichiometric ^a mixture of Yb and Yb(OH) ₃ + 4% PEG
Yb + Yb(OH) ₃	Yb(OH) ₃ + 10% Yb + 4%PEG
Yb + PVOH ^b	Stoichiometric mixture of Yb and PVOH
Yb + Al(OH) ₃	Stoichiometric mixture of Yb and Al(OH) ₃ + 4%PEG
Yb + Te(OH) ₆ + KF ^c	0.25 Te(OH) ₆ to 3 Yb to 1.75 KF by number
Yb + Te(OH) ₆ + KF ^c	0.5 Te(OH) ₆ to 3 Yb to 1.5 KF by number
Yb + Te(OH) ₆ + KF ^c	0.17 Te(OH) ₆ to 3 Yb to 1.83 KF by number
Yb + Te(OH) ₆	Stoichiometric mixture of Yb and Te(OH) ₆
Yb + Te(OH) ₆	Stoichiometric mixture of Yb and Te(OH) ₆ + 4%PEG

^a Stoichiometric mixture refers to equal ratio of Yb to O to H by number.

^b PVOH is polyvinyl alcohol.

^c These target recipes were determined by Graceson Aufderheide.

studies. Unfortunately, other batches of Te(OH)₆ + Yb+ KF targets performed much more poorly, and we abandoned the Te(OH)₆ + Yb+ KF targets due to this lack of reproducibility from target to target. On the other hand, the stoichiometric Yb + Yb(OH)₃ targets produce large amounts of YbOH and the performance is very consistent from target to target. Additionally, when testing the other target compositions and recipes listed in Table 3.1, we found that all other recipes performed, at best, equivalently but often worse than the stoichiometric Yb + Yb(OH)₃ targets. The stoichiometric Yb + Yb(OH)₃ targets have become our standard as we have not found any targets that perform better.

The parameter space of both mixture ratios and OH-containing compounds has

only been minimally explored by the set of targets given in Table 3.1. It is very possible that a target composition and recipe which produces targets which surpass the stoichiometric $\text{Yb} + \text{Yb}(\text{OH})_3$ targets in performance exists. Therefore, further testing of different target compositions and recipes is warranted. Additionally, production procedures which differ or expand upon the simple grind and press procedure used here could very well produce targets with better properties. All the targets described here suffer from the fact that they are relatively soft and powdery compared to sintered or metal targets. Experimental efforts have shown that harder, denser, and more homogeneous targets tend to ablate better (higher yield, more consistent, less decay)¹³. Unfortunately, sintering is not beneficial for YbOH targets, as the OH bond tends to dissociate at temperatures lower than those needed to cause the target structure to reorganize into a denser more solid form. However, other production methods besides sintering may be able to create denser, harder, and more homogeneous YbOH targets.

3.5 Testing cell with mesh aperture

In addition to the initial testing of the CBGB source, we experimented with a new cell aperture made from copper mesh. This section describes the testing of this aperture. Note that, outside of this section, the data described in this dissertation was taken with a different aperture which consisted of a 5-mm-diameter hole in a solid copper plate. Though copper mesh had been used for second-stage cell apertures [111], to our knowledge, it had not been used to make an aperture for a single stage buffer gas cell. The aperture was made by punching a 3/16th-inch hole in the center of a 1.5 inch x 1.5 inch square of copper 101 size 80 mesh. 4-40 clearance holes were also punched in the mesh so that it can be mounted using the 4-40 threaded rods. In front of the mesh, a 0.25-inch-thick mesh holder was placed to clamp down the copper mesh. A front view of the mesh aperture is shown in Fig. 3.16. The cell assembly used with the mesh aperture is as follows (in order from gas inlet to aperture); gas inlet, 0.5 inch blank, 1.0 inch window with snorkel, 0.5 inch blank, 0.5 inch window, mesh aperture, 0.25 inch mesh holder.

Experimentation with the mesh aperture resulted from our hypothesis that an aperture of this type may be able to provide a more effusive and therefore slower beam. The copper mesh would provide a semi-transparent end to the cell which helium (and the species of interest) would be both reflected from and flow through. The partial reflection of the helium should keep the helium density in the cell high enough so

¹³For example, solid metals like Yb generally ablate better than the pressed powder targets.

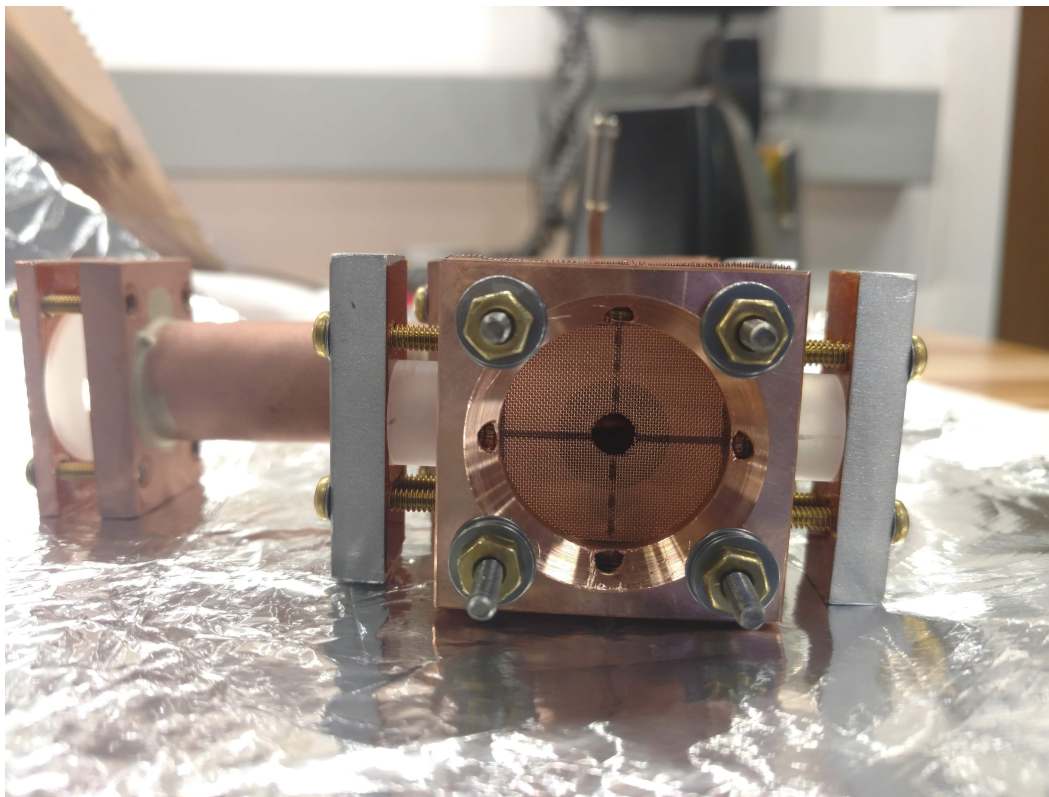


Figure 3.16: Mesh aperture. The aperture consists of a 3/16th-inch-diameter hole in copper 101 size 80 mesh. The darker circle surrounding the aperture hole is the cylindrical bore of the buffer gas cell.

that adequate thermalization can occur while providing the helium an alternative path (other than the aperture) to flow out of the cell. With a normal aperture, all the helium must exit the cell through the aperture. This causes the helium density near the aperture to increase, causing more collision near the aperture to occur. This results in boosting. The semi-transparent nature of the mesh aperture should, in theory, allow the helium to flow out through it while still directing some out of the open aperture. The alternative flow path through the mesh should lower the helium density and the number of collisions near the aperture compared to a normal aperture. Less collisions near the aperture will result in a lower Re and a more effusive, slower beam.

Testing of the cell with the mesh aperture and the resulting CBGB properties was performed with Yb atoms. CBGB properties (see Section 3.1) depend on either the buffer gas properties (mass, thermal velocities, etc.) or the ratio of the mass of the buffer gas to that of the species of interest, m_b/m_s . For Yb and YbOH, $m_b/m_{Yb} \approx m_b/m_{YbOH}$ and therefore a Yb and YbOH CBGB will have essentially

the same properties. Significantly larger amount of atomic Yb are produced via laser ablation, in comparison to YbOH, resulting in much larger signals, simplifying detection for CBGB diagnostics.

Extraction

Extraction of Yb atoms was measured using front-of-cell absorption spectroscopy on the $^1S_0 \rightarrow ^1P_1$ atomic Yb transition. The absorption probe laser passed directly in front of the cell aperture (see Fig. 3.15), and the integrated OD as a function of buffer gas flow was measured at two different ablation pulse energies. The number of atoms leaving the cell was determined using Eq. 3.11. The beam velocity v was determined using a combination of time-of-flight measurements and velocity measurements (velocity measurements are described below). Time-of-flight measurements were made via an absorption spectroscopy of the same Yb transition 47.3 cm downstream. Using the time of the peak of the front-of-cell and 47.3 cm-downstream absorption signals, the velocity was estimated. The measurements were made on resonance where $\sigma(\omega_{res}) = \sigma_0 \frac{g_u \gamma_0}{g_l \gamma_{tot}}$, where g_u and g_l are the upper and lower state degeneracies of 3 and 1 respectively, $\sigma_0 = \lambda^2/2\pi$, $\gamma_0 = 1/2\pi\tau$ is the natural line width, and γ_{tot} is the total linewidth from all broadening mechanisms. For the $^1S_0 \rightarrow ^1P_1$ atomic Yb transition, $\lambda = 398.9$ nm and $\tau = 5.5$ ns. γ_{tot} was measured by measuring the integrated OD as a function of laser frequency.

The number of Yb atoms in front of the cell as a function of buffer gas flow rate at ablation energies of 4.2 and 6.2 mJ/pulse is shown in Fig. 3.17. At an ablation energy of 4.2 mJ/pulse the extraction increases with increasing gas flow. The relative increase in extraction seems to decrease above 5 SCCM. For an ablation energy of 6.2 mJ/pulse, the extraction increases with increasing buffer gas flow up to 5 SCCM, but then the extraction decreases with increasing gas flow for buffer gas flows above 5 SCCM. For a given flow rate, the total number of atoms extracted is always greater for 6.2 mJ/pulse vs 4.2 mJ/pulse ablation energies as expected. The decrease in extraction at 6.2 mJ/pulse for the 6.2 mJ/pulse ablation energy may indicate that the mesh aperture may have a maximum limit on total number of extracted atoms (or molecules). This may be due to the fact that the mesh provides alternative flow paths out of the cell that the atoms (or molecules) may more readily pass through at higher buffer gas flow rates. It is possible that this maximum in extraction was not seen at an ablation energy of 4.2 mJ/pulse as the total number of extracted molecules was always below the maximum reached at 6.2 mJ/pulse. However, this explanation is speculative and more extraction data at both higher flow rates and ablation energies

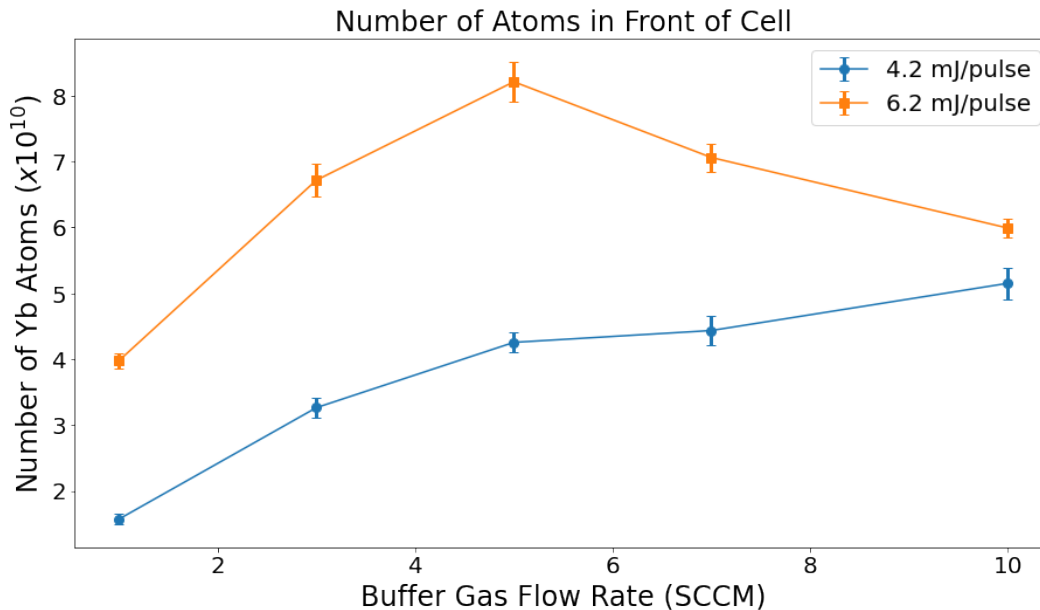


Figure 3.17: Number of atoms in front of cell aperture vs buffer gas flow rate at ablation laser pulse energies of 4.2 and 6.2 mJ/pulse. The number of atoms provides a relative measure of the extraction of atoms from the buffer gas cell through the mesh aperture. The data at 4.2 mJ/pulse was collected by Arian Jadbabaie.

would be needed to confirm this.

Beam velocity

CBGB velocity measurements were obtained via LIF measurements of the Doppler shift of the $^1S_0 \rightarrow ^1P_1$ atomic Yb transition. All velocity measurements were obtained with an ablation pulse energy of 3.4 mJ/pulse and performed in the beam extension region, 43.7 cm downstream from the cell. The observed frequency of an atomic/molecular transition due to the Doppler shift from the atoms/molecules moving at a velocity v is $f = (1 - \frac{v}{c})f_0$, where c is the speed of light and f_0 is the resonance frequency at zero velocity. The beam velocity can then be measured by measuring this Doppler shift,

$$v = -\frac{c}{f_0}(f - f_0), \quad (3.12)$$

Both the transverse and forward velocities of the beam were measured. The transverse velocity was measured with a probe beam perpendicular to the CBGB beam direction (transverse probe) while the forward velocity was measured with a laser beam directed down the axis of the CBGB beam, counter propagating with the CBGB beam direction (longitudinal probe). The transverse velocity probe is only

sensitive to components of the velocity perpendicular to the beam's forward direction and will therefore be centered at the zero velocity resonance frequency, f_0 . The mean frequency of the transverse LIF vs laser frequency provides a measurement of f_0 while the width of the transverse LIF vs laser frequency provides a measurement of the transverse velocity spread. The transverse LIF as a function of velocity¹⁴ at a buffer gas flow rate of 3 SCCM is shown in Fig. 3.18a. A Gaussian fit to this data resulted in a measured transverse velocity of 10.3 ± 0.3 m/s. The longitudinal LIF (LIF from the longitudinal probe laser beam) vs velocity¹⁵ for a buffer gas flow rate of 3 SCCM is shown in Fig. 3.18b. A Gaussian fit to the longitudinal LIF vs velocity resulted in a measured mean CBGB velocity of 90.7 ± 0.3 m/s and a forward velocity spread of 22.8 ± 0.4 m/s. A colormap of the longitudinal LIF magnitude as a function of both time and velocity, for a 3 SCCM buffer gas flow rate, is shown in Fig. 3.19. The two-dimensional colormap provides a more full picture of the CBGB velocity. The solid black curve in Fig. 3.19 is the time-of-flight curve, the time at which an atom/molecule leaving the buffer gas cell with velocity v at time $t = 0$ (the ablation time) should reach the detection region 47.3 cm downstream. Integrating Fig. 3.19 over the time axis results in the LIF vs velocity data shown in Fig. 3.18b.

To understand the effect of the buffer gas flow rate on the CBGB velocity, velocity measurements at lower (1 SCCM) and higher (6 SCCM) flow rates were performed. A two-dimensional colormap of the longitudinal LIF as a function of time and velocity at a 6 SCCM buffer gas flow rate is shown in Fig. 3.20. A Gaussian fit to the LIF vs velocity data resulted in a measured forward velocity at 6 SCCM of 106.7 ± 1.4 m/s and a forward velocity spread of 22.8 ± 1.8 m/s. The transverse velocity data resulted in a measured transverse velocity spread of 13.2 ± 0.8 m/s. The increased forward velocity with increased buffer gas flow rate is expected (see Eq. 3.5, 3.7, and 3.3).

A two-dimensional colormap of the longitudinal LIF intensity as a function of time and velocity for a 1 SCCM buffer gas flow rate is shown in Fig. 3.21. The Gaussian fit to the LIF vs velocity data provided a measured forward velocity of 64.3 ± 1.4 m/s and a forward velocity spread 22.7 ± 2.4 m/s for a buffer gas flow rate of 1 SCCM. The transverse LIF resulted in a measured transverse velocity spread of 8.0 ± 0.5

¹⁴The transverse LIF vs laser frequency was measured and then converted to velocity using Eq. 3.12 with the mean of a Gaussian fit of the LIF vs frequency as the value of f_0 .

¹⁵Again the LIF vs laser frequency was measured and the frequency was converted to velocity using Eq. 3.12 and the measured value of f_0 .

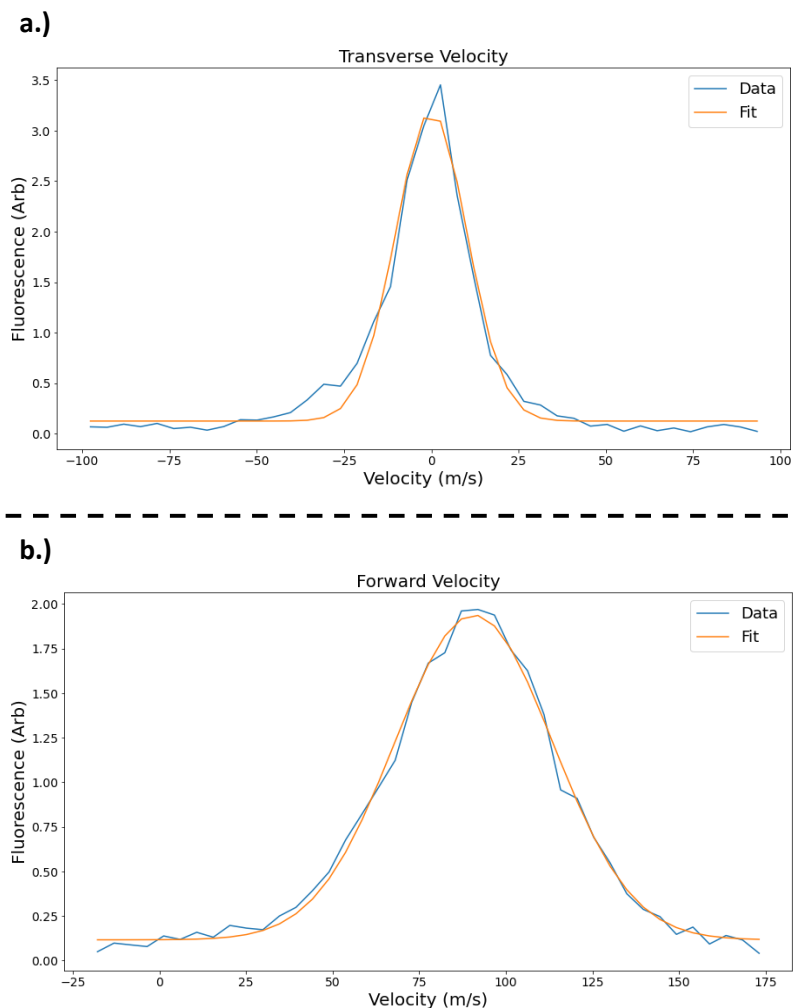


Figure 3.18: $^1S_0 \rightarrow ^1P_1$ atomic Yb LIF from transverse and axial probes as a function of velocity at a buffer gas flow rate of 3 SCCM. Gaussian fits were applied to the data to determine the mean velocity and velocity spread. **a.)** LIF from transverse probe. Mean from fit provides measurement of the zero velocity resonance frequency of the $^1S_0 \rightarrow ^1P_1$ atomic Yb transition. Measured transverse velocity spread of 10.3 ± 0.3 m/s **b.)** LIF from axial probe. Measured mean forward CBGB velocity of 90.7 ± 0.3 m/s and forward velocity spread of 22.8 ± 0.4 m/s.

m/s.

The LIF signal at 1 SCCM in Fig. 3.21 falls below the time of flight curve, in contrast to the LIF data at 3 and 6 SCCM falling above the time of flight curve in Fig. 3.19 and 3.20. This indicates that the atoms are detected earlier than they

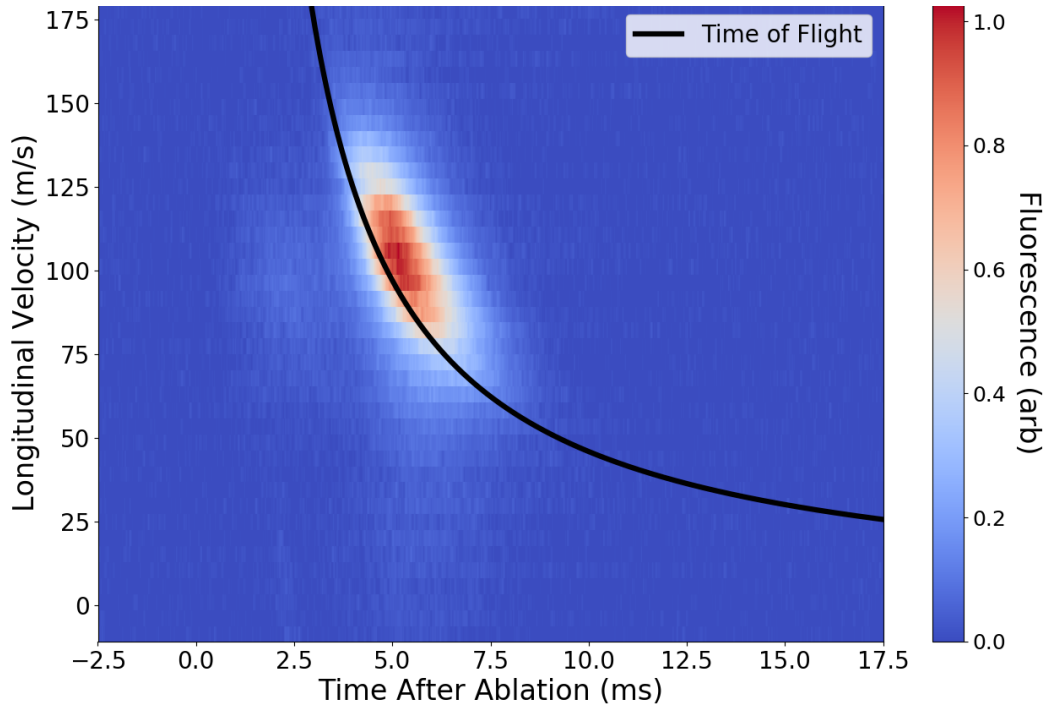


Figure 3.19: Two-dimensional colormap of $^1S_0 \rightarrow ^1P_1$ atomic Yb LIF magnitude vs time and velocity. Date recorded with buffer gas flow rate of 3 SCCM. Solid black curve is the time-of-flight curve $v = z/t$ where $z = 43.7$ cm is the distance from the cell aperture to the detection region. Integrating over the time axis results in the data shown in Fig. 3.18b. Measured mean forward velocity of 90.7 ± 0.3 m/s and forward velocity spread of 22.8 ± 0.4 m/s.

should for the velocity with which they are traveling. This could only be possible if the atoms were slowed after leaving the cell. The longitudinal probe beam is directly overlapped and counter propagating with the CBGB and therefore the atoms can scatter photons along the entire path from the cell to the detection region, resulting in laser slowing of the beam. We can estimate the initial velocity of the CBGB using the following kinematic equations,

$$v_f^2 = v_0^2 + 2ad \quad (3.13)$$

and

$$v_f = v_0 + at. \quad (3.14)$$

The detection region is 43.7 cm downstream and the atoms arrive at approximately 6 ms. Using $d = 43.7$ cm and $t = 6.0$ ms, we can solve for the acceleration by plugging Eq. 3.14 into Eq. 3.13. This gives an acceleration of -2840 m/s². Using this acceleration in Eq. 3.14 gives an initial CBGB velocity of 81.3 m/s. This is

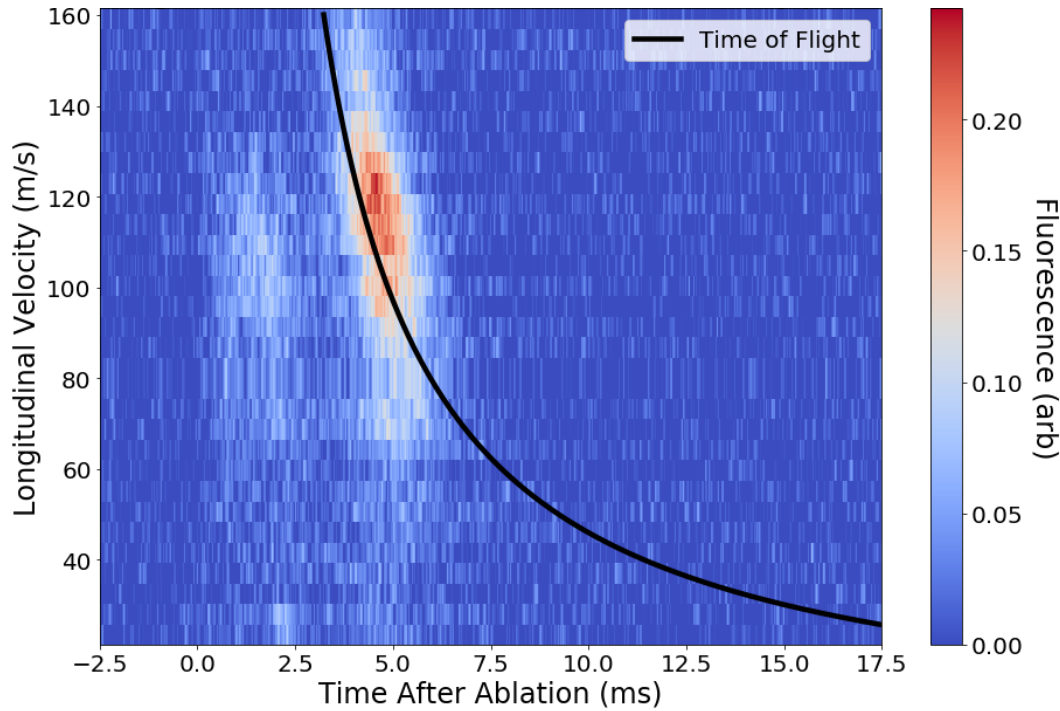


Figure 3.20: Two-dimensional colormap of $^1S_0 \rightarrow ^1P_1$ atomic Yb LIF magnitude vs time and velocity at a buffer gas flow rate of 6 SCCM. Solid black curve is the time-of-flight curve $v = z/t$ where $z = 43.7$ cm is the distance from the cell aperture to the detection region. Measured mean forward velocity of 106.7 ± 1.4 m/s and forward velocity spread of 22.8 ± 1.8 m/s. The measured fluorescence occurring at ~ 2 ms is from another Yb isotope.

a more realistic estimation of the CBGB forward velocity at 1 SCCM. Each photon scatter results in a momentum transfer of $\hbar k$ where $k = 2\pi/\lambda$ is the magnitude of the wavevector. Therefore, the change in momentum is given by, $\Delta p = m\Delta v = N_{photon}\hbar k$, and the total number of photons scattered is $N_{photon} \approx 3000$.

The measured CBGB velocity as a function of buffer gas flow rate and a linear fit is shown in Fig. 3.22. Eq. 3.3 and Eq. 3.5 indicate that the forward velocity should be linearly dependent on the buffer gas flow for the Reynolds numbers in the range $1 \lesssim Re \lesssim 10$. Fig. 3.22 indicates that the forward velocity vs flow rate is very linear for the buffer gas flow rates measured and therefore indicates that the buffer gas cell with the mesh aperture is operating in the $1 \lesssim Re \lesssim 10$ regime.

The ~ 80 m/s CBGB obtained at a 1 SCCM flow rate is much slower than typical single stage CBGB forward velocities of ~ 120 m/s [108]. This is especially promising for laser slowing applications. While more thorough characterizations of this mesh aperture are needed, the initial results presented here indicate that this

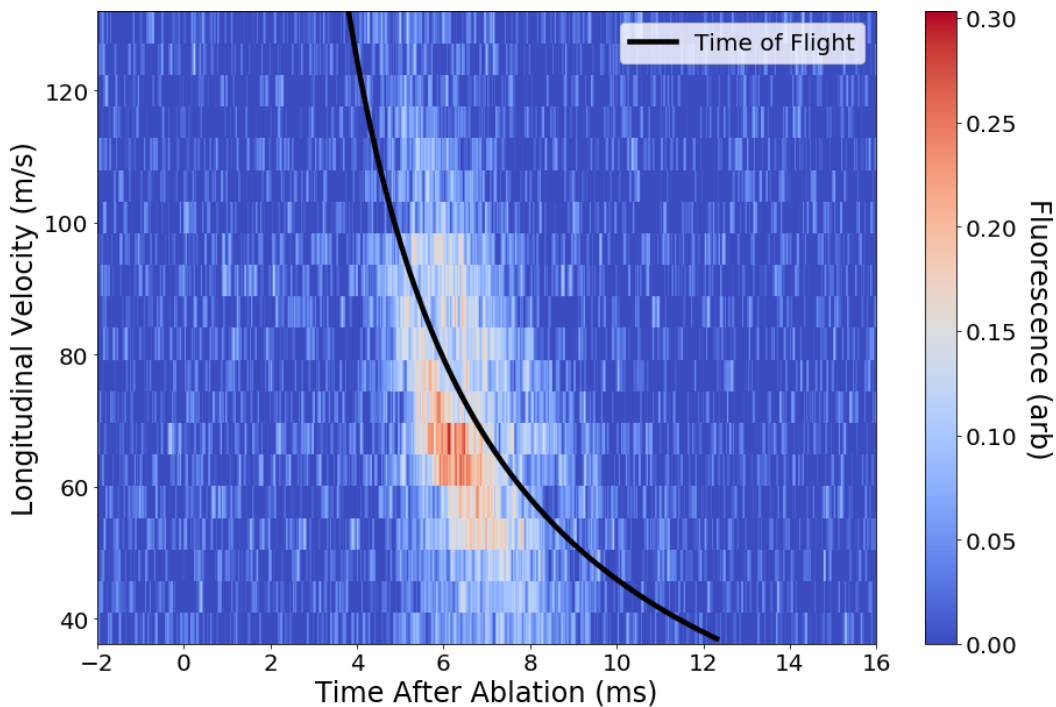


Figure 3.21: Two-dimensional colormap of $^1S_0 \rightarrow ^1P_1$ atomic Yb LIF magnitude vs time and velocity at a buffer gas flow rate of 1 SCCM. Solid black curve is the time-of-flight curve $v = z/t$ where $z = 43.7$ cm is the distance from the cell aperture to the detection region. Measured mean forward velocity of 64.3 ± 1.4 m/s and forward velocity spread of 22.7 ± 2.4 m/s. Note that the LIF falls below the time of flight curve. This is due to unintentional laser slowing of the beam, described in the text.

aperture design may be very beneficial for the production of very slow CBGBs. This mesh aperture may prove advantageous in combination with a second-stage cell as well.

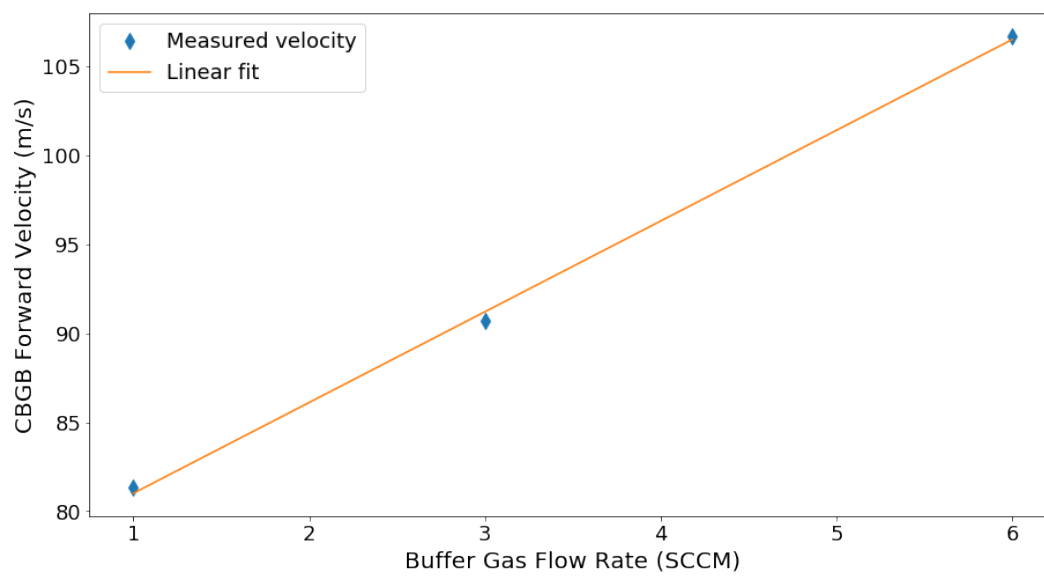


Figure 3.22: CBGB forward velocity vs buffer gas flow rate. The solid line shows the linear fit to the data and indicates that the velocity is linearly dependent on the flow rate. This indicates that the buffer gas cell with the mesh aperture is operating in the $1 \lesssim Re \lesssim 10$ intermediate regime.

Chapter 4

The Pure Rotational Spectrum of YbOH

This chapter describes the pump-probe microwave optical double resonance (PPMODR) spectroscopy of the $\tilde{X}^2\Sigma^+(0, 0, 0)$ state of the $^{174}\text{YbOH}$ isotopologue. Prior to our work, only one spectroscopic study of YbOH had been performed [105], which characterized the $\tilde{A}^2\Pi_{1/2}(0, 0, 0) - \tilde{X}^2\Sigma^+(0, 0, 0)$ and $\tilde{A}^2\Pi_{1/2}(1, 0, 0) - \tilde{X}^2\Sigma^+(0, 0, 0)$ bands of YbOH in a high-temperature sample ($N \geq 30$). With the onset of our experiments, Timothy Steimle and his group at ASU remeasured these bands at high resolution using a cold sample derived from a supersonic molecular beam source [116]. The PPMODR spectroscopy of the $\tilde{X}^2\Sigma^+(0, 0, 0)$ state, described here, supplemented the re-characterization of these bands as the microwave measurements allowed the parameters of $\tilde{X}^2\Sigma^+(0, 0, 0)$ state to be determined to much higher precision than could be achieved with optical measurements. This PPMODR study also resolved the YbOH proton hyperfine splitting for the first time. The $\tilde{A}^2\Pi_{1/2}(0, 0, 0) - \tilde{X}^2\Sigma^+(0, 0, 0)$ origin band is the main cycling transition used in the laser cooling of YbOH and also often used for molecular detection when characterizing CBGB performance. The work described in this chapter was published in [93].

4.1 Pump Probe Microwave Optical Double Resonance (PPMODR) spectroscopy

PPMODR spectroscopy combines the high resolution of microwave measurements with the efficiency of optical detection. Here we used PPMODR spectroscopy to record the pure rotational spectrum of the $\tilde{X}^2\Sigma^+(0, 0, 0)$ state of $^{174}\text{YbOH}$. The measurements described here were performed in the laboratory of Timothy Steimle at ASU. A simplified diagram of the PPMODR experimental setup and method is shown in Fig. 4.1. This work utilized a supersonic YbOH molecular beam, generated using laser ablation as described in previous PPMODR studies [117, 118]. Following ablation, molecular production, and expansion cooling, the rotational population of the molecules is distributed according to an approximate 10 K Boltzmann distribution. To illustrate how the technique works we will focus on only two rotational levels of the $\tilde{X}^2\Sigma^+(0, 0, 0)$ ground state, N' and N'' (Fig. 4.1a). Following molecular production, the molecular beam is exposed to a strong pump laser (~ 100

mW) resonant with the $\tilde{A}^2\Pi_{1/2}(0, 0, 0) - \tilde{X}^2\Sigma^+(0, 0, 0)$ transition originating from the N' rotational level of the $\tilde{X}^2\Sigma^+(0, 0, 0)$ ground state (Fig. 4.1b). The pump laser will optically pump population out of the N' rotational state. Following the pump beam, the molecules are exposed to microwave radiation (Fig. 4.1c). Finally, the molecular beam is measured with a weak (~ 5 mW) probe beam, resonant with the same $\tilde{A}^2\Pi_{1/2}(0, 0, 0) - \tilde{X}^2\Sigma^+(0, 0, 0)$ rotational transition as the pump beam, and the resulting LIF is detected with a PMT (Fig. 4.1d). When the microwave radiation is resonant with the $N'' \rightarrow N'$ rotational transition in the $\tilde{X}^2\Sigma^+(0, 0, 0)$ state, molecular population will be transferred from N'' into N' and there will be an increase in the monitored LIF signal. By measuring the LIF as a function of the microwave frequency, rotational transitions terminating in the N' rotational state are measured. Different pump/probe transitions will allow the measurement of rotational transitions terminating in different N' rotational states. This method avoids the radiative broadening of the excited states as it maps population from one state to another using narrow microwave transitions. The optical excitations are used only for state preparation and readout and, therefore, the high resolution provided by the microwave transitions is preserved.

The pump/probe laser beams were generated from the same cw-dye laser, ensuring they are at exactly the same frequency. The microwave radiation was generated using a 0-20 GHz synthesizer and active harmonic multipliers. A rubidium standard was utilized as the time base for the synthesizer. Approximately $1 \mu\text{W}$ of microwave radiation was introduced into the chamber with a homemade 26° ‘‘H-plane’’ horn antenna. Microwave powers above $1 \mu\text{W}$ resulted in broadening of the spectral lines. The frequency of the the microwave radiation was stepped in increments of 6 kHz and, the LIF from ~ 600 ablation shots was summed at each frequency step. The LIF from excitation of the $\tilde{X}^2\Sigma^+(0, 0, 0) \rightarrow \tilde{A}^2\Pi_{1/2}(0, 0, 0)$ transition was detected on resonance using photon counting techniques. In principal, PPMODR spectroscopy is a background-free technique if 100% pumping efficiency is achieved.

4.2 Microwave spectrum of the $\tilde{X}^2\Sigma^+(0, 0, 0)$ state

Observation and analysis

Rotational transitions terminating in the $J = N + S$ spin rotation components were detected using pump/probe light resonant with the Q_{11} branch features of the $\tilde{X}^2\Sigma^+(0, 0, 0) \rightarrow \tilde{A}^2\Pi_{1/2}(0, 0, 0)$ transition while rotational transitions terminating in the $J = N - S$ spin rotation component were detected with the pump/probe laser resonant with the Q_{12} or R_{12} branch features [116]. Using the

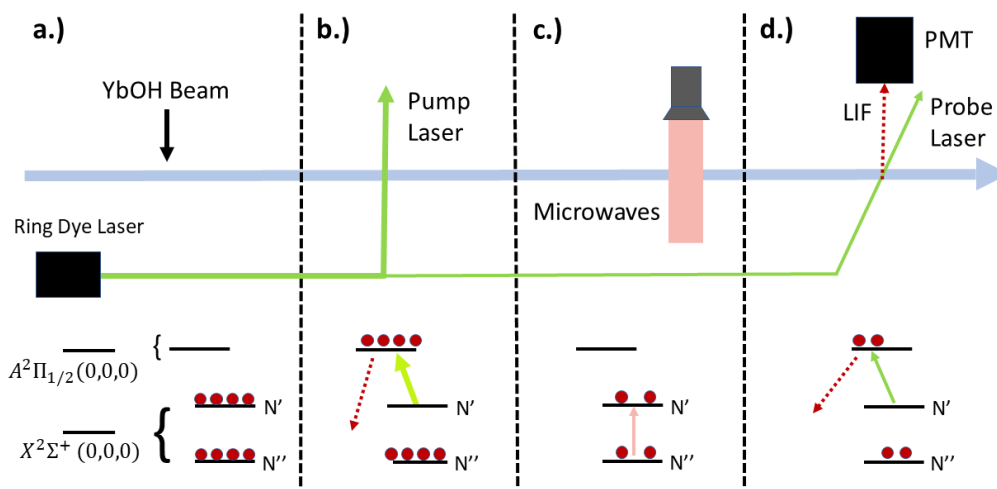


Figure 4.1: Pump-probe microwave optical double resonance spectroscopy (PP-MODR) experimental setup and method. **a.)** A supersonic molecular beam ($T \sim 10$ K) is produced with rotational populations (N' and N'') distributed according to a thermal Boltzmann distribution. **b.)** The YbOH beam is exposed to strong (~ 100 mW) pump beam resonant with a $\tilde{X}^2\Sigma^+(0,0,0) \rightarrow \tilde{A}^2\Pi(0,0,0)$ transition originating from the N' level of the $\tilde{X}^2\Sigma^+(0,0,0)$ state. This depletes the population in the N' rotational state. **c.)** Following depletion of the N' rotational state, the molecular beam is exposed to tuneable microwave radiation. When the microwave radiation is on resonance with a rotational transitions terminating in the N' rotational state, population will be transferred from another rotational state, N'' to N' . **d.)** Finally, the molecular beam is exposed to a weak probe beam (~ 5 mW), resonant with the same $\tilde{X}^2\Sigma^+(0,0,0) \rightarrow \tilde{A}^2\Pi(0,0,0)$ transition as the pump beam, and the resulting LIF is measured with a PMT. If a rotational transition in the $\tilde{X}^2\Sigma^+(0,0,0)$ state is driven by the microwave radiation it will result in an increase in the measured LIF.

PPMODR technique, 12 rotational lines were measured and assigned to 18 rotational transition frequencies. The measured spectral feature of the overlapped $N'' = 5, J'' = 11/2, F'' = 5 \rightarrow N' = 6, J' = 13/2, F' = 6$ and $N'' = 5, J'' = 11/2, F'' = 6 \rightarrow N' = 6, J' = 13/2, F' = 7$ transitions is presented in Fig. 4.2. The energy levels and assignments for these transitions is also presented in Fig. 4.2. The measured transition frequencies and the associated quantum number assignments for the transitions can be found in Table A.1 in Appendix A.

The energy levels of the $\tilde{X}^2\Sigma^+(0,0,0)$ state of YbOH were modeled using the

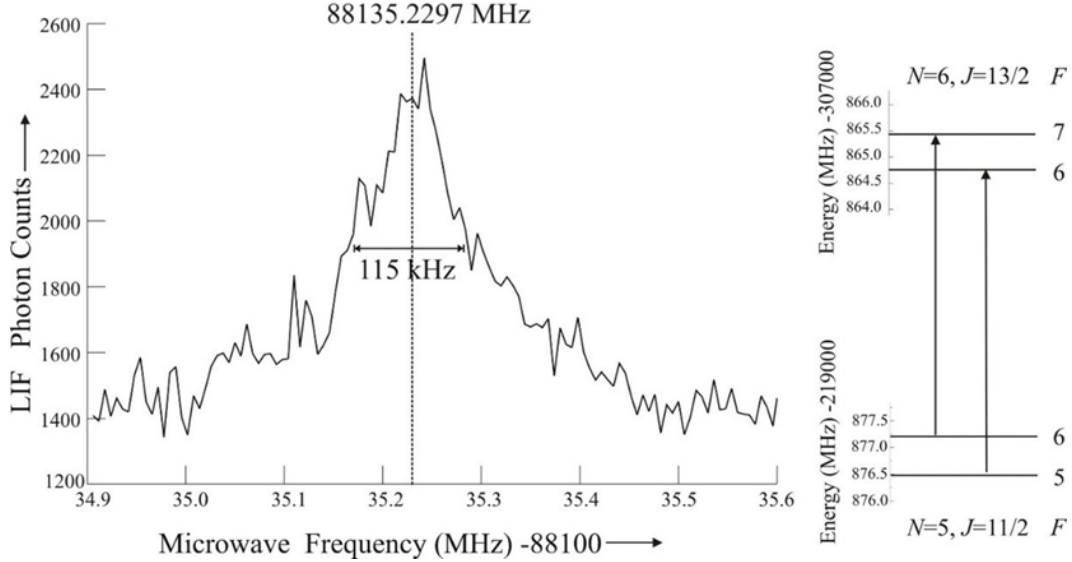


Figure 4.2: PPMODR spectral feature and associated energy levels of the overlapped $N'' = 5, J'' = 11/2, F'' = 5 \rightarrow N' = 6, J' = 13/2, F' = 6$ and $N'' = 5, J'' = 11/2, F'' = 6 \rightarrow N' = 6, J' = 13/2, F' = 7$ pure rotational transitions in the $\tilde{X}^2\Sigma^+(0,0,0)$ ground state of YbOH. This figure was prepared by Timothy Steimle and is from Ref. [93].

following effective Hamiltonian:

$$\begin{aligned} \hat{H}_{eff}(\tilde{X}^2\Sigma^+) = & BN^2 - D(N^2)^2 + \gamma\mathbf{N} \cdot \mathbf{S} + \gamma_D[\mathbf{N} \cdot \mathbf{S}, N^2]_+ \\ & + b_F(H)\mathbf{I} \cdot \mathbf{S} + \frac{c(H)}{3}(3I_zS_z - \mathbf{I} \cdot \mathbf{S}). \end{aligned} \quad (4.1)$$

This effective Hamiltonian accounts for rotation (B), centrifugal distortion (D), spin rotation and spin rotation centrifugal distortion (γ and γ_D), and the Fermi contact (b_F) and dipole-dipole (c) magnetic hyperfine interactions due to the proton in the H atom. The energy levels were calculated by constructing and diagonalizing a 4x4 Hamiltonian¹ in a case ($a_{\beta J}$) basis. The matrix elements for the terms in \hat{H}_{eff} were taken from Ref. [89, 92]. The eigenvalues and the measured transition frequencies were input into a non-linear least squares fitting algorithm to determine the parameters ($B, D, \gamma, \gamma_D, b_F$, and c) of the $\tilde{X}^2\Sigma^+(0,0,0)$ state. The results of the fit are presented in Table 4.1. The fit residuals (observed-calculated transition frequencies) are presented in Table A.1 in Appendix A. The standard deviation of the fit was 23 kHz which is commensurate with the measurement error.

¹The effective Hamiltonian is block diagonal in F and therefore can be split into 4x4 blocks.

Results and discussion

The optimal spectroscopic parameters for the $\tilde{X}^2\Sigma^+(0,0,0)$ state of YbOH determined in this PPMODR study are given in Table 4.1. Also presented in Table 4.1 are the previous values from the high-temperature study [105] and the equivalent parameters for the $X^2\Sigma^+(\nu = 0)$ state of YbF [119]. The rotational (B) and centrifugal distortion (D) parameters are similar to those determined in the previous high-temperature study but more precise. If we assume that the O-H bond length is the same as it is in BaOH, 0.9270 Å, [120] the rotational constant measured here gives a Yb-O bond length of 2.0397 Å. This is extremely similar to the Yb-F bond length of 2.0165 Å for the isoelectronic molecule ^{174}YbF [119].

Table 4.1: Optimal parameters for the $\tilde{X}^2\Sigma^+(0,0,0)$ state of YbOH obtained from the PPMODR measurements. Also presented for comparison are the previous values from the higher-temperature study of YbOH and the equivalent parameters for the $X^2\Sigma^+(\nu = 0)$ state of ^{174}YbF .

Parameter	PPMODR Values ^a	Previous Values ^b	$^{174}\text{YbF} (\nu = 0)^c$
B	7348.40053(29)	7357.92(39)	7233.827(17)
D	0.006084(39)	0.006535(84)	0.007159(fixed)
γ	-81.150(57)	28.90(42)	-13.41679(13)
γ_D	0.00476(56)		0.0039840(15)
b_F	4.80(18)		170.26374(20)
c	2.46(48)		85.4028(19)

^a Numbers in parenthesis represent estimated 2σ error.

^b Ref. [105].

^c Ref. [119].

This table was reproduced from [93].

While the rotational parameters between this PPMODR study and the high-temperature analysis are in good agreement, the determined spin rotation parameters, γ , have a large discrepancy (-81.150(57) MHz vs 28.90(42) MHz). The value for γ determined from the PPMODR spectra is not only about three times larger than the

value determined with the high-temperature sample but it is also of the opposite sign. This large discrepancy prompted a re-analysis of the high-temperature data by the original authors [106] in which a re-assignment of the Q_{11} and R_{12} branches of the $^{174}\text{YbOH}$ and $^{172}\text{YbOH}$ high-temperature data produced a negative value of γ consistent with the value measured in this PPMODR study. The negative value of γ and a comparison with YbF is discussed in detail in Section 4.3 below.

Finally, the high-resolution provided by the PPMODR technique allowed the magnetic hyperfine parameters due to the hydrogen to be determined. The measured values of $b_F(H)$ (4.80(18) MHz) and $c(H)$ (2.46(48) MHz) are very small and similar to those measured for the $\tilde{X}^2\Sigma^+(0, 0, 0)$ state of SrOH , $b_F(H) = 1.713(2)$ MHz and $c(H) = 1.673(5)$ MHz [121]. Additionally, the measured values of $b_F(H)$ and $c(H)$ for YbOH are over an order of magnitude smaller than the equivalent values for the isoelectronic molecule YbF (here the magnetic hyperfine is due to the F instead of H). The smaller hyperfine splittings in YbOH were expected and result from the spin polarization of two bonds (as opposed to one in YbF). This essentially results in the hydrogen residing further from the Yb-centered valence electron. The small hyperfine splitting due to the H was not observed in the optical spectrum of YbOH [116]. This small hyperfine splitting indicates that the hyperfine components will not need to be individually addressed when optically cycling on the $\tilde{A}^2\Pi_{1/2}(0, 0, 0) - \tilde{X}^2\Sigma^+(0, 0, 0)$ transition.

4.3 Negative spin rotation parameter and perturbing states

As discussed in Section 2.7, the spin rotation parameter, γ , is dominated by second-order effects, $\gamma^{(2)}$. These second-order effects arise from the mixing of the $\tilde{X}^2\Sigma^+(0, 0, 0)$ state with other excited vibronic states through the combination of the rotational and spin orbit interactions. Therefore, even though we only measured rotational transitions in the $\tilde{X}^2\Sigma^+(0, 0, 0)$ ground state, the determined spin rotation parameter can provide a significant amount of insight into the excited electronic states of YbOH . For the $\tilde{X}^2\Sigma^+(0, 0, 0)$ ground state $\Lambda = 0$, therefore the second term in Eq. 2.56 is zero and the second-order contribution to γ arises solely from the mixing with excited $^2\Pi$ states. In this case, the dominate contribution to γ is given by [89, 122],

$$\gamma^{(2)} = 2 \sum_{^2\Pi, v'} |\langle v'' | v' \rangle|^2 \frac{\langle ^2\Sigma_{-1/2}^+ | BL_- | ^2\Pi_{1/2} \rangle \langle ^2\Pi_{1/2} | \sum_i a_i l_i^+ s_i^- | ^2\Sigma_{1/2}^+ \rangle}{E_{\Pi, v'} - E_{\Sigma, v''}}, \quad (4.2)$$

where the sum is taken over all excited ${}^2\Pi$ states and all vibrational levels, ν' , of each excited ${}^2\Pi$ state. Here, $\nu'' = 0$ and is the vibrational level of the ${}^2\Sigma^+$ state. $|\langle \nu'' | \nu' \rangle|^2$ is the FCF between the ν'' and ν' levels of the ${}^2\Sigma^+$ and ${}^2\Pi$ states. In Eq. 4.2 we have used the microscopic form of \hat{H}_{SO} , where l_i^+ and s_i^- are the raising and lowering operators for the single electron angular momentum and spin respectively and the sum is taken over all electrons.

In the alkaline earth mono-halides (e.g., CaF) the observed spin-rotation parameter, γ , of the $X^2\Sigma^+$ state can be quantitatively predicted using Eq. 4.2 and the known electronic state distribution. Specifically, $\gamma(X^2\Sigma^+)$ for CaF ($=0.0131 \text{ cm}^{-1}$) is readily predicted by including only the $X^2\Sigma^+ \leftrightarrow A^2\Pi_{1/2}$ interactions in Eq. 4.2 [123]. Like YbOH (and YbF), the $X^2\Sigma^+$ and $A^2\Pi_{1/2}$ states of the alkaline earth mono-halides are atomic in nature and can be well approximated by linear combination of atomic orbitals. Therefore, if the electronic state distributions and FCFs for YbOH are reasonably well known, γ can be estimated using Eq. 4.2 and the known atomic parameters of the Yb^+ ion.

When comparing the determined γ value of YbOH (and YbF) with that of the alkaline earth mono-halides, the most striking difference is that it is of opposite sign, negative as opposed to positive. The negative value of γ determined in this study indicates that YbOH has other interacting excited ${}^2\Pi$ states. We can see this by first considering the contributions to $\gamma^{(2)}$ that arise from the $\tilde{A}^2\Pi_{1/2}$ state.

The ground state of YbOH has a valence electron configuration given by

$$\tilde{X}^2\Sigma^+ : [Xe]4f^{14}\sigma_{\text{Yb}^+(6s6p)}^1 \quad (4.3)$$

Here we have only considered the Yb-centered electrons and neglected the valence configuration of the OH^- radical as it acts as a closed shell and does not contribute to matrix elements in Eq. 4.2. The $[Xe]4f^{14}$ term indicates that the Yb^+ ion has the same filled electron configuration as Xe surrounded by a filled $4f^{14}$ shell. $\sigma_{\text{Yb}^+(6s6p)}^1$ indicates that YbOH has a single unpaired electron in a σ orbital comprised of a combination of the Yb^+ $6s$ and $6p$ hybrid atomic orbitals. The wavefunction of the $\tilde{X}^2\Sigma^+$ state can then be approximated by²

$$|\tilde{X}^2\Sigma^+\rangle \approx x_s|6s\sigma\rangle + x_p|6p\sigma\rangle, \quad (4.4)$$

where $|6s\sigma\rangle = |n = 6, l = 0, \lambda = 0\rangle$ and $|6p\sigma\rangle = |n = 6, l = 1, \lambda = 0\rangle$ (λ is the projection of l on the internuclear axis) are the Yb^+ $6s\sigma$ and $6p\sigma$ atomic orbitals.

²We have neglected contributions from the Yb^+ $5d\sigma$ and $4f13\sigma$ orbitals as the contributions should be small.

Measurements of the hyperfine parameters of the odd isotopologues (see Section 5.5) indicate that $|x_s|^2 \approx 0.54$. Assuming contributions from other atomic orbitals (e.g., $5d\sigma$) are small, $< 1\%$, gives $|x_p|^2 \approx 0.46$.

The configuration for the $\tilde{A}^2\Pi_{1/2}$ state is given by

$$\tilde{A}^2\Pi : [Xe]4f^{14}\pi_{Yb^+(6p5d)}^1, \quad (4.5)$$

where here $\pi_{Yb^+(6p5d)}^1$ indicates a single unpaired electron in a π orbital comprised of a combination of the Yb $6p$ and $5d$ hybrid atomic orbitals. The wavefunction of the $\tilde{A}^2\Pi_{1/2}$ state can be approximated by

$$|\tilde{A}^2\Pi_{1/2}\rangle \approx a_p|6p\pi\rangle + a_d|5d\pi\rangle, \quad (4.6)$$

where $|6p\pi\rangle = |n = 6, l = 1, \lambda = 1\rangle$ and $|5d\pi\rangle = |n = 5, l = 2, \lambda = 1\rangle$ are the Yb⁺ atomic $6p\pi$ and $5d\pi$ orbitals. If we parameterize the atomic spin orbit interaction as $\zeta_{n,l} \cdot s$ [124] and use the Yb⁺ atomic ion values, $\zeta_{6p} = 2220 \text{ cm}^{-1}$ and $\zeta_{5d} = 549 \text{ cm}^{-1}$ [125], as well as the measured spin orbit parameter of the $\tilde{A}^2\Pi$ state of YbOH, $A = 1350 \text{ cm}^{-1}$ [105], we estimate $|a_p|^2 \approx 0.48$ and $|a_d|^2 \approx 0.52$.

We can use the electronic wavefunctions given in Eq. 4.4 and 4.6 and the pure precession hypothesis [89]

$$l^\pm |n, l, \lambda\rangle = \sqrt{l(l+1) - \lambda(\lambda \pm 1)} |n, l, \lambda \pm 1\rangle \quad (4.7)$$

to determine the matrix elements of Eq. 4.2. Note that the l^\pm operator will only connect atomic states with $\Delta n = \Delta l = 0$ and $\Delta \lambda = \mp 1$. Therefore, the $L_- = \sum_i l_i^-$ and l_i^+ operators will only result in non-zero matrix elements between the $|6p\sigma\rangle$ and $|6p\pi\rangle$ components of the $|\tilde{X}^2\Sigma^+\rangle$ and $|\tilde{A}^2\Pi_{1/2}\rangle$ wavefunctions. Therefore, the matrix elements in Eq. 4.2 for the $\tilde{A}^2\Pi_{1/2}$ state are

$$\langle \tilde{X}^2\Sigma^+ | BL_- | \tilde{A}^2\Pi_{1/2} \rangle = Bx_p a_p \langle 6p\sigma | l_i^- | 6p\pi \rangle = Bx_p a_p \sqrt{2} \quad (4.8)$$

and

$$\langle \tilde{A}^2\Pi_{1/2} | \sum_i l_i^+ s_i^- | \tilde{X}^2\Sigma^+ \rangle = a_p x_p \langle 6p\pi | \zeta_{6p} l_i^+ | 6p\sigma \rangle = x_p a_p \zeta_{6p} \sqrt{2}. \quad (4.9)$$

Note that the $s_i^- |^2\Sigma^+\rangle = |^2\Sigma^+\rangle$ and $\zeta_{6p} = 2220 \text{ cm}^{-1}$ [124, 125].

The FCFs and energies, $E_{2\Pi, \nu'}$, can be estimated using the harmonic approximation, the measured vibrational frequencies, ω_i , [116] of the Yb-O stretching mode and

the measured bond lengths³ of the $\tilde{X}^2\Sigma^+$ and $\tilde{A}^2\Pi_{1/2}$ states. We have neglected the FCFs involving the bending and O-H stretching modes as they are extremely small. Using the measured values, the harmonic approximation gives the following FCFs: $|\langle v'' = 0 | v' = 0 \rangle|^2 = 0.8723$, $|\langle v'' = 0 | v' = 1 \rangle|^2 = 0.1123$, $|\langle v'' = 0 | v' = 2 \rangle|^2 = 0.0138$, $|\langle v'' = 0 | v' = 3 \rangle|^2 = 0.0014$, and $|\langle v'' = 0 | v' = 1 \rangle|^2 = 0.001$. FCFs from higher vibrational states were not included as they are extremely small. In the harmonic approximation, the energies of the $\tilde{A}^2\Pi_{1/2}$ state are given by $E_{2\Pi, v'} = T_0(\tilde{A}^2\Pi_{1/2}) + \omega(\tilde{A}^2\Pi_{1/2})v'$. Using these FCFs, energies, and the matrix elements given in Eq. 4.8 and 4.9 results in the following value for the contribution to the spin rotation parameter from the $\tilde{A}^2\Pi_{1/2}$ state

$$\gamma(\tilde{A}^2\Pi_{1/2}) = +0.0276 \text{ cm}^{-1} = +828 \text{ MHz.} \quad (4.10)$$

Contributions to γ from the $\tilde{A}^2\Pi_{1/2}$ state are only positive and cannot account for the negative value of γ . Therefore, interactions with additional $^2\Pi$ states must be contributing to the sum in Eq. 4.2. More specifically, the additional $^2\Pi$ states must provide negative contributions to γ that are larger in magnitude than those from the $\tilde{A}^2\Pi_{1/2}$ state. Adding additional single-electron $^2\Pi$ states (derived from $p\pi$ and $d\pi$ orbitals) will not resolve the issue as the contributions from these states will also be positive.

Now consider the case where one of the Yb $4f$ electrons jumps up to the $\sigma_{Yb^+(6s6p)}$ orbital. It is reasonable to assume states of this nature exist in YbOH as there are similar states in the Yb⁺ ion (e.g., the $^2F_{7/2}^o$ and $^2F_{5/2}^o$ states derived from the $[Xe]4f^{13}6s^2$ configurations [126]). This will result in the following electron configuration:

$$[Xe]4f^{13}\sigma_{Yb^+(6s6p)}^2. \quad (4.11)$$

It is convenient to think about this $4f^{13}$ configuration as a single hole (e.g. a positron) in a single Yb $4f$ orbital instead of 13 electrons (12 paired and 1 unpaired) in the $4f$ shell. This $4f$ hole has 4 possible projections of angular momentum on the internuclear axis, $m_l = 0, 1, 2, 3$. Therefore, the configuration given in Eq. 4.11 will result in 4 electronic states, $^2\Sigma^+$, $^2\Pi$, $^2\Delta$, and $^2\Phi$. Only the $^2\Pi$ state will contribute to $\gamma^{(2)}$ and we will write this electron configuration in the following way:

$$(4f^{13})^2\Pi : [Xe]\pi_{Yb^+(4f)}^{1+}\sigma_{Yb^+(6s6p)}^2, \quad (4.12)$$

³ $r_e(\tilde{X}^2\Sigma^+)$ was measured in this study, $r_e(\tilde{A}^2\Pi_{1/2})$ was determined from the rotational constant measured in Ref. [116].

where $\pi_{Yb^+(4f)}^{1+}$ indicates a hole in the Yb $4f$ orbital. Since the charge of the hole is opposite of the electron, it will result in a negative value of a_i in the spin orbit interaction⁴. Therefore, states derived from the electron configuration given in Eq. 4.12 result in negative contributions to $\gamma^{(2)}$. Therefore, the only way to account for the negative value of γ determined in this work is the existence of $^2\Pi$ states in YbOH which contain contributions from the electron configuration given in Eq. 4.12. We refer to the states resulting from a Yb $4f^{13}$ configuration as perturbing states. Additionally, the negative value of γ also indicates that the negative contributions from the perturbing states outweigh those from the $\tilde{A}^2\Pi_{1/2}$ or other excited $^2\Pi$ states.

The isoelectronic molecule YbF also has a negative spin rotation parameter in the $X^2\Sigma^+(\nu = 0)$ ground state [119], and it was concluded that this is also the result of $4f^{13}$ perturbing states [122, 124]. However, the value of γ for YbF is approximately 6 times smaller than that of YbOH. This indicates that the perturbing states provide a larger contribution to γ in YbOH than they do in YbF.

⁴This is observed in the Yb⁺ atomic ion energy levels, the $^2F_{7/2}^o$ state is lower in energy than the $^2F_{5/2}^o$ state, e.g., $\zeta_{4f^{+1}} < 0$.

Spectroscopy of Odd Isotopologues, $^{171,173}\text{YbOH}$

This chapter details both the development of enhanced YbOH production via laser-enhanced chemical reactions and the observation, assignment, and analysis of the $\tilde{A}^2\Pi_{1/2}(0, 0, 0) - \tilde{X}^2\Sigma^+(0, 0, 0)$ band of $^{171}\text{YbOH}$ and $^{173}\text{YbOH}$. The electric quadrupole deformation of the ^{173}Yb nucleus is proposed to make it extremely sensitive for measurements of an NMQM [33], and $^{173}\text{YbOH}$ is the YbOH isotopologue with which we are developing experiments to measure a NMQM. The nuclear spin ($I = 1/2$) of the ^{171}Yb nucleus makes the $^{171}\text{YbOH}$ isotopologue sensitive for measurements of NSD-PV [127], though we are not pursuing the development of such experiments. A simultaneous measurement and analysis of the $^{171}\text{YbOH}$ and $^{173}\text{YbOH}$ spectra provided a systematic check of the analytical methods since the measured magnetic hyperfine parameters scale by the magnetic moments of each respective nuclei. Finally, measurements of the spectral features of the odd isotopologues proved extremely difficult due to the complex, overlapping structure of all the YbOH isotopologues. In order to simplify the otherwise overlapped spectra, a novel spectroscopic technique utilizing the laser-enhanced chemical reactions was developed and utilized. The development of the increased YbOH production via laser-enhanced chemical reactions is published in Ref. [128] and the spectroscopic studies of $^{171,173}\text{YbOH}$ are published in Ref. [129]. Some portions of the material published in Ref. [129] are reproduced here with permission from AIP.

5.1 Laser-enhanced chemical reactions: Enhancement of YbOH production

Gas-phase YbOH created by ablation of a solid precursor is believed to be produced primarily in the high-temperature plasma created by ablation. Collisions with the buffer gas cool this plasma resulting in a quenching of the chemical reactions as the reactants cool to cryogenic temperatures. In addition to YbOH, the ablation process also produces atomic Yb (orders of magnitude more than YbOH), indicating that unused reactants are still present in the buffer gas cell following the cooling of the ablation produced plasma. Chemical reactions of ground state (1S_0) Yb atoms with many reactants, such as H_2O , are endothermic at cryogenic temperature and therefore do not proceed in the buffer gas cell. However, excitation of the Yb atoms to an excited electronic state can provide exothermic reaction pathways through

which YbOH production can proceed. Studies of excited state chemistry have shown that reactants in excited states have access to additional reaction pathways and transition states [130] and can result in modified product state distributions [131]. Laser excitation of reactants has also been used to produce the molecular species of interest in spectroscopic studies [132, 133].

We find that excitation of the $^3P_1 \leftarrow ^1S_0$ atomic Yb transition results in a factor of ~ 10 increase of the number of YbOH molecules both inside the buffer gas cell and in the CBGB. Unless otherwise stated, all data was collected when driving the $^3P_1 \leftarrow ^1S_0$ transition of the ^{174}Yb isotope and probing the $^{174}\text{YbOH}$ isotopologue. Experimentally, we observed this increased YbOH production by monitoring the in cell OD and in front of cell OD with and without the $^3P_1 \leftarrow ^1S_0$ laser excitation (enhancement light or enhancement laser) applied. The optical depth was measured via absorption spectroscopy of the $^2Q_{11}(2)$ line of the $\tilde{A}^2\Pi_{1/2}(0, 0, 0) - \tilde{X}^2\Sigma^+(0, 0, 0)$ $^{174}\text{YbOH}$ transition [116], directly probing the number of molecules in the $N = 2$ rotational level of the $\tilde{X}^2\Sigma^+(0, 0, 0)$ state. With the enhancement light blocked, there is an un-enhanced yield of 4×10^{10} molecules in the cell and 7×10^9 molecules in front of the cell. With the enhancement light unblocked there is an enhanced yield of 3×10^{11} molecules in the cell and 8×10^{10} molecules in front of the cell. In both cases, in cell and in front of cell, the number of molecules is increased by a factor of ~ 10 . This enhancement is dependent on the geometry in which the enhancement laser is introduced into the cell. We found that the largest enhancement in YbOH production occurs when the enhancement light is introduced through the absorption probe window, as opposed to down the cell bore through the aperture or through the ablation window attached to the snorkel.

To characterize the enhanced production we define a quantity called the enhancement factor, the ratio of the integrated OD with the enhancement light on and off. This ratio of the integrated ODs is equal to the ratio of the number of YbOH molecules with and without the enhancement light. We observe that the frequency dependence of the enhancement factor follows that of an atomic resonance. The enhancement factor is maximized when the enhancement laser is on resonance with the $^3P_1 \leftarrow ^1S_0$ atomic Yb transition and decreases exponentially when the enhancement laser is detuned from the atomic resonance. For large detunings from the atomic resonance, the enhancement factor reaches a value of 1 (same amount of YbOH with and without the enhancement light), indicating that the off resonant light does not increase YbOH production. The power dependence of the enhancement factor also indicates

that the enhanced YbOH production is due to driving an optical resonance. The enhancement factor increases linearly for low powers and saturates at high powers, with the crossover occurring for an intensity of $\sim 10 \text{ W/cm}^2$. This saturation indicates that the enhancement is proportional to the excited 3P_1 Yb population.

The resonant nature of the enhancement factor allows specific selection of which YbOH isotopologue has enhanced production: driving the $^3P_1 \leftarrow ^1S_0$ transition of one Yb isotope only¹ enhances the production of that isotopologue of YbOH². For the odd isotope/isotopologue $^{173}\text{Yb}/^{173}\text{YbOH}$, we investigated the effect of driving different hyperfine components of the $^1S_0 \rightarrow ^3P_1$ ^{173}Yb transition on the enhancement factor. The enhancement factor for both the $G = 2$ and $G = 3$ ($G = I + S$ see Section 2.6) hyperfine states of $^{173}\text{YbOH}$ when driving each of the three ($F = 5/2 \rightarrow F' = 3/2, 5/2, 7/2$) ^{173}Yb transitions is shown in Fig. 5.1. The enhancement factor for the $G = 2$ and $G = 3$ states of $^{173}\text{YbOH}$ were probed through absorption spectroscopy of the $^oP_{12}(2)$ and $^oP_{13}(2)$ ³ lines of the $\tilde{X}^2\Sigma^+(0, 0, 0) \rightarrow \tilde{A}^2\Pi_{1/2}(0, 0, 0)$ $^{173}\text{YbOH}$ transition respectively. For all ^{173}Yb transitions, the enhancement factor in the $^{173}\text{YbOH}$ $G = 2$ and $G = 3$ states is equal in magnitude, as expected for a thermalized sample. However, the enhancement factor is smaller when driving the $F = 5/2 \rightarrow F' = 3/2$ ^{173}Yb transition. We attribute this decrease in the enhancement factor to the overlap of the ^{173}Yb $F = 5/2 \rightarrow F' = 3/2$ and ^{171}Yb $F = 1/2 \rightarrow F' = 3/2$ transitions, which are separated by only $\sim 3 \text{ MHz}$ [134]. This overlap will result in excitation of both ^{171}Yb and ^{173}Yb to the 3P_1 state which will allow production of $^{171}\text{YbOH}$ as well. The increased $^{171}\text{YbOH}$ production will deplete the available population of reactions with which $^{173}\text{YbOH}$ can be formed.

It is important to note that in addition to the enhancement of a specific isotopologue of YbOH, we also observe a small increase in the populations of other YbOH isotopologues. For example, when driving the ^{174}Yb transition we observe an increase in the population of $^{172}\text{YbOH}$. We call this effect cross enhancement. The cross enhancement factor is small, a factor of ~ 2 -3, compared to the resonant enhancement. Interestingly, the cross enhancement is a resonant effect as well. When detuning the Yb excitation light off of the ^{174}Yb transition and toward the ^{172}Yb transition, the cross enhancement decreases and eventually disappears. Therefore, the cross

¹We see some cross enhancement between YbOH isotopologues, discussed below.

²For example driving the $^1S_0 \rightarrow ^3P_1$ ^{174}Yb transition enhances the production of $^{174}\text{YbOH}$ while driving the $^1S_0 \rightarrow ^3P_1$ ^{172}Yb transition enhances the production of $^{172}\text{YbOH}$.

³Here the branch designations are given by $^{\Delta N} \Delta J_{IG}(N'')$. This is described in more detail in Section 5.4.

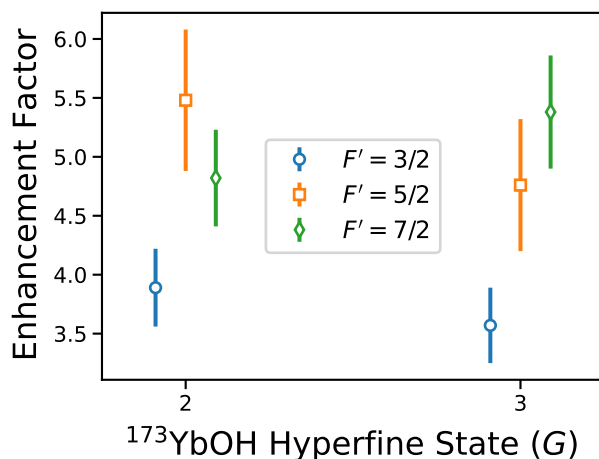


Figure 5.1: Enhancement of the $N = 2$, $G = 2, 3$ hyperfine states of $^{173}\text{YbOH}$ when driving each of the three $F = 5/2 \rightarrow F' = 3/2, 5/2, 7/2$ atomic ^{173}Yb transitions. $G = S + I_{Yb}$ results from the coupling of the electron spin to the spin of the ^{173}Yb nucleus.

enhancement is not due to power broadening as it would increase when tuning the laser towards the ^{172}Yb transition. Instead the cross enhancement is proportional to the amount of excited ^{174}Yb . This perhaps suggests that excitation exchanging collisions are occurring inside the buffer gas cell, resulting in excited ^{172}Yb (and other isotopes) when only one isotope, ^{174}Yb , is resonantly excited. We have observed cross enhancement in other isotopologues of YbOH in addition to $^{172}\text{YbOH}$.

Finally, we investigated the effect of the laser enhanced chemical reactions on the internal state distributions of the resulting YbOH molecules. The enhancement factor as a function of rotational and vibrational state is shown in Fig. 5.2. The rotational states were probed via absorption spectroscopy of the $^{\mathcal{Q}}Q_{11}(N)$ transitions of the origin band [116]. The enhancement factor of the $\tilde{X}^2\Sigma^+(1, 0, 0)$ vibrational state were measured via absorption spectroscopy of the $\tilde{A}^2\Pi_{1/2}(1, 0, 0) - \tilde{X}^2\Sigma^+(1, 0, 0)$ transition at 17378.58 cm^{-1} [116], while the $\tilde{X}^2\Sigma^+(0, 2^2, 0)$ was probed via absorption spectroscopy of a tentatively assigned line at 17345.09 cm^{-1} . Based on initial dispersed LIF (DLIF) measurements of YbOH [135], the line at 17345.09 cm^{-1} was believed to a rotational component of the diagonal $\tilde{X}^2\Sigma^+(0, 1, 0) \rightarrow \tilde{A}^2\Pi_{1/2}(0, 1, 0)$ band. However, recent high-resolution spectroscopic measurements (described in Section 6.6) indicate that this original assignment may be incorrect, and a tentative re-assignment attributes the band at 17345 cm^{-1} to the $\tilde{X}^2\Sigma^+(0, 2^2, 0) \rightarrow [18.00]$

transition. Here, [18.00] designates an excited state residing around 18000 cm^{-1} . The existence of an excited state at around 18000 cm^{-1} is speculative and, at the time of writing, direct excitation from the $\tilde{X}^2\Sigma^+(0,0,0)$ state to [18.00] has not yet been observed. Experiments to definitively confirm the existence of the [18.00] state are underway.

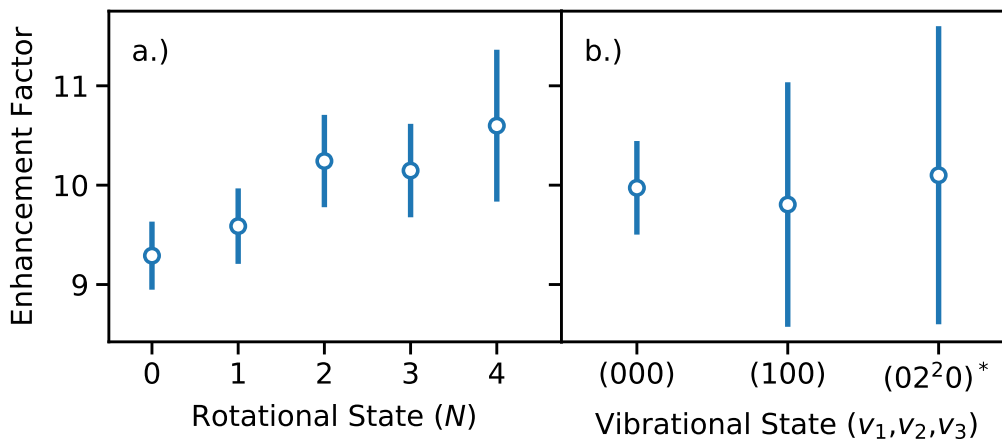


Figure 5.2: Enhancement of the rotational and vibrational states of $^{174}\text{YbOH}$. **a.)** Enhancement as a function of ground state rotational level, N . The rotational populations were probed via absorption spectroscopy of the $^{\mathcal{Q}}Q_{11}(N)$ lines of the $\tilde{X}^2\Sigma^+(0,0,0) \rightarrow \tilde{A}^2\Pi_{1/2}(0,0,0)$ transition. **b.)** Enhancement as a function of the ground state vibrational level. Here (ν_1, ν_2^l, ν_3) indicates the vibrational quanta in the Yb-O stretch, O bend, and O-H stretch respectively, and the superscript l indicates the projection of the bending angular momentum along the molecular symmetry axis. The enhancement factor for the $\tilde{X}^2\Sigma^+(0,0,0)$ state is an average of the $N = 0$ through $N = 4$ values shown in **a**. The $\tilde{X}^2\Sigma^+(1,0,0)$ state was probed via absorption spectroscopy of the $\tilde{X}^2\Sigma^+(1,0,0) \rightarrow \tilde{A}^2\Pi_{1/2}(1,0,0)$ transition at 17378.58 cm^{-1} . The $\tilde{X}^2\Sigma^+(0,2^2,0)$ state was probed via the tentatively assigned transition at 17345.09 cm^{-1} . A more thorough description of this tentative assignment is given in the text.

The energy scales of the Yb excitation, and therefore the chemical reactions, are orders of magnitude larger than the rotational or vibration energies of YbOH. Due to this large energy difference, we expect the resulting YbOH population to be distributed over many rotational and vibrational states. However, following the chemical reactions, the product YbOH should collide with the background 4 K helium, quickly thermalizing the rotational and translational degrees of freedom of the molecules. The relatively uniform enhancement factor for the lowest rotational states, Fig. 5.2a, indicates that this rotational thermalization does indeed

occur. Conversely, helium collisions provide poor vibrational thermalization [71] which results in non-thermal vibrational distributions in CBGB sources. Therefore, we expect this lack of vibrational thermalization to result in an enhanced non-thermal vibrational population (uniform enhancement factor across multiple vibrational states). This enhanced non-thermal vibrational population is indeed observed and shown in Fig. 5.2b.

Laser-enhanced chemical reactions are not limited to the production of YbOH and have recently been used for the production of a CaOH CBGB for the laser cooling and trapping of CaOH [60]. Enhanced production via laser excitation of atomic metal centers could also aid in the production of other Yb, Ca, Sr, Ba, Ra, or Al containing molecules, especially for the case of rare isotopologues where efficient production is critical. Laser-enhanced chemical reactions also prove to be a useful spectroscopic resource. The increased population of excited vibrational states following the reactions provides a non-thermal molecular sample in which spectroscopy of transitions originating from these excited vibrational states can be performed. We utilized this to measure and characterize the $\tilde{A}^2\Pi_{1/2}(1, 0, 0) \rightarrow \tilde{X}^2\Sigma^+(3, 0, 0)$ transition of YbOH and identify the vibrational repumping transitions for laser cooling, see Section 6.5. Additionally, comparing molecular spectra with and without the chemical enhancement will allow the disentangling of complex isotopologue structure and identification of the spectrum of specific molecules and molecular isotopologues. The development and implementation of a novel spectroscopic technique utilizing these laser-enhanced chemical reactions is described in Sections 5.3 and 5.4. This technique was critical for the observation of the spectrum of the odd isotopologues, $^{171,173}\text{YbOH}$, described in this chapter. Characterizations of the laser-enhanced chemical reactions with respect to additional laser and CBGB source parameter as well as quantum chemical calculations of these chemical reactions can be found in [128].

5.2 Experimental setup for $^{171,173}\text{YbOH}$ spectroscopy

Initial studies of $^{171,173}\text{YbOH}$ were performed using the molecular beam LIF spectrometer at ASU. This spectrometer was used in the previous high-resolution optical studies of $^{172,174}\text{YbOH}$ [93, 116]. Briefly, YbOH is produced by laser ablating (532 nm, ~ 10 mJ/pulse, 20 Hz) a Yb rod in the presence of a methanol/argon supersonic expansion. The resulting beam is skimmed to produce a well-collimated beam with a temporal pulse width of ~ 40 μs in the detection region. The molecular beam is probed by an unfocused (~ 5 mm), low power (~ 5 mW), single-frequency cw-dye

laser approximately 0.5 m downstream. It is estimated that the laser probes approximately 1×10^9 YbOH molecules in each molecular beam pulse. The resulting on-resonance LIF signal was viewed through a 580 ± 10 nm bandpass filter, detected by a photomultiplier tube (PMT), and processed using gated photon counting. Typically, the photon counts from 35 ablation pulses at each excitation laser frequency are summed. The absolute excitation wavelength is determined by co-recording a sub-Doppler I_2 spectrum [136], and the relative wavelength is measured by co-recording the transmission of an actively stabilized etalon (free spectral range of 751.393 MHz).

High-resolution absorption spectroscopy measurements of $^{171,173}\text{YbOH}$ were recorded at Caltech using the 4 K CBGB source described in Ch. 3. The cell configuration used for these measurements is as follows: gas inlet, 0.125-inch blank, diffuser plate, 0.5-inch blank, 1.0-inch window piece for ablation (with snorkel), 0.5-inch blank, 0.5-inch window piece for spectroscopy (spectroscopy window), and 0.25-inch aperture plate (5-mm aperture). All measurements were performed inside the buffer-gas cell, as opposed to in the extracted beam. YbOH molecules created by ablating (532 nm, ~ 30 mJ/pulse, ~ 5 Hz) either a stoichiometric Yb + Yb(OH)₃ or a Yb + Te(OH)₆+KF target. The mixture ratios for the Yb + Te(OH)₆+KF were 0.17 : 3 : 1.83 and 0.25 : 3 : 1.75 (Te(OH)₆ : Yb : KF).

To measure the absorption spectra, three cw-laser beams are passed through the spectroscopy window: the primary tunable absorption spectroscopy beam (1 mm diameter, ~ 30 μW), the normalization laser (1 mm diameter, ~ 40 μW) used to monitor the shot-to-shot fluctuations in YbOH production, and the chemical enhancement laser (3 mm diameter, ~ 300 mW), which increases the molecular yield by exciting atomic Yb to the metastable 3P_1 state as described above in Section 5.1.

The normalization laser is fixed to either the $^O P_{12}(2)$ or $^R R_{11}(2)$ line of the $\tilde{A}^2\Pi_{1/2}(0,0,0) - \tilde{X}^2\Sigma^+(0,0,0)$ transition of $^{172}\text{YbOH}$ at 17322.1732 cm^{-1} and 17327.0747 cm^{-1} , respectively [116], and is used to monitor molecular production. The $^O P_{12}(2)$ or $^R R_{11}(2)$ line of the $\tilde{A}^2\Pi_{1/2}(0,0,0) - \tilde{X}^2\Sigma^+(0,0,0)$ transition of $^{172}\text{YbOH}$ were used for normalization as they are unblended. The frequency of the enhancement laser is fixed to the $^3P_1 \leftarrow ^1S_0$ transition of the desired Yb isotope. Specifically, the $^{174}\text{Yb}(17992.0003$ $\text{cm}^{-1})$, $^{176}\text{Yb}(17991.9685$ $\text{cm}^{-1})$, $F'' = 1/2 \rightarrow F' = 1/2$ ^{171}Yb (17991.9292 cm^{-1}) and the $F'' = 5/2 \rightarrow F' = 7/2$ ^{173}Yb (17991.9207 cm^{-1}) transitions [137] were used. The fixed lasers are locked to a stabilized HeNe laser via a scanning transfer cavity and active feedback (~ 5 MHz

resolution). The primary absorption laser is continuously scanned in frequency and the resulting absorption is detected with a photodiode. The absolute frequency of the primary absorption laser is monitored by a digital wavemeter, and the relative frequency is tracked in a separate transfer cavity with respect to a stabilized HeNe laser (~ 7 MHz resolution). The absolute transition frequencies are calibrated using known $^{172}\text{YbOH}$ and $^{174}\text{YbOH}$ spectral features [116]. The light of the enhancement laser is switched on and off using a mechanical shutter so that both enhanced and unenhanced spectra of the desired isotopologue can be measured in successive shots.

5.3 Novel spectroscopic technique utilizing laser-enhanced chemical reactions

The seven fairly abundant naturally occurring isotopes of Yb (see Section 2.11 for abundances) result in a very complicated and congested isotopologue spectroscopic structure in YbOH. The small isotopic spectral shifts (due to the similarity of the potential energy surfaces of $\tilde{X}^2\Sigma^+(0,0,0)$ and $\tilde{A}^2\Pi_{1/2}(0,0,0)$ states) result in an especially congested spectrum in the bandhead region of the $\tilde{A}^2\Pi_{1/2}(0,0,0) - \tilde{X}^2\Sigma^+(0,0,0)$ band, from 17323.50 cm^{-1} to 17323.85 cm^{-1} . Though this region of the spectrum contains many overlapped lines from all seven isotopologues, it is dominated by the two most abundant $^{172}\text{YbOH}$ and $^{174}\text{YbOH}$ isotopologues. The absorption spectrum of this bandhead region is shown in Fig. 5.3 with some of the dominate $^{172,174}\text{YbOH}$ spectral features indicated. Several "strong" isolated $^{173}\text{YbOH}$ features are also indicated in in Fig.5.3. As can be seen, the $^{173}\text{YbOH}$ lines are several factors smaller than those of the more dominant even $^{172,174}\text{YbOH}$ isotopologues. Therefore, observation and assignment of the $^{173}\text{YbOH}$ spectral features in this region using traditional methods is extremely challenging due to their overlap with the much stronger even $^{172,174}\text{YbOH}$ features. The same situation occurs with $^{171}\text{YbOH}$ isotopologue as well, though in contrast to $^{173}\text{YbOH}$, not even a single line is isolated enough to be observed.

In order to observe the spectrum of the odd isotopologues in the bandhead and other regions, we developed a novel spectroscopic technique which utilizes the laser-enhanced chemical reactions (chemical enhancement). This technique is illustrated for $^{171}\text{YbOH}$ in Fig. 5.4 and described below. Both the enhanced and non-enhanced spectra are recorded using in cell absorption spectroscopy. The OD is integrated over the duration of the molecular pulse and normalized by the integrated OD of the normalization probe. The normalization accounts for shot to shot fluctuations in molecule production so that the intensities of different lines can be reliably compared.

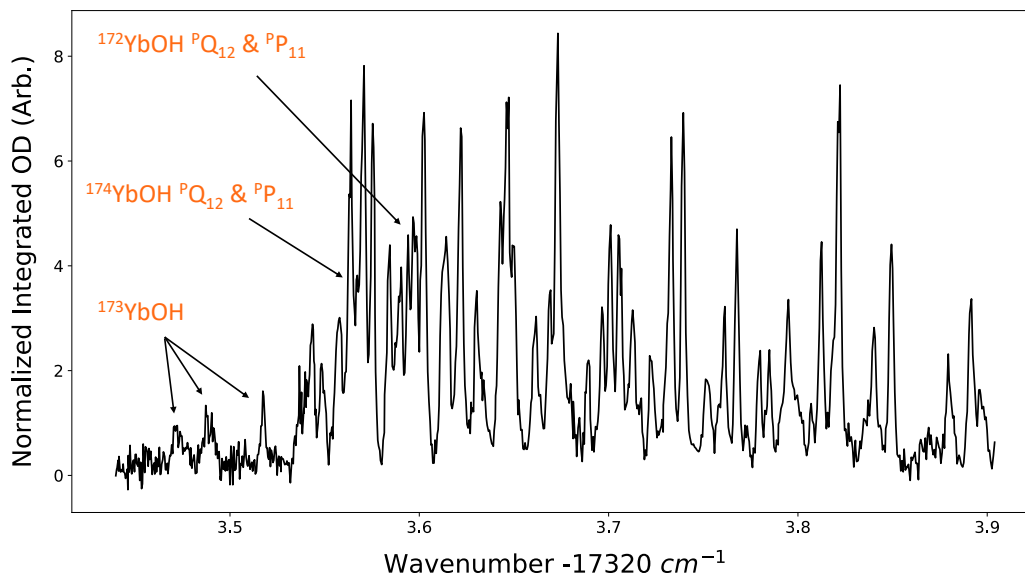


Figure 5.3: Absorption spectrum of the bandhead region of the $\tilde{A}^2\Pi_{1/2}(0,0,0) - \tilde{X}^2\Sigma^+(0,0,0)$ band of YbOH. Several $^PQ_{12}$ and $^PP_{11}$ branch features of the $^{172,174}\text{YbOH}$ isotopologues are indicated as well as several isolated $^{173}\text{YbOH}$ features.

The normalized signal at a single laser frequency without the enhancement light (Fig. 5.4a) is $S_{UE} = S_{171} + S_B$, where S_{171} is the measured integrated OD for $^{171}\text{YbOH}$, and S_B is the background integrated OD from all other overlapping YbOH isotopologues or other molecules. The measured normalized integrated OD with the enhancement light on and on resonance with the atomic ^{171}Yb transition (Fig. 5.4b) is $S_E = ES_{171} + S_B$. Here, $E = N_E/N_0$ is the enhancement factor (defined in Section 5.1) or the ratio of the number of molecules ($^{171}\text{YbOH}$ molecules in this case) produced with the enhancement laser on, N_E , to the number produced with the enhancement laser off, N_0 . Taking the difference between the enhanced and non-enhanced signals $S_E - S_{UE} = (E - 1)S_{171}$ (Fig. 5.4c) results in the spectrum from only the $^{171}\text{YbOH}$ isotopologue. For the odd isotopologues it is observed that the in-cell enhancement factor, E , is typically ~ 4 to 8 . As shown in Fig. 5.4, this novel technique utilizing the chemical enhancement both isolates the spectrum of the desired isotopologue and increases the signal to noise ratio by a factor of $(E - 1) \sim 3 - 5$. Finally, this technique generalizes to all other isotopologues of YbOH and other molecules that can be produced via laser-enhanced chemical reactions.

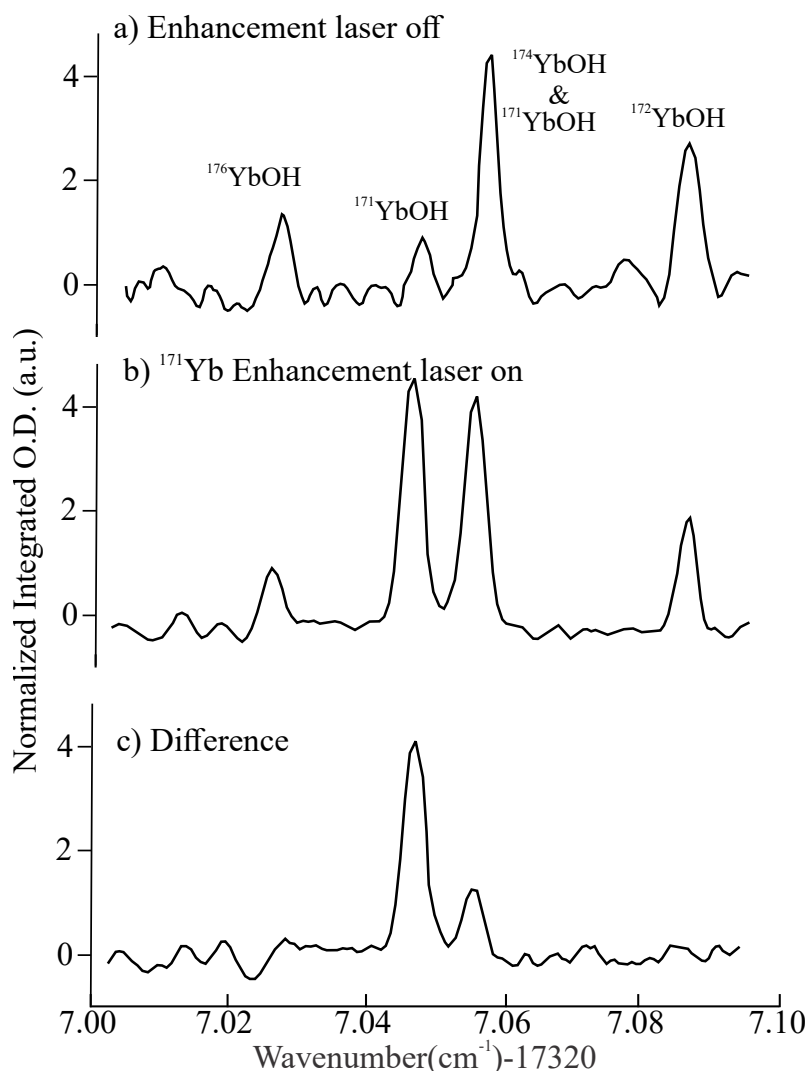


Figure 5.4: Extraction of the $^{171}\text{YbOH}$ spectral features in the region of the even isotopologue $^R R_{11}(2)$ lines using chemical enhancement. The data was collected via absorption spectroscopy in the buffer gas cell. **a.)** The spectrum with no chemical enhancement (with the chemical enhancement laser blocked). The lines of each isotopologue are indicated. The $^{174}\text{YbOH}$ $^R R_{11}(2)$ line is overlapped with a much weaker $^{171}\text{YbOH}$ line. **b.)** The spectrum with $^{171}\text{YbOH}$ chemical enhancement (with the chemical enhancement laser unblocked and on resonance with the ^{171}Yb transition). **c.)** Difference of the enhanced and non-enhanced spectrum (**a-b**), this spectrum is purely from the $^{171}\text{YbOH}$ isotopologue. This figure was reproduced from Ref. [129] with permission from AIP.

5.4 Observation of the $^{171,173}\text{YbOH}$ spectra

The analysis here focuses on the $\tilde{A}^2\Pi_{1/2}(0, 0, 0) - \tilde{X}^2\Sigma^+(0, 0, 0)$ band of the odd isotopologues, $^{171,173}\text{YbOH}$. A description of the $\tilde{A}^2\Pi_{1/2}(0, 0, 0) - \tilde{X}^2\Sigma^+(0, 0, 0)$ band for the even isotopologues, $^{172,174}\text{YbOH}$, can be found in Ref. [116]. The spectrum of the odd isotopologues is much more complex than that of the even isotopologues due to the strong ^{171}Yb ($I = 1/2$, $\mu = +0.49367\mu_N$) and ^{173}Yb ($I = 5/2$, $\mu = -0.67989\mu_N$) magnetic hyperfine interactions as well as the large nuclear electric quadrupole hyperfine interaction ($Q = 280.0 \pm 4.0 \text{ fm}^2$) in $^{173}\text{YbOH}$ [138]. This strong magnetic hyperfine interaction in the odd isotopologues results in coupling of the electron spin, S , to the nuclear spin of the Yb, I_{Yb} to give the intermediate approximately good quantum number $G = S + I_{Yb}$. G then couples to the rotation to give the intermediate quantum number $F_1 = G + N$ which in then couples to the proton nuclear spin, I_H , to give the total angular momentum F . Therefore, the low rotational energy levels of the $\tilde{X}^2\Sigma^+(0, 0, 0)$ state of the odd isotopologues are best described by a Hund's case ($b_{\beta S}$) coupling scheme and the corresponding coupling limit wavefunction, $|(SI_{Yb})G, (GN)F_1, (F_1I_H)F\rangle$. On the other hand, both the Yb and H hyperfine interactions in the excited $\tilde{A}^2\Pi_{1/2}(0, 0, 0)$ state are small compared to the rotation and Λ -doubling such that the energy levels of the $\tilde{A}^2\Pi_{1/2}(0, 0, 0)$ state of the odd isotopologues are best described by a near sequentially coupled Hund's case ($a_{\beta J}$) coupling scheme and the corresponding coupling limit wavefunction, $|\eta, \Lambda\rangle|S, \Sigma\rangle|J, \Omega, (JI_{Yb})F_1, (F_1I_H)F\rangle$. Besides small broadening of the low rotational branch features of the molecular beam LIF spectra, no evidence of the proton hyperfine splitting was observed.

Here we used the same branch designations previously utilized for the description of the $A^2\Pi_{1/2}(v = 0) - X^2\Sigma^+(v = 0)$ band of the even and odd isotopologues of YbF [139]. The even isotopologues of YbOH exhibit 6 bands, $^P P_{11}$, $^Q Q_{11}$, $^R R_{11}$, $^P Q_{12}$, $^O P_{12}$, and $^Q R_{12}$, which are labeled according to the $^{\Delta N} \Delta J_{F'_i, F''_i}(N'')$ convention appropriate for a $^2\Pi_{1/2}$ (Hund's case (a)) - $^2\Sigma$ (Hund's case (b)) band. For the odd isotopologues of YbOH, these six branches split and regroup into eight branches labeled $^O P_{1G}$, $^P P_{1G} + ^P Q_{1G}$, $^Q Q_{1G} + ^Q R_{1G}$, and $^R R_{1G}$, appropriate for a $^2\Pi_{1/2}$ (Hund's case ($a_{\beta J}$)) - $^2\Sigma$ (Hund's case ($b_{\beta S}$)) band. For $^{171}\text{YbOH}$ $G = 0$ and 1 and for $^{173}\text{YbOH}$ $G = 2$ and 3. The $\tilde{A}^2\Pi_{1/2}(0, 0, 0) - \tilde{X}^2\Sigma^+(0, 0, 0)$ band of YbOH exhibits a blue degraded bandhead formed by the low rotational lines of the $^P Q_{12}$ and $^P P_{11}$ even isotopologue and $^P P_{1G} + ^P Q_{1G}$ odd isotopologue branches. The $^O P_{12}$ and $^R R_{11}$ even isotopologue and $^O P_{1G}$ and $^R R_{1G}$ odd isotopologue branches form relatively unblended progressions in N'' , with adjacent separations of $\sim 4B''$, to the

red (${}^O P_{12}$ and ${}^O P_{1G}$) and blue (${}^R R_{11}$ and ${}^R R_{1G}$) of the band head. As discussed in the previous section, the small isotope shifts result in the even isotopologue ${}^P P_{11}$, ${}^P Q_{12}$, ${}^Q Q_{11}$, and ${}^Q R_{12}$, and odd isotopologue ${}^P P_{1G} + {}^P Q_{1G}$, and ${}^Q Q_{1G} + {}^Q R_{1G}$ branches to be severely overlapped (Fig. 5.3).

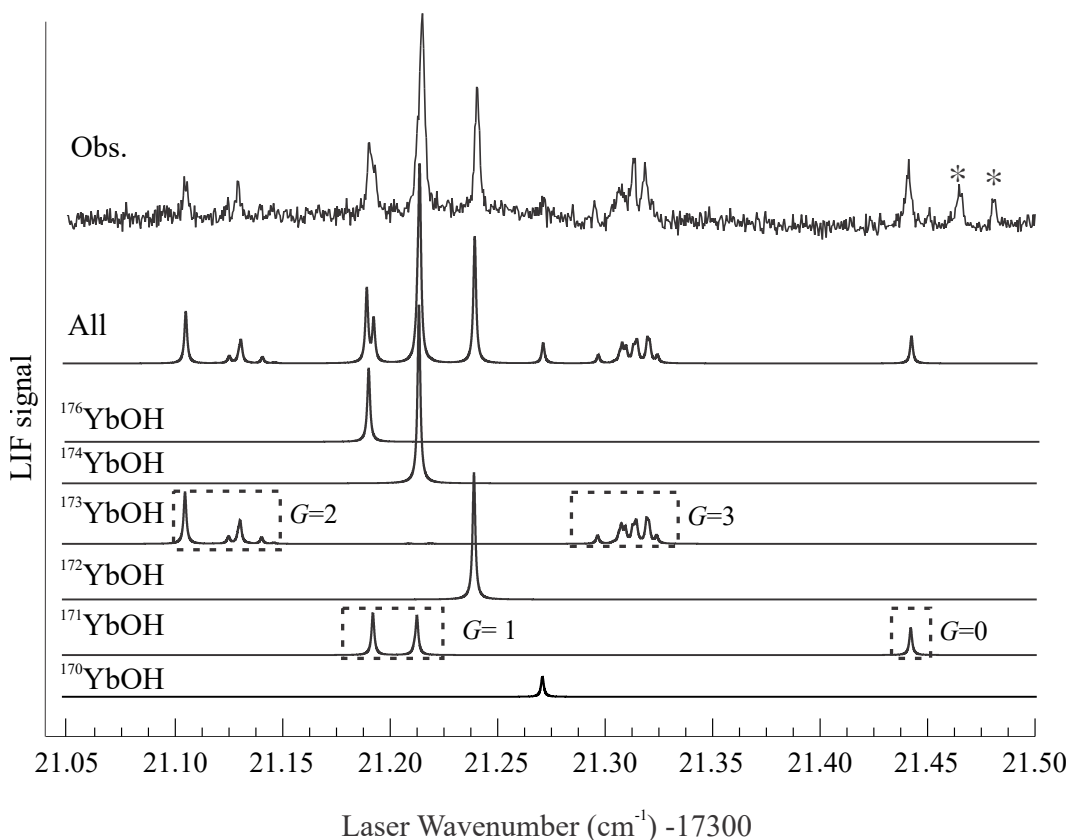


Figure 5.5: Observed molecular beam LIF spectra and calculated predictions of the ${}^O P_{12}(3)$ even isotopologue and ${}^O P_{1G}$ odd isotopologue branch features of the $\tilde{A}^2\Pi_{1/2}(0, 0, 0) - \tilde{X}^2\Sigma^+(0, 0, 0)$ band of YbOH. The even isotopologue spectrum was predicted using the optimized parameters (or isotopically scaled values) given in Ref. [116]. The predicted ${}^{171,173}\text{YbOH}$ spectra were calculated using the optimized parameters determined in this study and given in Table 5.1. A temperature of 15 K and Lorentzian full width at half maximum (FWHM) of 30 MHz was used for all predictions. The lines marked with * are unidentified. This figure was reproduced from Ref. [129] with permission from AIP.

The molecular beam LIF data and calculated spectrum in the region of the even ${}^O P_{12}(3)$ and odd ${}^O P_{1G}(3)$ lines is shown in Fig. 5.5. The calculated spectrum for the even ${}^{172,174}\text{YbOH}$ isotopologues were obtained using the optimized parameters given in Ref. [116], while for the even ${}^{170,176}\text{YbOH}$ isotopologues these parameters were scaled by their expected isotopic dependence. The calculated spectrum for the

odd isotopologues was obtained using the optimized parameters determined in this study and given in Table 5.1. For all calculated spectra, a rotational temperature of 15 K and a Lorentzian line shape with a full width at half maximum (FWHM) of 30 MHz was used.

For a Hund's case ($b_{\beta S}$) state, the Fermi contact hyperfine interaction has only diagonal matrix elements which are given by [140]

$$\begin{aligned} & \langle (SI_{Yb})G, (GN)F | b_F \mathbf{I} \cdot \mathbf{S} | (SI_{Yb})G, (GN)F \rangle \\ & = \frac{b_F}{2} [G(G+1) - I(I+1) - S(S+1)], \end{aligned} \quad (5.1)$$

where here we have neglected the effects of the proton nuclear spin as they are unresolved in the spectrum. For a $^2\Sigma^+$ state (the ground state of the odd isotopologues of YbOH) the quantum number G takes two values, $G_1 = I + S$ and $G_2 = I - S$, and the Fermi contact interaction splits these two states by $\frac{b_F}{2} [G_1(G_1+1) - G_2(G_2+1)]$. This splitting results in the separation of the $^O P_{10}(3)$ and $^O P_{11}(3)$ lines of $^{171}\text{YbOH}$ by $\sim b_F \sim +6750$ MHz and the $^O P_{12}(3)$ and $^O P_{13}(3)$ lines of $^{173}\text{YbOH}$ by $\sim 3b_F \sim -5660$ MHz. Additionally, the ordering of the energy levels of different G values is opposite in $^{173}\text{YbOH}$ compared to $^{171}\text{YbOH}$, with the lower G states ($G = 0$) lower in energy in $^{171}\text{YbOH}$ while the higher G states ($G = 3$) lower in energy in $^{173}\text{YbOH}$. The opposite ordering is due to the opposite sign of the nuclear magnetic moments of the ^{171}Yb and ^{173}Yb nuclei. This is reflected in the opposite ordering of the $^O P_{1G}(3)$ lines in Fig. 5.5 (states lower in energy result in higher energy transitions). The splitting between the $^O P_{1G}(N'')$ (and also the $^R R_{1G}(N'')$) branches remains constant for different values of N'' since the energy splitting from the Fermi contact interaction remains constant over all rotational states.

As discussed in Section 5.3 and shown in Fig. 5.3, the bandhead region of the YbOH spectrum is dominated by the $^P P_{11}$, $^Q Q_{11}$, $^P Q_{12}$, and $^Q R_{12}$ even isotopologue branch features. The dominance of the even isotopologues makes the observation and assignment of the odd isotopologue $^P P_{1G} + ^P Q_{1G}$ and $^Q Q_{1G} + ^Q R_{1G}$ branch features nearly impossible. Therefore, utilizing the chemical enhancement technique, described in Section 5.3, proved critical in the measurement of the odd isotopologue branch features in the band head region. The observed and predicted high-resolution absorption spectrum of the cryogenic buffer gas cooled (CBGC) sample in the band-head region is presented in Fig. 5.6. Fig. 5.6a is the spectrum with no enhancement light (same as Fig. 5.3), while Fig. 5.6b is the spectrum with the enhancement light applied and on resonance with the atomic ^{173}Yb transition. The enhanced pro-

duction due to the atomic excitation provides approximately a factor of 4 increase in the $^{173}\text{YbOH}$ signals. The difference between the enhanced and non-enhanced spectra (**b-a**) is presented in Fig. 5.6c and is the spectrum of only the $^{173}\text{YbOH}$ isotopologue. The prediction of the $^{173}\text{YbOH}$ spectrum in this region is presented in Fig. 5.6d. The prediction was made using the optimized parameters determined in this study (Table 5.1), a rotational temperature of 5 K, and a 90 MHz FWHM lineshape. A comparison of Fig. 5.6a and c shows that the chemical enhancement technique developed here provides a significant simplification of the observed spectrum as well as an improvement in the signal to noise ratio. While the chemical enhancement technique allowed the isolation of the $^{173}\text{YbOH}$ spectrum, the spectral features presented in Fig. 5.6c are still a blend of many lines. The feature marked "A" in Fig. 5.6 is primarily a blend of the ${}^P P_{12} + {}^P Q_{12}(1)(F''_1 = 3 \rightarrow F'_1 = 3)$ and ${}^P P_{12} + {}^P Q_{12}(2)(F''_1 = 4 \rightarrow F'_1 = 4)$ $^{173}\text{YbOH}$ transitions. The feature marked "B" in Fig. 5.6 is primarily a blend of the ${}^P P_{12} + {}^P Q_{12}(3)(F''_1 = 5 \rightarrow F'_1 = 5)$, ${}^P P_{12} + {}^P Q_{12}(1)(F''_1 = 2 \rightarrow F'_1 = 3)$, and ${}^P P_{12} + {}^P Q_{12}(3)(F''_1 = 4 \rightarrow F'_1 = 4)$ $^{173}\text{YbOH}$ transitions.

The high-resolution absorption spectrum in the bandhead region is also presented in Fig. 5.7. Fig. 5.7a is again the spectrum without chemical enhancement but now Fig. 5.7b is the spectrum with chemical enhancement of $^{171}\text{YbOH}$ via the excitation of the $F'' = 1/2 \rightarrow F' = 1/2$ ${}^3P_1 - {}^1S_0$ ^{171}Yb transition. The difference between the enhanced $^{171}\text{YbOH}$ and unenhanced spectrum (**a-b**) is shown in Fig. 5.7c, this is the spectrum from only the $^{171}\text{YbOH}$ isotopologue. A prediction of the $^{171}\text{YbOH}$ spectrum in the bandhead region is presented in Fig. 5.7d. Here, the prediction was also made using the optimized parameters given in Table 5.1, a rotational temperature of 5 K, and a 90 MHz FWHM lineshape. The $^{171}\text{YbOH}$ bandhead at 17323.55 cm^{-1} is an unresolved blend of the ${}^P P_{11} + {}^P Q_{11}(1)$, ${}^P P_{11} + {}^P Q_{11}(2)$, and ${}^P P_{11} + {}^P Q_{11}(3)$ features. In contrast to the $^{173}\text{YbOH}$ spectrum (shown in Fig. 5.6c), the $^{171}\text{YbOH}$ spectrum has several unblended features in the bandhead region. For example the feature labeled "A" in Fig. 5.7 is the ${}^Q Q_{11} + {}^Q R_{11}(1)(F''_1 = 1 \rightarrow F'_1 = 1)$ transition, the feature labeled "B" is the ${}^P P_{11} + {}^P Q_{11}(5)(F''_1 = 5 \rightarrow F'_1 = 5)$ transition and the feature marked "C" is the ${}^Q Q_{11} + {}^Q R_{11}(2)(F''_1 = 2 \rightarrow F'_1 = 2)$ transition.

Though the odd isotopologue ${}^R R_{1G}$ branch features are relatively isolated (similar to the ${}^O P_{1G}$ features shown in Fig. 5.5), recording the chemically enhanced absorption spectrum proved critical for the disentanglement and assignment of the branch features in this region as well. The disentangling of the $^{171}\text{YbOH}$ ${}^R R_{11}(2)$ lines is

demonstrated in Fig. 5.8. The left side of Fig. 5.8 presents the molecular beam LIF in the region of the even isotopologue ${}^R R_{11}(2)$ and odd isotopologue ${}^R R_{1G}(2)$ lines. The right side of Fig. 5.8 presents the CBGC absorption spectrum in this same region. The predicted spectrum presented in Fig. 5.8 used the optimized YbOH parameters, rotational temperatures of 15 K and 5 K, and FWHM linewidths of 30 MHz and 90 MHz for the molecular beam LIF and CBGC absorption spectra respectively. Fig. 5.8a is the CBGC absorption spectrum with no enhancement light, while Fig. 5.8b, c, and d are the absorption spectra with ${}^{176}\text{YbOH}$, ${}^{174}\text{YbOH}$, and ${}^{171}\text{YbOH}$ enhancement respectively. Each isotopologue is enhanced by driving the ${}^3P_1 - {}^1S_0$ transition of each respective Yb isotope (${}^{176}\text{Yb}$, ${}^{174}\text{Yb}$, and ${}^{171}\text{Yb}$). The pure ${}^{171}\text{YbOH}$ spectrum is shown in Fig. 5.8e and was obtained by taking the difference of the enhanced and unenhanced spectra, **d-a**. The pure ${}^{171}\text{YbOH}$ spectrum in Fig. 5.8e reveals a small ${}^{171}\text{YbOH}$ feature that was obscured in the high-resolution LIF data by the much stronger ${}^{174}\text{YbOH}$ ${}^R R_{11}(2)$ line. This illustrates the power and ability of the novel chemical enhancement based spectroscopic technique to produce model-independent isolation of the ${}^{171}\text{YbOH}$ spectrum.

A total of 94 spectral features of the $\tilde{A}^2\Pi_{1/2}(0, 0, 0) - \tilde{X}^2\Sigma^+(0, 0, 0)$ band of ${}^{173}\text{YbOH}$ were measured and assigned to 128 transitions. The measured transition wavenumbers, assignments, associated quantum numbers, and the difference between the observed and calculated transition wavenumbers are given in Table A.2 in Appendix A. A total of 65 spectral features of the $\tilde{A}^2\Pi_{1/2}(0, 0, 0) - \tilde{X}^2\Sigma^+(0, 0, 0)$ band of ${}^{171}\text{YbOH}$ were measured and assigned to 70 transitions. The measured transition wavenumbers, assignments, associated quantum numbers, and the difference between the observed and calculated transition wavenumbers are given in Table A.3 in Appendix A.

5.5 Analysis and discussion

Analysis of the $\tilde{A}^2\Pi_{1/2}(0, 0, 0) - \tilde{X}^2\Sigma^+(0, 0, 0)$ bands of ${}^{171,173}\text{YbOH}$

The optimal effective Hamiltonian parameters for the $\tilde{X}^2\Sigma^+(0, 0, 0)$ and $\tilde{A}^2\Pi_{1/2}(0, 0, 0)$ states of ${}^{171,173}\text{YbOH}$ were determined via a weighted least-squares optimization routine that utilized the measured transition wavenumbers (given in Tables A.2 and A.3 in Appendix A) as inputs. The molecular beam LIF data was given twice the weight compared to the CBGB absorption data due to the higher spectral resolution and the fact that the absolute frequency was more accurately calibrated with the co-recorded I_2 spectrum. The effective Hamiltonian used to model the $\tilde{X}^2\Sigma^+(0, 0, 0)$

state is

$$\begin{aligned}
\hat{H}_{eff}(\tilde{X}^2\Sigma^+) = & B\mathbf{R}^2 - D\mathbf{R}^2\mathbf{R}^2 + \gamma\mathbf{N} \cdot \mathbf{S} \\
& + b_F(^{171,173}Yb, H)\mathbf{I} \cdot \mathbf{S} \\
& + \frac{1}{3}c(^{171,173}Yb, H)(3I_zS_z - \mathbf{I} \cdot \mathbf{S}) \\
& + e^2Qq_0(^{173}Yb)\frac{3I_z^2 - \mathbf{I}^2}{4I(2I - 1)}.
\end{aligned} \tag{5.2}$$

This effective Hamiltonian accounts for rotation (B and D), spin rotation (γ), the Fermi contact and dipole-dipole magnetic hyperfine interactions of either the ^{171}Yb or ^{173}Yb nucleus and also the H nucleus (b_F and c), and in the case of $^{173}\text{YbOH}$, the nuclear electric quadrupole interaction (e^2Qq_0). Note that this effective Hamiltonian is cast in the \mathbf{R}^2 formalism, as opposed to the \mathbf{N}^2 formalism discussed in Ch. 2. The effective Hamiltonian used to model the $\tilde{A}^2\Pi_{1/2}(0, 0, 0)$ state is

$$\begin{aligned}
\hat{H}_{eff}(\tilde{A}^2\Pi_{1/2}) = & T_{00} + AL_zS_z + B\mathbf{R}^2 - D\mathbf{R}^2\mathbf{R}^2 \\
& + \frac{1}{2}(p + 2q)(J_+S_+e^{-2i\theta} + J_-S_-e^{+2i\theta}) \\
& + a(^{171,173}Yb)I_zL_z \\
& + \frac{1}{2}d(^{171,173}Yb)(S_+I_+e^{-2i\theta} + S_-I_-e^{+2i\theta}) \\
& + e^2Qq_0(^{173}Yb)\frac{3I_z^2 - \mathbf{I}^2}{4I(2I - 1)}.
\end{aligned} \tag{5.3}$$

This effective Hamiltonian accounts for the origin (T_{00}), spin-orbit (A), rotation (B and D), Λ -doubling ($p + 2q$), magnetic hyperfine (a) and parity-dependent magnetic hyperfine (d) interactions from the ^{171}Yb or ^{173}Yb nucleus, and in the case of $^{173}\text{YbOH}$ the nuclear electric quadrupole interaction (e^2Qq_0). For the $\tilde{A}^2\Pi_{1/2}(0, 0, 0)$ state hyperfine interactions from the H nucleus are very small and were not included. The data set is not sensitive to the perpendicular nuclear electric quadrupole interaction, e^2Qq_2 , which only has matrix elements between the far separated $\tilde{A}^2\Pi_{1/2}$ and $\tilde{A}^2\Pi_{3/2}$ spin-orbit components.

The $\tilde{A}^2\Pi_{1/2}(0, 0, 0)$ state is best described by a Hund's case ($a_{\beta J}$) basis, in which the diagonal matrix elements of the magnetic hyperfine interactions are given by [141]

$$\begin{aligned}
& \langle \psi(a_{\beta J}) | aI_zS_z + b_F\mathbf{I} \cdot \mathbf{S} + \frac{1}{3}c(I_zS_z - \mathbf{I} \cdot \mathbf{S}) | \psi(a_{\beta J}) \rangle \\
& = \left(a - \frac{b_F}{2} - \frac{c}{3} \right) \frac{F(F+1) - I(I+1) - S(S+1)}{4J(J+1)}.
\end{aligned} \tag{5.4}$$

Therefore, the magnetic hyperfine interaction is only dependent on the linear combination $h_{1/2} \equiv a - \frac{b_F}{2} - \frac{c}{3}$, and the effect of the three magnetic hyperfine interactions is indistinguishable. Due to this, only the diagonal $aI_z S_Z$ term is needed to effectively model the magnetic hyperfine interaction in the $\tilde{A}^2\Pi_{1/2}(0, 0, 0)$ state.

The energy levels of the $\tilde{X}^2\Sigma^+(0, 0, 0)$ and $\tilde{A}^2\Pi_{1/2}(0, 0, 0)$ states were calculated by diagonalizing the 24×24 ($= (2S + 1)(2I_1 + 1)(2I_2 + 1)$) and 48×48 ($= 2(2S + 1)(2I_1 + 1)(2I_2 + 1)$) matrices for $^{173}\text{YbOH}$ and 8×8 and 16×16 matrices for $^{171}\text{YbOH}$. The matrices for both states were constructed in a sequentially coupled Hund's case ($a_{\beta J}$) basis. A Hund's case ($a_{\beta J}$) basis set was used for the $\tilde{X}^2\Sigma^+(0, 0, 0)$ instead of the more appropriate Hund's case ($b_{\beta S}$) basis set to simplify the intensity calculations (described below) resulting from additional change of basis operations.

In the analysis, optimizations were performed for various combinations of floated parameters. In all optimization cases, the proton magnetic hyperfine parameters of the $\tilde{X}^2\Sigma^+(0, 0, 0)$ state were fixed to the values determined in the microwave study of $^{174}\text{YbOH}$ ($b_F = 4.80$ MHz and $c = 2.46$ MHz, see Ch. 4) [93]. The spin orbit parameter was fixed to the previously determined value, $A = 1350$ cm^{-1} [105]. The results of the analysis are relatively insensitive to the value of A , other than the general offset in the value of T_{00} . The rotationally induced spin-uncoupling effect is negligible in the $\tilde{A}^2\Pi_{1/2}(0, 0, 0)$ state, e.g. $B/A \sim 10^{-4}$. It was found that floating the centrifugal distortion parameter, D , for both the $\tilde{X}^2\Sigma^+(0, 0, 0)$ and $\tilde{A}^2\Pi_{1/2}(0, 0, 0)$ states and the spin rotation parameter, γ , for the $\tilde{X}^2\Sigma^+(0, 0, 0)$ state had little to no effect on the optimization results and they were therefore fixed to the values predicted from the extrapolation of the $^{174}\text{YbOH}$ values using the expected isotopic dependence. The $^{173}\text{YbOH}$ dataset was adequately fit by optimizing 10 parameters and the $^{171}\text{YbOH}$ dataset was fit by optimizing 8 parameters. The standard deviation of the fits was 27 and 25 MHz for $^{171}\text{YbOH}$ and $^{173}\text{YbOH}$ respectively, both commensurate with the estimated weighted measurement uncertainty. The optimized parameters and associated errors for $^{171,173}\text{YbOH}$ are presented in Table 5.1. Also presented are the equivalent values for ^{171}YbF [142, 143] and ^{173}YbF [139] for comparison.

Predictions of the molecular spectra were critical for both the assignment and analysis of the $\tilde{A}^2\Pi_{1/2}(0, 0, 0) - \tilde{X}^2\Sigma^+(0, 0, 0)$ bands of $^{171,173}\text{YbOH}$. The spectral predictions were obtained in the following manner. The electric dipole transition moment matrix was calculated in a sequentially coupled Hund's case ($a_{\beta J}$) basis which was then cross multiplied by the eigenvectors to obtain the transition

moments. The relative transition intensities were determined by the product of the square of the transition moment, a Boltzmann factor, and the relative Yb isotopic abundance. The spectra was then predicted using the transitions frequencies, relative intensities, and a Lorentzian lineshape. The $^{171}\text{YbOH}$ and $^{173}\text{YbOH}$ parameters determined in this study were used in the predictions. The parameters for $^{174}\text{YbOH}[\tilde{X}^2\Sigma^+(0,0,0)]$ were taken from the microwave analysis (Ch. 4) [93], while the parameters for $^{174}\text{YbOH}[\tilde{A}^2\Pi_{1/2}(0,0,0)]$, $^{172}\text{YbOH}[\tilde{X}^2\Sigma^+(0,0,0)]$, and $^{172}\text{YbOH}[\tilde{A}^2\Pi_{1/2}(0,0,0)]$ were taken from the previous optical analysis [116]. The parameters for $^{170}\text{YbOH}$ and $^{176}\text{YbOH}$ were determined via extrapolation of the known $^{171}\text{YbOH}$, $^{172}\text{YbOH}$, $^{173}\text{YbOH}$, and $^{174}\text{YbOH}$ parameters using the expected mass dependence. For all isotopologues, the $\tilde{X}^2\Sigma^+(0,0,0)$ proton magnetic hyperfine parameters were fixed to the $^{174}\text{YbOH}$ values determined in the microwave study, while the proton hyperfine parameters in the $\tilde{A}^2\Pi_{1/2}(0,0,0)$ state were set to zero. The parameters for the $\tilde{X}^2\Sigma^+(0,0,0)$ and $\tilde{A}^2\Pi_{1/2}(0,0,0)$ states of all the YbOH isotopologues of YbOH that were used in these predictions can be found in Table S3 of the supplementary material of Ref. [129].

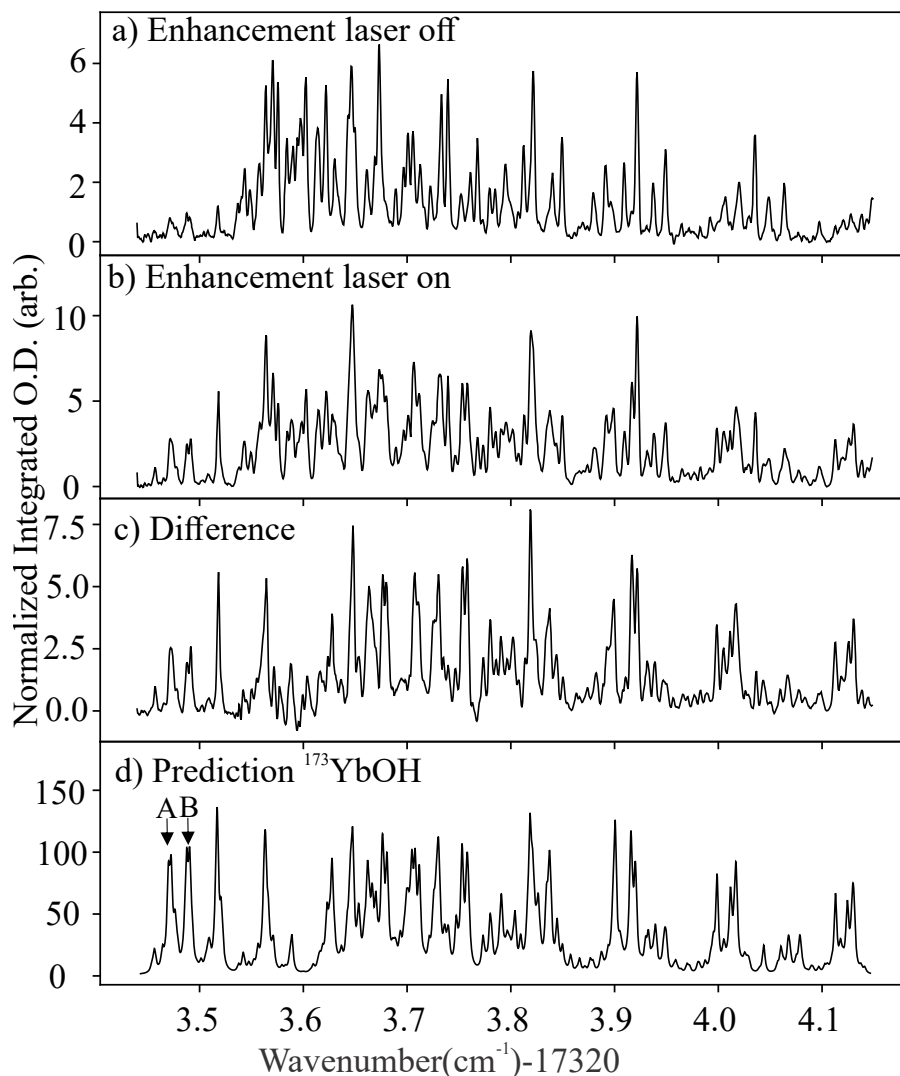


Figure 5.6: High-resolution absorption spectra in the bandhead region of the $\tilde{A}^2\Pi_{1/2}(0,0,0) - \tilde{X}^2\Sigma^+(0,0,0)$ band of YbOH. **a.)** The spectrum with no chemical enhancement. **b.)** The spectrum with chemical enhancement of the $^{173}\text{YbOH}$ isotopologue. Here the enhancement laser excited the $F'' = 5/2 \rightarrow F' = 7/2$ $^3P_1 - ^1S_0$ ^{173}Yb transition. **c.)** Difference of the enhanced and unenhanced spectra (**b-a**). This is the spectrum due to only the $^{173}\text{YbOH}$ isotopologue. **d.)** Prediction of the $^{173}\text{YbOH}$ spectrum using the optimized parameters given in Table 5.1, a rotational temperature of 5 K, and a FWHM linewidth of 90 MHz. The y-axis of **d** is arbitrary. The features marked "A" and "B" are described in the text. This figure was reproduced from Ref. [129] with permission from AIP.

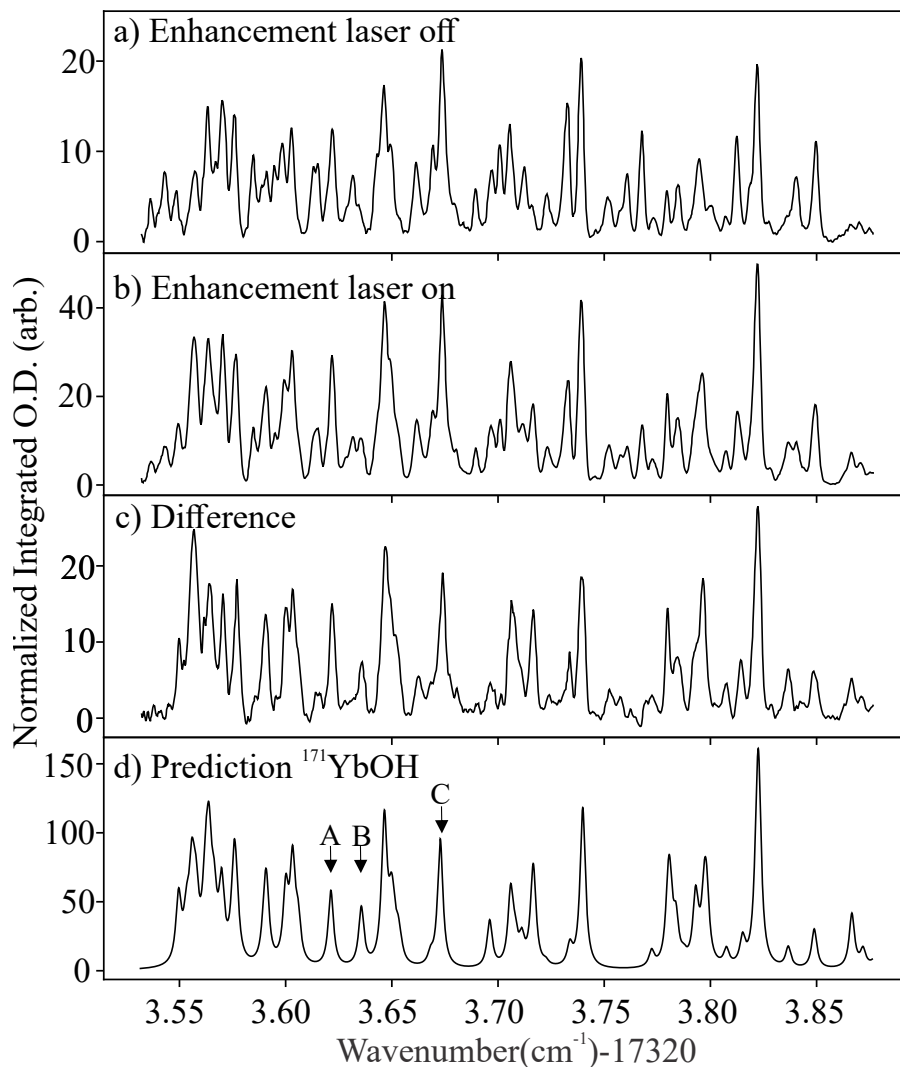


Figure 5.7: High-resolution absorption spectra in the bandhead region of the $\tilde{A}^2\Pi_{1/2}(0,0,0) - \tilde{X}^2\Sigma^+(0,0,0)$ band of YbOH. **a.)** The spectrum with no chemical enhancement. **b.)** The spectrum with chemical enhancement of the $^{171}\text{YbOH}$ isotopologue. Here the enhancement laser excited the $F'' = 1/2 \rightarrow F' = 1/2$ $^3P_1 - ^1S_0$ ^{171}Yb transition. **c.)** Difference of the enhanced and unenhanced spectra (**b-a**). This is the spectrum due to only the $^{171}\text{YbOH}$ isotopologue. **d.)** Prediction of the $^{171}\text{YbOH}$ spectrum using the optimized parameters given in Table 5.1, a rotational temperature of 5 K, and a FWHM linewidth of 90 MHz. The y-axis of **d** is arbitrary. The features marked "A", "B", and "C" are described in the text. This figure was reproduced from Ref. [129] with permission from AIP.

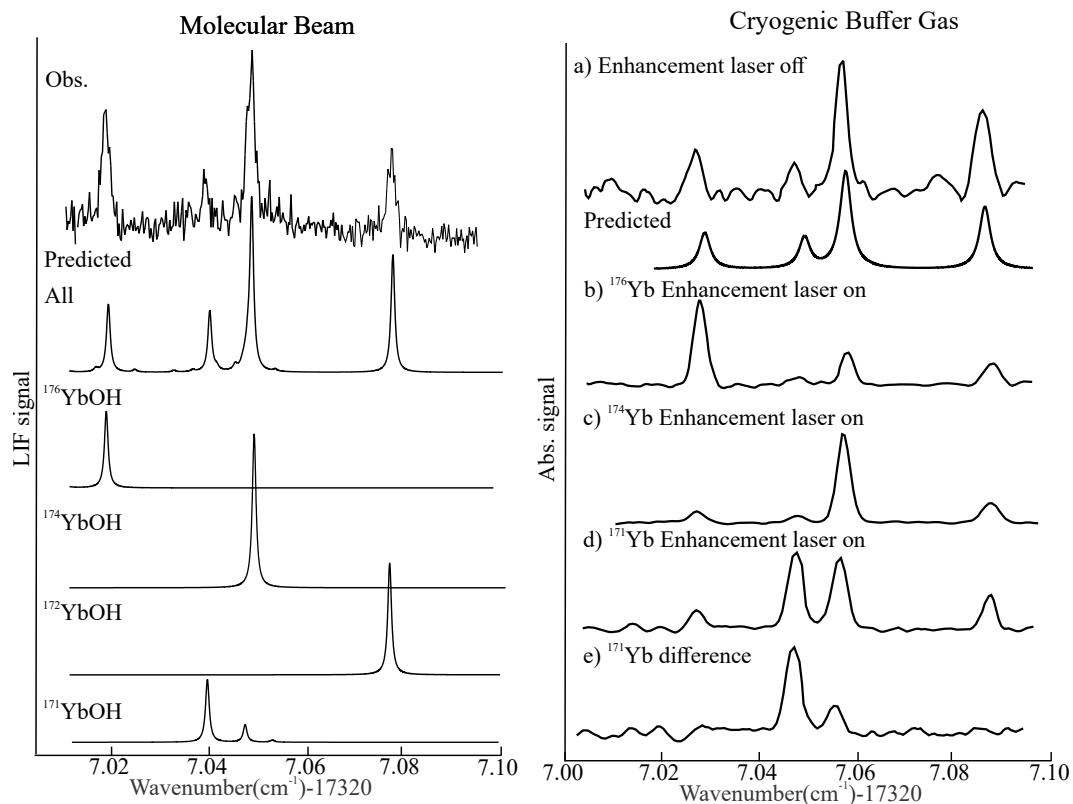


Figure 5.8: Molecular beam (MB) LIF (left side) and cryogenic buffer gas cooled (CBGC) absorption spectra (right side) in the region of the even isotopologue $^R R_{11}(2)$ and odd isotopologue $^R R_{1G}(2)$ lines of the $\tilde{A}^2\Pi_{1/2}(0,0,0) - \tilde{X}^2\Sigma^+(0,0,0)$ transition of YbOH. Predicted MB LIF spectrum was calculated with a 15 K rotational temperature and FWHM=30 MHz linewidth while the predicted CBGC absorption spectrum was calculated with a 5 K rotational temperature and a FWHM=90 MHz linewidth. Both predictions used the optimized YbOH parameters given in Table S3 of the supplemental material of Ref. [129]. **a.)** Absorption spectrum with no chemical enhancement (enhancement laser blocked). **b.)** Absorption spectrum with $^{176}\text{YbOH}$ enhancement, excitation of the $^3P_1 - ^1S_0$ ^{176}Yb transition. **c.)** Absorption spectrum with $^{174}\text{YbOH}$ enhancement, excitation of the $^3P_1 - ^1S_0$ ^{174}Yb transition. **d.)** Absorption spectrum with $^{171}\text{YbOH}$ enhancement, excitation of the $F'' = 1/2 \rightarrow F' = 1/2$ $^3P_1 - ^1S_0$ ^{171}Yb transition. **e.)** Difference of **d** and **a** (**d-a**). This is purely the spectrum from the $^{171}\text{YbOH}$ isotopologue. This provides direct, model-independent isolation of the $^{171}\text{YbOH}$ spectrum from that of the other isotopologues. This figure was reproduced from Ref. [129] with permission from AIP.

Table 5.1: Optimized parameter for the $\tilde{X}^2\Pi_{1/2}(0, 0, 0)$ and $\tilde{A}^2\Pi_{1/2}(0, 0, 0)$ states of $^{171}\text{YbOH}$ and $^{173}\text{YbOH}$ and the $X^2\Sigma^+(\nu = 0)$ and $A^2\Pi_{1/2}(\nu = 0)$ states of ^{171}YbF and ^{173}YbF . All parameters are given in cm^{-1} . Numbers in parenthesis represent the 2σ error. This table was reproduced from Ref. [129] with permission from AIP.

Par.	$^{171}\text{YbOH}$	$^{171}\text{YbF}^{a,b}$	$^{173}\text{YbOH}$	$^{173}\text{YbF}^c$
$\tilde{X}^2\Sigma^+$				
B	0.245 497(22)	0.241 710 98(6)	0.245 211(18)	0.241 434 8 (12)
$D \times 10^6$	0.252 4(fix)	0.219 8(17)	0.219 0(fix)	0.227(fix)
γ	-0.002 697 (fix)	-0.000 448(1)	-0.002 704(fix)	-0.000 446 4 (24)
$b_F(\text{Yb})$	0.227 61(33)	0.242 60(37)	-0.062 817(67)	-0.067 04 (8)
$c(\text{Yb})$	0.007 8(14)	0.009 117(12)	-0.002 73(45)	-0.002 510 (12)
e^2Qq_0	N/A	N/A	-0.110 7(16)	-0.109 96 (6)
$b_F(\text{H or F})$	0.000 160(fix)	0.005 679(fix)	0.000 160(fix)	0.005 679(fix)
$c(\text{H or F})$	0.000 082(fix)	0.002 849(fix)	0.000 082(fix)	0.002 849(fix)
$\tilde{A}^2\Pi_{1/2}$				
A	1 350 (fix)	1 365.3(fix)	1 350.0(fix)	1 365.294 (fix)
B	0.253 435(24)	0.248 056 8(35)	0.253 185(16)	0.247 79 (6)
$D \times 10^6$	0.260 8 (fix)	0.203 2 (fix)	0.240 5(fix)	0.203 2 (fix)
$p + 2q$	-0.438 667(82)	-0.397 62(fix)	-0.438 457(64)	-0.397 20 (fix)
$a(\text{Yb})$	0.014 8(15)	0.012 8(61)	-0.004 22(20)	-0.005 07(18)
$d(\text{Yb})$	0.031 99(58)	0.033 1(16)	-0.008 73(13)	-0.008 85 (18)
$e^2Qq_0(\text{Yb})$	N/A	N/A	-0.064 2(17)	-0.064 7(12)
T_{00}	17 998.636 19(24)	18 788.650 2(4)	17 998.602 68(13)	18 788.859 39

^a $X^2\Sigma^+(\nu = 0)$ values from Ref. [142].

^b $A^2\Pi_{1/2}(\nu = 0)$ values from Ref. [143].

^c From the combined fit of optical and microwave data, Ref. [139].

Discussion

The primary goal of this study was to precisely determine the parameters of the $\tilde{X}^2\Sigma^+(0, 0, 0)$ and $\tilde{A}^2\Pi_{1/2}(0, 0, 0)$ states of $^{171,173}\text{YbOH}$ and to demonstrate the chemical enhancement spectroscopic technique. The odd isotopologue parameters determined here will allow the accurate calculation of the $^{173}\text{YbOH}$ energy levels needed for the design of NMQM experiment state preparation and readout schemes. Additionally, the spectroscopic work here provides an essential starting point for the investigation of excited electronic and vibrational states of $^{173}\text{YbOH}$, such as the $\tilde{X}^2\Sigma^+(0, 1, 0)$ science state, needed for the final implementation of an NMQM measurement with $^{173}\text{YbOH}$. The chemical enhancement spectroscopic technique demonstrated in this work will be critical in the characterization of other states in the odd isotopologues of YbOH.

In addition to the design and implementation of an NMQM measurement, the characterization of the $\tilde{A}^2\Pi_{1/2}(0, 0, 0) - \tilde{X}^2\Sigma^+(0, 0, 0)$ bands of the odd isotopologues allows the identification of rotationally closed photon cycling schemes for $^{171}\text{YbOH}$ and $^{173}\text{YbOH}$. For the even isotopologues, this is accomplished by driving the ${}^P Q_{12}(1)$ and ${}^P P_{12}(1)$ transitions terminating in the $J = 1/2 +$ parity level of the $\tilde{A}^2\Pi_{1/2}(0, 0, 0)$ state. For the even isotopologues the $J = 1/2 +$ parity state can only decay back down to the $N'' = 1$ levels of the $\tilde{X}^2\Sigma^+(0, 0, 0)$ state, providing rotational closure. For the odd isotopologues, the measurements performed in this study indicate that the branching ratio for the $(J = 1/2, +)\tilde{A}^2\Pi_{1/2}(0, 0, 0) \rightarrow (N = 3, -)\tilde{X}^2\Sigma^+(0, 0, 0)$ transition is approximately 1% relative to the $(J = 1/2, +)\tilde{A}^2\Pi_{1/2}(0, 0, 0) \rightarrow (N = 1, -)\tilde{X}^2\Sigma^+(0, 0, 0)$ branching. Therefore, the equivalent ${}^P Q_{1G} + {}^P P_{1G}(1)$ transitions of $^{171}\text{YbOH}$ and $^{173}\text{YbOH}$ are not rotationally closed and leakage to the $N' = 3$ level of the $\tilde{X}^2\Sigma^+(0, 0, 0)$ state will occur after about 100 photon scatters. This branching to the $N = 3$ state is primarily due to the hyperfine interactions mixing the $J = 1/2$ and $J = 3/2, +$ parity levels of $\tilde{A}^2\Pi_{1/2}(0, 0, 0)$ state.

We can estimate the extent of this mixing with first-order perturbation theory. The free field the eigenstates are best described in the parity symmetrized Hund's case $(a_{\beta J})$ basis,

$$|J, F_1, \pm\rangle = \frac{1}{\sqrt{2}}(|\eta, \Lambda\rangle|S, \Sigma\rangle|J, \Omega, (JI_{Yb})F_1\rangle \pm (-1)^{J-S}|\eta, -\Lambda\rangle|S, -\Sigma\rangle|J, -\Omega, (JI_{Yb})F_1\rangle). \quad (5.5)$$

Here the only the total angular momentum minus the proton nuclear spin, F_1 is con-

sidered since the proton hyperfine effects in the $\tilde{A}^2\Pi_{1/2}(0, 0, 0)$ state are negligible. To see the effect of the mixing we will split the Hamiltonian into two parts so that $\hat{H} = \hat{H}_0 + \hat{H}_1$, where \hat{H}_0 is the zero-order Hamiltonian and \hat{H}_1 is the perturbing Hamiltonian causing the mixing. The zero-order Hamiltonian includes the rotation, Λ -doubling, and the diagonal components of the hyperfine interactions,

$$\hat{H}_0 = \hat{H}_R + \hat{H}_{\Lambda D} + \sum_{J, F_1} \langle J, F_1, \pm | \hat{H}_{HF} | J, F_1, \pm \rangle. \quad (5.6)$$

We have neglected the origin and spin-orbit contributions as they provide a constant offset to all states and are not relevant. Centrifugal distortions are not included since we will only be considering the lowest rotational levels and where centrifugal distortion effects are negligible. The perturbing Hamiltonian is then the off-diagonal hyperfine terms,

$$\hat{H}_1 = \sum_{J \neq J'} \langle J, F_1, \pm | \hat{H}_{HF} | J', F_1, \pm \rangle. \quad (5.7)$$

The hyperfine Hamiltonian is given by,

$$\begin{aligned} \hat{H}_{HF} = & a(^{171,173}\text{Yb}) I_z L_z + \frac{1}{2} d(^{171,173}\text{Yb}) (S_+ I_+ e^{-2i\theta} + S_- I_- e^{2i\theta}) \\ & + e^2 Q q_0 (^{173}\text{Yb}) \frac{3I_z^2 - \mathbf{I}^2}{4I(2I-1)}, \end{aligned} \quad (5.8)$$

where the electric quadrupole term is only included for $^{173}\text{YbOH}$. To first-order in perturbation theory the “true” $J = 1/2, +$ parity state is given by

$$|1/2, F_1, +\rangle' = |1/2, F_1, +\rangle + \frac{\langle 1/2, F_1, + | \hat{H}_1 | 3/2, F_1, + \rangle}{E_{J=1/2, F_1, +} - E_{J=3/2, F_1, +}} |3/2, F_1, +\rangle, \quad (5.9)$$

where the unprimed states and the energies, E , are the solutions to the zero order Hamiltonian. The diagonal and off diagonal hyperfine matrix elements can be found in [144],

$$\begin{aligned} \langle J, F_1, + | \hat{H}_{HF} | J, F_1, + \rangle = & \left(a - (-1)^{J-S} d(J+1/2) \right) \frac{R(J, I, F_1)}{4J(J+1)} \\ & + e^2 Q q_0 W(J, I, F_1) (3/4 - J(J+1)) \end{aligned} \quad (5.10)$$

and

$$\begin{aligned} \langle J-1, F_1, + | \hat{H}_{HF} | J, F_1, + \rangle = \\ - P(J, I, F_1) \left(a - (-1)^{J-S} \frac{1}{2} d + \frac{3}{2} e^2 Q q_0 T(J, I, F_1) \right) \end{aligned} \quad (5.11)$$

where

$$R(J, I, F) = F(F+1) - I(I+1) - J(J+1) \quad (5.12)$$

$$W(J, I, F) = \frac{3R(J, I, F)(R(J, I, F) + 1) - 4I(I + 1)J(J + 1)}{8I(2I - 1)J(J + 1)(2J - 1)(2J + 3)} \quad (5.13)$$

$$P(J, I, F) = \frac{1}{4J} \sqrt{(F + I + J + 1)(I + J - F)(F + J - I)(F + I - J + 1)} \quad (5.14)$$

and

$$T(J, I, F) = \frac{R(J, I, F) + J + 1}{4I(2I - 1)(J - 1)(J + 1)}. \quad (5.15)$$

Using these matrix elements an estimate of the mixing of the $J = 1/2$ and $J = 3/2$ + parity states is given by

$$|1/2, F_1, +\rangle' = |1/2, F_1, +\rangle + \epsilon(I, F_1)|3/2, F_1, +\rangle, \quad (5.16)$$

where

$$\epsilon(I, F_1) = \frac{-P(\frac{3}{2}, I, F_1) \left(a + \frac{1}{2}d + \frac{3}{2}e^2 Qq_0 T(\frac{3}{2}, I, F_1) \right)}{-3B - \frac{3}{2}(p + 2q) + \Delta E_{HF}(I, F_1)}. \quad (5.17)$$

$\Delta E_{HF}(I, F_1)$ is the energy difference between the $J = 1/2$ and $J = 3/2$ + parity states resulting from the hyperfine interaction and is given by

$$\begin{aligned} \Delta E_{HF}(I, F_1) &= \frac{1}{3}R(\frac{1}{2}, I, F_1)(a - d) - \frac{1}{15}R(\frac{3}{2}, I, F_1)(a + 2d) \\ &+ 3W(\frac{3}{2}, I, F_1)e^2 Qq_0. \end{aligned} \quad (5.18)$$

Eq. 5.17 provides an estimate of the amount of $J = 1/2$ and $J = 3/2$ + parity mixing resulting from the hyperfine interactions. For $^{171}\text{YbOH}$ $I = 1/2$, $F_1 = 1$, and there is no electric quadrupole interaction giving

$$\epsilon_{171}(\frac{1}{2}, 1) = \frac{-\frac{\sqrt{2}}{3}(a + \frac{1}{2}d)}{-3B - \frac{3}{2}(p + 2q) + \frac{1}{6}(2a + d)} = -0.010. \quad (5.19)$$

For $^{173}\text{YbOH}$ $I = 5/2$, and there are two separate hyperfine states, $F_1 = 2$ and $F_1 = 3$ with which mixing of the $J = 1/2$ and $J = 3/2$ + parity levels occurs (the hyperfine interactions preserve F_1 , $\Delta F_1 = 0$). Additionally, the electric quadrupole interaction will also add to the mixing. This gives (omitting the functional form)

$$\epsilon_{173} \left(\frac{5}{2}, 2 \right) = 0.028 \quad (5.20)$$

and

$$\epsilon_{173} \left(\frac{5}{2}, 3 \right) = 0.009. \quad (5.21)$$

In both cases, $^{171}\text{YbOH}$ and $^{173}\text{YbOH}$, these estimates indicate that the $|J = 1/2, F_1, +\rangle$ state is approximately 1-3% $|J = 3/2, F_1, +\rangle$. This accounts for the $\sim 1\%$ branching to the $N = 3$ level of the $\tilde{X}^2\Sigma^+(0, 0, 0)$ state.

Even though there are strong hyperfine interactions in $^{171,173}\text{YbOH}$, the mixing of the $J = 1/2$ and $J + 3/2$ + parity states is primarily due to the small energy spacing (~ 3 GHz) between them. This results from the combination of the relatively small rotational constant and the large, negative Λ -doubling parameter. The relatively large (in comparison to the rotational parameter) Λ -doubling parameter results in an energy level pattern with pairs of same-parity rotational levels of $J = N \pm 1/2$ lying close in energy ⁴. This small separation of adjacent same-parity rotational levels is what allows the hyperfine interactions to cause significant mixing. Eq. 5.17 provides a good estimate of the mixing of the $J = 1/2$ and $J = 3/2$ + parity levels in a $^2\Pi_{1/2}$ state and can be used to estimate if this mixing will cause significant rotational losses when photon cycling in any molecule which utilizes an excited $^2\Pi_{1/2}$ state in the cycling or repumping transitions.

The hyperfine parameters of $^{171,173}\text{YbOH}$ measured in this study are especially interesting as they are sensitive probes of the nature of the electronic wavefunctions in the vicinity of the nucleus. Additionally, accurate predictions of these hyperfine parameters provide the most direct experimental confirmation of the computational methodologies used to calculate the molecular P,T-violating coupling constants, W_s , W_d , W_Q , and W_M . These coupling constants are present in the P,T-odd effective molecular Hamiltonian [33]

$$\hat{H}_{P,T} = (k_s W_s + W_d d_e) \mathbf{S} \cdot \hat{n} + W_Q \frac{Q}{I} \mathbf{I} \cdot \hat{n} - \frac{W_M M}{2I(2I - 1)} \mathbf{S} \hat{\mathbf{T}} \hat{n}, \quad (5.22)$$

where k_s is the P,T-odd scalar-pseudoscalar nucleon-electron current interaction constant, d_e is the eEDM, Q is the nuclear Schiff moment, M is the NMQM and W_s , W_d , W_Q , and W_M are the corresponding P,T-violating coupling constants. $\hat{H}_{P,T}$ describes the P,T-violating energy shifts in a molecule resulting from any or all of the P,T-violating electromagnetic moments or interactions, such as an eEDM or NMQM. These energy shifts are what molecular eEDM or NMQM experiments aim

⁴This energy level pattern in the $\tilde{A}^2\Pi_{1/2}(0, 0, 0)$ state closely resembles that of a $^2\Sigma^-$ state. However, $^2\Sigma^+ \rightarrow ^2\Sigma^-$ transitions are electric dipole forbidden and not consistent with the observed intensities.

to measure. The P,T-violating coupling constants are critical to these experiments as they allow the magnitude and value of the P,T-violating electromagnetic moment to be determined from the measured molecular P,T-violating energy shifts. These coupling constants are a purely theoretical quantity which cannot be measured experimentally. However, the computational methodologies used to calculate them are nearly identical to those used to calculate the molecular hyperfine parameters. Therefore, comparison of the measured and calculated hyperfine parameters can provide experimental confirmation, and benchmark the accuracy, of the methodologies used to calculate W_s , W_d , W_Q , or W_M .

As part of calculation of the NMQM coupling constant, W_M , in YbOH [70], the ground state magnetic hyperfine parameter $A_{||}$ ($= b_F + \frac{2}{3}c$) and the axial electric quadrupole coupling constant e^2Qq_0 , were predicted. The calculations were performed using numerical gradients of a four-component Dirac Coulomb Hamiltonian with electronic correlation addressed using the multireference Fock-space coupled cluster method (FSCC). Similarly, a calculation of both W_d and W_s for YbOH [145] provided predictions of both ground state magnetic hyperfine parameters, $A_{||}$ and A_{\perp} ($= b_F - \frac{1}{3}c$) for $^{173}\text{YbOH}$. This calculation was carried out using quasi-relativistic two-component calculations with many-body interactions at the level of complex generalized Hartree-Fock (cGHF) and complex generalized KOHN-Sham (cGKS) density functional theory. Finally, a prediction of the ground state value of e^2Qq_0 for $^{173}\text{YbOH}$ was made using analytic gradients formulated from spin-orbit CCSD(T) theory, computed against an atomic mean-field scalar relativistic (SFX2C-AMF) Hamiltonian [146]. These predictions are compared to the measured values in Tables 5.2 and 5.3. There are no predictions for the $\tilde{A}^2\Pi_{1/2}(0, 0, 0)$ state hyperfine parameters.

The $^{171,173}\text{YbOH}$ hyperfine parameters calculated via relativistic coupled cluster methods are in excellent agreement with the measured values. The magnetic hyperfine parameters differ by only 2.5% [70] while the e^2Qq_0 parameters differ by 5.5% [70] and 5.2% [146]. The larger discrepancy in the electric quadrupole parameter may indicate that it is more difficult to calculate the core polarization than the valence electron structure. The excellent agreement between the measured and calculated hyperfine parameters suggests that the calculated value of W_M for the $\tilde{X}^2\Sigma^+(0, 0, 0)$ state of $^{173}\text{YbOH}$ in Ref. [70] and the effective electric field, E_{eff} (W_d), calculated in Ref. [69]⁵ are accurate. The values of W_M and E_{eff} will be

⁵The calculation of E_{eff} in Ref. [69] and W_M in Ref. [70] used the same methods.

relevant to the NMQM search in $^{173}\text{YbOH}$ and the eEDM search in $^{174}\text{YbOH}$ that the work of this dissertation aids in developing. The magnetic hyperfine parameters of $^{173}\text{YbOH}$ calculated via DFT methods differed from the measured values by $\sim 15\%$ and $\sim 31\%$ for the cGHF and cGKS methods respectively.

Table 5.2: Comparison of measured hyperfine parameters of the $\tilde{X}^2\Sigma^+(0, 0, 0)$ state of $^{171,173}\text{YbOH}$ to those calculated using relativistic couple cluster methods. All values are in MHz. This table was reproduced from Ref [129] with permission from AIP.

Isotopologue	Parameter	Measured	Theory Ref. [70]	Theory Ref. [146]
$^{171}\text{YbOH}$	A_{\parallel}^a	6979 (35)	7174.9	
$^{171}\text{YbOH}$	A_{\perp}^b	6745 (15)		
$^{173}\text{YbOH}$	A_{\parallel}	-1929 (11)	-1976.3	
$^{173}\text{YbOH}$	A_{\perp}^b	-1856 (5)		
$^{173}\text{YbOH}$	e^2Qq_0	-3319 (48)	-3502	-3492

^a For a σ orbital $A_{\parallel} = b_F + \frac{2}{3}c$.

^b For a σ orbital $A_{\perp} = b_F - \frac{1}{3}c$.

Table 5.3: Comparison of measured magnetic hyperfine parameters of the $\tilde{X}^2\Sigma^+(0, 0, 0)$ state of $^{173}\text{YbOH}$ to those calculated using density functional theory (DFT) methods. All values are in MHz. Calculated values from Ref. [145]. This table was reproduced from Ref. [129] with permission from AIP.

Isotopologue	Parameter	Measured	DFT method:	
			cGHF	cGKS
$^{173}\text{YbOH}$	A_{\parallel}^a	-1929 (11)	-1600	-1300
$^{173}\text{YbOH}$	A_{\perp}^b	-1856 (5)	-1600	

^a For a σ orbital $A_{\parallel} = b_F + \frac{2}{3}c$.

^b For a σ orbital $A_{\perp} = b_F - \frac{1}{3}c$.

While advanced high-level relativistic calculation provide very accurate predictions

of the hyperfine parameters, it is often useful to examine a molecular orbital based approach, which uses atomic information, as well. While less accurate than the high-level calculation, the molecular orbital based approach provides chemical insight, allows trends between similar molecules to be examined, and can provide estimates for excited state hyperfine parameters which are not provided by the high-level calculations. The dependence of the $\tilde{X}^2\Sigma^+(0, 0, 0)$ state hyperfine parameters on various averages over the electron's spatial coordinates are given in Section 2.8 (see there for more details) and are reproduced here for convenience [89, 94],

$$b_F/Hz = \frac{\mu_0}{4\pi h} \frac{8\pi}{3} g_e g_N \mu_B \mu_N \frac{1}{S} \langle \Lambda, \Sigma = S | \sum_i \mathbf{s}_i \delta(r) | \Lambda, \Sigma = S \rangle, \quad (5.23)$$

$$c/Hz = \frac{\mu_0}{4\pi h} \frac{3}{2} g_e g_N \mu_B \mu_N \frac{1}{S} \langle \Lambda, \Sigma = S | \sum_i \mathbf{s}_i \frac{(3 \cos^2 \theta_i - 1)}{r_i^3} | \Lambda, \Sigma = S \rangle, \quad (5.24)$$

and

$$e^2 Q q_0 / Hz = -Q \frac{e^2}{4\pi \epsilon_0 h} \langle \Lambda | \sum_i \frac{(3 \cos^2(\theta_i) - 1)}{r_i} | \Lambda \rangle, \quad (5.25)$$

where for b_F and c the sum is only over the valence electrons while the sum is over all electrons for $e^2 Q q_0$. The ratio of the measured $\tilde{X}^2\Sigma^+(0, 0, 0)$ state Fermi contact parameters, $b_F(^{171}\text{YbOH})/b_F(^{173}\text{YbOH}) = -3.62 \pm 0.04$ is in excellent agreement with the ratio of the nuclear g-factors, $g_N(^{171}\text{Yb})/g_N(^{173}\text{Yb}) = -3.630$. The ratio of the less well-determined dipolar parameter, $c(^{171}\text{YbOH})/c(^{173}\text{YbOH}) = -2.86 \pm 0.57$, is within two standard deviations of the g-factor ratio. The dominant electron configuration of the $\tilde{X}^2\Sigma^+(0, 0, 0)$ state can be approximated as a single valence electron in a $6s/6p/6d$ hybridized σ -type, Yb^+ -centered orbital that is polarized away from the Yb-O bond. This hybridization is the result of stabilization achieved through the polarization of the valence electron charge away from the electrophilic end of the Yb^+OH^- molecule. If we assume that b_F is primarily due to the $6s$ component of the σ -orbital than a comparison of the measured b_F values of $^{171}\text{YbOH}$ and $^{171}\text{Yb}^+(4f^{13}6s^1)$ ($b_F = 0.4217 \text{ cm}^{-1}$) [147], indicates that the σ -type orbital is $\sim 54\%$ $6s$ character. When comparing to the isoelectronic molecule YbF , the b_F values of $^{171,173}\text{YbOH}$ are $\sim 7\%$ smaller than the corresponding b_F values of $^{171,173}\text{YbF}$. This indicates that the OH^- ligand more effectively polarizes (larger $6s/6p/6d$ hybridization) the valence electron away from the bonding region than the F^- ligand. This is consistent with the point charge electrostatic model prediction which correctly predicted the ground state electric dipole moments of YbOH and YbF [116].

In contrast to b_F , the electric quadrupole parameter, e^2Qq_0 in the ground states of $^{173}\text{YbOH}$ and ^{173}YbF are almost identical. This indicates that the core polarization provides a significant contribution to e^2Qq_0 . We can recast Eq. 5.25 to separate the contributions from the valence and core electrons

$$e^2Qq_0/Hz = -Q \frac{e^2}{4\pi\epsilon_0 h} \times \left(\langle \Lambda | \sum_i \frac{(3 \cos^2(\theta_i) - 1)}{r_i} | \Lambda \rangle + \langle \Lambda | \sum_j \frac{(3 \cos^2(\theta_j) - 1)}{r_j} | \Lambda \rangle \right), \quad (5.26)$$

where now the sum over i is over only the valence electrons and the sum over j is over the core electrons. Noting that there is only a single valence electron, we can also recast Eq. 5.24 in the following way

$$\begin{aligned} c/Hz \left(\frac{2 \times 4\pi h}{3\mu_0 g_e g_N \mu_B \mu_N} \right) &= \frac{1}{S} \langle \Lambda, \Sigma = S | s_i \frac{(3 \cos^2 \theta_i - 1)}{r_i^3} | \Lambda, \Sigma = S \rangle \\ &= \frac{1}{S} S \langle \Lambda | \frac{(3 \cos^2 \theta_i - 1)}{r_i^3} | \Lambda \rangle \\ &= \langle \Lambda | \frac{(3 \cos^2 \theta_i - 1)}{r_i^3} | \Lambda \rangle. \end{aligned} \quad (5.27)$$

Therefore, we can combine Eq. 5.26 and 5.27 to get the contribution to e^2Qq_0 from only the unpaired valence electron

$$e^2Qq_0(\text{unpaired}) = -c \left(\frac{2Qe^2}{3\mu_0 g_e g_N \mu_B \mu_N \epsilon_0} \right). \quad (5.28)$$

Using a value of $Q = 280 \text{ fm}^2$ and $g_N = -0.27195$ gives $e^2Qq_0(\text{unpaired}) = -0.0461 \text{ cm}^{-1}$. This is $\sim 40\%$ of the e^2Qq_0 value determined for the ground $\tilde{X}^2\Sigma^+(0, 0, 0)$ state of $^{173}\text{YbOH}$. The remaining -0.0646 cm^{-1} is due to the core polarization.

Interpretation of the $\tilde{A}^2\Pi_{1/2}(0, 0, 0)$ state magnetic hyperfine parameters is more difficult as b_F and c were constrained to zero and the measured value of a actually corresponds to the linear combination $a - \frac{b_f}{2} - \frac{c}{3}$. However, the value of the parity-dependent hyperfine parameter, d is well determined. The dependence of d on the various averages of the electron's spatial coordinates is given in Eq. 2.71. The ratio of the measured d values, $d(^{171}\text{YbOH})/d(^{173}\text{YbOH}) = 3.66$ is in agreement with the ratio of the nuclear g-factors. Additionally, the measured values of d are identical between $^{171,173}\text{YbOH}$ and $^{171,173}\text{YbF}$. This indicates that the electron configurations for the A states of YbOH and YbF are similar and the same rational

that was applied to the observed d value of YbF can be applied to YbOH [141]. This analysis indicates that the orbital of the sole unpaired electron in the $\tilde{A}^2\Pi_{1/2}(0, 0, 0)$ state of YbOH is a mixture of Yb⁺ $6s$, Yb $6s$ and Yb $5d$ orbitals.

Upon excitation from the $\tilde{X}^2\Sigma^+(0, 0, 0)$ state to the $\tilde{A}^2\Pi_{1/2}(0, 0, 0)$ state, the electric quadrupole parameter decreases from -0.1107 cm^{-1} to -0.0642 cm^{-1} . The angular expectation value for a p orbital is given by

$$\langle p_m | 3 \cos^2 \theta - 1 | p_m \rangle = \int_0^{2\pi} d\phi \int_0^\pi \sin \theta d\theta Y_{l=1}^m(\theta, \phi)^* (3 \cos^2 \theta - 1) Y_{l=1}^m(\theta, \phi), \quad (5.29)$$

where $m = 0$ for a $p\sigma$ orbital and $m = \pm 1$ for a $p\pi$ orbital. Therefore, the angular expectation value for the $6p$ contribution to the valence σ -orbital of the $\tilde{X}^2\Sigma^+(0, 0, 0)$ state is $\langle p_0 | 3 \cos^2 \theta - 1 | p_0 \rangle = 4/5$ and for the $6p$ contribution valence π -orbital of the $\tilde{A}^2\Pi_{1/2}(0, 0, 0)$ state is $\langle p_\pm | 3 \cos^2 \theta - 1 | p_\pm \rangle = -2/5$. If we assume that the $\tilde{X}^2\Sigma^+(0, 0, 0)$ σ -orbital and the $\tilde{A}^2\Pi_{1/2}(0, 0, 0)$ π -orbital have the same $6p$ contribution, then $e^2Qq_0(\text{unpaired})$ in the $\tilde{A}^2\Pi_{1/2}(0, 0, 0)$ state would be, $\sim 0.0231 \text{ cm}^{-1}$, or -0.5 times that in the $\tilde{X}^2\Sigma^+(0, 0, 0)$ state. If we assume that the core polarization contribution to e^2Qq_0 is the same in the $\tilde{X}^2\Sigma^+(0, 0, 0)$ and $\tilde{A}^2\Pi_{1/2}(0, 0, 0)$ states, then this estimation predicts an e^2Qq_0 value of -0.0415 cm^{-1} for the $\tilde{A}^2\Pi(0, 0, 0)$ state. This value is in qualitative agreement with the measured value considering the assumptions about the orbital compositions made.

Chapter 6

Frequency Modulation Spectroscopy of YbOH

This chapter describes the implementation of frequency modulation (FM) absorption spectroscopy in the cryogenic buffer gas cell and the spectroscopy of YbOH performed using this FM technique. The final implementation provided a factor of ~ 100 improvement in the signal to noise ratio (SNR) compared to direct absorption. This allowed the spectra of weak bands in YbOH to be recorded. Specifically, the FM absorption spectrum of the $\tilde{A}^2\Pi_{1/2}(1, 0, 0) - \tilde{X}^2\Sigma^+(3, 0, 0)$, [17.68], and [17.64] bands of $^{174}\text{YbOH}$ were measured at high resolution. The FM spectrum was used to identify the $\tilde{A}^2\Pi_{1/2}(1, 0, 0) - \tilde{X}^2\Sigma^+(3, 0, 0)$ repumping transitions needed for laser cooling as well as determine the molecular parameters of the $\tilde{X}^2\Sigma^+(3, 0, 0)$ state for the first time. The [17.68] and [17.64] bands were initially assigned to originate from the $\tilde{X}^2\Sigma^+(0, 0, 0)$ state and terminate in excited vibronic states at 17680 cm^{-1} and 17640 cm^{-1} respectively [135]. Dispersed LIF measurements of the [17.68] and [17.64] bands indicated that these excited states should contain $\tilde{A}^2\Pi_{1/2}(0, 1, 0)$ character [135], which could be useful for state preparation and readout in both the eEDM and NMQM experiments. However, the measurements described here, indicate that the [17.68] and [17.64] bands do not originate from the $\tilde{X}^2\Sigma^+(0, 0, 0)$ ground state.

6.1 Frequency modulation absorption spectroscopy: Theory

Frequency modulation absorption spectroscopy (FM spectroscopy) allows the sensitive measurement of the absorption (or dispersion) signals of very weak spectral features [148–150]. This is accomplished by pushing the absorption and dispersion signals into the radio frequency (rf) regime. Dealing with rf signals reduces the $1/f$ noise in the system while additional noise rejection is provided via phase-sensitive detection of the rf signals. Working in the rf regime is especially beneficial in our CBGB source as many of the noise sources are in the Hz-kHz range (the pulse tube operates at 4 Hz and the laser locks at kHz frequencies) and FM spectroscopy enables significant suppression of these noise sources.

A brief description of the theory behind FM spectroscopy is given below; more thorough descriptions can be found in Ref. [148, 151, 152]. The electric field of a

single-frequency laser is given by [148, 151]

$$E_0(t) = E_0 \exp i\omega_0 t + c.c., \quad (6.1)$$

where ω_0 is the carrier frequency of the unmodulated laser light. The laser beam is then passed through a phase modulator that is driven by a sinusoidal rf field of frequency ω_m , the modulation frequency. Following the phase modulator, the electric field of the laser is given by

$$\begin{aligned} E_{PM} &= E_0 \exp [i(\omega_0 t + M \sin \omega_m t)] + c.c. \\ &= E_0 \exp(i\omega_0 t) \sum_{n=-\infty}^{\infty} J_n(M) \exp(i(\omega_0 + n\omega_m)t) + c.c., \end{aligned} \quad (6.2)$$

where $J_n(M)$ is the order n Bessel function of argument M . M is the modulation depth which is dependent on the amplitude of the rf field driving the phase modulator. The frequency spectrum of the phase modulated laser will contain a component at the carrier frequency, ω_0 , and sideband components located at integer multiples of $\pm\omega_m$ from the carrier.

Now consider a sample with a frequency-dependent absorption coefficient, $\alpha(\omega)$, and frequency-dependent index of refraction, $\eta(\omega)$. The amplitude attenuation (absorption¹) is given by $\delta(\omega) = \alpha(\omega)l/2$ and the phase shift is given by $\phi(\omega) = \eta(\omega)l\omega/c$ (dispersion)². The frequency dependence of $\delta(\omega)$ and $\phi(\omega)$ are the absorption and dispersion lineshapes, respectively. Then the transmission function of the sample is [151]

$$T(\omega) = \exp [-\delta(\omega) - i\phi(\omega)]. \quad (6.3)$$

If the frequency modulated laser is passed through the sample the electric field of the resulting, transmitted laser beam is

$$E_T = E_0 \exp(i\omega_0 t) \sum_{n=-\infty}^{\infty} T(\omega_0 + n\omega_m) J_n(M) \exp(i(\omega_0 + n\omega_m)t) + c.c. \quad (6.4)$$

If the transmitted laser is detected with a fast photodiode, the signal will be proportional to the intensity of the laser, $I_T(\omega) = |\bar{E}_T|^2$. The signal will then contain frequency components at dc and at integer multiples of ω_m , due to the beating of any pair of the laser frequency components separated by integer multiples of ω_m .

¹If this expression is compared to Eq. 3.8 in Ch. 3, we can see that $2\delta(\omega) = \sigma(\omega)n(t)l$ and therefore, $\alpha(\omega) = \sigma(\omega)n(t)$.

² c is the speed of light and l is path length.

If phase sensitive detection is used, the terms oscillating at a frequency of ω_m can be isolated. Expanding Eq. 6.4 in the limit of weak absorption and dispersion and only keeping the terms with a frequency of ω_m gives

$$\begin{aligned}
|\bar{E}_T|_{\omega_m} &= E_0^2 \exp[-2\delta(\omega_0)] \\
&\times \left[2 \cos \omega_m t \sum_{n=0}^{\infty} J_n(M) J_{n+1}(M) [\delta(\omega_0 - (n+1)\omega_m) - \delta(\omega_0 + (n+1)\omega_m) \right. \\
&\quad \left. + \delta(\omega_0 - n\omega_m) - \delta(\omega_0 + n\omega_m)] \right. \\
&\quad \left. + 2 \sin \omega_m t \sum_{n=0}^{\infty} J_n(M) J_{n+1}(M) [\phi(\omega_0 - (n+1)\omega_m) - \phi(\omega_0 - n\omega_m) \right. \\
&\quad \left. + \phi(\omega_0 + (n+1)\omega_m) - \phi(\omega_0 + n\omega_m)] \right].
\end{aligned} \tag{6.5}$$

Phase sensitive detection is accomplished by mixing the photodiode signal with a pickoff of the original rf drive via an rf mixer. The resulting dc signal will depend on the phase angle, θ , the phase difference between the two paths from the rf oscillator to the rf mixer. At an arbitrary value of θ , the mixer output will be a sine and cosine weighted mixture of the absorption and dispersion signals [151]

$$I_{FM}(\omega) = \cos \theta A_{FM}(\omega) + \sin \theta D_{FM}(\omega), \tag{6.6}$$

where

$$\begin{aligned}
A_{FM}(\omega) &= E_0^2 \exp[-2\delta(\omega)] \sum_{n=0}^{\infty} J_n(M) J_{n+1}(M) \\
&\quad \times [\delta(\omega - (n+1)\omega_m) - \delta(\omega + (n+1)\omega_m) \\
&\quad \quad + \delta(\omega - n\omega_m) - \delta(\omega + n\omega_m)]
\end{aligned} \tag{6.7}$$

is the FM absorption signal and

$$\begin{aligned}
D_{FM}(\omega) &= E_0^2 \exp[-2\delta(\omega)] \sum_{n=0}^{\infty} J_n(M) J_{n+1}(M) \\
&\quad \times [\phi(\omega - (n+1)\omega_m) - \phi(\omega - n\omega_m) \\
&\quad \quad + \phi(\omega + (n+1)\omega_m) - \phi(\omega + n\omega_m)]
\end{aligned} \tag{6.8}$$

is the FM dispersion signal.

FM spectroscopy is often conducted in the low modulation depth limit, $M \lesssim 1$, where the frequency spectrum of the laser consists of the carrier and only the two first order

sidebands. In this limit $J_0(M) \approx 1$, $J_{\pm 1}(M) \approx M/2$, and $J_{|n| \geq 2}(M) \sim \mathcal{O}(M^2) \approx 0$ and Eq. 6.7 and 6.8 reduce to [151]

$$A_{FM}(\omega)[M \leq 1] = \frac{E_0^2}{2} \exp[-2\delta(\omega)] M [\delta(\omega - \omega_m) - \delta(\omega + \omega_m)] \quad (6.9)$$

and

$$D_{FM}(\omega)[M \leq 1] = \frac{E_0^2}{2} \exp[-2\delta(\omega)] M [\phi(\omega - \omega_m) + \phi(\omega + \omega_m) - 2\phi(\omega)]. \quad (6.10)$$

Note that in the above equations the amplitude of both A_{FM} and D_{FM} are proportional to M , the modulation depth. Therefore, operating at higher modulation depths will increase the FM signal size. However, at high enough modulation depths, higher-order sidebands will no longer be negligible and will need to be accounted for. Eq. 6.9 and 6.10 provide a good intuitive understanding of how FM absorption works. The FM absorption signal is the result of the differential absorption between the two sidebands, while the FM dispersion signal is the difference between the average phase shift of the sidebands and twice the phase shift of the carrier.

The enhanced sensitivity provided by FM absorption is often used to measure weak absorption features. In the case of weak absorption, the amplitude attenuation of the carrier due to absorption of the sample will be negligible. In this limit (absorption of $\lesssim 1\%$), the factor of $\exp[-2\delta(\omega)] \approx 1$ in Eq. 6.7, 6.8, 6.9, and 6.10. If the absorption is $\gtrsim 1\%$, then the carrier will be attenuated and this effect will need to be accounted for in the lineshape.

I_{FM} given in Eq. 6.6 is referred to as the in phase signal, the demodulated signal that is in phase with the rf reference at the mixer. Experimentally, the phase angle θ describing the mixing of the absorption and dispersion components in I_{FM} is not easily determined. Therefore, it is also convenient to measure the in-quadrature signal as well. This is accomplished with an I and Q demodulator, which is a dual output mixer, mixing the input signal with the rf reference (I channel) and the input signal with the rf reference after a 90° phase shift is applied (Q channel). The quadrature FM signal is given by [151]

$$Q_{FM}(\omega) = \sin \theta A_{FM}(\omega) - \cos \theta D_{FM}(\omega). \quad (6.11)$$

With a simultaneous measurement of both I_{FM} and Q_{FM} the phase angle, θ can be determined. Examples of absorption, dispersion, in-phase and in-quadrature FM signals are shown in Section 6.2 and 6.3 below. A discussion of the lineshapes themselves is also given.

6.2 FM lineshapes and determining optimal modulation frequency

Both the $A_{FM}(\omega)$ and $D_{FM}(\omega)$ lineshapes have a critical dependence on the fractional modulation frequency, the ratio of the modulation frequency (ω_m) to the linewidth (the FWHM, Γ) of the absorption lineshape ($\delta(\omega)$). $A_{FM}(\omega)$ lineshapes at various values of ω_m/Γ resulting from a Gaussian absorption lineshape are shown in Fig. 6.1. The Gaussian absorption lineshape is also presented in Fig. 6.1. $D_{FM}(\omega)$ lineshapes at various values of ω_m/Γ resulting from a Gaussian dispersion lineshape, as well as the Gaussian dispersion lineshape itself, are shown in Fig. 6.2. The model used to generate these lineshapes is discussed in Section 6.3 below. For the lineshapes presented here, and for all other lineshapes presented in this chapter, the weak absorption limit was applied, e.g., $\exp(-2\delta(\omega)) \approx 1$, and the lineshapes were modeled to second order, e.g., the effects of both the first- and second-order sidebands were included.

The $A_{FM}(\omega)$ lineshapes take an intuitive form due to their origin from the differential absorption between the sidebands. The FM absorption lineshapes are always comprised of a negative and positive peak separated by twice the modulation frequency. The amplitude of these peaks grows with increasing ω_m/Γ until around $\omega_m/\Gamma \sim 0.5$ where the peak to peak amplitude saturates. For a single isolated line, as shown in Fig. 6.1, $A_{FM}(\omega) = 0$ at the resonance frequency of the transition, ω_{res} . Therefore, the accuracy a measurement of the transition frequency is determined by the accuracy at which the zero-crossing between the negative and positive peaks of the $A_{FM}(\omega)$ signal can be measured. With increasing values of ω_m/Γ , the separation between the negative and positive peaks of $A_{FM}(\omega)$ grows, resulting in a reduction in the slope of $A_{FM}(\omega)$ at ω_{res} and ultimately a reduction in the accuracy with which the zero crossing can be measured.

The form of the $D_{FM}(\omega)$ lineshapes is somewhat less intuitive, but their dependence on ω_m/Γ is clear. For low values of ω_m/Γ the FM dispersion line shape, $D_{FM}(\omega)$, resembles a smaller version of the absorption line shape. As was the case with the $A_{FM}(\omega)$, the amplitude of $D_{FM}(\omega)$ increases with increasing ω_m/Γ and saturates at $\omega_m/\Gamma \sim 1$. As with $A_{FM}(\omega)$, $D_{FM}(\omega) = 0$ at ω_{res} . However, in contrast to $A_{FM}(\omega)$, the slope of the $D_{FM}(\omega)$ lineshape at ω_{res} increases with increasing ω_m/Γ saturating at a value of $\omega_m/\Gamma \sim 1$.

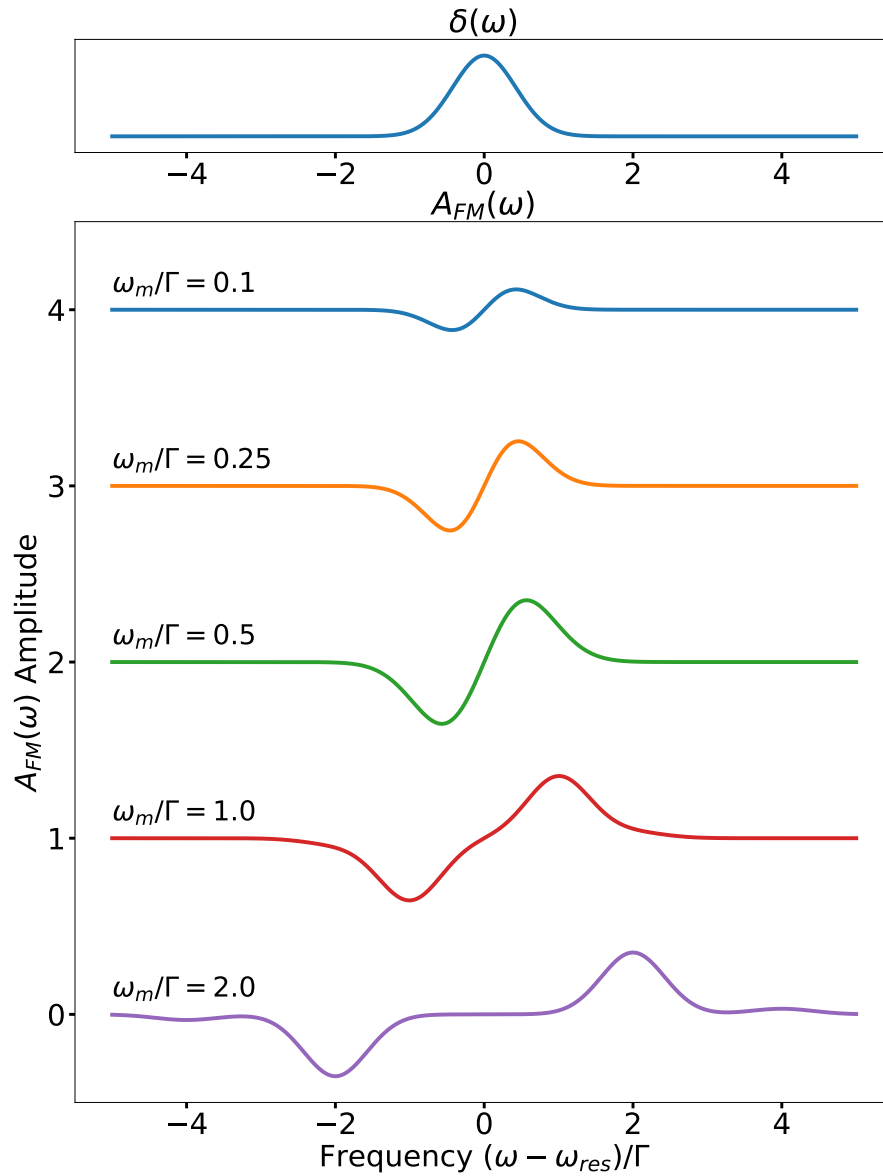


Figure 6.1: FM absorption lineshapes, $A_{FM}(\omega)$, at various values of the fractional modulation frequency, ω_m/Γ , for a Gaussian absorption lineshape, $\delta(\omega)$, with FWHM of Γ . The $A_{FM}(\omega)$ lineshapes are intentionally offset by integer values for clarity. The x-axis is the relative normalized frequency, $(\omega - \omega_{res})/\Gamma$, where ω_{res} is the linecenter of the absorption lineshape. The absolute amplitude of the the $A_{FM}(\omega)$ signals is arbitrary while the relative amplitude between different lineshapes is accurate.

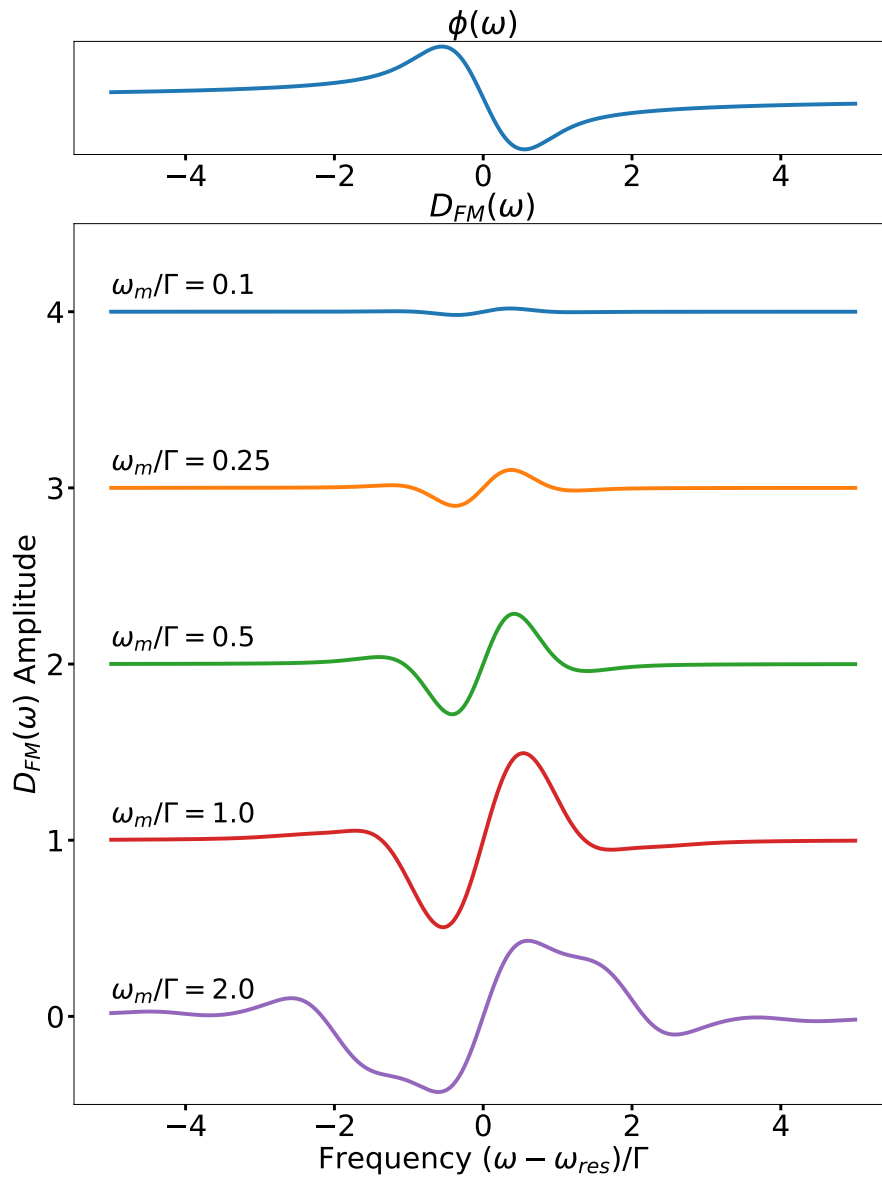


Figure 6.2: FM dispersion lineshapes, $D_{FM}(\omega)$, at various values of the fractional modulation frequency, ω_m/Γ , for a Gaussian dispersion lineshape, $\phi(\omega)$. Γ is the FWHM of the corresponding absorption lineshape, $\delta(\omega)$. The $D_{FM}(\omega)$ lineshapes are intentionally offset by integer values for clarity. The x-axis is the relative normalized frequency, $(\omega - \omega_{res})/\Gamma$, where ω_{res} is the linecenter of the absorption lineshape. The absolute amplitude of the the $D_{FM}(\omega)$ signals is arbitrary while the relative amplitude between different lineshapes is accurate.

The optimal modulation frequency at which to operate depends on the goal of the FM measurement. In our case, we are utilizing FM spectroscopy to measure the spectrum of weak bands of YbOH. In our measurements, we want to aim to optimize the signal-to-noise ratio of the FM signal while preserving the ability to accurately measure transition frequencies. Therefore, we want to maximize both the amplitude of the FM signal as well as the slope at ω_{res} . The peak to peak amplitude of both $A_{FM}(\omega)$ and $D_{FM}(\omega)$ as a function of ω_m/Γ is shown in Fig. 6.3. The amplitude of $A_{FM}(\omega)$ is maximized at $\omega_m/\Gamma = 0.67$ though it is very near maximum for $\omega_m/\Gamma \gtrsim 0.5$. $D_{FM}(\omega)$ has a maximum peak to peak amplitude at $\omega_m/\Gamma = 1.18$ and a peak to peak amplitude greater than that of $A_{FM}(\omega)$ for $\omega_m/\Gamma \gtrsim 0.6$. The maximum FM sensitivity is obtained at the total maximum peak-to-peak amplitude at $\omega_m/\Gamma = 1.18$. However, since the measured FM signals, $I_{FM}(\omega)$ and $Q_{FM}(\omega)$, are linear combinations of $A_{FM}(\omega)$ and $D_{FM}(\omega)$, operating at values of ω_m/Γ above ~ 0.5 where the amplitude of $A_{FM}(\omega)$ begins to saturate will only provide nominal improvements in sensitivity. Utilizing FM spectroscopy for improved sensitivity sets a minimum value for the modulation frequency of $\omega_m/\Gamma = 0.5$.

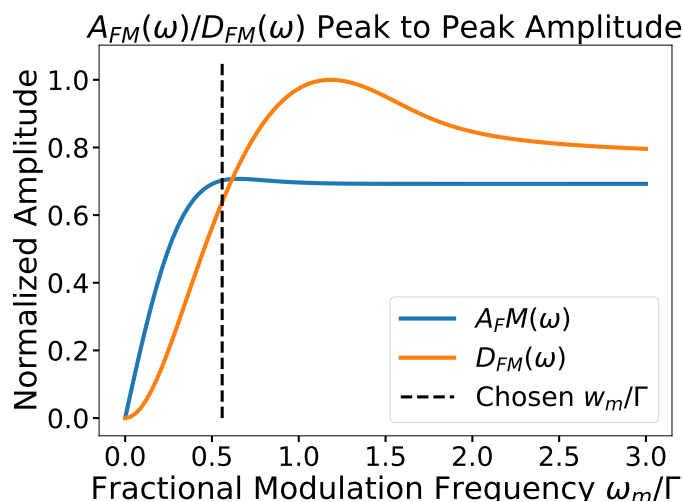


Figure 6.3: Normalized peak-to-peak amplitude of $A_{FM}(\omega)$ and $D_{FM}(\omega)$ as a function of the fractional modulation frequency, ω_m/Γ , for a Gaussian absorption lineshape, $\delta(\omega)$. Γ is the full width at half maximum (FWHM) of the absorption lineshape. The peak-to-peak amplitude of both $A_{FM}(\omega)$ and $D_{FM}(\omega)$ were normalized to the larger of the two maximum peak-to-peak amplitudes, that of $D_{FM}(\omega)$. The horizontal dashed line indicates the modulation frequency at which we operate, $\omega_m/\Gamma = 0.56$.

In addition to improving sensitivity, we also want to measure the transition frequen-

cies of YbOH lines at high resolution. Therefore, we want to operate in a regime where the FM signals have a non-zero, and preferably large, slope at the transition frequency, ω_{res} . The slope (derivative) of the $A_{FM}(\omega)$ and $D_{FM}(\omega)$ lineshapes at ω_{res} as a function of ω_m/Γ is shown in Fig. 6.4. When examining Fig. 6.4 it is important to note that the value at which the combined amplitudes are maximized, $\omega_m/\Gamma = 1.18$, the slope of $A_{FM}(\omega)$ is near zero. Additionally, the slope of $A_{FM}(\omega)$ is also very small when the slope of $D_{FM}(\omega)$ is maximized ($\omega_m/\Gamma = 0.91$). Due to the reduction of the slope of $A_{FM}(\omega)$ for $\omega_m/\Gamma > 0.39$, the combined slopes of the absorption and dispersion FM signals is optimized near the point where they cross, at $\omega_m/\Gamma \approx 0.45$. While the slope of $A_{FM}(\omega)$ decreases for $\omega_m/\Gamma \gtrsim 0.45$, the slope remains larger than half the maximum slope for ω_m/Γ up to ≈ 0.79 . Additionally, the slope of $D_{FM}(\omega)$ is continually increasing, and larger than the max slope of $A_{FM}(\omega)$, over this range. Therefore, operating at a modulation frequency in the range $0.45 \lesssim \omega_m/\Gamma \lesssim 0.79$ will allow the FM signals to have a nonzero and relatively large slope at ω_{res} .

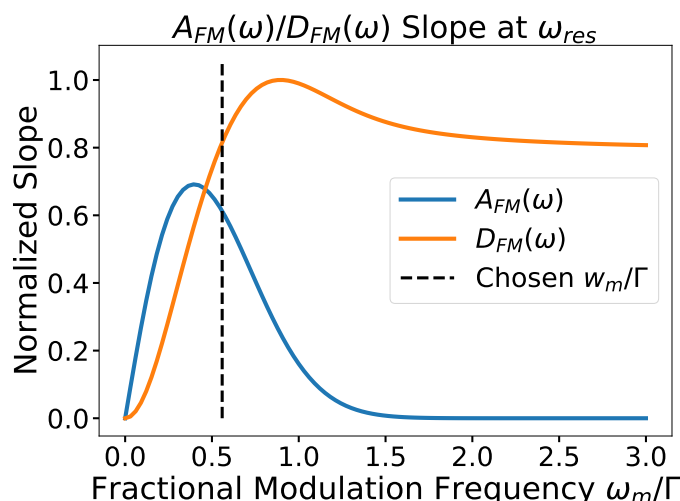


Figure 6.4: Normalized slope of $A_{FM}(\omega)$ and $D_{FM}(\omega)$ at the resonance frequency (or linecenter of $\delta(\omega)$), ω_{res} , as a function of the fractional modulation frequency, ω_m/Γ , for a Gaussian absorption lineshape, $\delta(\omega)$. Γ is the full width at half maximum (FWHM) of the absorption lineshape. The slopes at ω_{res} of both $A_{FM}(\omega)$ and $D_{FM}(\omega)$ were normalized to the larger of the two maximum slopes, that of $D_{FM}(\omega)$. The horizontal dashed line indicates the modulation frequency at which we operate, $\omega_m/\Gamma = 0.56$.

By considering the modulation frequencies which maximize signal size ($\omega_m/\Gamma > 0.5$) as well as provide nonzero and relatively large slope at ω_{res} ($0.45 \lesssim \omega_m/\Gamma \lesssim$

0.79) I determined that a modulation frequency in the range $0.5 \lesssim \omega_m/\Gamma \lesssim 0.79$ is ideal for our spectroscopic purposes. Specifically, we operate at a modulation frequency of $\omega_m/\Gamma \approx 0.56$, indicated by the vertical dashed line in Fig. 6.3 and 6.4. The specific value of ω_m/Γ was determined partially due to the fact that we already had a $2\pi \times 50.3$ MHz EOM in the laboratory. A $2\pi \times 50.3$ MHz modulation frequency falls in the optimal range for FM spectroscopy inside our buffer gas cell (the measured in cell linewidth is $\Gamma \sim 2\pi \times 90$ MHz).

6.3 Modeling FM lineshapes

For isolated spectral lines, a measurement of the zero crossing of the FM lineshape, either $I_{FM}(\omega)$, or $Q_{FM}(\omega)$, or both, provides a very accurate measurement of the transition frequency. However, for blended lines and in congested regions of the spectrum, the FM lineshapes become distorted, and zero crossing measurements may no longer provide an accurate measurement of the transition frequencies. Additionally, when there are multiple transitions within a single spectral linewidth, the FM signals will not have a zero crossing for each transition present and a simple zero crossing measurement will not account for all the transitions. Therefore, fitting the measured FM lineshapes to modeled FM lineshapes is the best method for measuring the transition frequencies of blended features and in congested regions. Here we describe our FM lineshape model and our fitting method.

Experimentally, we are measuring the FM spectrum in the buffer gas cell where Doppler broadening dominates. Therefore, our absorption lineshape is best modeled as a Gaussian

$$\delta(\omega) = A \exp\left(-\frac{(\omega - \omega_{res})^2}{2(\Gamma/2.355)^2}\right), \quad (6.12)$$

where A is the amplitude of the lineshape, ω_{res} is the linecenter, and Γ is the full width at half maximum (FWHM). The dispersion lineshape can be calculated from the absorption lineshape using the Kramers-Kronig relationship [153]

$$\phi(\omega) = \frac{1}{\pi} P \int_{-\infty}^{\infty} \frac{\delta(\omega')}{\omega' - \omega} d\omega', \quad (6.13)$$

where P is the Cauchy principal value³. It turns out that the Kramers-Kronig relation is a Hilbert transform of the absorption line shape [155]. The Hilbert transform of

³This integral, to my knowledge, does not have a closed form solution for a Gaussian lineshape. However, the Kramers-Kronig relationship does have a closed form solution for a Lorentzian lineshape [154].

a function $f(x)$ is given by

$$H(f)(y) = \frac{1}{\pi} P \int_{-\infty}^{\infty} \frac{f(x)}{y-x} dx. \quad (6.14)$$

Therefore, given the absorption lineshape, $\delta(\omega')$ the dispersion line shape is given by the negative Hilbert transform of the absorption lineshape

$$\phi(\omega) = -H(\delta)(\omega). \quad (6.15)$$

If we make the substitution $u = (\omega' - \omega_{res})/(\sqrt{2}\sigma)$ where $\sigma = \Gamma/2.355$ then $du = 1/(\sqrt{2}\sigma)d\omega'$, $\delta(\omega') = f(u) = A \exp(-u^2)$ and

$$\begin{aligned} \phi(\omega) &= \frac{1}{\pi} P \int_{-\infty}^{\infty} \frac{f(u)}{u - \frac{\omega - \omega_{res}}{\sqrt{2}\sigma}} du \\ &= \frac{1}{\pi} P \int_{-\infty}^{\infty} \frac{-A \times \exp(-u^2)}{t - u} du \\ &= -A H[\exp(-u^2)](t), \end{aligned} \quad (6.16)$$

where $t = (\omega - \omega_{res})/(\sqrt{2}\sigma)$. The Hilbert transform of $f(u) = \exp(-u^2)$ is known and is related to the Dawson function [155, 156]

$$H[\exp(-u^2)](t) = \frac{2}{\sqrt{\pi}} F(t), \quad (6.17)$$

where $F(t)$ is the Dawson function. Therefore, the dispersion lineshape is given by

$$\phi(\omega) = -A \frac{2}{\sqrt{\pi}} F\left(\frac{(\omega - \omega_{res})}{\sqrt{2}(\Gamma/2.355)}\right). \quad (6.18)$$

The dispersion lineshape given in Eq. 6.18 is convenient for numerical modeling since the Dawson function is a built in function in several programming languages⁴. Simulated Gaussian absorption and dispersion lineshapes (Eq. 6.12 and 6.18) are shown in the top left and right panels of Fig. 6.5, respectively.

Ultimately, we want to model a true absorption spectrum which will contain an arbitrary superposition of Gaussian lineshapes

$$\delta_{tot}(\omega) = \sum_i \delta_i(\omega) = \sum_i A_i \exp\left(-\frac{(\omega - \omega_i)^2}{2(\Gamma_i/2.355)}\right), \quad (6.19)$$

⁴The Dawson function is a built in special function in python, which is the language used here to model the FM lineshapes.

where i denotes the absorption lineshape due to the i th transition, and ω_i is the resonance frequency of the i th transition. Therefore, the total dispersion lineshape due to the combination of multiple transitions is given by

$$\begin{aligned}\phi_{tot}(\omega) &= \frac{1}{\pi} P \int_{-\infty}^{\infty} \frac{\delta_{tot}(\omega')}{\omega' - \omega} d\omega' \\ &= \sum_i A_i \frac{2}{\sqrt{\pi}} F \left(\frac{(\omega - \omega_i)}{\sqrt{2}(\Gamma_i/2.355)} \right).\end{aligned}\tag{6.20}$$

The simulated total Gaussian absorption and dispersion lineshapes for five closely spaced and blended transitions are shown in the top left and right panels of Fig. 6.6, respectively.

With Eq. 6.19 and 6.20, any arbitrary absorption and dispersion line shape can be modeled. Any arbitrary FM lineshape can be modeled by using Eq. 6.19 and 6.20 in Eq. 6.7, 6.8, 6.6, and 6.11. However, Eq. 6.7 and 6.8 account for the attenuation of the carrier due to strong absorption as well as the effects of the sidebands of all orders. While modeling the FM lineshapes using Eq. 6.7 and 6.8 would provide the most accurate models, including the aforementioned effects is excessive and could complicate the fitting by providing too large of an optimization space.

We are specifically utilizing FM spectroscopy to measure weak absorption lines so operating in the weak absorption limit, discussed in Section 6.1, is justified. Therefore, in our FM lineshape model we assume $\exp[-2\delta(\omega)] \approx 1$. Additionally, Eq. 6.9 and 6.10 indicate that at lower modulation depth $A_{FM}(\omega)/D_{FM}(\omega) \propto M$ and therefore, operating at higher modulation depths will result in larger FM signals. Experimentally, we observe this trend with larger signal sizes for larger modulation depths. In order to maximize our FM signal sizes we operate at a modulation depth of $M = 0.84$. The modulation depth is fixed to this value for all modeled FM lineshapes shown in this chapter. At this modulation depth we find that the amplitude of the first-order sidebands is $\approx 20\%$ of the carrier amplitude and the amplitude of second-order sidebands are $\approx 1\%$ of the carrier amplitude. In order to include the effects of the second order sidebands we model the $A_{FM}(\omega)$ and $D_{FM}(\omega)$ lineshapes to second order (the $n=0,1$ terms in Eq. 6.7 and 6.8). Therefore,

in the small absorption limit the FM absorption lineshape is given by [153]

$$\begin{aligned}
 A_{FM}^{2nd}(\omega) &= J_0(M)J_1(M) [\delta(\omega - \omega_m) - \delta(\omega + \omega_m)] \\
 &+ J_1(M)J_2(M) [\delta(\omega - 2\omega_m) - \delta(\omega + 2\omega_m) + \delta(\omega - \omega_m) - \delta(\omega + \omega_m)],
 \end{aligned} \tag{6.21}$$

and the FM dispersion lineshape is given by

$$\begin{aligned}
 D_{FM}^{2nd}(\omega) &= J_0(M)J_1(M) [\phi(\omega - \omega_m) + \phi(\omega + \omega_m) - 2\phi(\omega)] \\
 &+ J_1(M)J_2(M) [\phi(\omega - 2\omega_m) + \phi(\omega + 2\omega_m) - \phi(\omega - \omega_m) - \phi(\omega + \omega_m)].
 \end{aligned} \tag{6.22}$$

Given a set of transitions (each with transition frequency ω_i , width Γ_i , and amplitude A_i) and a phase angle, θ , the $I_{FM}(\omega)$ and $Q_{FM}(\omega)$ lineshapes are calculated using Eq. 6.6 and 6.11 respectively, where $A_{FM}(\omega)$ is given by Eq. 6.21, $D_{FM}(\omega)$ is given by Eq. 6.22, $\delta(\omega)$ is given by Eq. 6.19, and $\phi(\omega)$ is given by Eq. 6.20. The simulated I and Q FM lineshapes at various values of θ between $\theta = 0$ and $\theta = \pi$ for a single transition with a Gaussian absorption lineshape are shown in Fig. 6.5. A modulation frequency of $\omega_m/\Gamma = 0.56$, the same modulation frequency used in our FM setup, was used when modeling the lineshapes in Fig. 6.5. The simulated I and Q FM lineshapes at various values of θ between $\theta = 0$ and $\theta = \pi$ for five closely spaced transitions are shown in Fig. 6.6. Here, the FWHM of all transitions was set to 90 MHz and a modulation frequency of 50.3 MHz was used ($\omega_m/\Gamma = 0.56$). In Fig. 6.6 several of the transitions are blended to illustrate the resulting FM lineshapes when blended lines are present. In all cases, both isolated transitions in Fig. 6.5 and blended transitions in Fig. 6.6, at a phase angle of $\theta = 0$ $I_{FM}(\omega)(\theta = 0) = A_{FM}(\omega)$ and $Q_{FM}(\omega)(\theta = 0) = -D_{FM}(\omega)$. As the phase angle increases the I and Q signals become mixtures of $A_{FM}(\omega)$ and $D_{FM}(\omega)$ up to $\theta = \pi/2$ where $I_{FM}(\omega)(\theta = \pi/2) = D_{FM}(\omega)$ and $Q_{FM}(\omega)(\theta = \pi/2) = A_{FM}(\omega)$. For phase angles between $\pi/2$ and π the I and Q signals are again a mixture of $A_{FM}(\omega)$ and $D_{FM}(\omega)$. At $\theta = \pi$ $I_{FM}(\omega)(\theta = \pi) = -I_{FM}(\omega)(\theta = 0) = -A_{FM}(\omega)$ and $Q_{FM}(\omega)(\theta = \pi) = -Q_{FM}(\omega)(\theta = 0) = D_{FM}(\omega)$. For phase angles of $\pi < \theta < 2\pi$ $I_{FM}(\omega)(\theta) = -I_{FM}(\omega)(\theta' = \theta - \pi)$ and $Q_{FM}(\omega)(\theta) = -Q_{FM}(\omega)(\theta' = \theta - \pi)$. In all cases $I_{FM}(\omega)(\theta + 2\pi) = I_{FM}(\omega)(\theta)$ and $Q_{FM}(\omega)(\theta + 2\pi) = Q_{FM}(\omega)(\theta)$.

Ultimately, we want to perform a simultaneous fit of our modeled I and Q FM lineshapes to the measured I and Q FM data. This is accomplished with a non-linear

least squares optimization⁵ which takes the FM data and initial guesses for the phase angle and the parameters of each transition present (the transition frequency, width, and amplitude of each transition) as inputs. The optimization works to minimize the set of residuals provided to it. To accomplish the simultaneous fit the following residual function was used

$$R(\omega) = \sqrt{[I_{calc}(\omega) - I_{data}(\omega)]^2 + [Q_{calc}(\omega) - Q_{data}(\omega)]^2}, \quad (6.23)$$

where $I_{calc}(\omega)$ ($Q_{calc}(\omega)$) is the calculated value of I_{FM} (Q_{FM}) at the frequency ω and $I_{data}(\omega)$ ($Q_{data}(\omega)$) is the measured value of I_{FM} (Q_{FM}) at the frequency ω . The sum of the squares of the individual I and Q residuals as opposed to just the sum of the I and Q residuals was used to prevent the residual from taking on inaccurately small values due to a cancellation resulting from the I and Q residuals being opposite in sign. In the fit, the phase angle θ and the lineshape parameters ω_i , Γ_i , and A_i are floated. Any arbitrary number of transitions can be fit by the algorithm. An example of a fit of the model to FM data is shown later in this chapter in Fig. 6.11. For isolated lines, we find that the linecenters extracted from the fit exactly match our zero crossing measurements and have equivalent or smaller errors.

⁵The lmfit Python package [157] is used for the non-linear least squares fitting.

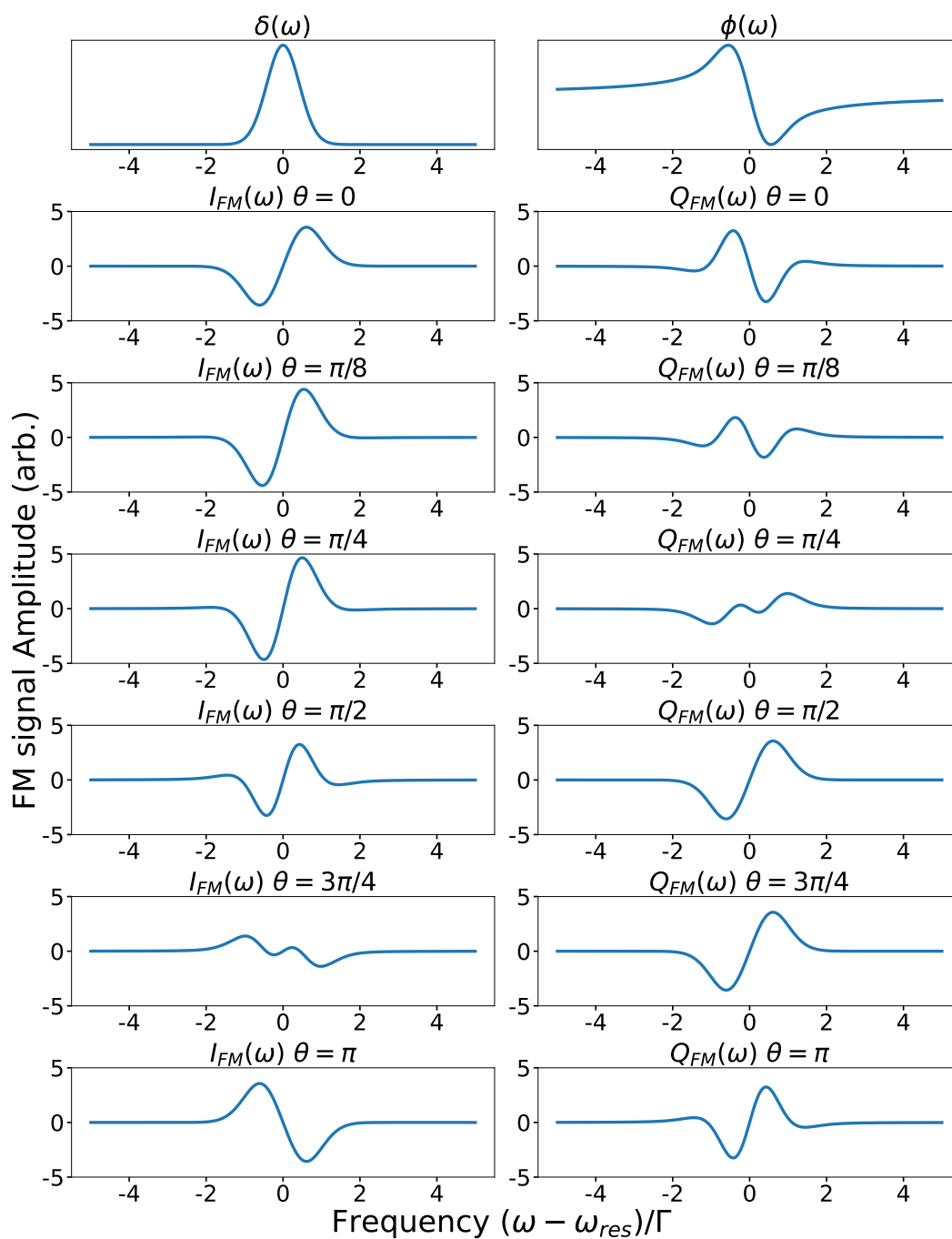


Figure 6.5: Simulated in-phase, $I_{FM}(\omega)$, and in-quadrature, $Q_{FM}(\omega)$, FM signals for an isolated spectral feature with a Gaussian absorption, $\delta(\omega)$, and dispersion, $\phi(\omega)$, lineshape. The in-phase and in-quadrature signals are shown for various phase angles, θ , ranging from $\theta = 0$ to $\theta = \pi$. For phase angles $> \pi$ $I_{FM}(\omega)(\theta = \pi + \phi) = -I_{FM}(\omega)(\theta = \phi)$ and $Q_{FM}(\omega)(\theta = \pi + \phi) = -Q_{FM}(\omega)(\theta = \phi)$ for $0 \leq \phi \leq \pi$.

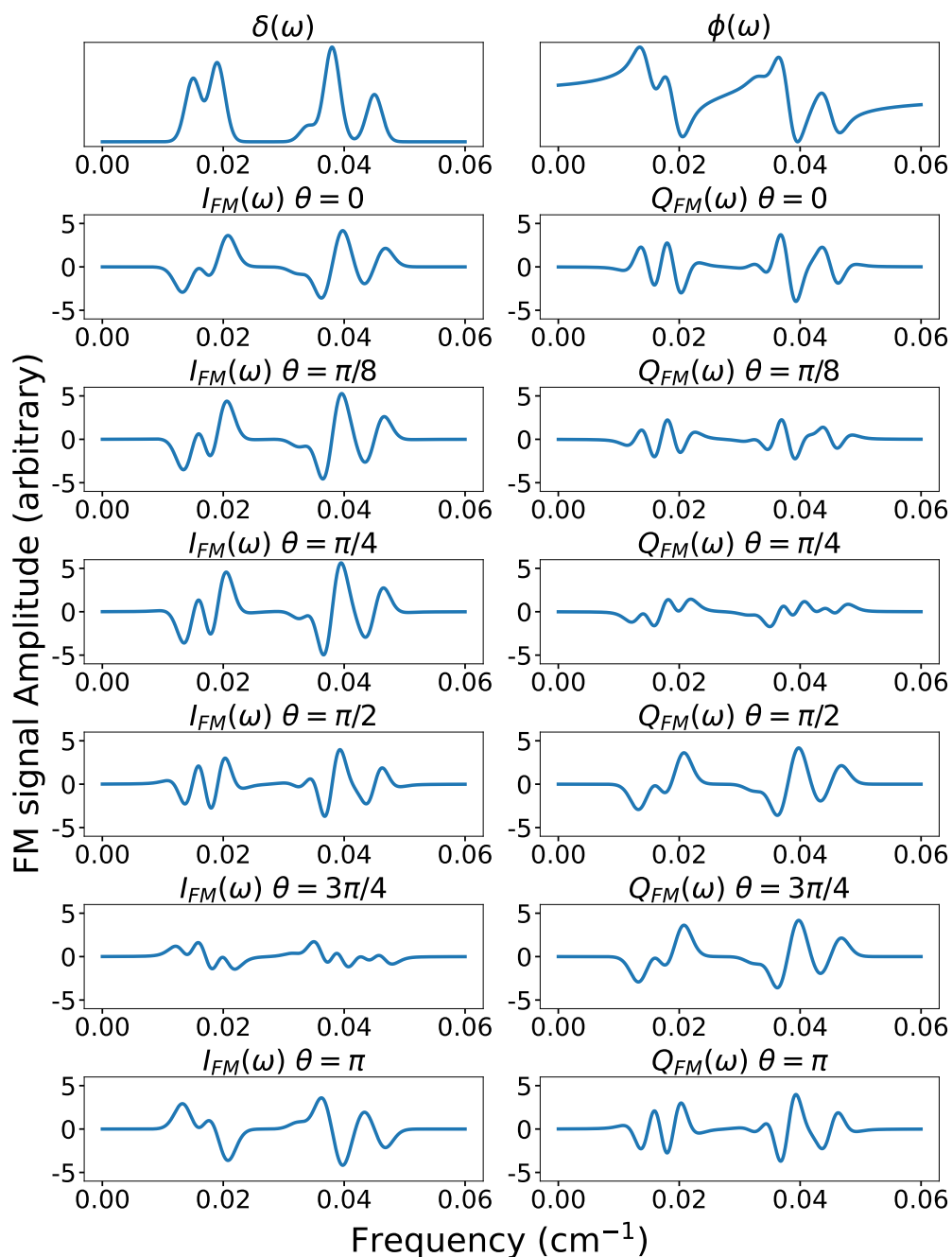


Figure 6.6: Simulated in-phase, $I_{FM}(\omega)$, and in-quadrature, $Q_{FM}(\omega)$, FM signals for five closely spaced and blended spectral features. All five spectral features were modeled with a Gaussian absorption, $\delta(\omega)$, and dispersion, $\phi(\omega)$, lineshape. The in-phase and in-quadrature signals are shown for various phase angles, θ , ranging from $\theta = 0$ to $\theta = \pi$. For phase angles $> \pi$ $I_{FM}(\omega)(\theta = \pi + \phi) = -I_{FM}(\omega)(\theta = \phi)$ and $Q_{FM}(\omega)(\theta = \pi + \phi) = -Q_{FM}(\omega)(\theta = \phi)$ for $0 \leq \phi \leq \pi$. A modulation frequency of 50.3 MHz and a FWHM for all transitions of 90 MHz were used in the simulations. The absolute value of the frequency of the x-axis is arbitrary.

6.4 Experimental implementation of FM absorption in buffer gas cell

A diagram of the experimental FM absorption spectroscopy setup is shown in Fig. 6.7. In our case we are performing FM spectroscopy inside a cryogenic buffer gas cell. As previously mentioned, the measured spectral linewidths inside the cell are ≈ 90 MHz and dominated by Doppler broadening. The tunable laser light used for the FM spectroscopy is derived via the sum-frequency generation of a CW Ti:Sapph and 1550 nm fiber laser⁶. This laser system can tune over much of the visible range and has a linewidth of < 50 kHz.

Sidebands are applied to the laser with a resonant electro-optic phase modulator (EOM) (Thorlabs EO-PM-R-50.3-C4). The EOM is driven by a 69.8 mW (18.44 dBm) 50.3 MHz sinusoidal rf drive. This rf power corresponds to a modulation depth of $M = 0.84$. The EOM was pre-calibrated to determine the relationship between applied rf power and modulation depth. This was accomplished by measuring the amplitude of the carrier, first-, and second-order sidebands as a function of the applied rf power with a scanning Fabry-Perot cavity. The normalized amplitudes (normalized to the amplitude of the carrier when with no rf power applied) vs rf power of the carrier, first- and second-order sidebands were fit to the square of the $n = 0, 1, 2$ Bessel functions, $J_n^2(M = a\sqrt{P})$, respectively. The fits determined the proportionality coefficient, a , which allows the conversion of the applied rf power P to the modulation depth. Experimentally, this conversion was found to be very accurate and reproducible.

The 50.3 rf drive is supplied from a Novatech (409B) signal generator. The amplitude of the Novatech output is set such that there is 69.8 mW of rf power at the EOM. The output of the Novatech is immediately split with a 50/50 splitter. One output of the 50/50 splitter feeds a 24 dB amplifier (Mini-Circuits ZHL-3A+) which in turn drives the EOM. The other output of the 50/50 splitter passes through a 25 dB low-noise amplifier (Mini-Circuits ZX60-P103LN+), a 1 dB attenuator, a voltage controlled phase shifter (Mini-Circuits JSPHS-51+), and into the local oscillator (LO) port of the I and Q demodulator (Pulsar Microwave Corp. IDO-03-412). The 25 dB amplifier and 1 dB attenuator set the rf power going into the phase shifter to 7.6 dBm. It was experimentally found that this phase shifter input power optimized the FM signal SNR. Phase shifter input powers higher than ~ 7 dBm provided no significant improvement in the SNR. The phase shifter allows the phase of the rf

⁶Sirah Mattise Ti:Sapph and and NKT ADJUSTIK+BOOSTIK (1550 nm fiber laser) combined in a Sirah MixTrain.

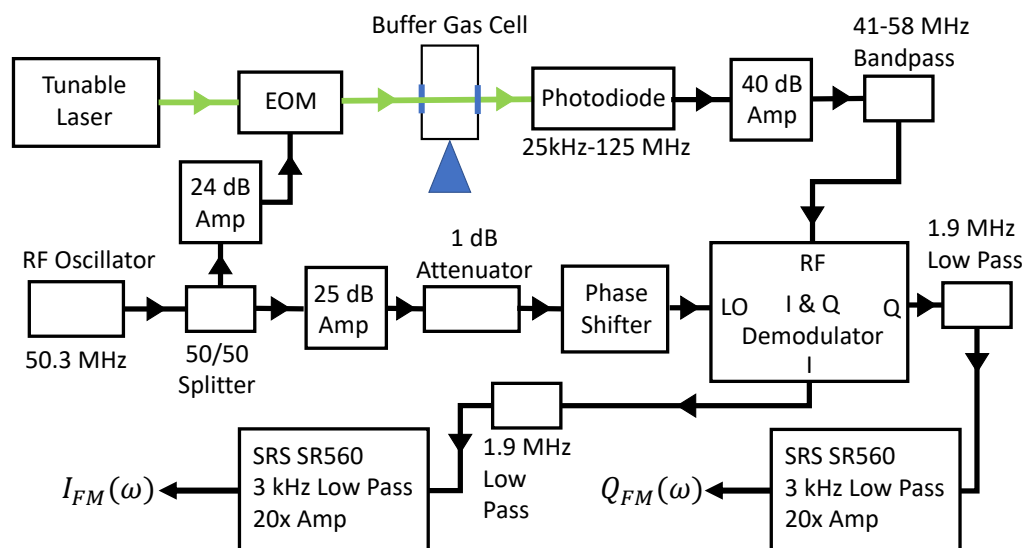


Figure 6.7: Diagram of experimental FM absorption spectroscopy setup. The green lines indicate the laser path and the black lines indicate the rf (or DC after demodulation) signal path. Detailed descriptions of the components and their functions are given in the text.

reference to be tuned, which allows the phase angle, θ , of the $I_{FM}(\omega)$ and $Q_{FM}(\omega)$ signals to be adjusted. We generally operate at a phase shifter voltage where the $I_{FM}(\omega)$ and $Q_{FM}(\omega)$ signals are approximately equal in magnitude.

After sidebands are applied to the laser with the EOM, the laser beam passes through the buffer gas cell and is detected with an AC-coupled fast photodiode (New Focus 1801 photoreceiver) with a 25 kHz - 125 MHz bandwidth. The resulting AC signal is then amplified with a 40 dB low-noise amplifier (Mini-Circuits ZKL-1R5+) and passed through a 41-58 MHz band pass filter before being input into the RF port of the I and Q demodulator. Multiple combinations of a second amplifier and additional bandpass, low-pass, and high-pass filters were tried, none resulted in improved SNR compared to the single amplifier and bandpass filter.

The I and Q demodulator is essentially two rf mixers and a 90° phase shifter. The output of the I port is the in-phase demodulated DC signal resulting from the mixing of the photodiode signal (RF port) and the rf reference (LO port). The output of the Q port is the in-quadrature demodulated DC signal resulting from the mixing of the photodiode signal (RF port) and the rf reference (LO port) with a 90° phase shift. The outputs of both the I and Q ports are passed through 1.9 MHz low-pass filters and input into SRS SR560 low noise pre-amplifiers. The SR560s are set to

have a 12dB/oct 3 kHz low-pass filter and 20x amplification. Due to the fact that the molecular pulse is ~ 1 ms long, setting the low-pass filter cutoff any lower begins to filter out the DC FM signal. The outputs of both of the SR560s are the measured $I_{FM}(\omega)$ and $Q_{FM}(\omega)$ signals.

It is important to note that before we used the rf circuit described above, we originally tried to accomplish FM detection using an SRS SR 844 rf lock-in amplifier. This rf lock-in had all the same features as the discrete rf circuit in one package and with the ability to tune the filter cutoffs and amplification. However, we found that the lock-in introduced a large amount of ~ 60 Hz and ~ 120 Hz line noise which could not be easily filtered out. Therefore, we abandoned the rf lock-in and moved to the discrete rf circuit as it provided much better SNR.

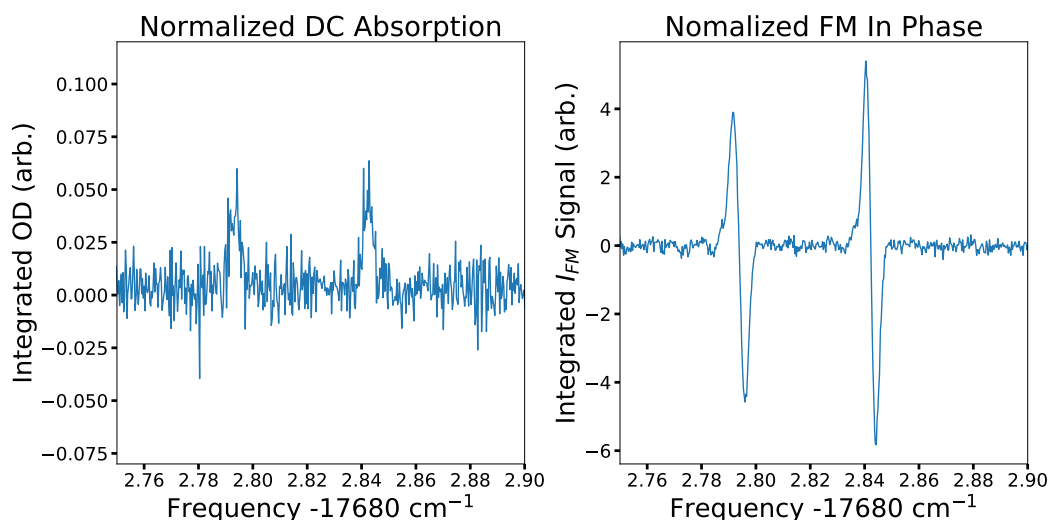


Figure 6.8: DC absorption and in-phase FM absorption of two lines of the [17.68] band of YbOH. For this scan four ablation shots were taken at each frequency step and averaged. A frequency step of 9 MHz was used. Both the integrated DC optical depth and the integrated I_{FM} signal were normalized by the integrated OD from a normalization probe fixed to the ${}^R R_{11}(0)$ line of the $\tilde{A}^2\Pi_{1/2}(0, 0, 0) - \tilde{X}^2\Sigma^+(0, 0, 0)$ band of YbOH [116].

The implementation of FM absorption spectroscopy in the cryogenic buffer gas cell provided a factor of ~ 10 improvement in the SNR. This improvement in SNR is illustrated in Fig. 6.8 and 6.9 where comparisons of DC and FM absorption signals of spectral features of the weak [17.68] band of YbOH⁷ are shown. In Fig. 6.8 and 6.9, both the DC (integrated OD) and FM (integrated I_{FM} signal) signals are

⁷The spectrum of this band is discussed later in Section 6.6.

normalized to the integrated OD from a normalization probe fixed to the ${}^R R_{11}(0)$ line of the $\tilde{A}^2\Pi_{1/2}(0,0,0) - \tilde{X}^2\Sigma^+(0,0,0)$ band of YbOH [116]. Fig. 6.8 shows a slow scan over two isolated lines from in the [17.68] band. Here the laser frequency was stepped in 9 MHz intervals and the average of four ablation shots at each frequency step was taken. The resulting DC OD and in-phase FM signal, I_{FM} , were integrated over the time of the molecular pulse to obtain the spectrum in Fig. 6.8. The DC absorption spectrum in Fig. 6.8 has a SNR of 1.6 while the in-phase FM spectrum has a SNR of 17.2, a factor of 10.7 improvement. Here SNR is defined as the ratio of the DC or FM signal amplitude⁸ to the max positive amplitude of the noise.

Another portion of the [17.68] spectrum recorded at a faster scanning speed, a speed more typically used when taking broadband high-resolution spectra, is shown in Fig. 6.9. For this faster scan, the laser was continuously scanned at ~ 10 MHz/sec, data collected at a repetition rate of 8.7142 Hz and every eight neighboring data points averaged to provide DC and FM signals every ~ 10 MHz. In this case, essentially no spectral features are visible in the DC absorption spectrum. However, the drastically improved SNR from the FM absorption allows clear identification of many spectral features including very weak features such as the one observed at ~ 17681.77 cm^{-1} . It is clear that the implementation of FM absorption spectroscopy in the buffer gas cell allows the measurement of weak transitions which are otherwise impossible to measure via more traditional means, such as DC absorption.

⁸In the case of the FM signals this is the maximum of the positive peak of the FM signal.

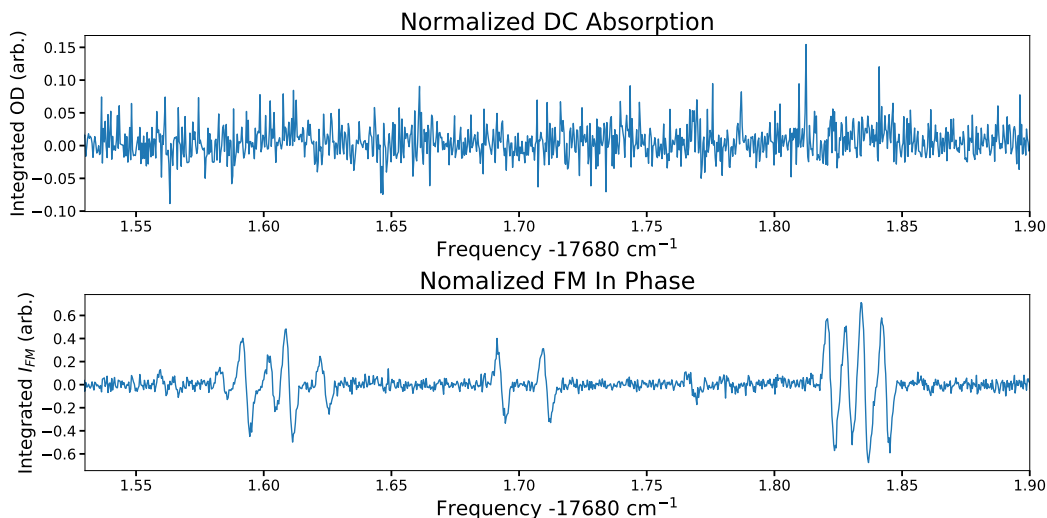


Figure 6.9: DC absorption and in-phase FM absorption of a portion of the [17.68] band of YbOH. Here the laser was continuously scanned, ablation shots were taken every ~ 1.3 MHz, and sets of the 8 nearest ablation shots were averaged resulting in data points every ~ 10 MHz. Both the integrated DC optical depth and the integrated I_{FM} signal were normalized by the integrated OD from a normalization probe fixed to the ${}^R R_{11}(0)$ line of the $\tilde{A}^2\Pi_{1/2}(0, 0, 0) - \tilde{X}^2\Sigma^+(0, 0, 0)$ band of YbOH [116].

6.5 FM spectroscopy of $\tilde{A}^2\Pi_{1/2}(1, 0, 0) - \tilde{X}^2\Sigma^+(3, 0, 0)$ band of ${}^{174}\text{YbOH}$

The one-dimensional laser cooling of ${}^{174}\text{YbOH}$ has been accomplished [54]; however, when this laser cooling was performed, only the $\tilde{X}^2\Sigma^+(1, 0, 0)$, $\tilde{X}^2\Sigma^+(2, 0, 0)$, and $\tilde{X}^2\Sigma^+(0, 2^0, 0)$ vibrational losses were addressed and only about ~ 500 photons were scattered. In order to laser cool and trap YbOH, $\sim 10,000$ photons need to be scattered and, therefore, higher vibrational losses must be addressed. FM spectroscopy in a cryogenic buffer gas cell is an optimal method with which to identify repumping transitions for two major reasons. First, FM spectroscopy provides the needed sensitivity to be able to measure weak repumping transitions. Second, as discussed in Section 5.1, the laser-enhanced chemical reactions which occur in our cell increase the population of excited vibrational states and provide the needed excited state vibrational populations from which repumping transitions can be driven. Here, we measure the spectrum of the $\tilde{A}^2\Pi_{1/2}(1, 0, 0) - \tilde{X}^2\Sigma^+(3, 0, 0)$ band of YbOH using in cell FM spectroscopy.

Experiment

The same experimental FM spectroscopy setup described in Section 6.4 was used to measure the $\tilde{A}^2\Pi_{1/2}(1, 0, 0) - \tilde{X}^2\Sigma^+(3, 0, 0)$ transition. The following buffer

gas cell configuration was used (see Section 3.2): gas inlet, 0.125-inch blank, diffuser plate, 0.5-inch blank, 1.0-inch window piece for ablation (with snorkel), 0.5-inch blank, 0.5-inch window piece for spectroscopy (spectroscopy window), and 0.25-inch aperture plate. Molecule production is accomplished by ablating a stoichiometric Yb + Yb(OH)₃ + PEG target with a pulsed Nd:YAG laser (532 nm, 42 mJ/pulse). Laser-enhanced chemical reactions were driven with the enhancement laser (~3 mm in diameter, ~300 mW) which is fixed to the $^3P_1 \leftarrow ^1S_0$ ^{174}Yb transition at $17992.0003\text{ cm}^{-1}$ [137]. The enhancement laser was introduced into the cell through the spectroscopy window and was applied for every ablation shot. In the absence of the enhancement light, no FM signals were present and, therefore, the FM signals observed with the enhancement light present were due to only the $^{174}\text{YbOH}$ isotopologue.

FM spectroscopy was performed with a 3.5 mW CW laser (~1 mm in diameter) which was derived from, as described previously, the sum-frequency generation of a CW Ti:Sapph and 1550 nm fiber laser. The FM laser is introduced into the cell through the spectroscopy window. To record the spectrum, the FM spectroscopy laser was continuously scanned and the signal from every five consecutive shots averaged, resulting in ~10 MHz spacing between data points. The frequency of the FM laser is continuously recorded with a HighFinesse wavemeter (WS7-30 VIS/Standard model) which is used to track the relative frequency spacing between data points. The sub-Doppler saturated absorption spectrum of I₂ is co-recorded with the FM spectrum and used for absolute frequency calibration. Absolute frequency calibration with the sub-Doppler I₂ spectrum results in an absolute frequency error of $\lesssim 6$ MHz.

In addition to the FM spectroscopy laser, a normalization laser is also introduced into the cell through the spectroscopy window. The normalization laser is fixed to the $^R R_{11}(0)$ line of the $\tilde{A}^2\Pi_{1/2}(0, 0, 0) - \tilde{X}^2\Sigma^+(0, 0, 0)$ band of YbOH [116] and is used to track the shot-to-shot fluctuations in molecular production. The measured in-phase and in-quadrature FM signals are integrated over the duration of the molecular pulse and normalized by the integrated DC OD from the normalization probe to produce the in-phase, $I_{FM}(\omega)$, and in-quadrature, $Q_{FM}(\omega)$, spectrum.

Observation and assignment

The observed in-phase, $I_{FM}(\omega)$, and in-quadrature, $Q_{FM}(\omega)$, FM spectrum of a portion of the bandhead region of the $\tilde{A}^2\Pi_{1/2}(1, 0, 0) - \tilde{X}^2\Sigma^+(3, 0, 0)$ spectrum of

$^{174}\text{YbOH}$ is presented in Fig. 6.10. Also presented are the predicted in-phase and in-quadrature FM spectra. The predictions were made using the optimized parameters determined in this study (Table 6.1), a phase angle of 5.90 radians, a linewidth of 108 MHz⁹, a temperature of 5 K, and the FM lineshape model described in Section 6.3. The utilization of the laser-enhanced chemical reactions allowed the isolation of only the $^{174}\text{YbOH}$ spectrum. The chemical enhancement technique used to isolate $^{174}\text{YbOH}$ spectrum is similar to the approach used to isolate the odd isotopologue spectra in Section 5.3 and [129]. No evidence of H ($\mathbf{I} = 1/2$) hyperfine splittings was observed in the spectrum and, therefore, the typical $^2\Pi$ Hund's case (a) - $^2\Sigma^+$ Hund's case (b) branch designation $^{\Delta N}\Delta J_{F'_i F''_i}$ is used to label the measured transitions. For the $\tilde{X}^2\Sigma^+(3, 0, 0)$ state $F''_i = 1$ for $J'' = N'' + 1/2$ and $F''_i = 2$ for $J'' = N'' - 1/2$. For the $\tilde{A}^2\Pi_{1/2}(1, 0, 0)$ state $F'_i = 1$.

The $\tilde{A}^2\Pi_{1/2}(1, 0, 0) - \tilde{X}^2\Sigma^+(3, 0, 0)$ band of $^{174}\text{YbOH}$ contains a blue degraded bandhead comprised of the low- J $^P P_{11}$, $^Q Q_{11}$, $^P Q_{12}$, and $^Q R_{12}$ branches. As with the previously measured $\tilde{A}^2\Pi_{1/2}(1, 0, 0) - \tilde{X}^2\Sigma^+(0, 0, 0)$ band [116], the large Λ -doubling parameter, $p+2q' > 2B'$, in the $\tilde{A}^2\Pi_{1/2}(1, 0, 0)$ state results in an abnormal spectral pattern in the bandhead region where $^Q Q_{11}$ and $^Q R_{12}$ branch features fall to the red of the $^P P_{11}$ and $^P Q_{12}$ branch features. To the red of the bandhead lies the relatively unblended $^O P_{12}$ branch. Only a single feature of this branch, the $^O P_{12}(2)$ line, was measured in this study. To the blue of the bandhead lies the also relatively unblended $^R R_{11}$ branch. Two of the features of this branch, the $^R R_{11}(0)$ and $^R R_{11}(1)$ lines, were measured in this study.

The observed intensities of the $^P Q_{12}$ and $^Q Q_{11}$ branch features (Fig. 6.10a and c) are weaker than those of the $^Q R_{12}$ and $^P P_{11}$ branches. This is in contrast to the predicted intensities (Fig. 6.10b and d) where the opposite is the case. This discrepancy between the observed and predicted relative intensities between different branch features was also observed the $\tilde{A}^2\Pi_{1/2}(1, 0, 0) - \tilde{X}^2\Sigma^+(0, 0, 0)$ band [116]. The reduction of the intensities of the $^P Q_{12}$ and $^Q Q_{11}$ branch features (or the increase in the intensity of the $^Q R_{12}$ and $^P P_{11}$ branch features) may be due to perturbations arising from the mixing of the $\tilde{X}^2\Sigma^+$ and/or the $\tilde{A}^2\Pi_{1/2}$ states with other vibronic states.

The transition wavenumbers were determined via a simultaneous non-linear least squares fit of the measured in-phase and in-quadrature FM lineshapes to the lineshape

⁹The phase angle and spectral linewidth used in the predictions are the average of the measured phase angles and linewidths determined from a non-linear least squares fit of the FM lineshapes.

model described in Section 6.3. The simultaneous fit of the ${}^P Q_{12}(4)$, ${}^Q Q_{11}(5)$, and ${}^P P_{11}(4)$ lines is presented in Fig. 6.11. The line centers (transition wavenumber), linewidths (FWHM), and relative heights of the Gaussian absorption profiles as well as the phase angle between the in-phase and in-quadrature FM signals are floated in the fit. The data set was cut so that a minimum number of spectral features were fit at a single time. An average phase angle of 5.90 radians and an average linewidth of 108 MHz were measured from the fits of the FM data. This linewidth is consistent with the previously measured DC absorption linewidth of ~ 90 MHz.

Assignments of the spectral features were made using both combination differences¹⁰ and spectral predictions. Combination differences were used to assign low J spectral features and determine the energies of the $N = 1, J = 3/2$, $N = 2, J = 3/2$ and $N = 2, J = 5/2$, levels of the $\tilde{X}^2\Sigma^+(3, 0, 0)$ state. These energy levels were then used to estimate the origin, T_0 , the rotational constant, B'' , and spin rotation parameter, γ'' , of the $\tilde{X}^2\Sigma^+(3, 0, 0)$ state. These estimated parameters were then used in conjunction with the previously determined parameters for the $\tilde{A}^2\Pi_{1/2}(1, 0, 0)$ state [116] to predict the $\tilde{A}^2\Pi_{1/2}(1, 0, 0) - \tilde{X}^2\Sigma^+(3, 0, 0)$ spectrum, with which the remaining spectral assignments were made. The 35 measured transition wavenumbers along with the assignments and associated quantum numbers are presented in Table A.4 of Appendix A. Also presented in Table A.4 are the differences between the observed and calculated transition frequencies. The calculated transition frequencies were obtained using the optimized parameters given in Table 6.1. In addition to the 35 assigned transitions, 3 unassigned transitions were also observed and are listed in Table A.4.

¹⁰Combination differences are matching frequency spacings between the measured spectral features and, in this case, the calculated energy levels of the $\tilde{A}^2\Pi_{1/2}(1, 0, 0)$ state. The energy levels of the $\tilde{A}^2\Pi_{1/2}(1, 0, 0)$ state were calculated using the previously determined parameters [116]. A combination difference match indicates that a pair of transitions originate from the same ground state and provides a definitive assignment of the excited state of each transition.

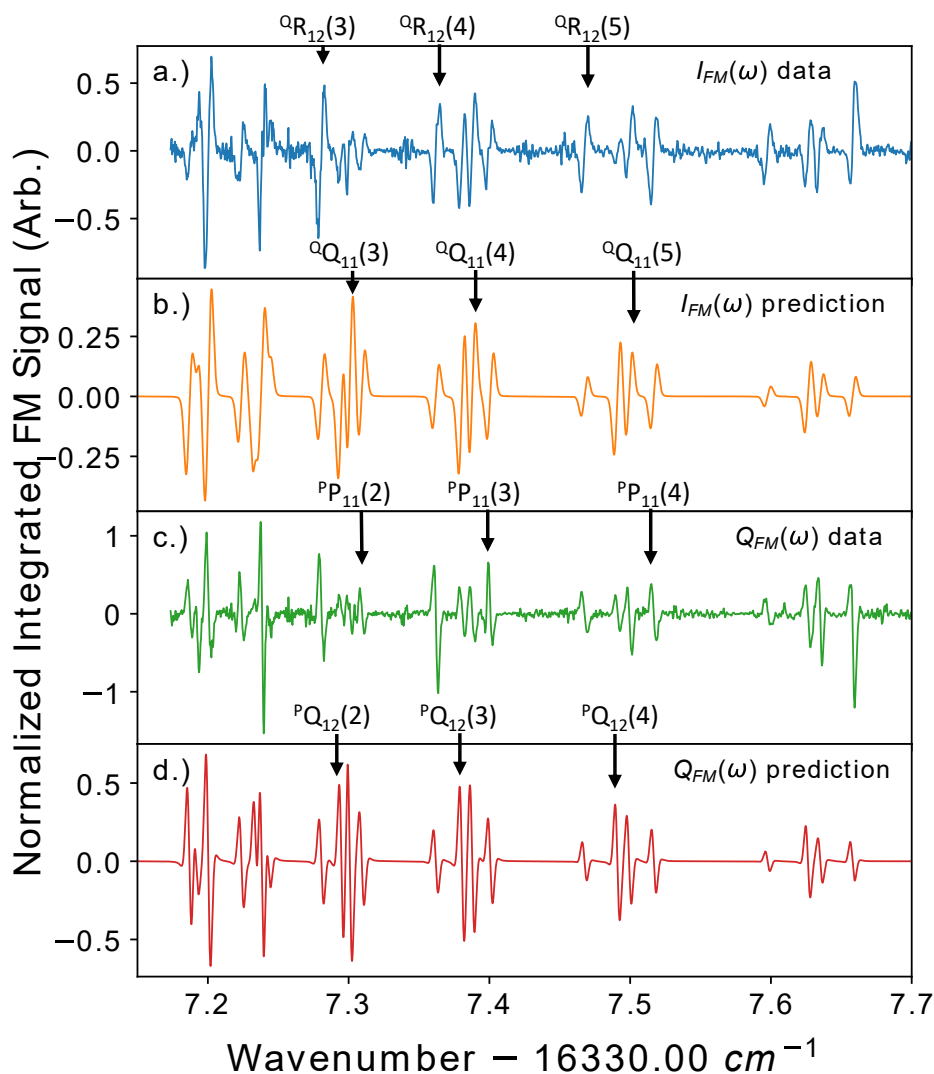


Figure 6.10: Measured and predicted FM spectrum in the bandhead region of the $\tilde{A}^2\Pi_{1/2}(1, 0, 0) - \tilde{X}^2\Sigma^+(3, 0, 0)$ band of $^{174}\text{YbOH}$. Several features of the $^Q R_{12}$, $^Q Q_{11}$, $^P P_{11}$, and $^P Q_{12}$ branches are indicated in separate plots for clarity. **a.)** Measured in-phase FM spectrum, $I_{FM}(\omega)$. **b.)** Predicted in-phase FM spectrum. **c.)** Measured in-quadrature FM spectrum, $Q_{FM}(\omega)$. **d.)** Predicted in-quadrature FM spectrum. The predicted in-phase and in-quadrature FM spectra were obtained using the FM lineshape model described in Section 6.3. The transition frequencies and relative amplitudes input into the module were calculated using the optimized parameters given in Table 6.1. A phase angle of 5.90 radians, FWHM Gaussian absorption linewidth of 108 MHz, and a temperature of 5 K were used in the predictions.

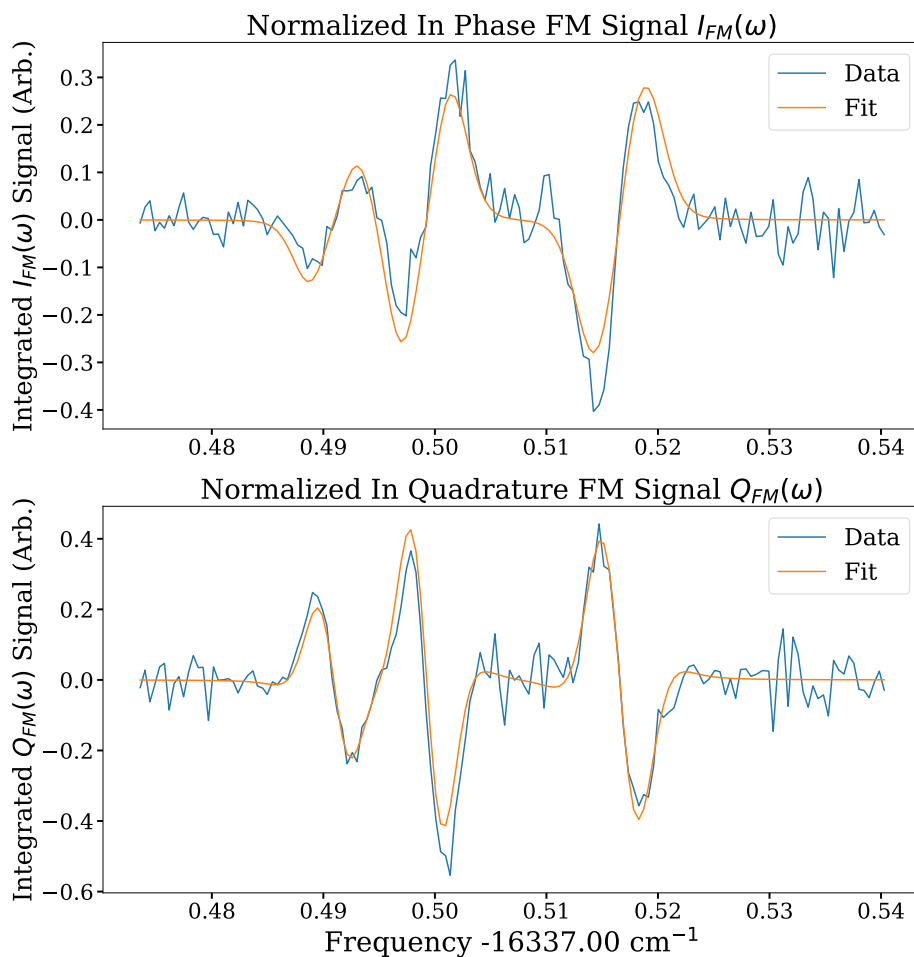


Figure 6.11: Simultaneous fit of the in-phase and in-quadrature FM spectrum of the (in order of increasing frequency) ${}^P Q_{12}(4)$, ${}^Q Q_{11}(5)$, and ${}^P P_{11}(4)$ lines of the $\tilde{A}^2\Pi_{1/2}(1, 0, 0) - \tilde{X}^2\Sigma^+(3, 0, 0)$ band of ${}^{174}\text{YbOH}$ to the FM lineshape model given in Section 6.3. The line center, linewidth, and relative amplitude of the Gaussian absorption lineshape of each transition, as well as the overall phase angle between the in-phase and in-quadrature signals were floated in the fit. The line centers resulting from the fit provide a measurement of each transition frequency.

Analysis

The 35 transition frequencies of the $\tilde{A}^2\Pi_{1/2}(1, 0, 0) - \tilde{X}^2\Sigma^+(3, 0, 0)$ band, measured here, were combined with the 65 previously measured transitions frequencies of the $\tilde{A}^2\Pi_{1/2}(1, 0, 0) - \tilde{X}^2\Sigma^+(0, 0, 0)$ band (measured via molecular beam LIF) [116] and used as inputs in a non-linear least squares fitting procedure. The two data sets share the same excited $\tilde{A}^2\Pi_{1/2}(1, 0, 0)$ state and simultaneous fit of both data sets was performed in order to obtain the optimized parameters of the $\tilde{X}^2\Sigma^+(3, 0, 0)$ state as well as improved parameters for the $\tilde{A}^2\Pi_{1/2}(1, 0, 0)$ state. The $\tilde{A}^2\Pi_{1/2}(1, 0, 0) - \tilde{X}^2\Sigma^+(3, 0, 0)$ FM transitions frequencies were determined to approximately a factor of two higher precision as compared to the molecular beam LIF data of the $\tilde{A}^2\Pi_{1/2}(1, 0, 0) - \tilde{X}^2\Sigma^+(0, 0, 0)$ band and, therefore, the FM data of the $\tilde{A}^2\Pi_{1/2}(1, 0, 0) - \tilde{X}^2\Sigma^+(3, 0, 0)$ band was weighted twice that of the previously recorded $\tilde{A}^2\Pi_{1/2}(1, 0, 0) - \tilde{X}^2\Sigma^+(0, 0, 0)$ molecular beam LIF data in the fitting procedure. The increased precision of the FM data is due to both the high intrinsic sensitivity of the FM absorption method for measuring transition frequencies (measuring simultaneous zero crossing of in-phase and in-quadrature line shapes) as well as the isolation of the $^{174}\text{YbOH}$ spectrum from that of the other isotopologues with the laser-enhanced chemical reactions.

The energy levels of the $\tilde{X}^2\Sigma^+(0, 0, 0)$, $\tilde{X}^2\Sigma^+(3, 0, 0)$, and the $\tilde{A}^2\Pi_{1/2}(1, 0, 0)$ states were modeled using an effective Hamiltonian approach. The effective Hamiltonian used to model the $\tilde{X}^2\Sigma^+(0, 0, 0)$ state is

$$\hat{H}_{eff} [\tilde{X}^2\Sigma^+(0, 0, 0)] = B\mathbf{R}^2 - D\mathbf{R}^2\mathbf{R}^2 + \gamma\mathbf{N} \cdot \mathbf{S} + \gamma_D [\mathbf{N} \cdot \mathbf{S}, \mathbf{R}^2]_+ \quad (6.24)$$

which accounts for rotation (B), centrifugal distortions (D), spin-rotation (γ), and spin-rotation centrifugal distortions (γ_D). In the least-squares fit and for all spectral predictions the parameters of the $\tilde{X}^2\Sigma^+(0, 0, 0)$ state were fixed to the values determined with PPMODR microwave spectroscopy (see Ch. 4) [93]. The effective Hamiltonian used to model the $\tilde{X}^2\Sigma^+(3, 0, 0)$ state is

$$\hat{H}_{eff} [\tilde{X}^2\Sigma^+(3, 0, 0)] = T_0 + B\mathbf{R}^2 - D\mathbf{R}^2\mathbf{R}^2 + \gamma\mathbf{N} \cdot \mathbf{S}. \quad (6.25)$$

This effective Hamiltonian is the same as that of the $\tilde{X}^2\Sigma^+(0, 0, 0)$ state with the addition of an origin (T_0) to account for the vibrational energy and the removal of the term accounting for the spin-rotation centrifugal distortions. The FM spectrum recorded in the cryogenic buffer gas cell only probed lower J transitions and is not sensitive to spin-rotation centrifugal distortions. The effective Hamiltonian used to

model the $\tilde{A}^2\Pi_{1/2}(1, 0, 0)$ state is

$$\begin{aligned} \hat{H}_{eff} [\tilde{A}^2\Pi_{1/2}(1, 0, 0)] = & T_0 + AL_zS_z + BR^2 - DR^2R^2 \\ & + \frac{1}{2}(p + 2q)(J_+S_+e^{-2i\theta} + J_-S_-e^{+2i\theta}) \\ & + (p + 2q)_D \left[\frac{1}{2}(J_+S_+e^{-2i\theta} + J_-S_-e^{+2i\theta}), \mathbf{R}^2 \right]_+ \end{aligned} \quad (6.26)$$

which accounts for the origin of the electronic state (T_0), spin-orbit (A), rotation (B), centrifugal distortions (D), Λ -doubling ($p + 2q$), and Λ -doubling centrifugal distortions ($(p + 2q)_D$). Since no evidence of hyperfine splittings due to the H were observed, hyperfine interactions were not included in the effective Hamiltonians.

Even though the $\tilde{X}^2\Sigma^+(0, 0, 0)$ and $\tilde{X}^2\Sigma^+(3, 0, 0)$ states are best described by a Hund's case (b) basis, all effective Hamiltonian's were constructed in a Hund's case (a) basis, $|\eta, \Lambda\rangle|S, \Sigma\rangle|J, \Omega\rangle$. The energy levels and eigenstates of the $\tilde{X}^2\Sigma^+(0, 0, 0)$ and $\tilde{X}^2\Sigma^+(3, 0, 0)$ states were determined by constructing and diagonalizing the full 34×34 ($2(N_{max} + 1)$) Hamiltonian for all $N = 0 - N = 16$ rotational levels while the energy levels and eigenstates of the $\tilde{A}^2\Pi_{1/2}(1, 0, 0)$ state were determined by construction and diagonalizing the full 66×66 ($4N_{max} + 2$) Hamiltonian for all $N = 1 - N = 16$ rotational levels. The matrix elements used in the calculation of the effective Hamiltonians were taken from Ref. [89, 92].

The origin (T_0), rotational parameter (B''), and the spin-rotation parameter (γ'') of the $\tilde{X}^2\Sigma^+(3, 0, 0)$ state and the origin (T_0), rotational parameter (B'), Λ -doubling parameter ($p + 2q$), and Λ -doubling centrifugal distortion parameter ($(p + 2q)_D$) were floated (a total of seven parameters) in the final least-squares fit to the measured transition frequencies. The spin-orbit parameter, A , of the $\tilde{A}^2\Pi_{1/2}(1, 0, 0)$ state was fixed to the value from the high temperature analysis [105]. Fits floating various parameters were performed and an f-test with a 95% confidence interval was used to determine if floating additional parameters (such as $(p + 2q)'_D$, D'' , or D') was statistically justified. While the f-test indicated floating D in both the $\tilde{X}^2\Sigma^+(3, 0, 0)$ and $\tilde{A}^2\Pi_{1/2}(1, 0, 0)$ states was statistically justified, the error in the resulting fit D parameters was $\sim 20\%$ of the fitted value. This indicated that floating the D parameters resulted in optimized values for D'' and D' that were not well determined. Therefore, the value of D in the $\tilde{X}^2\Sigma^+(3, 0, 0)$ state was fixed to the value extrapolated from the D values of the $\tilde{X}^2\Sigma^+(0, 0, 0)$ and $\tilde{X}^2\Sigma^+(1, 0, 0)$ states using the expected vibrational dependence [81]. The value of D in the $\tilde{A}^2\Pi_{1/2}(1, 0, 0)$ state was fixed to the extrapolated value given in Ref. [116]. The

optimized parameters of the $\tilde{X}^2\Sigma^+(3, 0, 0)$ and $\tilde{A}^2\Pi_{1/2}(1, 0, 0)$ states resulting from the least-squares fit to the transition frequencies are presented in Table 6.1. Also, presented in Table 6.1 are the parameters of the $\tilde{X}^2\Sigma^+(1, 0, 0)$ state for comparison. The fit resulted in an RMS of the residuals of 25 MHz (0.00084 cm^{-1}), which is commensurate with the measurement uncertainty of the combined data set. The difference between the observed and calculated transition frequencies (fit residuals) for the $\tilde{A}^2\Pi_{1/2}(1, 0, 0) - \tilde{X}^2\Sigma^+(3, 0, 0)$ and $\tilde{A}^2\Pi_{1/2}(1, 0, 0) - \tilde{X}^2\Sigma^+(0, 0, 0)$ bands are given in Table A.4 and A.5, respectively, in Appendix A.

Spectral predictions were made in the following manner. First, the transition moment matrix is calculated in a Hund's case (a) basis and cross multiplied by the eigenvectors to determine the transition moments. The relative transition amplitudes are given by the product of the square of the transition moment and a Boltzmann factor. To produce simulated FM spectra, such as those shown in Fig. 6.10, the total absorption lineshape, $\delta_{tot}(\omega)$, is calculated by summing individual Gaussian lineshapes for each transition, using Eq. 6.19. The transition frequencies and relative amplitudes from the spectral predictions are used for the line centers and amplitudes of the Gaussian lineshapes and a FWHM of 108 MHz (the averaged measured linewidth) is used as the linewidth for all transitions. The total dispersion lineshape, $\phi_{tot}(\omega)$ is calculated in a similar manner using Eq. 6.20. Finally, the simulated in-phase, $I_{FM}(\omega)$, and in-quadrature, $Q_{FM}(\omega)$, FM lineshapes are calculated using Eq. 6.21 and 6.22 and a phase angle of 5.90 radians, the average of the measured phase angle.

Table 6.1: Spectroscopic parameters of the $\tilde{X}^2\Sigma^+(0,0,0)$, $\tilde{X}^2\Sigma^+(3,0,0)$, and $\tilde{A}^2\Pi_{1/2}(1,0,0)$ states of $^{174}\text{YbOH}$. The parameters of the $\tilde{X}^2\Sigma^+(1,0,0)$ state are also presented for comparison. All values are in cm^{-1} . Values in parenthesis are the standard errors resulting from the combined fit of the $\tilde{A}^2\Pi_{1/2}(1,0,0) - \tilde{X}^2\Sigma^+(0,0,0)$ and $\tilde{A}^2\Pi_{1/2}(1,0,0) - \tilde{X}^2\Sigma^+(3,0,0)$ bands.

Electronic		Vibrational State		
State	Parameter	(0,0,0)	(1,0,0)	(3,0,0)
$\tilde{X}^2\Sigma^+$	B''	0.245116257 ^a	0.243681 ^b	0.240795(4)
	$10^7 D''$	2.029 ^a	2.168 ^b	2.45 ^c (fixed)
	γ''	-0.002707 ^a	-0.00369 ^b	-0.00575(3)
	$10^7 \gamma''$	1.59 ^a		
	T_0		529.3269 ^b	1570.6697(2)
$\tilde{A}^2\Pi_{1/2}$	A'		1350 ^d (fixed)	
	B'		0.253197(2)	
	$10^7 D'$		2.478 ^b (fixed)	
	$p + 2q'$		-0.53459(4)	
	$10^6(p + 2q)'_D$		-17.3(3)	
	T_0		18582.8707(1)	

^a Fixed to PPMODR values in fit, Section 4 and Ref [93].

^b From Ref. [116].

^c Fixed to value extrapolated from that of the $\tilde{X}^2\Sigma^+(0,0,0)$ and $(1,0,0)$ states.

^d Fixed to value from high-temperature analysis [105].

Discussion

The main goals of this study were to demonstrate the utility of laser-enhancement and FM spectroscopy for measuring transitions originating from excited vibrational states, to identify the $\tilde{X}^2\Sigma^+(3,0,0)$ repumping transitions needed to laser cool and trap YbOH, and to determine the spectroscopic parameters of the $\tilde{X}^2\Sigma^+(3,0,0)$ state. The measured FM spectrum of the $\tilde{A}^2\Pi_{1/2}(1,0,0) - \tilde{X}^2\Sigma^+(3,0,0)$ band

demonstrates that the chemical enhancement does indeed provide enough excited vibrational state population for transitions originating from excited vibrational states to be observed. Additionally, the in buffer gas cell FM absorption technique provides the needed sensitivity to observe the weak $\tilde{A}^2\Pi_{1/2}(1, 0, 0) - \tilde{X}^2\Sigma^+(3, 0, 0)$ band. This combination of chemical enhancement and in cell FM absorption spectroscopy is a promising technique with which to measure transitions originating from excited vibrational states, in both YbOH and other molecules.

The majority of the interest in the $\tilde{A}^2\Pi_{1/2}(1, 0, 0) - \tilde{X}^2\Sigma^+(3, 0, 0)$ band of YbOH stems from its utility as a repumping pathway through which population lost to the $\tilde{X}^2\Sigma^+(3, 0, 0)$ state when laser cooling can be returned to the cooling cycle. Repumping is accomplished by driving the rotationally closed $^PQ_{12}(1)$ and $^PP_{11}(1)$ transitions¹¹ [100]. While the analysis of the data assigned the $^PP_{11}(1)$ line to the transition at 16337.2431 cm⁻¹, no assignment for the $^PQ_{12}(1)$ line was originally made. The prediction of the $\tilde{A}^2\Pi_{1/2}(1, 0, 0) - \tilde{X}^2\Sigma^+(3, 0, 0)$ spectrum using the optimized parameters from Table 6.1 places the $^PQ_{12}(1)$ line at 16337.2342 cm⁻¹. The in-phase and in-quadrature FM data and simulated spectra in the region of the predicted $^PQ_{12}(1)$ line and the measured $^Q R_{12}(2)$, $^Q Q_{11}(2)$ and $^PP_{11}(1)$ lines are presented in Fig. 6.12. The simulated FM spectra were calculated using the optimized parameters from Table 6.1, a Gaussian FWHM linewidth of 108 MHz, a phase angle of 5.90 radians, and a temperature of 5 K. When comparing the prediction to the data, particularly the in-phase data, the $^PQ_{12}(1)$ line appears to be missing. However, upon closer examination, the asymmetry in the in-phase and in-quadrature positive and negative peak heights of the $^Q Q_{11}(2)$ line as well as the small positive peak to the red of the $^Q Q_{11}(2)$ line in the in quadrature data indicate that there is a small spectral feature just to the red of and blended with the $^Q Q_{11}(2)$ feature. When fitting the data in this region to the FM lineshape model, fits both with and without a line to account for this small feature were performed (fits to 3 or 4 spectral features). Adding a line to account for this small feature did not improve the fit. Therefore, a line accounting for this small blended feature was not added to the fit and no transition wavenumber was assigned to this feature. When examining the FM data and the prediction made with the optimized parameters, particularly the in-quadrature data and prediction, this small feature is almost directly overlapped with the predicted $^PQ_{12}(1)$ line. Therefore, even though the observed intensity is much smaller than the predicted intensity, this small feature can be assigned to

¹¹To achieve rotational closure both the $^PQ_{12}(1)$ and $^PP_{11}(1)$ transitions must be simultaneously driven.

the ${}^P Q_{12}(1)$ transition. The blending of this feature with the much more intense ${}^Q Q_{11}(2)$ line precludes measurement of the transition frequency via fitting to the FM lineshape or by zero-crossing measurement. Instead the transition frequency was measured by noting that the maximum of the positive peak of the in-quadrature signal is ~ 50.3 MHz to the red of the center of the Gaussian absorption lineshape. Using this method the ${}^P Q_{12}(1)$ line was assigned to 16337.2348 ± 0.0036 cm^{-1} , which disagrees with the predicted value by 18 MHz (0.0006 cm^{-1}). The generous error of one average measured linewidth is given due to the approximate method used for measuring the transition frequency. The assigned values of the ${}^P Q_{12}(1)$ and ${}^P P_{11}(1)$ transitions can be immediately used for the implementation of laser cooling of YbOH.

The combined fit of the $\tilde{A}^2\Pi_{1/2}(1, 0, 0) - \tilde{X}^2\Sigma^+(3, 0, 0)$ and $\tilde{A}^2\Pi_{1/2}(1, 0, 0) - \tilde{X}^2\Sigma^+(0, 0, 0)$ data sets allowed the parameters of the $\tilde{X}^2\Sigma^+(3, 0, 0)$ state to be determined for the first time. The determined value of the origin, $T_0 = 1570.6697(2)$ cm^{-1} , matches the value of $1572(5)$ cm^{-1} measured using a dispersed LIF technique [95]. The vibrational dependence of the rotational constant, B , is [81]

$$B_\nu = B_e - \alpha_e(\nu + 1/2). \quad (6.27)$$

Fitting the measured values of B for the $\tilde{X}^2\Sigma^+(0, 0, 0)$ and $\tilde{X}^2\Sigma^+(1, 0, 0)$ states to Eq. 6.27 (up to only the linear term) results in, $B_e = 0.245834$ cm^{-1} and $\alpha_e = 0.001435$ cm^{-1} . Using these values in Eq. 6.27 predicts B for the $\tilde{X}^2\Sigma^+(3, 0, 0)$ state of 0.240810 cm^{-1} . This is in fairly good agreement with the measured value of $0.240795(4)$ cm^{-1} , especially considering the quadratic and higher-order terms in Eq. 6.27 were ignored.

The value of γ for the $\tilde{X}^2\Sigma^+(3, 0, 0)$ state determined here is negative, as is the case in the $\tilde{X}^2\Sigma^+(0, 0, 0)$ and $\tilde{X}^2\Sigma^+(1, 0, 0)$ states. As was discussed in Section 4.3, the value of γ is dominated by second-order contributions which result from the mixing of the $\tilde{X}^2\Sigma^+$ state with excited ${}^2\Pi_{1/2}$ states through the combination of the rotational and spin orbit interactions. The second-order contributions to gamma are given in Eq. 4.2 which is reproduced here for convenience

$$\gamma^{(2)} = 2 \sum_{{}^2\Pi, \nu''} |\langle \nu'' | \nu' \rangle|^2 \frac{\langle {}^2\Sigma_{-1/2}^+ | BL_- | {}^2\Pi_{1/2} \rangle \langle {}^2\Pi_{1/2} | \sum_i a_i l_i^+ s_i^- | {}^2\Sigma_{1/2}^+ \rangle}{E_{\Pi, \nu''} - E_{\Sigma, \nu''}}. \quad (6.28)$$

In Section 4.3, known YbOH molecular and Yb^+ atomic information were used in Eq. 6.28 to estimate the contribution to γ from the $\tilde{A}^2\Pi_{1/2}$ state, $\gamma_{\nu_1=0}(\tilde{A}^2\Pi_{1/2}) =$

0.02761 cm^{-1} . The same procedure can be used to estimate the contribution of the $\tilde{A}^2\Pi_{1/2}$ state to the value γ in the $\tilde{X}^2\Sigma^+(1, 0, 0)$ and $\tilde{X}^2\Sigma^+(3, 0, 0)$ states.

We can again assume that the wavefunction of the $\tilde{X}^2\Sigma^+$ state can then be approximated by

$$|\tilde{X}^2\Sigma^+\rangle \approx x_s|6s\sigma\rangle + x_p|6p\sigma\rangle, \quad (6.29)$$

where $|6s\sigma\rangle$ and $|6p\sigma\rangle$ are the Yb^+ $6s\sigma$ and $6p\pi$ atomic orbitals. Measurements of the b_F hyperfine parameter of the odd isotopologues (see Section 5.5) indicate that $|x_s|^2 \approx 0.54$, and assuming contributions from other atomic orbitals (e.g., $5d\sigma$) are small, $< 1\%$, gives $|x_p|^2 \approx 0.46$. The wavefunction of the $\tilde{A}^2\Pi_{1/2}$ state can be approximated by

$$|\tilde{A}^2\Pi_{1/2}\rangle \approx a_p|6p\pi\rangle + a_d|5d\pi\rangle, \quad (6.30)$$

where $|6p\pi\rangle$ and $|5d\pi\rangle$ are the Yb^+ atomic $6p\pi$ and $5d\pi$ orbitals. As before, if we parameterize the atomic spin orbit interaction as $\zeta_{n,l}l \cdot s$ and use the Yb^+ atomic ion values, $\zeta_{6p} = 2220 \text{ cm}^{-1}$ and $\zeta_{5d} = 549 \text{ cm}^{-1}$ [124, 125], as well as the measured spin orbit parameter of the $\tilde{A}^2\Pi$ state of YbOH , $A = 1350 \text{ cm}^{-1}$ [105], we estimate $|a_p|^2 \approx 0.48$ and $|a_d|^2 \approx 0.52$. Using these wavefunctions, the electronic matrix elements in Eq. 6.28 are

$$\begin{aligned} & \langle \tilde{X}^2\Sigma^+ | BL_- | \tilde{A}^2\Pi_{1/2} \rangle \langle \tilde{A}^2\Pi_{1/2} | \sum_i a_i l_i^+ s_i^- | \tilde{X}^2\Sigma^+ \rangle \\ &= B |x_p|^2 |a_p|^2 \langle 6p\sigma | l_i^- | 6p\pi \rangle \langle 6p\pi | \zeta_{6p} l_i^+ | 6p\sigma \rangle \\ &= 2B |x_p|^2 |a_p|^2 \zeta_{6p}, \end{aligned} \quad (6.31)$$

where we have used the pure precession hypothesis, Eq. 4.7, to evaluate the atomic matrix elements.

The FCFs, $|\langle \nu'' | \nu' \rangle|^2$, can be reliably estimated using the measured value of the stretching vibrational frequency ($\omega_{\nu_1} = 529.3269 \text{ cm}^{-1}$), the measured bond lengths ($r_e(\tilde{X}^2\Sigma^+(0, 0, 0)) = 2.0397 \text{ \AA}$ and $r_e(\tilde{A}^2\Pi_{1/2}(0, 0, 0)) = 2.0062 \text{ \AA}$), and the harmonic approximation. The bending and O-H stretching modes can be neglected as the FCFs between them and the stretching (or (0,0,0)) states are negligible. In the harmonic approximation, the energies of the $\tilde{A}^2\Pi_{1/2}$ state are $E_{\Pi, \nu'} = T_0(\tilde{A}^2\Pi_{1/2}(0, 0, 0, \nu_1)) + \omega_{\nu_1} \nu_1$. Using the values of $|x_p|^2$, $|a_p|^2$, ζ_{6p} , and ω_{nu_1} indicated above, the measured value of $T_0(\tilde{A}^2\Pi_{1/2}(0, 0, 0))$ [116], the values of B and $T_0 = E_{\Sigma, \nu''}$ given in Table 6.1, and the FCFs calculated in the harmonic approximation with Eq. 6.28 gives $\gamma_{\nu_1=1}(\tilde{A}^2\Pi_{1/2}) = 0.02737 \text{ cm}^{-1}$ and $\gamma_{\nu_1=3}(\tilde{A}^2\Pi_{1/2}) = 0.02686 \text{ cm}^{-1}$.

These positive contributions from the $\tilde{A}^2\Pi_{1/2}$ state cannot account for the observed negative values of γ nor would adding in additional $^2\Pi$ states as those contributions would be positive as well. As was discussed in Section 4.3, the negative values of γ in the $\tilde{X}^2\Sigma^+$ state are most likely the result of perturbing states derived from a $\text{Yb}^+ [Xe]4f^{13}6s\sigma^2$ electronic configuration. These states have negative spin orbit parameters (e.g., $\zeta_{4f} < 0$ for the $^2F_{7/2}^0$ and $^2F_{5/2}^0$ states of the Yb^+ ion [126]), which will result in negative contributions to γ . Using the above estimates and assuming that only the $\tilde{A}^2\Pi_{1/2}$ state and $4f^{13}6s\sigma^2$ states contribute to γ gives; $\gamma_{\nu_1=0}(4f^{13}6s\sigma^2) = -0.03032 \text{ cm}^{-1}$, $\gamma_{\nu_1=1}(4f^{13}6s\sigma^2) = -0.03106 \text{ cm}^{-1}$, and $\gamma_{\nu_1=3}(4f^{13}6s\sigma^2) = -0.03261 \text{ cm}^{-1}$, where $\gamma_{\nu_1}(4f^{13}6s\sigma^2)$ indicates the sum of the contributions to γ_{ν_1} from all electronic states derived from the $4f^{13}6s\sigma^2$ Yb^+ atomic electronic configuration.

The three gamma values presented in Table 6.1 indicate that the vibrational dependence of γ in the $\tilde{X}^2\Sigma^+$ state is linear with respect to the stretching vibration, ν_1 , with a slope of $\Delta\gamma/\Delta\nu_1 \sim -0.001 \text{ cm}^{-1}$. Additionally, the values of γ increase in magnitude with increased stretching vibration. This is in contrast to the vibrational dependence of the estimated $\tilde{A}^2\Pi_{1/2}$ state contributions to γ , which decrease in magnitude with increasing stretching vibration at a linear rate which has a slope that is about five times smaller than the observed rate of change of the γ values. This further indicates that the determined values of γ in the $\tilde{X}^2\Sigma^+$ state can not be accounted for by interactions solely with the $\tilde{A}^2\Pi_{1/2}$ state and other excited electronic states must be involved.

In addition to determining the parameters for the $\tilde{X}^2\Sigma^+(3, 0, 0)$ state, the combined fit of the $\tilde{A}^2\Pi_{1/2}(1, 0, 0) - \tilde{X}^2\Sigma^+(3, 0, 0)$ and $\tilde{A}^2\Pi_{1/2}(1, 0, 0) - \tilde{X}^2\Sigma^+(0, 0, 0)$ data sets allowed a more accurate determination of the parameters of the $\tilde{A}^2\Pi_{1/2}(1, 0, 0)$ state. The values of the origin, T_0 , rotational constant, B , and Λ -doubling centrifugal distortion parameter, $(p + 2q)_D$, agree with the previously measured values [116] and are more precisely determined, with the estimated errors a factor of 2/3 to 3 smaller. The determined value of the Λ -doubling parameter, $p + 2q$, not only agrees with the previously determined value but is an order of magnitude more precise.

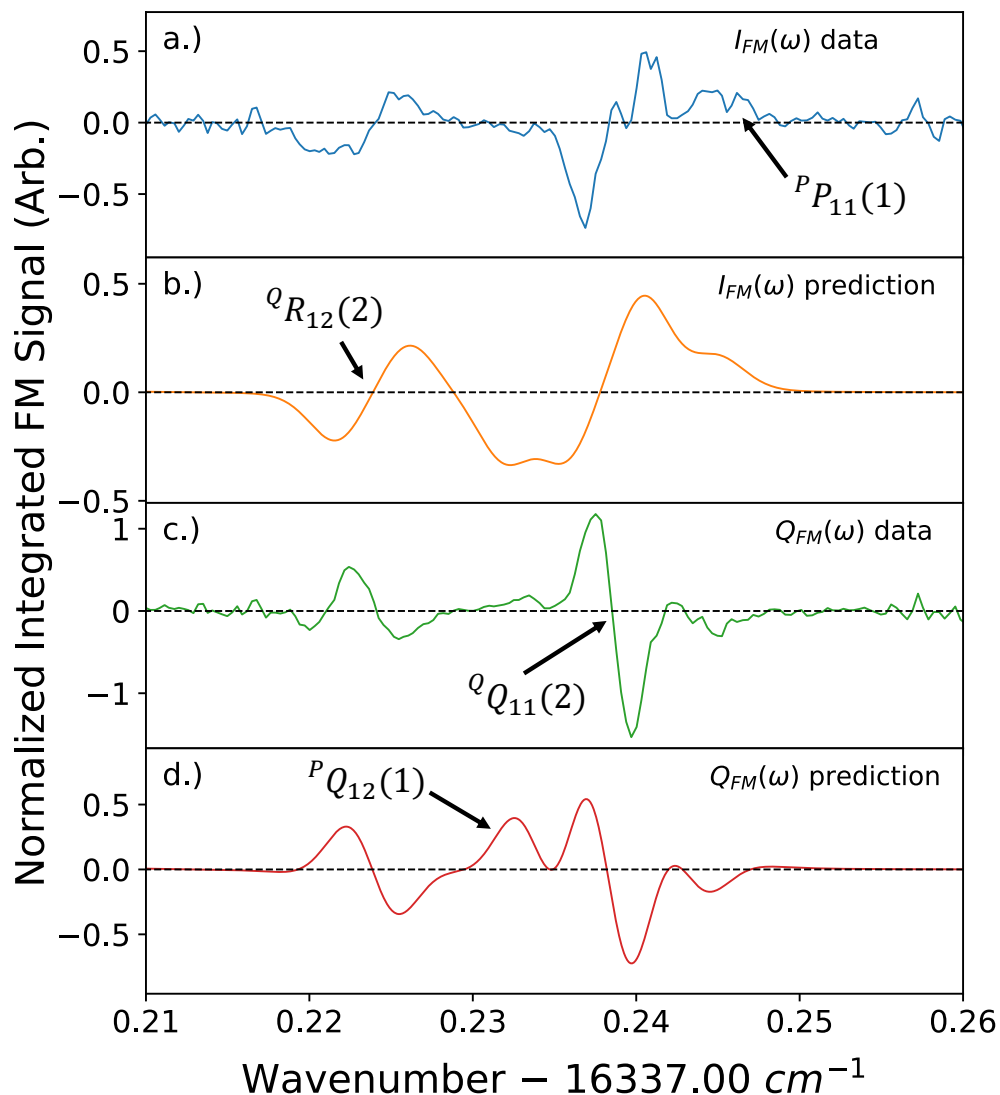


Figure 6.12: Measured and predicted FM spectrum of the ${}^Q R_{12}(2)$, ${}^P Q_{12}(1)$, ${}^Q Q_{11}(2)$ and ${}^P P_{11}(1)$ transitions of the $\tilde{A}^2\Pi_{1/2}(1, 0, 0) - \tilde{X}^2\Sigma^+(3, 0, 0)$ band of ${}^{174}\text{YbOH}$. **a.)** The measured in-phase FM spectrum, $I_{FM}(\omega)$. **b.)** The predicted in-phase FM spectrum. **c.)** The measured in-quadrature FM spectrum, $Q_{FM}(\omega)$. **d.)** The predicted in-quadrature FM spectrum. Predictions were made using optimized parameters from Table 6.1, a Gaussian FWHM linewidth of 108 MHz, a phase angle of 5.90 radians, and a temperature of 5 K. Each transition is indicated in a different plot for clarity.

6.6 FM spectroscopy of the [17.68] and [17.64] bands of $^{174}\text{YbOH}$

Dispersed LIF (DLIF) measurements of YbOH identified several bands in the region just to the blue of the the origin band. Of these bands, two are of particular interest regarding state preparation and readout of the $\tilde{X}^2\Sigma^+(0, 1, 0)$ science state. The first band is at at 17680 cm^{-1} , denoted [17.68], and the second at 17640 cm^{-1} , denoted [17.64] [135]. The measurements performed in Ref. [135] indicate that the [17.68] and [17.64] bands both originate from the ground $\tilde{X}^2\Sigma^+(0, 0, 0)$ state and terminate at excited states residing at 17680 cm^{-1} and 17640 cm^{-1} respectively. The DLIF study also measured the branching ratios of these excited states. The state at 17680 cm^{-1} was measured to have a branching ratio of 54.1% to the $\tilde{X}^2\Sigma^+(0, 0, 0)$ ground state and a branching ratio of 21.8% to the $\tilde{X}^2\Sigma^+(0, 1, 0)$ science state. The state at 17640 cm^{-1} was measured to have a branching ratio of 8.4% to the $\tilde{X}^2\Sigma^+(0, 0, 0)$ ground state and a branching ratio of 73.1% to the $\tilde{X}^2\Sigma^+(0, 1, 0)$ science state [135]. These branching ratio measurements indicate that both these states have strong bending character¹² and are coupled to both the ground and science states. Therefore, these states could prove useful for state preparation and readout, especially as optical pumping pathways for initial population of the $\tilde{X}^2\Sigma^+(0, 1, 0)$ science state. Finally, since these states are strongly coupled to the $\tilde{X}^2\Sigma^+(0, 1, 0)$ state, characterization of these excited states may aid in the spectroscopy of the $\tilde{X}^2\Sigma^+(0, 1, 0)$ science state.

Experiment

Since the [17.68] and [17.64] bands are weak compared to the origin band of YbOH, ~ 100 times weaker, in-cell FM absorption spectroscopy was used to measure the spectrum of these bands. The experimental FM setup is nearly the same as that used for the FM absorption spectroscopy of the $\tilde{A}^2\Pi_{1/2}(1, 0, 0) - \tilde{X}^2\Sigma^+(3, 0, 0)$ band, Section 6.5. The same buffer gas cell configuration as that described in Section 6.5 was used. Just as before, molecules were produced via ablation of a pressed stoichiometric Yb + Yb(OH)₃ + PEG target with a pulsed Nd:YAG laser (532 nm, $\sim 30\text{-}40\text{ mJ/pulse}$, $\sim 8.74\text{ Hz}$). Again, laser-enhanced chemical reactions were driven with the same enhancement laser ($\sim 3\text{ mm}$ in diameter, $\sim 300\text{ mW}$) which is fixed to the $^3P_1 - ^1S_0$ ^{174}Yb transition [137]. In the absence of the enhancement light, no FM signals were present and, therefore, the FM signals observed with the enhancement light present were due to only the $^{174}\text{YbOH}$ isotopologue.

¹²The initial theory is that these states were some mixture of the $\tilde{A}^2\Pi_{1/2}(0, 1, 0)$ state and a perturbing state derived from the $4f^{13}6s^2\text{ Yb}^+$ electronic configuration.

FM spectroscopy was performed using the same CW laser described in Section 6.4 and 6.5 with $\sim 100 \mu\text{W}$ and $\sim 110 \mu\text{W}$ of power for the [17.68] and [17.64] bands respectively. The laser was continuously scanned, and the signal from every consecutive 7 shots were averaged resulting in ~ 10 MHz steps between data points. The relative (and absolute) frequency between data points was monitored with a High Finesse wavemeter (WS7-30 VIS/Standard model). For the [17.68] data the phase shifter voltage was set to maximize (minimize) the in-phase (in-quadrature) FM signal, while for the [17.64] data the phase shifter voltage was set to split the FM signal evenly between the in-phase and in-quadrature channels. A portion of the FM absorption beam was picked off after passing through the buffer gas cell and directed into a DC photodiode to allow the simultaneous recording of both the FM and DC absorption data. As before, a normalization probe fixed to the ${}^R R_{11}(0)$ line of the $\tilde{A}^2\Pi_{1/2}(0,0,0) - \tilde{X}^2\Sigma^+(0,0,0)$ band was used to monitor shot-to-shot fluctuations in molecular production. The spectrum of both bands was co-recorded with the subdoppler saturated absorption spectrum of I_2 .

Measurements of the observed transitions frequencies of the [17.68] and [17.64] bands were made by measuring the frequencies of the zero crossings of the in-phase FM lineshapes¹³. The error in the zero-crossing measurements was limited by the step size between the data points to ~ 10 MHz. In this case, the zero crossing measurements were made using the High Finesse wavemeter as the absolute and relative frequency reference. The relative frequency between data points provided by the High Finesse wavemeter is accurate. For other scenarios, absolute frequency calibration with the co-recorded I_2 data results in the correction of the absolute frequency measured with the wavemeter by accounting for a general offset in frequency of -12 ± 3 MHz. Since the absolute frequency recorded by the High Finesse wavemeter was used for the transition frequency measurements, each measurement has an absolute frequency error of ~ 12 MHz. However, since this error is common and the same for all measured transition frequencies, measured spacings between transition frequencies, such as those used for combination differences, are accurate and only limited by the error in the zero-crossing measurements themselves. From zero-crossing measurements a total of 65 and 62 transition frequencies were measured for the [17.68] and [17.64] bands respectively. The measured transition frequencies are listed in Table A.6 and A.7 in Appendix A.

¹³The transition frequencies measured via zero-crossing measurements are consistent with the transition frequencies measured via simultaneous fitting of the in-phase and in-quadrature FM data to the lineshape model.

FM spectroscopy of the [17.68] band

The measured in-phase FM spectrum of the [17.68] band is presented in Fig. 6.13. When examining the spectrum it is clear that the band is split into two distinct parts, the red half and blue half, separated by $\sim 1 \text{ cm}^{-1}$. A higher-resolution view of the red half and blue half of the [17.68] spectrum are presented in Fig. 6.13 as well. This large spacing resembles the spectrum of a ${}^2\Sigma - {}^2\Sigma$ transitions which would have separated *P* and *R* branches and no *Q* branch. Spectra for ${}^2\Sigma - {}^2\Sigma^+$ transitions¹⁴ were simulated and these indicated that there should be a transition originating from the $N = 0$ level of the ground state in the empty region of the spectrum, which was not observed. Another plausible explanation for the gap in the spectrum is that the red and blue halves of the spectrum result from transitions to two different Renner-Teller components of an excited bending state. Another plausible explanation for the observed spectral pattern is that the red half of the observed spectrum is primarily comprised of the $\Delta J = -1, 0$ *P* and *Q* branches with a red degraded bandhead and the blue half of the spectrum is comprised of the $\Delta J = 0, 1$ *Q* and *R* branches.

[17.68] and $\tilde{X}^2\Sigma^+(0, 0, 0)$ combination differences

In Ref. [135], the [17.68] band was assigned to a transition originating from the $\tilde{X}^2\Sigma^+(0, 0, 0)$ state and terminating in an excited vibronic state at 17680 cm^{-1} . If this assignment is correct then combination differences with the energy levels of the $\tilde{X}^2\Sigma^+(0, 0, 0)$ state should allow the measured transitions to be assigned. The parameters of the $\tilde{X}^2\Sigma^+(0, 0, 0)$ state are well determined (Ch. 4 and [93]) and combination differences between the calculated ground state energy levels and measured [17.68] transition frequencies were determined¹⁵. A total of 23 combination differences were found. Almost all of the combination differences were matches of the spin rotation splittings in the ground state to line splittings in the [17.68] spectrum. If the [17.68] band does originate from the $\tilde{X}^2\Sigma^+(0, 0, 0)$ state, then each of these combination differences provides an assignment for the ground state from which each transition originates.

The [17.68] spectrum with the rotational level of the $\tilde{X}^2\Sigma^+(0, 0, 0)$ state from which the spin rotation splitting matches the [17.68] line spacing is presented in Fig. 6.14.

¹⁴In these simulations, the ground state parameters were fixed to the measured microwave parameters of the $\tilde{X}^2\Sigma^+(0, 0, 0)$ state and the parameters of the excited state were varied.

¹⁵A combination difference in this case is when a splitting between two measured transition frequencies matches an energy splitting between two levels in the $\tilde{X}^2\Sigma^+(0, 0, 0)$ state. A combination difference hit indicates that the two transitions originate from the pair of $\tilde{X}^2\Sigma^+(0, 0, 0)$ levels and terminate in the same excited state.

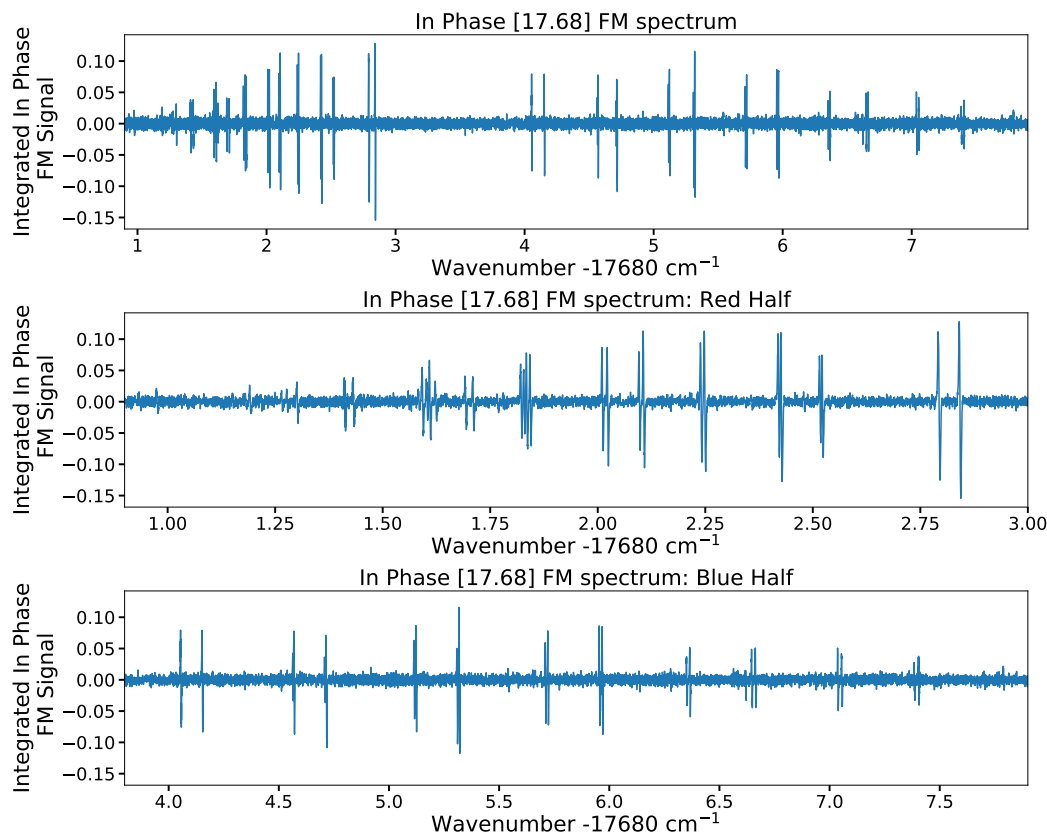


Figure 6.13: In-phase FM spectrum of the [17.68] band of $^{174}\text{YbOH}$. The full recorded spectrum is shown in the top panel. Zoomed-in view of the red half and blue half of the spectrum are shown in the middle and bottom panels respectively.

There is a clear pattern in both the red half and blue half of the spectrum with the combination difference matches increasing in ground state rotational level going to the red and to the blue in the red half and blue half of the spectrum respectively. Even though there are clear patterns in the combination differences, there are multiple anomalies as well. First, there were only a few combination differences involving spacings between different rotational levels in the ground state. Second, there are many strong pairs of lines that were not involved combination difference matches, as seen in Fig. 6.14. Lastly, there were no combination differences matches involving the $N = 0$ and $N = 1$ levels of the $\tilde{X}^2\Sigma^+(0, 0, 0)$ state.

Depletion spectroscopy of the [17.68] band

Due to the anomalies in the combination differences between the [17.68] spectrum and the $\tilde{X}^2\Sigma^+(0, 0, 0)$ state energy levels, the ground state assignments made from the spin rotation splitting matches, such as those indicated in Fig. 6.14, are in question.

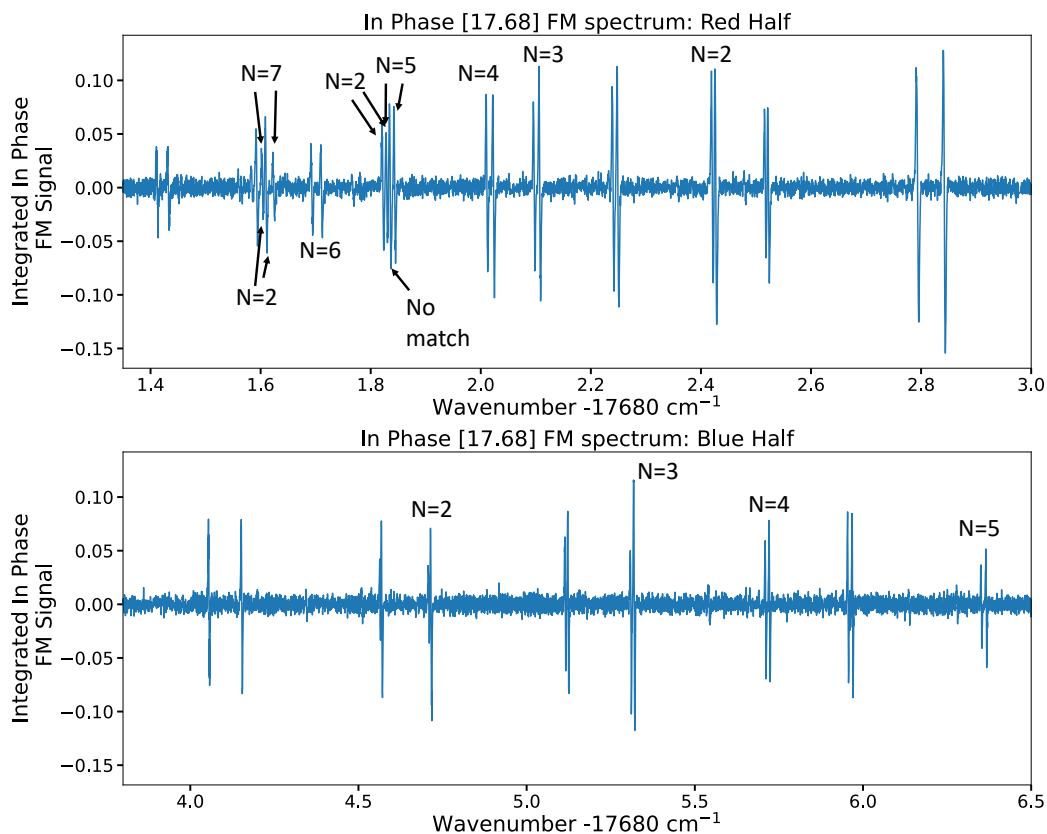


Figure 6.14: Combination differences matches of line splittings from the [17.68] band and the spin-rotation splittings in the $\tilde{X}^2\Sigma^+(0,0,0)$ state. The rotational level, N , of the $\tilde{X}^2\Sigma^+(0,0,0)$ spin-rotation splitting which matches the [17.68] line splittings are indicated. The top panel shows the red half of the [17.68] spectrum while the bottom panel shows the blue half of the [17.68] spectrum.

To confirm that the [17.68] band originates from the $\tilde{X}^2\Sigma^+(0,0,0)$ ground state and to confirm the ground state assignments from the combination differences, depletion spectroscopy of the [17.68] was performed. A diagram of the experimental depletion spectroscopy setup is shown in Fig. 6.15. The depletion spectroscopy was conducted in the beam extension region of the CBGB source, see Section 3.2, and works in the following manner. First, the extracted molecular beam is exposed to a depletion laser (~ 300 mW, elliptical shaped and multi-passed ≥ 10 times) which is resonant with a transition in the $\tilde{A}^2\Pi_{1/2}(0,0,0) - \tilde{X}^2\Sigma^+(0,0,0)$ band that originates from the $|N, J\rangle$ rotational/spin-rotational level of the $\tilde{X}^2\Sigma^+(0,0,0)$ state. The depletion laser is shuttered on and off for consecutive molecular pulses using a mechanical shutter so that the depletion laser is applied for every other molecular beam pulse. When the depletion laser is unblocked, it depletes the molecular population in the

$|N, J\rangle$ level of the $\tilde{X}^2\Sigma^+(0, 0, 0)$ state. Downstream from the depletion region, the molecular beam is exposed to a probe laser ($\sim 700 \mu\text{W}$) resonant with a transition in the [17.68] band and the resulting LIF is collected and detected by a PMT. If the [17.68] transition probed by the probe laser originates from the same $|N, J\rangle$ level of the $\tilde{X}^2\Sigma^+(0, 0, 0)$ state depleted by the depletion laser, there will be a reduction in the detected probe LIF when the depletion laser is unblocked as compared to when the depletion laser is blocked. The depletion spectroscopy setup was calibrated with the $\tilde{A}^2\Pi_{1/2}(1, 0, 0) - \tilde{X}^2\Sigma^+(0, 0, 0)$ band where depletion of the measured LIF was clearly visible. The calibration also indicated that at the depletion laser power used, the transitions were power broadened to a level where both spin-rotation components of the N rotational level, $|N, J = N + S\rangle$ and $|N, J = N - S\rangle$, were depleted.

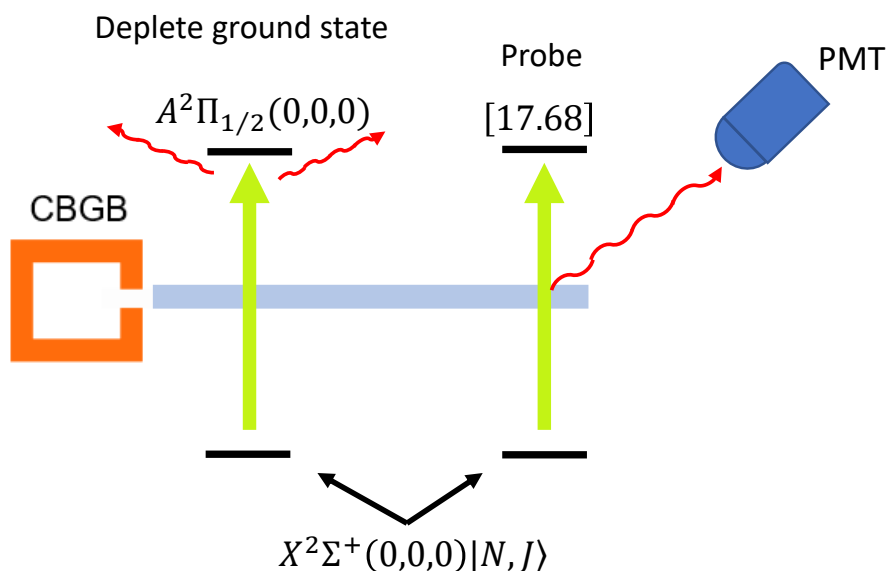


Figure 6.15: Depletion spectroscopy setup. A CBGB of YbOH is produced in the CBGB source (Ch. 3). The extracted molecular beam first passes through a depletion laser which depletes the population of molecules in the $|N, J\rangle$ level of the $\tilde{X}^2\Sigma^+(0, 0, 0)$ state. The depletion laser is turned on and off with a mechanical shutter for alternating molecular beam pulses. Following the depletion, the molecular beam passes through a probe beam, a laser beam resonant with a transition in [17.68] band. If the transition in the [17.68] band originates from the $|N, J\rangle$ level of the $\tilde{X}^2\Sigma^+(0, 0, 0)$ state, the fluorescence from the probe will be reduced when the depletion laser is on.

The spin-rotation combination difference matches with the $\tilde{X}^2\Sigma^+(0, 0, 0)$ state provide ground state assignments for the [17.68] transitions involved in the combination

difference match. Therefore, we used these assignments as a guide for which $|N, J\rangle$ level of the $\tilde{X}^2\Sigma^+(0, 0, 0)$ state to deplete and which [17.68] transitions to probe. A summary of the [17.68] depletion measurements is presented in Table 6.2, including the [17.68] transitions probed, the ground state assignment from the combination differences, which line of the $\tilde{A}^2\Pi_{1/2}(0, 0, 0) - \tilde{X}^2\Sigma^+(0, 0, 0)$ band was used for depletion, and if depletion was seen. No depletion was seen for any of the [17.68] transitions probed, indicating that the combination differences involving those transitions are just happenstance.

Table 6.2: Summary of [17.68] depletion measurements.

[17.68] Line (cm^{-1})	Ground State Assignment (N'', J'') ^a	Depletion Line ^b	Depletion?
17682.4207	$N'' = 2, J'' = 1.5$	$Q_{R_{12}(2)}, Q_{Q_{11}(2)}$	No
17684.7094	$N'' = 2, J'' = 1.5$	$Q_{R_{12}(2)}$	No
17684.7155	$N'' = 2, J'' = 2.5$	$Q_{R_{12}(2)}, Q_{Q_{11}(2)}$	No
17682.1071	$N'' = 3, J'' = 3.5$	$Q_{R_{12}(3)}, Q_{Q_{11}(3)}$	No
17682.0972	$N'' = 3, J'' = 2.5$	$Q_{R_{12}(3)}, Q_{Q_{11}(3)}$	No
17685.3197	$N'' = 3, J'' = 3.5$	$Q_{R_{12}(3)}, Q_{Q_{11}(3)}$	No

^a Ground state assignments were made using the combination differences with the $\tilde{X}^2\Sigma^+(0, 0, 0)$ state.

^b The $\tilde{A}^2\Pi_{1/2}(0, 0, 0) - \tilde{X}^2\Sigma^+(0, 0, 0)$ transitions were used for depletion. Line positions from Ref. [116].

Discussion of [17.68] measurements

The absence of depletion confirms that the combination difference matches involving the $N = 2$ and $N = 3$ spin rotation splittings in the $\tilde{X}^2\Sigma^+(0, 0, 0)$ state are incorrect. Therefore, there are no combination difference matches with any of the $N = 0 - 3$ levels of the $\tilde{X}^2\Sigma^+(0, 0, 0)$ state in the [17.68] spectrum. This also puts the other spin-rotation splitting matches into question. The lack of depletion, incorrect combination differences, and a lack of combination differences involving splittings between different rotational levels in the $\tilde{X}^2\Sigma^+(0, 0, 0)$ state, provide strong evidence

that the [17.68] band does not originate from the $\tilde{X}^2\Sigma^+(0, 0, 0)$ state as previously assigned [135]. Therefore, the combination difference matches found between the [17.68] splittings and the $\tilde{X}^2\Sigma^+(0, 0, 0)$ state energy levels are just due to happenstance.

The group of Michael Heaven confirmed that the [17.68] band does indeed belong to YbOH, as opposed to a contaminant such as YbO or YbOCH₃, with resonant enhanced multi-photon ionization (REMPI) spectroscopy¹⁶. Therefore, the [17.68] band likely originates from an excited state in YbOH, most likely an excited vibrational level of the $\tilde{X}^2\Sigma^+$ state. This would explain the lack of combination differences with rotational splittings in the $\tilde{X}^2\Sigma^+(0, 0, 0)$ state as higher vibrational states will have different rotational constants. Additionally, all of the accidental spin rotation splitting matches indicate that the ground state of the [17.68] band should have a spin-rotation splitting (or other splitting) similar to that of the $\tilde{X}^2\Sigma^+(0, 0, 0)$ state. The spin-rotation splittings of the $\tilde{X}^2\Sigma^+(0, 1, 0)$ state are expected to be similar to that of the $\tilde{X}^2\Sigma^+(0, 0, 0)$ state. Additionally, the bending angular momentum in the $\tilde{X}^2\Sigma^+(0, 1, 0)$ state results in a reduced spin-rotation splitting in the $N = 1$ state (there is no $N = 0$ state), see Section 2.7. The spin-rotation splitting for higher N asymptotically approaches the linear case with increasing N . This would account for the lack of accidental $N = 1$ and $N = 0$ spin-rotation matches in the combination differences. All this points to the [17.68] band originating from a $\tilde{X}^2\Sigma^+(0, 1, 0)$ ground state.

The experimental measurements of the [17.68] band presented here suggest that the [17.68] band is actually a transition from the $\tilde{X}^2\Sigma^+(0, 1, 0)$ state to an excited vibronic state at $\approx 18000 \text{ cm}^{-1}$ (here called the [18.00] state), $T_0(\tilde{X}^2\Sigma^+(0, 1, 0)) = 319 \text{ cm}^{-1}$ [135]. This tentative re-assignment¹⁷ could be consistent with the previous DLIF measurements as the decay from [18.00] $\rightarrow \tilde{X}^2\Sigma^+(0, 0, 0)$ would be overlapped with the decay of the strong $^3P_1 - ^1S_0$ atomic Yb transition at $17992.007 \text{ cm}^{-1}$ which was excited by the amplified stimulated emission of the pulsed dye laser [135]. Experiments aimed at confirming this assignment by measuring DLIF to the blue of the excitation of the [17.68] band at 17680 cm^{-1} with a cw laser are currently underway.

¹⁶Private communication from Michel Heaven.

¹⁷Arian Jadbabaie played a significant role in determining this assignment.

FM spectroscopy of the [17.64] band

The in-phase FM absorption spectrum of the [17.64] band of YbOH is presented in Fig. 6.16. The spectral patterns in the [17.64] band are much different from that of the [17.68] band. Most importantly, there is no “gap” in the spectrum. There seem to be three distinct sections in the [17.64] spectrum: a section to the red (second panel from top in Fig. 6.16) which is comprised of the strongest and most congested lines which resemble a red degraded bandhead; a middle section (third panel from top in Fig. 6.16) which is comprised of four weak doublets; and a section to the blue (bottom panel in Fig. 6.16). The blue section of the spectrum has two sets of five lines which seem to be comprised of a pair of doubles followed by a single line. The lines in the blue region of the spectrum are also larger in intensity than those in the middle section yet smaller than the large lines in the red section of the spectrum. There also is a weak line to the red of the red section of the spectrum that may be one on the low J lines of a P branch.

Just as with the [17.68] state, combination differences between the [17.64] line spacings and the energy levels of the $\tilde{X}^2\Sigma(0, 0, 0)$ state were determined. However, in contrast to the [17.68] spectrum, several [17.64] line splittings matched rotational splittings in the $\tilde{X}^2\Sigma(0, 0, 0)$ state. There were several spin-rotation splitting matches with the [17.64] line splittings as well, though many of them contradicted each other. Additionally, there are several strong and several weak lines which had no combination difference matches. Ultimately, no definitive assignments were made using the combination differences.

Depletion spectroscopy was performed on one line the the [17.64] spectrum, the line at $17639.1319\text{ cm}^{-1}$. The combination differences assign the ground state of this line to the $|N = 2, J = 2.5\rangle$ level of the $\tilde{X}^2\Sigma(0, 0, 0)$ state which was depleted by driving the $^oQ_{11}(2)$ line of the $\tilde{A}^2\Pi_{1/2}(0, 0, 0) - \tilde{X}^2\Sigma^+(0, 0, 0)$ transition. No depletion was observed. As with the [17.68] band we believe that this lack of depletion and assignments from the combination differences indicate that the [17.64] band may also originate from the $\tilde{X}^2\Sigma(0, 1, 0)$ state. However, this claim is slightly more speculative than that made about the [17.68] state as a depletion measurement of only one line in the [17.64] band was taken.

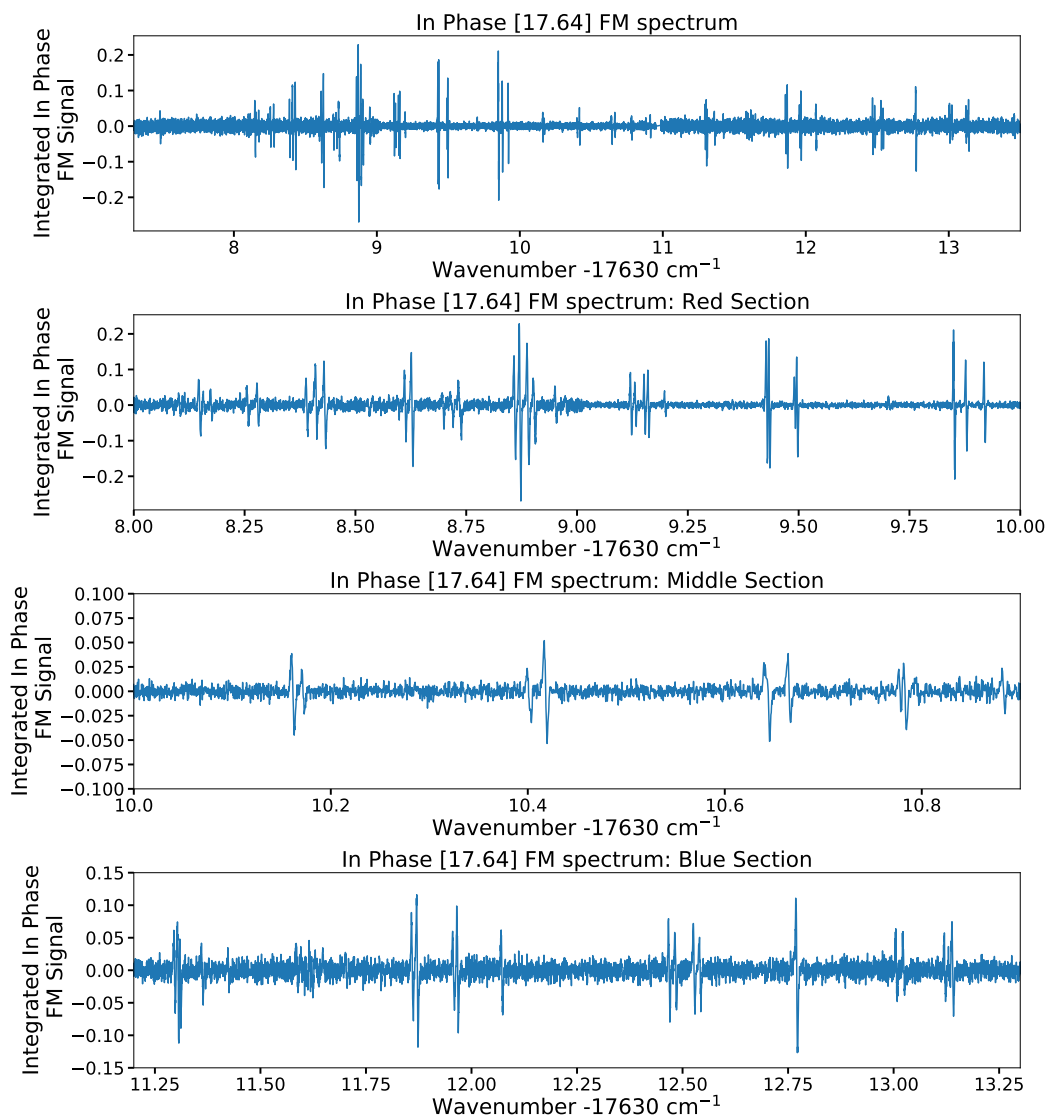


Figure 6.16: In-phase FM absorption spectrum of the [17.64] band. In addition to a view of the entire [17.64] spectrum (top panel), a closer view of the red section of the spectrum (panel second from top), the middle of the spectrum (panel second from bottom), and the blue section of the spectrum (bottom panel) are also shown.

Chapter 7

Relevance of This Work to EDM Searches with YbOH

This dissertation describes the cryogenic buffer gas production and high-resolution spectroscopy of ytterbium monohydroxide, YbOH, with the ultimate aim of developing next generation CP-violation experiments with cold polyatomic molecules. These experimental efforts are still a work in progress, and I will defer detailed discussions of these efforts to the future dissertations and manuscripts of my colleagues, who will perform this work. However, to provide a larger context for the work described here, I will conclude by providing a brief overview of the current status of these experiments as well as some “lessons learned” which may be of benefit to future students.

The NMQM apparatus

The 4 K CBGB source described in this dissertation will serve as the molecular source for the NMQM experiment, providing cold, high-intensity beams of YbOH molecules. At the time of writing, initial spin precession tests on the ground state of YbOH have been performed in the beam extension region of the 4 K CBGB source¹. Additionally, the first-generation NMQM science chamber, and associated optical and electromagnetic field components, are under construction. This science chamber will be integrated with the CBGB source, replacing or extending the current beam extension. The selection of non-magnetic vacuum components has been completed² and three-layer magnetic shields³ have been fabricated and are under assembly. The shields will soon be integrated with the 4 K CBGB source and NMQM science chamber.

Ongoing and future spectroscopy

As described in this dissertation, many of the prerequisite spectroscopic studies of YbOH have already been completed. Characterization of the $\tilde{X}^2\Sigma^+(0, 1, 0)$ science state, which is critical for future eEDM and NMQM measurements with YbOH, is currently underway. At the time of writing, this state has been observed in the 4 K CBGB source by driving the extremely weak, symmetry-forbidden $\tilde{A}^2\Pi_{1/2}(0, 0, 0) -$

¹These tests were carried out by Arian Jadbabaie and Yuiki Takahashi.

²The selections were made in collaboration with Arian Jadbabaie and Chandler Conn.

³The magnetic shields were designed by Chandler Conn.

$\tilde{X}^2\Sigma^+(0, 1, 0)$ transition of the $^{174}\text{YbOH}$ isotopologue and recording the off-diagonal fluorescence at high resolution. From this spectrum, initial estimates of the molecular parameters of the $\tilde{X}^2\Sigma^+(0, 1, 0)$ state have been obtained. Additionally, the stark spectroscopy of selected lines of the $\tilde{A}^2\Pi_{1/2}(0, 0, 0) - \tilde{X}^2\Sigma^+(0, 1, 0)$ transition have been performed.

Our ability to observe the extremely weak $\tilde{A}^2\Pi_{1/2}(0, 0, 0) - \tilde{X}^2\Sigma^+(0, 1, 0)$ band, which is ~ 1000 times weaker than the $\tilde{A}^2\Pi_{1/2}(0, 0, 0) - \tilde{X}^2\Sigma^+(0, 0, 0)$ origin band, is enabled by a series of technical features of the 4 K CBGB source. These features include: 1.) cryogenic buffer gas production of cold, bright YbOH beams, 2.) isotopologue-resolved laser enhancement of YbOH production including increased production of excited, athermal vibrational populations, 3.) blackening and light control in the beam extension region, 4.) increased cryogenic and mechanical pumping to prevent beam attenuation, 5.) optimization of fluorescence light collection and filtering. The high-sensitivity fluorescence, FM absorption (Ch. 6), and novel technique utilizing laser enhancement for isotopologue resolution (Ch. 5) have been essential for the measurement and interpretation of the weak, congested, overlapped, and/or perturbed bands of YbOH, such as the $\tilde{A}^2\Pi_{1/2}(0, 0, 0) - \tilde{X}^2\Sigma^+(0, 1, 0)$, $\tilde{A}^2\Pi_{1/2}(1, 0, 0) - \tilde{X}^2\Sigma^+(3, 0, 0)$, [17.68], and [17.64] bands of $^{174}\text{YbOH}$ and the $\tilde{A}^2\Pi_{1/2}(0, 0, 0) - \tilde{X}^2\Sigma^+(0, 0, 0)$ bands of $^{171,173}\text{YbOH}$. These capabilities and techniques will become even more critical, if not essential, for the investigation of the bending modes and perturbed excited states of the $^{173}\text{YbOH}$ isotopologue, the isotopologue with which the NMQM measurement will be performed. The success of the 4 K CBGB source as a high-sensitivity, high-resolution spectrometer will hopefully serve as an example and a guide for future cold, gas-phase, high-resolution spectrometers.

State preparation, readout, and spin precession

In order to perform an eEDM or NMQM experiment, transitions which can be utilized for state preparation and readout must also be characterized. To be utilized for state preparation or readout, a transition must originate from the $\tilde{X}^2\Sigma^+(0, 1, 0)$ state. The [17.68] and [17.64] bands recorded in this work may be used for state preparation and readout. Though transition assignments and the molecular parameters of the states involved in these transitions were not determined here, this work provides extremely compelling evidence that these states do not originate from the $\tilde{X}^2\Sigma^+(0, 0, 0)$ state, as previously assigned. Instead we expect these transitions to originate from the $\tilde{X}^2\Sigma^+(0, 1, 0)$ state. Experiments to definitively determine

this are currently being designed. Additionally, if these transitions do originate from the $\tilde{X}^2\Sigma^+(0, 1, 0)$ state, then combination differences with the energy levels of the $\tilde{X}^2\Sigma^+(0, 1, 0)$ state will allow the assignment of the spectral features. Combination differences using the initial estimates of the molecular parameters of the $\tilde{X}^2\Sigma^+(0, 1, 0)$ state are promising, but tentative.

When designing state preparation and readout schemes, the energy levels of the molecular state must be accurately modeled in magnetic and electric fields. To achieve this, the molecular parameters of the state in question must be known to high precision. The parameters of the $\tilde{X}^2\Sigma(0, 0, 0)$ state of $^{174}\text{YbOH}$ were determined to high precision in Ch. 4 and used to design the state preparation and readout schemes in the initial spin precession tests mentioned above. The parameters of the $\tilde{X}^2\Sigma^+(0, 0, 0)$ and $\tilde{A}^2\Pi_{1/2}(0, 0, 0)$ states of $^{173}\text{YbOH}$ were determined at high resolution in Ch. 5. These parameters can be used to implement initial ground state spin precession tests with $^{173}\text{YbOH}$, as well as estimate the parameters of the $^{173}\text{YbOH}$ bending mode for prototyping and simulating NMQM state preparation and readout.

Laser cooling of YbOH

In order to achieve order of magnitude improvements in future eEDM sensitivity, both high flux and long coherence times will be needed. The PolyEDM collaboration aims to achieve this with the direct laser cooling and trapping of polyatomic molecules. One-dimensional laser cooling of YbOH [54] has been demonstrated by our PolyEDM collaborators in the Doyle group at Harvard. Three-dimensional optical trapping and sub-doppler cooling have been demonstrated for the lighter, isoelectronic, triatomic molecule CaOH [60]. Based on our collaborators' experience trapping CaOH, it is believed that $\sim 10,000$ photons need to be scattered to slow and trap YbOH. In the one-dimensional laser cooling of YbOH, the photon budget was ~ 500 , which was accomplished by driving the $\tilde{A}^2\Pi_{1/2}(0, 0, 0) - \tilde{X}^2\Sigma^+(0, 0, 0)$ transition, for which the PPMODR measurements of the $\tilde{X}^2\Sigma^+(0, 0, 0)$ state are detailed in Ch. 4, and repumping vibrational losses out of the $\tilde{X}^2\Sigma^+(1, 0, 0)$, $\tilde{X}^2\Sigma^+(2, 0, 0)$, and $\tilde{X}^2\Sigma^+(0, 2^0, 0)$ states. High resolution DLIF measurements of YbOH, in combination with quasi-diabatic ab initio vibronic calculations, [107] indicate that vibrational losses to the $\tilde{X}^2\Sigma^+(0, 1, 0)$, $\tilde{X}^2\Sigma^+(1, 1, 0)$, $\tilde{X}^2\Sigma^+(1, 2^0, 0)$, and $\tilde{X}^2\Sigma^+(3, 0, 0)$ states must be addressed in order to scatter $\sim 10,000$ photons. The FM spectroscopy of the $\tilde{A}^2\Pi_{1/2}(1, 0, 0) - \tilde{X}^2\Sigma^+(3, 0, 0)$ band, recorded here (Ch. 6), identified the repumping transitions for the $\tilde{X}^2\Sigma^+(3, 0, 0)$ state. This FM

study also demonstrated the utility of the FM technique for measuring repumping transitions. Additionally, this study confirmed that the laser-enhanced chemical reactions do indeed provide large populations of excited vibrational states on which spectroscopy can be performed. This FM technique and the chemical enhancement will allow the other repumping transitions to be identified quickly and efficiently. This technique is not exclusive to YbOH and can be utilized to identify repumping transitions for other molecules as well.

The negative spin rotation parameters of the $\tilde{X}^2\Sigma^+(0, 0, 0)$ and $\tilde{X}^2\Sigma^+(3, 0, 0)$ states determined in this work indicate the existence of perturbing states in YbOH derived from a $\text{Yb}^+ 4f^{13}6s\sigma^2$ electronic configuration. The isoelectronic molecule YbF contains states of this nature as well [122, 124, 158], and experiments have found that decays to these states become relevant at the 10^{-5} level [158]. Therefore, losses to low-lying perturbing states will most likely need to be addressed if YbOH is to be laser cooled and magneto-optically trapped. Though transitions from these states to other excited states of YbOH may be weak, implementing a multi-pass (~ 10 passes) FM absorption setup may provide the needed sensitivity to measure these transitions. Additionally, since the energies involved in the laser-enhanced chemical reactions are larger than the energies of these perturbing states, the chemical enhancement may naturally provide the needed population on which the spectroscopy can be performed.

Finally, while the first-generation NMQM experiment will be performed in a beam, future generations may benefit from the enhanced state preparation and readout efficiency and longer coherence times provided by photon cycling and laser cooling. The measurements of the $\tilde{A}^2\Pi_{1/2}(0, 0, 0) - \tilde{X}^2\Sigma^+(0, 0, 0)$ transitions of the odd isotopologues have enabled rotationally closed photon cycling transitions in $^{171}\text{YbOH}$ and $^{173}\text{YbOH}$ to be identified. At the time of writing, rotationally closed photon cycling in the $^{171}\text{YbOH}$ and $^{173}\text{YbOH}$ isotopologues has been accomplished⁴.

⁴The work implementing photon cycling in the odd isotopologues was carried out by Yi Zeng.

*Appendix A***Measured YbOH Transitions**

This appendix provides lists of all the YbOH transitions measured or used in this work.

A.1 Pure rotational spectra of the $\tilde{X}^2\Sigma^+(0, 0, 0)$ state

Table A.1: Rotational transitions in the $\tilde{X}^2\Sigma^+(0, 0, 0)$ state of YbOH measured with PPMODR spectroscopy. Also presented are the differences between the observed (Obs.) and calculated (Calc.) transition wavenumbers. The calculated wavenumbers were obtained using the optimized parameters from the fit to the observed transition wavenumbers.

N'', J'', F''	N', J', F'	Obs. (MHz) ^a	Calc. (MHZ)	Obs. – Calc. (MHz)
3, 7/2, 4	4, 9/2, 5	58745.1654	58745.1640	0.0014
3, 7/2, 3	4, 9/2, 4	58745.2594	58745.2642	-0.0048
3, 5/2, 3	4, 7/2, 4	58826.0166	58826.0104	0.0062
3, 5/2, 2	4, 7/2, 3	58826.1460	58826.1334	0.0126
3, 5/2, 3	4, 7/2, 3	58827.5935	58827.6040	-0.0105
4, 9/2, 5	5, 11/2, 5	73438.2470	73438.2575	-0.0105
4, 9/2, 5	5, 11/2, 6	73440.5890	73440.5464	0.0426
4, 9/2, 4	5, 11/2, 5	73440.5890	73440.6109	-0.0219
4, 7/2, 3	5, 9/2, 4	73521.3229	73521.3677	-0.0448
4, 7/2, 4	5, 9/2, 5	73521.3229	73521.2922	0.0307
5, 11/2, 6	6, 13/2, 7	88135.2297	88135.2115	0.0182
5, 11/2, 5	6, 13/2, 6	88135.2297	88135.2565	-0.0268
5, 9/2, 5	6, 11/2, 6	88215.8438	88215.8150	0.0288
5, 9/2, 4	6, 11/2, 5	88215.8438	88215.8662	-0.0224
6, 13/2, 7	7, 15/2, 8	102829.0317	102829.0140	0.0177
6, 13/2, 6	7, 15/2, 7	102829.0317	102829.0472	-0.0155
6, 11/2, 6	7, 13/2, 7	102909.4589	102909.4405	0.0184
6, 11/2, 5	7, 13/2, 6	102909.4589	102909.4776	-0.0187

^aAverage error of 10 kHz

This table was reproduced from [93].

A.2 $\tilde{A}^2\Pi_{1/2}(0,0,0) - \tilde{X}^2\Sigma^+(0,0,0)$ bands of $^{171,173}\text{YbOH}$

Table A.2: The transition wavenumbers and assignments for the $\tilde{A}^2\Pi_{1/2}(0,0,0) - \tilde{X}^2\Sigma^+(0,0,0)$ band of $^{173}\text{YbOH}$. Also presented are the differences between the observed (Obs.) and calculated (Calc.) transition wavenumbers. The calculated values were obtained using the optimized parameters of the fit. Here p indicates the parity of the molecular state. This table is reproduced from Ref. [129] with permission from AIP.

Lines	N'', G'', F'', p	J', F', p	Obs. (-17300 cm^{-1})	Obs.– Calc. (MHz)
$^oP_{12}$	2, 2, 4, +	0.5, 3, -	22.0363	-13
	2, 2, 2, +	0.5, 3, -	22.0504	-1
	2, 2, 3, +	0.5, 3, -	22.0566	-8
	2, 2, 2, +	0.5, 2, -	22.0771	29
	2, 2, 3, +	0.5, 2, -	22.0826	0
	3, 2, 5, -	1.5, 4, +	21.107	5
	3, 2, 4, -	1.5, 4, +	21.1258	-33
	3, 2, 4, -	1.5, 3, +	21.1303	-45
	3, 2, 3, -	1.5, 2, +	21.1408	-24
	3, 2, 2, -	1.5, 1, +	21.146	-28
	4, 2, 6, +	2.5, 5, -	20.1905	-24
	4, 2, 5, +	2.5, 4, -	20.2117	22
4, 2, 4, +	2.5, 3, -	20.2202	12	
$^oP_{13}$	2, 3, 2, +	0.5, 3, -	22.2251	-6

Continued on next page

Table A.2 – *Continued from previous page*

Lines	N'', G'', F'', p	J', F', p	Obs. (-17300 cm^{-1})	Obs. -Calc. (MHz)
	2, 3, 3, +	0.5, 3, -	22.2407	-7
	2, 3, 4, +	0.5, 3, -	22.2463	-14
	2, 3, 3, +	0.5, 2, -	22.2664	-8
	3, 3, 1, -	1.5, 2, +	21.298	-3
	3, 3, 2, -	1.5, 2, +	21.309	-10
	3, 3, 5, -	1.5, 4, +	21.3176	17
	3, 3, 4, -	1.5, 3, +	21.3223	32
	4, 3, 2, +	2.5, 2, -	20.39	-15
	4, 3, 3, +	2.5, 3, -	20.39	-33
	4, 3, 4, +	2.5, 4, -	20.3951	-9
	4, 3, 4, +	2.5, 3, -	20.402	-16
	4, 3, 3, +	2.5, 2, -	20.402	-9
	4, 3, 5, +	2.5, 4, -	20.402	-28
${}^P Q_{12} + {}^P P_{12}$	1, 2, 1, -	0.5, 2, +	23.4572	37
	1, 2, 3, -	0.5, 2, +	23.4654	35
	1, 2, 2, -	0.5, 3, +	23.4916	45
	2, 2, 1, +	1.5, 2, -	23.4572	9
	2, 2, 4, +	1.5, 4, -	23.4725	0
	2, 2, 3, +	1.5, 3, -	23.4783	58
	3, 2, 5, -	2.5, 5, +	23.4877	13

Continued on next page

Table A.2 – *Continued from previous page*

Lines	N'', G'', F'', p	J', F', p	Obs. (-17300 cm^{-1})	Obs. -Calc. (MHz)
	3, 2, 4, -	2.5, 4, +	23.4916	34
	4, 2, 4, +	3.5, 4, -	23.5181	42
	4, 2, 6, +	3.5, 6, -	23.5181	46
	4, 2, 5, +	3.5, 5, -	23.5212	28
	5, 2, 7, -	4.5, 7, +	23.5642	80
	5, 2, 5, -	4.5, 5, +	23.5642	46
	6, 2, 7, +	5.5, 7, -	23.6277	35
${}^P Q_{13} + {}^P P_{13}$	1, 3, 2, -	0.5, 3, +	23.6474	1
	1, 3, 3, -	0.5, 2, +	23.6762	21
	2, 3, 2, +	1.5, 1, -	23.6535	29
	2, 3, 3, +	1.5, 2, -	23.6633	56
	2, 3, 4, +	1.5, 2, -	23.6672	28
	3, 3, 2, -	1.5, 3, +	23.6535	-3
	3, 3, 3, -	2.5, 3, +	23.6701	21
	3, 3, 4, -	2.5, 2, +	23.6762	-4
	3, 3, 6, -	2.5, 3, +	23.6802	10
	3, 3, 5, -	2.5, 4, +	23.6802	-11
	4, 3, 5, +	3.5, 4, -	23.707	5
	4, 3, 6, +	3.5, 5, -	23.7114	9
	4, 3, 7, +	3.5, 6, -	23.7114	1

Continued on next page

Table A.2 – *Continued from previous page*

Lines	N'', G'', F'', p	J', F', p	Obs. (-17300 cm^{-1})	Obs. -Calc. (MHz)
	5, 3, 4, -	4.5, 3, +	23.7396	8
	5, 3, 5, -	4.5, 4, +	23.7465	-4
	5, 3, 6, -	4.5, 5, +	23.7534	12
	5, 3, 7, -	4.5, 6, +	23.758	17
	5, 3, 8, -	4.5, 7, +	23.758	-11
${}^{\circ}R_{12} + {}^{\circ}Q_{12}$	0, 2, 2, +	0.5, 3, -	23.5181	53
	1, 2, 3, -	1.5, 4, +	23.5642	9
	1, 2, 2, -	1.5, 3, +	23.5879	-35
	1, 2, 1, -	1.5, 1, +	23.5879	18
	2, 2, 4, +	2.5, 5, -	23.6277	-10
	2, 2, 3, +	2.5, 4, -	23.6474	-5
	2, 2, 2, +	2.5, 3, -	23.6474	-26
	3, 2, 5, -	3.5, 6, +	23.707	-36
	3, 2, 4, -	3.5, 5, +	23.7256	-6
	3, 2, 1, -	3.5, 1, +	23.7351	-22
	4, 2, 6, +	4.5, 7	23.802	-70
	4, 2, 2, +	4.5, 2	23.8362	-38
	5, 2, 7, -	5.5, 8, +	23.9167	11
	5, 2, 6, -	5.5, 7, +	23.9315	-40
	5, 2, 5, -	5.5, 6, +	23.9387	-24

Continued on next page

Table A.2 – *Continued from previous page*

Lines	N'', G'', F'', p	J', F', p	Obs. (-17300 cm^{-1})	Obs. -Calc. (MHz)
	5, 2, 4, -	5.5, 5, +	23.9387	-44
	5, 2, 3, -	5.5, 3, +	23.948	-16
	10, 2, 9, +	10.5, 9, -	24.7546	20
	10, 2, 8, +	10.5, 8, -	24.7546	-26
${}^oR_{13} + {}^oQ_{13}$	0, 3, 3, +	0.5, 2, -	23.7305	1
	1, 3, 4, -	1.5, 4, +	23.7534	14
	1, 3, 4, -	1.5, 3, +	23.758	6
	1, 3, 2, -	1.5, 1, +	23.7734	9
	1, 3, 3, -	1.5, 3, +	23.7802	4
	1, 3, 3, -	1.5, 2, +	23.7907	-6
	2, 3, 5, +	2.5, 5, -	23.8189	7
	2, 3, 4, +	2.5, 4, -	23.8362	53
	2, 3, 4, +	2.5, 3, -	23.844	-18
	2, 3, 3, +	2.5, 2, -	23.8502	7
	3, 3, 6, -	3.5, 6, +	23.9012	12
	3, 3, 5, -	3.5, 5, +	23.9167	23
	3, 3, 4, -	3.5, 4, +	23.9219	44
	4, 3, 7, +	4.5, 7, -	23.9985	-14
	4, 3, 2, +	4.5, 3, -	24.0052	4
	4, 3, 1, +	4.5, 2, -	24.0052	-4

Continued on next page

Table A.2 – *Continued from previous page*

Lines	N'', G'', F'', p	J', F', p	Obs. (-17300 cm^{-1})	Obs. -Calc. (MHz)
	4, 3, 6, +	4.5, 6, -	24.0111	-26
	4, 3, 5, +	4.5, 5, -	24.0168	-10
	4, 3, 4, +	4.5, 4, -	24.0168	-38
	5, 3, 8, -	5.5, 8, +	24.1125	-20
	5, 3, 2, -	5.5, 3, +	24.1192	47
	5, 3, 7, -	5.5, 7, +	24.1254	21
	5, 3, 6, -	5.5, 6, +	24.1305	20
	5, 3, 5, -	5.5, 5, +	24.1305	-22
	9, 3, 11, -	9.5, 11, +	24.7284	-3
	9, 3, 10, -	9.5, 10, +	24.7411	19
	9, 3, 9, -	9.5, 9, +	24.7411	-11
	9, 3, 8, -	9.5, 8, +	24.7411	11
${}^R R_{12}$	0, 2, 2, +	1.5, 3	,24.9356	-7
	0, 2, 2, +	1.5, 2	,24.9356	-36
	0, 2, 2, +	1.5, 1	,24.9432	-11
	1, 2, 1, -	2.5, 2, +	25.9187	3
	1, 2, 1, -	2.5, 1, +	25.9239	19
	1, 2, 3, -	2.5, 3, +	25.9239	1
	1, 2, 1, -	2.5, 0, +	25.9272	24
	1, 2, 3, -	2.5, 4, +	25.9272	-7

Continued on next page

Table A.2 – *Continued from previous page*

Lines	N'', G'', F'', p	J', F', p	Obs. (-17300 cm^{-1})	Obs. -Calc. (MHz)
	1, 2, 2, -	2.5, 3, +	25.9448	18
	2, 2, 0, +	3.5, 1, -	26.93	-7
	2, 2, 4, +	3.5, 5, -	26.9355	-36
	2, 2, 1, +	3.5, 2, -	26.9355	-18
	2, 2, 1, +	3.5, 1, -	26.9401	-5
	2, 2, 2, +	3.5, 3, -	26.9456	-16
	2, 2, 3, +	3.5, 4, -	26.9509	-17
${}^R R_{13}$	0, 3, 3, +	1.5, 3, -	25.1245	8
	0, 3, 3, +	1.5, 4, -	25.1398	-21
	1, 3, 4, -	2.5, 4, +	26.1179	43
	1, 3, 4, -	2.5, 5, +	26.1331	-8
	1, 3, 3, -	2.5, 4, +	26.1383	-13
	2, 3, 3, -	3.5, 4, +	27.1351	-13
	2, 3, 5, -	3.5, 6, +	27.144	-1

${}^O P_{12}$ and ${}^O P_{13}$ transitions measured via LIF:

average error of 0.0005 cm^{-1} .

Other transitions measured via absorption spectroscopy:

average error of 0.001 cm^{-1} .

Std. dev. of fit: 25 MHz (0.00082 cm^{-1}); (128 lines to 94 features).

Table A.3: The transition wavenumbers and assignments for the $\tilde{A}^2\Pi_{1/2}(0,0,0) - \tilde{X}^2\Sigma^+(0,0,0)$ band of $^{171}\text{YbOH}$. Also presented are the differences between the observed (Obs.) and calculated (Calc.) transition wavenumbers. The calculated values were obtained using the optimized parameters of the fit. Here p indicates the parity of the molecular state. This table was reproduced from Ref. [129] with permission from AIP.

Lines	N'', G'', F'', p	J', F', p	Obs. (-17300 cm^{-1})	Obs.– Calc. (MHz)
$^oP_{11}$	2, 1, 1, +	0.5, 0, -	22.1144	1
	2, 1, 2, +	0.5, 1, -	22.1467	35
	3, 1, 2, -	1.5, 1, +	21.1929	-5
	3, 1, 3, -	1.5, 2, +	21.2133	-4
	4, 1, 3, +	2.5, 2, -	20.2756	-27
	4, 1, 4, +	2.5, 3, -	20.2969	-6
$^oP_{10}$	2, 0, 2, +	0.5, 1, -	22.376	5
	3, 0, 3, -	1.5, 2, +	21.4437	-4
	4, 0, 4, +	2.5, 3, -	20.5263	-39
$^pP_{11} + ^pQ_{11}$	1, 0, 2, -	0.5, 1, +	23.5567	-25
	2, 1, 2, +	1.5, 2, -	23.55	12
	2, 1, 3, +	1.5, 2, -	23.5567	42
	2, 1, 1, +	1.5, 1, -	23.5641	1
	3, 1, 3, -	2.5, 3, +	23.5641	53

Continued on next page

Table A.3 – *Continued from previous page*

Lines	N'', G'', F'', p	J', F', p	Obs. (-17300 cm^{-1})	Obs. -Calc. (MHz)
	3, 1, 4, -	2.5, 3, +	23.5706	32
	3, 1, 2, -	2.5, 2, +	23.5769	40
	4, 1, 4, +	3.5, 4, -	23.5905	-18
	4, 1, 5, +	3.5, 4, -	23.5997	0
	4, 1, 3, +	3.5, 3, -	23.6034	7
	4, 1, 4, +	3.5, 3, -	23.6045	-50
	5, 1, 5, -	4.5, 5, +	23.6357	0
	5, 1, 4, -	4.5, 4, +	23.647	12
	6, 1, 6, +	5.5, 6, -	23.6966	16
	6, 1, 5, +	5.5, 5, -	23.7056	-7
	6, 1, 7, +	5.5, 6, -	23.7088	33
	7, 1, 7, -	6.5, 7, +	23.7715	-27
	7, 1, 6, -	6.5, 6, +	23.7802	-22
${}^P P_{10} + {}^P Q_{10}$	1, 0, 1, -	0.5, 1, +	23.7836	-6
	2, 0, 2, +	1.5, 2, -	23.7802	2
	3, 0, 3, -	2.5, 3, +	23.7836	9
	4, 0, 4, +	3.5, 4, -	23.8212	-12
	4, 0, 4, +	3.5, 3, -	23.8354	-39
	5, 0, 5, -	4.5, 5, +	23.8665	4
	5, 0, 5, -	4.5, 4, +	23.8824	24

Continued on next page

Table A.3 – *Continued from previous page*

Lines	N'', G'', F'', p	J', F', p	Obs. (-17300 cm ⁻¹)	Obs. -Calc. (MHz)
	6, 0, 6, +	5.5, 6, -	23.928	30
	6, 0, 6, +	5.5, 5, -	23.9424	2
${}^{\circ}Q_{11} + {}^{\circ}R_{11}$	0, 1, 1, +	0.5, 1, -	23.622	25
	1, 1, 2, -	1.5, 2, +	23.6738	34
	2, 1, 2, +	2.5, 2, -	23.7164	-1
	2, 1, 2, +	2.5, 3, -	23.7329	-33
	2, 1, 3, +	2.5, 3, -	23.7384	-40
	3, 1, 3, -	3.5, 3, +	23.7969	-41
	3, 1, 3, -	3.5, 4, +	23.8157	10
	3, 1, 4, -	3.5, 4, +	23.8212	-40
	4, 1, 4, +	4.5, 4, -	23.8939	39
	4, 1, 3, +	4.5, 4, -	23.8939	-50
	4, 1, 4, +	4.5, 5, -	23.9126	5
	4, 1, 5, +	4.5, 5, -	23.9218	22
	5, 1, 4, -	5.5, 5, +	24.0045	8
	5, 1, 5, -	5.5, 5, +	24.0086	0
	5, 1, 5, -	5.5, 6, +	24.0258	16
	5, 1, 6, -	5.5, 6, +	24.0364	32
${}^{\circ}Q_{10} + {}^{\circ}R_{10}$	0, 0, 0, +	0.5, 1, -	23.8472	-46
	1, 0, 1, -	1.5, 1, +	23.8816	51

Continued on next page

Table A.3 – *Continued from previous page*

Lines	N'', G'', F'', p	J', F', p	Obs. (-17300 cm^{-1})	Obs. -Calc. (MHz)
	1, 0, 1, -	1.5, 2, +	23.8989	7
	2, 0, 2, +	2.5, 2, -	23.9472	14
	2, 0, 2, +	2.5, 3, -	23.9647	11
	3, 0, 3, -	3.5, 3, +	24.0294	15
	3, 0, 3, -	3.5, 4, +	24.0466	23
${}^R R_{11}$	0, 1, 1, +	1.5, 2, -	25.0257	14
	1, 1, 2, -	2.5, 3, +	26.0203	-37
	1, 1, 1, -	2.5, 2, +	26.0323	4
	2, 1, 3, +	3.5, 4, -	27.033	-22
	2, 1, 2, +	3.5, 3, -	27.0432	3
	3, 1, 4, -	4.5, 5, +	28.0612	-16
	3, 1, 3, -	4.5, 4, +	28.0703	17
${}^R R_{10}$	0, 0, 0, +	1.5, 1, -	25.2687	46
	1, 0, 1, -	2.5, 2, +	26.2617	-21
	2, 0, 1, +	2.5, 3, -	27.2721	-39

${}^O P_{11}$ and ${}^O P_{10}$ transitions measured via LIF:

average error of 0.0005 cm^{-1} .

Other transitions measured via absorption spectroscopy:

average error of 0.001 cm^{-1} .

Std. dev. of fit: 27 MHz (0.00089 cm^{-1}); (70 lines to 65 features).

A.3 $\tilde{A}^2\Pi_{1/2}(100) - \tilde{X}^2\Sigma^+(300)$ FM spectroscopy

Table A.4: The transition wavenumbers and assignments for the $\tilde{A}^2\Pi_{1/2}(1, 0, 0) - \tilde{X}^2\Sigma^+(3, 0, 0)$ band of $^{174}\text{YbOH}$ measured with in cell FM spectroscopy. Also presented are the differences between the observed (Obs.) and calculated (Calc.) transition wavenumbers. The calculated values were obtained using the optimized parameters from the combined fit of both the $\tilde{A}^2\Pi_{1/2}(1, 0, 0) - \tilde{X}^2\Sigma^+(3, 0, 0)$ and $\tilde{A}^2\Pi_{1/2}(1, 0, 0) - \tilde{X}^2\Sigma^+(0, 0, 0)$ data [116]. Here p indicates the parity of the molecular state.

Lines	N'', J'', p	J', p	Obs. ^a (cm ⁻¹)	Obs.– Calc. (MHz)
$^oP_{12}$	2, 1.5, +	0.5, -	16335.7340	15
$^pQ_{12}$	2, 1.5, +	1.5, -	16337.2948	-4
	3, 2.5, -	2.5, +	16337.3806	3
	4, 3.5, +	3.5, -	16337.4909	1
	5, 4.4, -	4.5, +	16337.6261	-6
	6, 5.5, +	5.5, -	16337.7863	-11
	7, 6.5, -	6.5, +	16337.9717	-10
	8, 7.5, +	7.5, -	16338.1833	23
	$^pP_{11}$	1, 1.5, -	0.5, +	16337.2431
2, 2.5, +		1.5, -	16337.3095	6
3, 3.5, -		2.5, +	16337.4005	-4
4, 4.5, +		3.5, -	16337.5166	-7
5, 5.5, -		4.5, +	16337.6577	-7
6, 6.5, +		5.5, -	16337.8237	-11

Continued on next page

Table A.4 – *Continued from previous page*

Lines	N'', J'', p	J', p	Obs. ^a (cm ⁻¹)	Obs. -Calc. (MHz)
	7, 7.5, -	6.5 +	16338.0150	-6
	8, 8.5, +	7.5, -	16338.2314	-1
${}^Q Q_{11}$	0, 0.5, +	0.5, -	16337.1876	21
	1, 1.5, -	1.5, +	16337.2004	4
	2, 2.5, +	2.5, -	16337.2384	5
	3, 3.5, -	3.5, +	16337.3004	-11
	4, 4.5, +	4.5, -	16337.3875	-8
	5, 5.5, -	5.5, +	16337.4993	2
	6, 6.5, +	6.5, -	16337.6347	-10
	7, 7.5, -	7.5, +	16337.7948	-11
	8, 8.5, +	8.5, -	16337.9793	-9
	9, 9.5, -	9.5, +	16338.1895	38
${}^Q R_{12}$	1, 0.5, -	0.5, +	16337.1922	17
	2, 1.5, +	2.5, -	16337.2240	4
	3, 2.5, -	3.5, +	16337.2801	-16
	4, 3.5, +	4.5, -	16337.3619	1
	5, 4.5, -	5.5, +	16337.4674	-5
	6, 5.5, +	6.5, -	16337.5974	-7
	8, 7.5, +	8.5, -	16337.9305	-5
${}^R R_{11}$	0, 0.5, +	1.5, -	16338.7486	9

Continued on next page

Table A.4 – *Continued from previous page*

Lines	N'', J'', p	J', p	Obs. ^a (cm ⁻¹)	Obs. -Calc. (MHz)
	1, 1.5, -	2.5, +	16339.8026	-6
	Unassigned		16338.6793	
	Unassigned		16338.7399	
	Unassigned		16339.5994	

^aAverage error of 0.0003 cm⁻¹.

RMS of combined fit with $\tilde{A}^2\Pi_{1/2}(1, 0, 0) - \tilde{X}^2\Sigma^+(0, 0, 0)$ data [116]:

25 MHz (0.00084 cm⁻¹).

$\tilde{A}^2\Pi_{1/2}(1, 0, 0) - \tilde{X}^2\Sigma^+(3, 0, 0)$ transition 35 lines.

$\tilde{A}^2\Pi_{1/2}(1, 0, 0) - \tilde{X}^2\Sigma^+(0, 0, 0)$ transition 65 lines.

Table A.5: The transition wavenumbers and assignments for the $\tilde{A}^2\Pi_{1/2}(1,0,0) - \tilde{X}^2\Sigma^+(0,0,0)$ band of $^{174}\text{YbOH}$ from Ref [116]. Also presented are the differences between the observed (Obs.) and calculated (Calc.) transition wavenumbers. The calculated values were obtained using the optimized parameters from the combined fit of both the $\tilde{A}^2\Pi_{1/2}(1,0,0) - \tilde{X}^2\Sigma^+(3,0,0)$ and $\tilde{A}^2\Pi_{1/2}(1,0,0) - \tilde{X}^2\Sigma^+(0,0,0)$ data. Here p indicates the parity of the molecular state.

Lines	N'', J'', p	J', p	Obs. ^a (cm^{-1})	Obs.– Calc. (MHz)
$^O P_{12}$	2, 1.5, +	0.5, -	17906.3830	35
	3, 2.5, -	1.5, +	17905.4024	15
	4, 3.5, +	2.5, -	17904.4382	8
	5, 4.5, -	3.5, +	17903.4897	-7
	6, 5.5, +	4.5, -	17902.5568	-29
	$^P Q_{12}$	1, 0.5, -	0.5, +	17907.8990
2, 1.5, +		1.5, -	17907.9442	29
3, 2.5, -		3.5, +	17908.0046	6
4, 3.5, +		3.5, -	17908.0810	-24
5, 4.5, -		4.5, +	17908.1752	-8
6, 5.5, +		5.5, -	17908.2853	-5
7, 6.5, -		6.5, +	17908.4137	56
8, 7.5, +		7.5, -	17908.5533	-40
9, 8.5, -		8.5, +	17908.7132	-21
10, 9.5, +		9.5, -	17908.8897	0.3

Continued on next page

Table A.5 – *Continued from previous page*

Lines	N'', J'', p	J', p	Obs. ^a (cm ⁻¹)	Obs. -Calc. (MHz)
	11, 10.5, -	10.5, +	17909.0810	-31
	12, 11.5, +	11.5, -	17909.2912	6
^P P ₁₁	1, 1.5, -	0.5, +	17907.9028	15
	2, 2.5, +	1.5, -	17907.9508	24
	3, 3.5, -	2.5, +	17908.0145	19
	4, 4.5, +	3.5, -	17908.0937	-8
	5, 5.5, -	4.5, +	17908.1901	-7
	6, 6.5, +	5.5, -	17908.3042	35
	7, 7.5, -	6.5, +	17908.4335	43
	8, 8.5, +	7.5, -	17908.5762	-40
	9, 9.5, -	8.5, +	17908.7388	-21
	10, 10.5, +	9.5, -	17908.9165	-43
	11, 11.5, -	10.5, +	17909.1120	-28
	12, 12.5, +	11.5, -	17909.3242	-9
	13, 13.5, -	12.5, +	17909.5545	53
	14, 14.5, +	13.5, -	17909.7992	47
^R R ₁₁	2, 2.5, +	3.5, -	17911.5217	-34
	3, 3.5, -	4.5, +	17912.5999	10
	4, 4.5, +	5.5, -	17913.6912	-42
	5, 5.5, -	6.5, +	17914.8019	-2

Continued on next page

Table A.5 – *Continued from previous page*

Lines	N'', J'', p	J', p	Obs. ^a (cm ⁻¹)	Obs. -Calc. (MHz)
Q_{11}	0, 0.5, +	0.5, -	17907.8571	15
	1, 1.5, -	1.5, +	17907.8603	15
	2, 2.5, +	2.5, -	17907.8793	10
	3, 3.5, -	3.5, +	17907.9132	-25
	4, 4.5, +	4.5, -	17907.9648	-4
	5, 5.5, -	5.5, +	17908.0321	15
	6, 6.5, +	6.5, -	17908.1130	-30
	7, 7.5, -	7.5, +	17908.2113	-23
	8, 8.5, +	8.5, -	17908.3256	-3
	9, 9.5, -	9.5, +	17908.4542	-21
	10, 10.5, +	10.5, -	17908.5992	-10
	11, 11.5, -	11.5, +	17908.7604	24
	12, 12.5, +	12.5, -	17908.9357	22
	13, 13.5, -	13.5, +	17909.1231	-75
	14, 14.5, +	14.5, -	17909.3319	14
15, 15.5, -	15.5, +	17909.5545	63	
Q_{R12}	1, 0.5, -	1.5, +	17907.8571	41
	2, 1.5, +	2.5, -	17907.8725	9
	3, 2.5, -	3.5, +	17907.9036	-29
	4, 3.5, +	4.5, -	17907.9535	22

Continued on next page

Table A.5 – *Continued from previous page*

Lines	N'', J'', p	J', p	Obs. ^a (cm ⁻¹)	Obs. -Calc. (MHz)
	5, 4.5, -	5.5, +	17908.0175	23
	6, 5.5, +	6.5, -	17908.0953	-35
	7, 6.5, -	7.5, +	17908.1908	-31
	8, 7.5, +	8.5, -	17908.3035	21
	9, 8.5, -	9.5, +	17908.4278	-45
	10, 9.5, +	10.5, -	17908.5719	18
	11, 10.5, -	11.5, +	17908.7297	30
	12, 11.5, +	12.5, -	17908.9024	29
	13, 12.5, -	13.5, +	17909.0869	-77
	14, 13.5, +	14.5, -	17909.2931	13

^aAverage error of 0.0005 cm⁻¹.

RMS of combined fit with $\tilde{A}^2\Pi_{1/2}(1, 0, 0) - \tilde{X}^2\Sigma^+(3, 0, 0)$ data:

25 MHz (0.00084 cm⁻¹).

$\tilde{A}^2\Pi_{1/2}(1, 0, 0) - \tilde{X}^2\Sigma^+(3, 0, 0)$ transition, 35 lines.

$\tilde{A}^2\Pi_{1/2}(1, 0, 0) - \tilde{X}^2\Sigma^+(0, 0, 0)$ transitions 65 lines.

A.4 [17.68] and [17.64] bands of $^{174}\text{YbOH}$

Table A.6: Measured FM transition wavenumbers of the [17.68] band of $^{174}\text{YbOH}$. All measured transition wavenumbers have a common $\sim 12 \pm 3$ MHz error in absolute frequency. Errors reported are from the error in the zero-crossing measurement of the in phase FM lineshape.

Transition Wavenumber (cm^{-1})	Error (cm^{-1})
17682.8422	0.0003
17682.7940	0.0003
17682.5227	0.0004
17682.5171	0.0004
17682.4271	0.0004
17682.4207	0.0003
17682.2490	0.0004
17682.2404	0.0004
17682.1071	0.0004
17682.0972	0.0003
17682.0232	0.0004
17682.0110	0.0004
17681.8437	0.0004
17681.8353	0.0003
17681.8292	0.0004
17681.8219	0.0004
17681.7676	0.0004

Continued on next page

Table A.6 – *Continued from previous page*

Transition Wavenumber (cm ⁻¹)	Error (cm ⁻¹)
17681.7107	0.0004
17681.6929	0.0004
17681.6239	0.0004
17681.6099	0.0004
17681.6034	0.0003
17681.5930	0.0004
17681.5844	0.0003
17681.4323	0.0003
17681.4125	0.0003
17681.3016	0.0003
17681.2787	0.0004
17681.2658	0.0003
17681.1921	0.0004
17681.1821	0.0004
17681.1524	0.0011
17680.9758	0.0003
17684.0558	0.0003
17684.1530	0.0006
17684.3455	0.0003
17684.5641	0.0004
17684.5697	0.0004

Continued on next page

Table A.6 – *Continued from previous page*

Transition Wavenumber (cm ⁻¹)	Error (cm ⁻¹)
17684.7094	0.0005
17684.7155	0.0005
17685.1149	0.0003
17685.1238	0.0003
17685.3099	0.0003
17685.3197	0.0004
17685.5423	0.0004
17685.6539	0.0004
17685.6662	0.0014
17685.6924	0.0005
17685.7103	0.0005
17685.7224	0.0004
17685.9557	0.0005
17685.9689	0.0005
17686.1373	0.0003
17686.2797	0.0004
17686.3523	0.0004
17686.3668	0.0004
17686.6475	0.0004
17686.6641	0.0004
17687.0381	0.0002

Continued on next page

Table A.6 – *Continued from previous page*

Transition Wavenumber (cm ⁻¹)	Error (cm ⁻¹)
17687.0561	0.0003
17687.7913	0.0006
17687.4058	0.0004
17687.3853	0.0003
17680.9757	0.0003
17680.5414	0.0004

Table A.7: Measured FM transition wavenumbers of the [17.64] band of ¹⁷⁴YbOH. All measured transition wavenumbers have a common $\sim 12 \pm 3$ MHz error in absolute frequency. Errors reported are from the error in the zero-crossing measurement of the in phase FM lineshape.

Transition Wavenumber (cm ⁻¹)	Error (cm ⁻¹)
17639.1217	0.0002
17639.1319	0.0003
17639.1388	0.0003
17639.1525	0.0003
17639.1615	0.0003
17639.1987	0.0003
17639.4283	0.0004

Continued on next page

Table A.7 – *Continued from previous page*

Transition Wavenumber (cm ⁻¹)	Error (cm ⁻¹)
17639.4339	0.0004
17639.4917	0.0004
17639.4967	0.0004
17639.8509	0.0004
17639.8781	0.0004
17639.9196	0.0005
17640.1615	0.0003
17640.1718	0.0003
17640.4007	0.0004
17640.4182	0.0004
17640.6438	0.0005
17640.6651	0.0005
17640.7779	0.0005
17640.7832	0.0005
17640.8833	0.0006
17640.9134	0.0005
17638.9522	0.0003
17638.9036	0.0003
17638.8892	0.0003
17638.8713	0.0004
17638.8593	0.0003

Continued on next page

Table A.7 – *Continued from previous page*

Transition Wavenumber (cm ⁻¹)	Error (cm ⁻¹)
17638.7352	0.0003
17638.7171	0.0017
17638.6976	0.0004
17638.6278	0.0003
17638.6125	0.0003
17638.4310	0.0003
17638.4120	0.0003
17638.3903	0.0004
17638.2794	0.0004
17638.2569	0.0004
17638.1744	0.0003
17638.1484	0.0003
17637.4855	0.0002
17637.0465	0.0003
17636.6820	0.0004
17641.1642	0.0010
17641.2966	0.0004
17641.3047	0.0004
17641.3099	0.0004
17641.3621	0.0015
17641.8599	0.0004

Continued on next page

Table A.7 – *Continued from previous page*

Transition Wavenumber (cm ⁻¹)	Error (cm ⁻¹)
17641.8717	0.0003
17641.9568	0.0004
17641.9673	0.0004
17642.0719	0.0003
17642.4682	0.0004
17642.4840	0.0004
17642.5273	0.0004
17642.5418	0.0004
17642.7707	0.0004
17643.0064	0.0003
17643.0243	0.0004
17643.1211	0.0003
17643.1401	0.0003

*Appendix B***Technical Drawings**

This appendix contains the technical drawings of the buffer gas cell and 4 K CBGB parts. Parts described in Ch. 3 which have no equivalent drawings in this appendix were custom machined by hand to the desired specifications. For example, no drawing for the cell aperture plate or gas inlet are shown.

B.1 Cryogenic buffer gas cell**Blank cell pieces**

The drawings of the blank cell pieces are below. Note that in these drawings there is a 0.063-inch thru all hole in the center. Before using these pieces to make a cell, this hole was machined out to 0.5 inches to create the cell body. The 0.25-inch blank piece was used to make both the cell aperture plate and the gas inlet. A description of how the aperture plate and the gas inlet were made from the 0.25-inch cell blank are given in the caption to Fig. B.1.

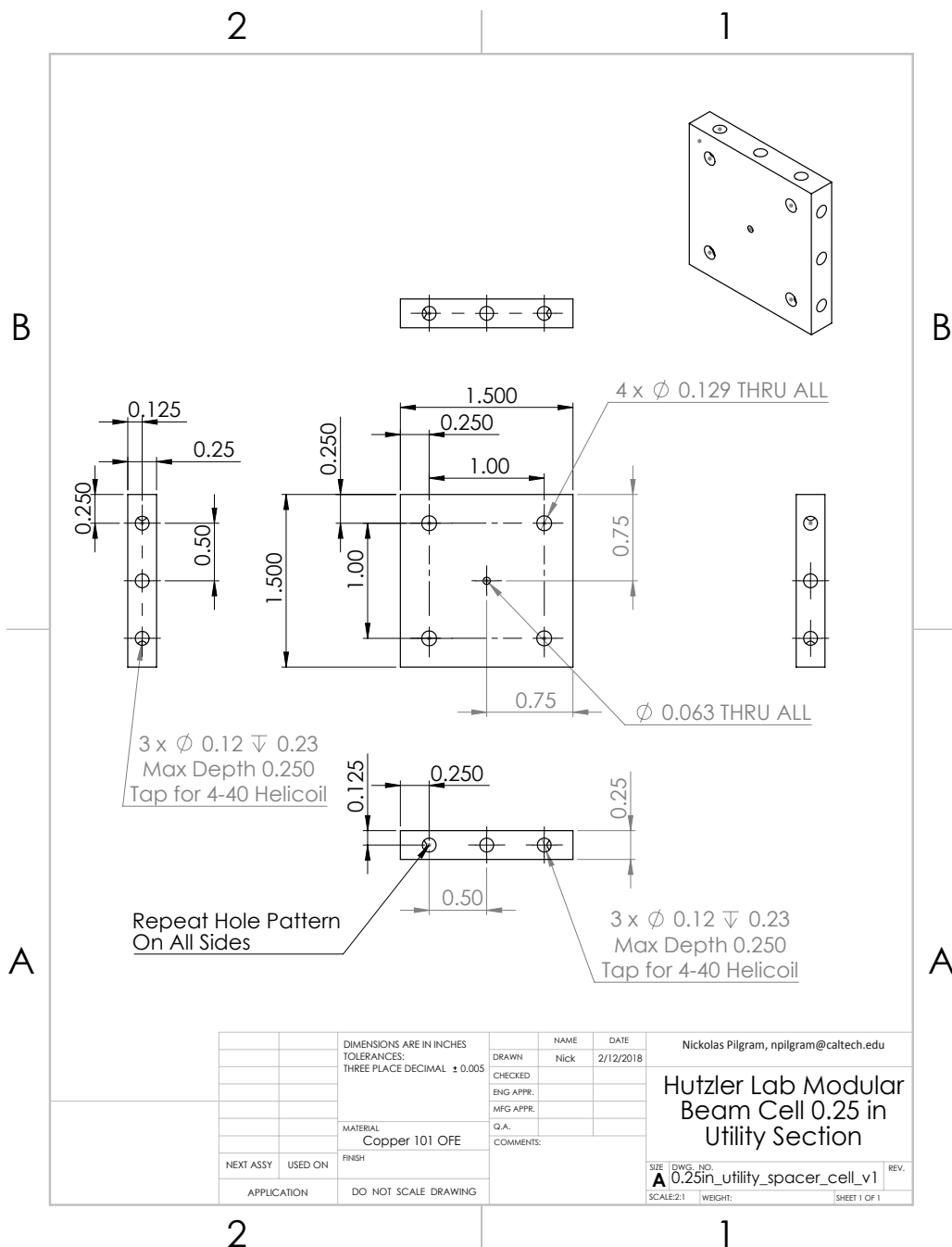


Figure B.1: 0.25-inch blank cell piece. The center 0.063-inch hole is machined out to 0.5 inches before use. This blank piece was machined to create the cell aperture and gas inlet. The aperture plate was made by drilling a 5-mm thru all hole and then machining out a 0.5-inch diameter, ~ 3/16-inch-deep pocket with a 0.5-inch counter sink. The counter sink was used to give the pocket a conical shape leading up to the aperture so that the aperture was just an opening in the cell and not a tube. To create the gas inlet, the 0.063 inch hole was machined out to 1/8 inch and a 1/8 inch copper 101 tube was soldered on.

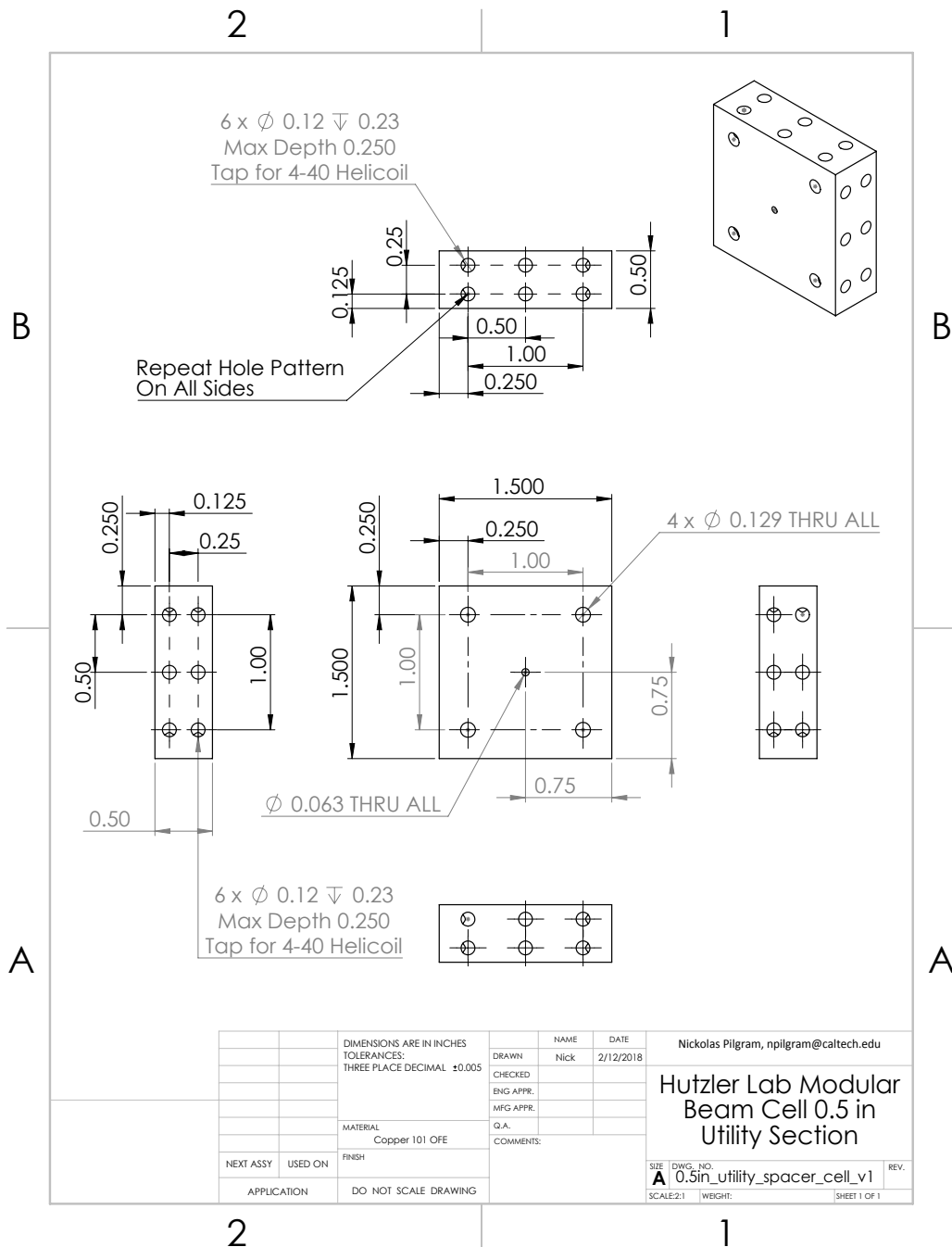


Figure B.2: 0.5-inch blank cell piece. The center 0.063-inch hole is machined out to 0.5 inches before use.

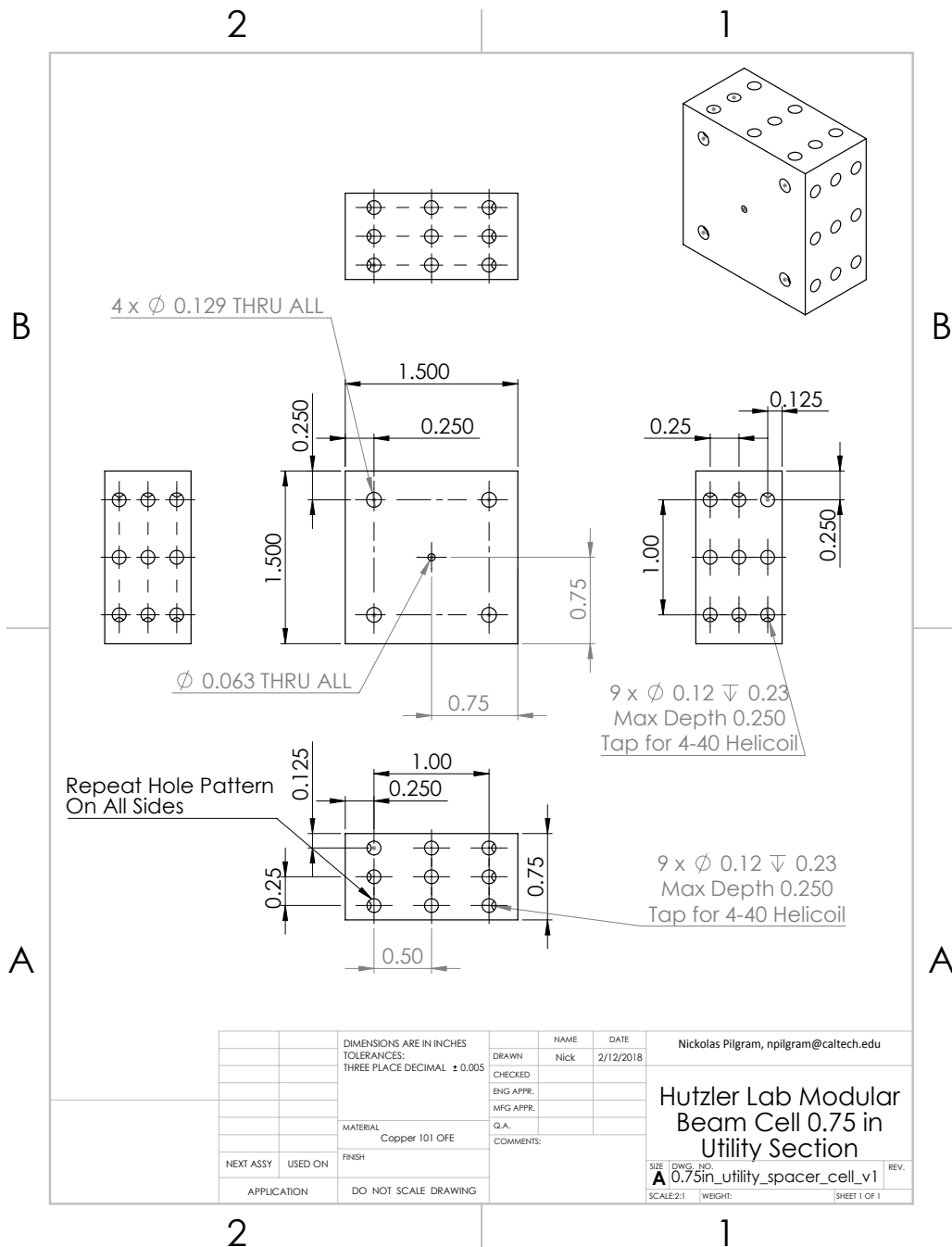


Figure B.3: 0.75-inch blank cell piece. The center 0.063-inch hole is machined out to 0.5 inches before use.

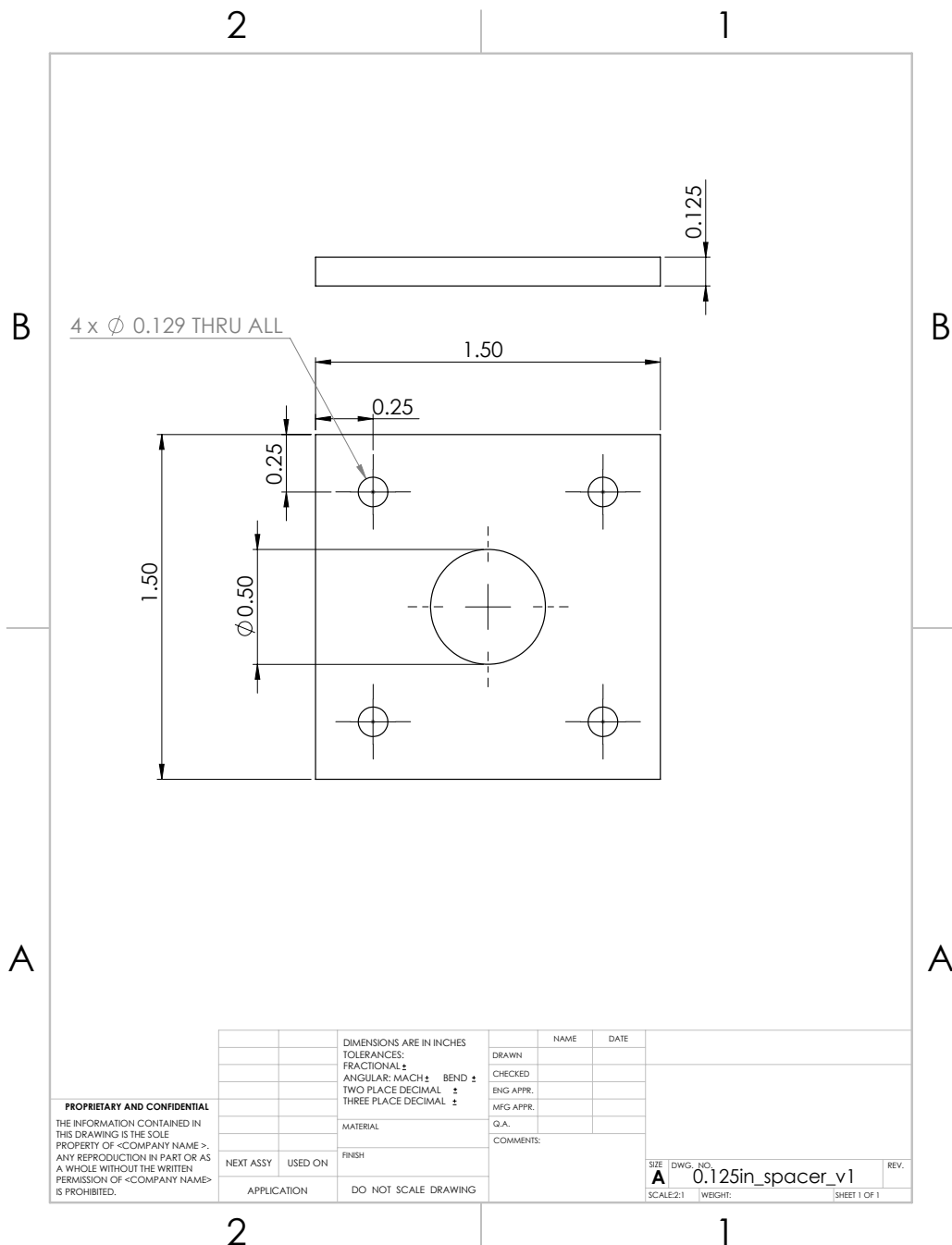


Figure B.5: 0.125-inch spacer. This piece was used to separate the diffuser from the gas inlet.

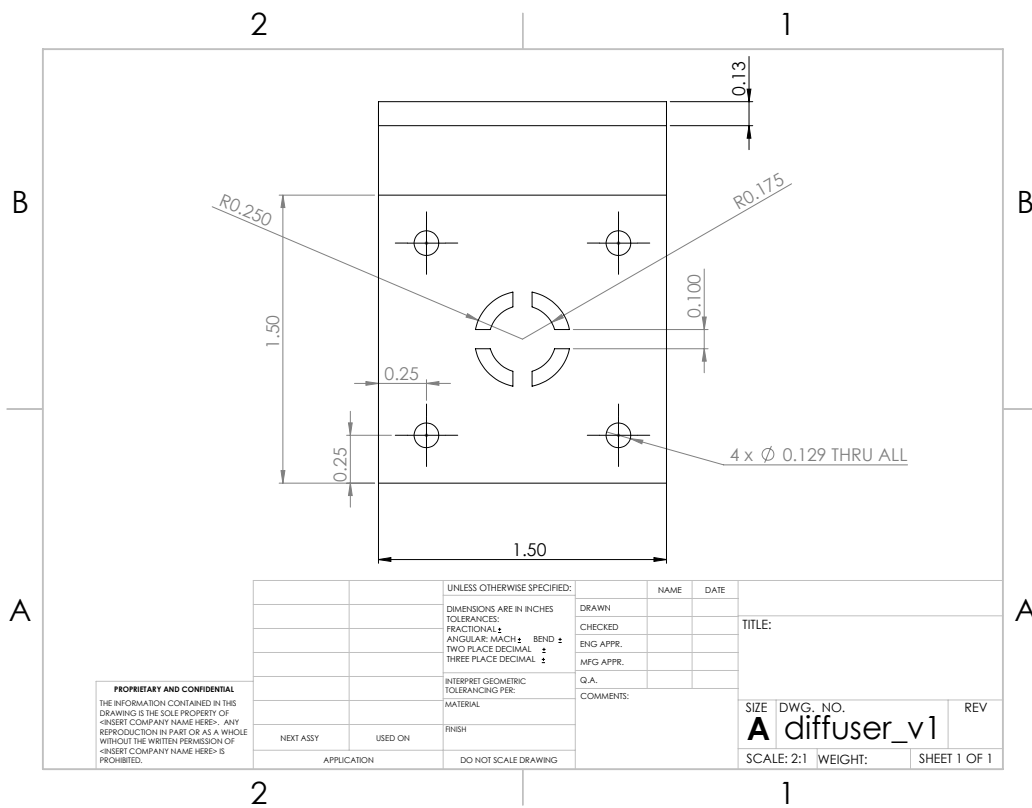


Figure B.6: Diffuser, used to more evenly distribute He flow in cell.

Window cell pieces

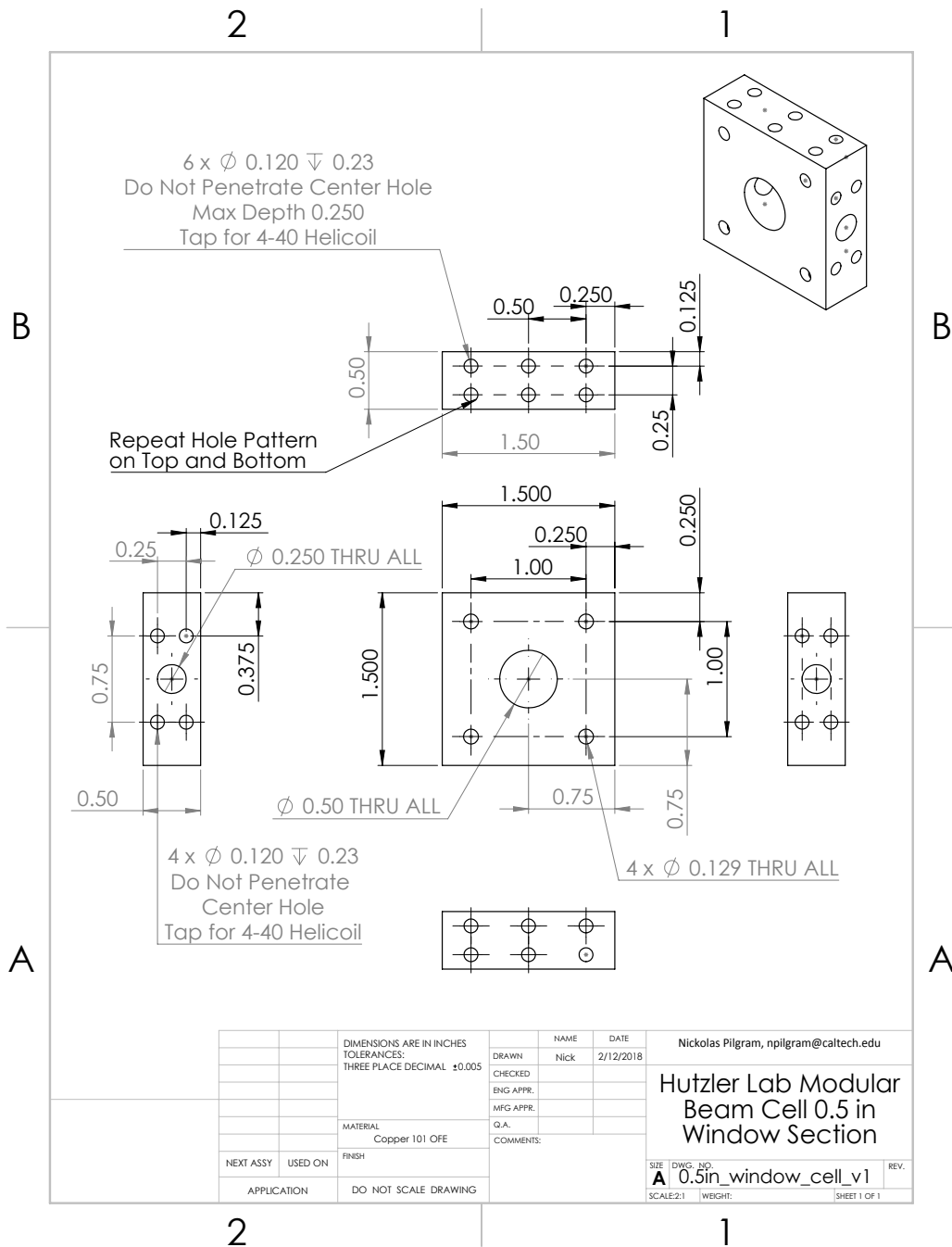


Figure B.7: 0.5-inch window cell piece.

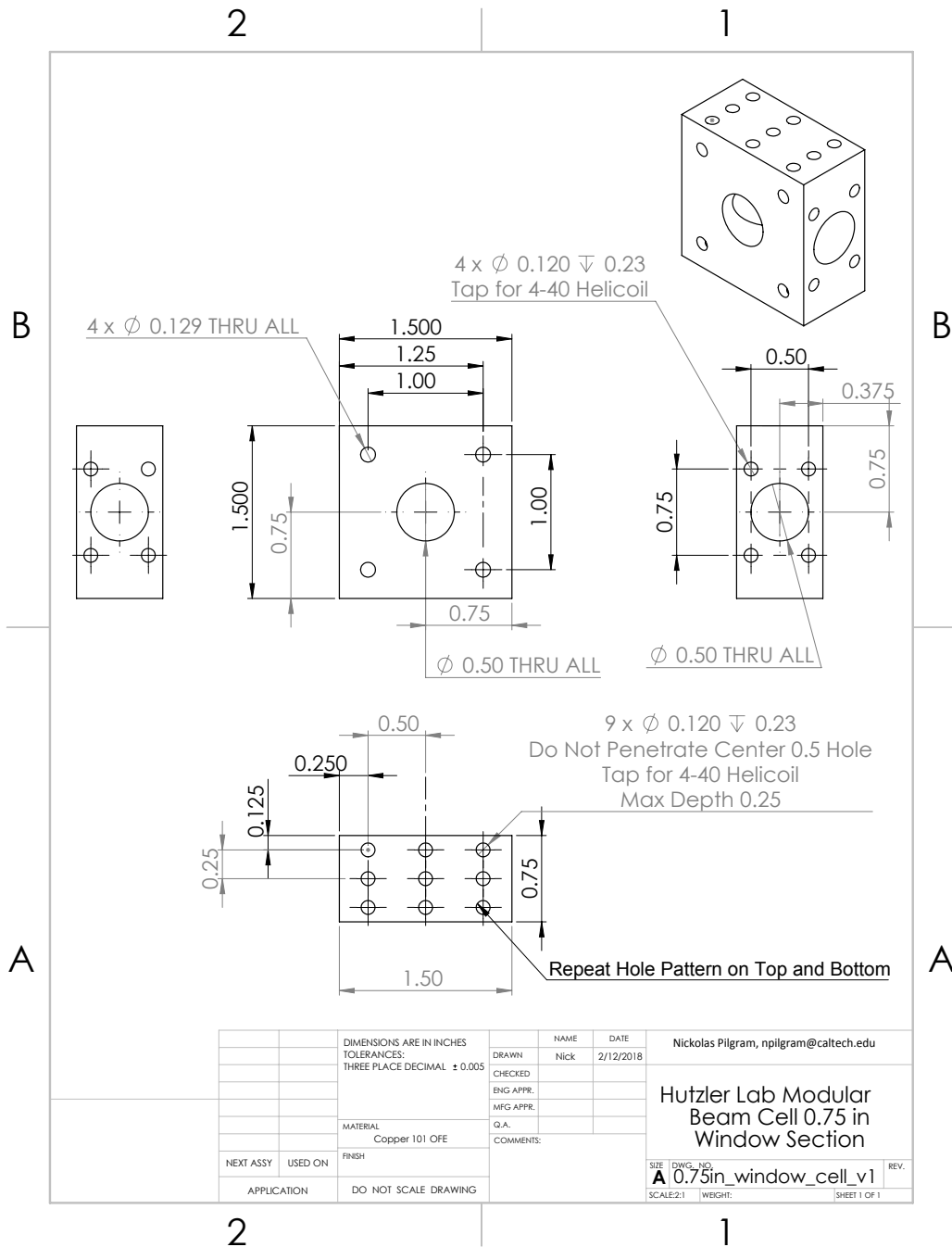


Figure B.8: 0.75-inch window cell piece.

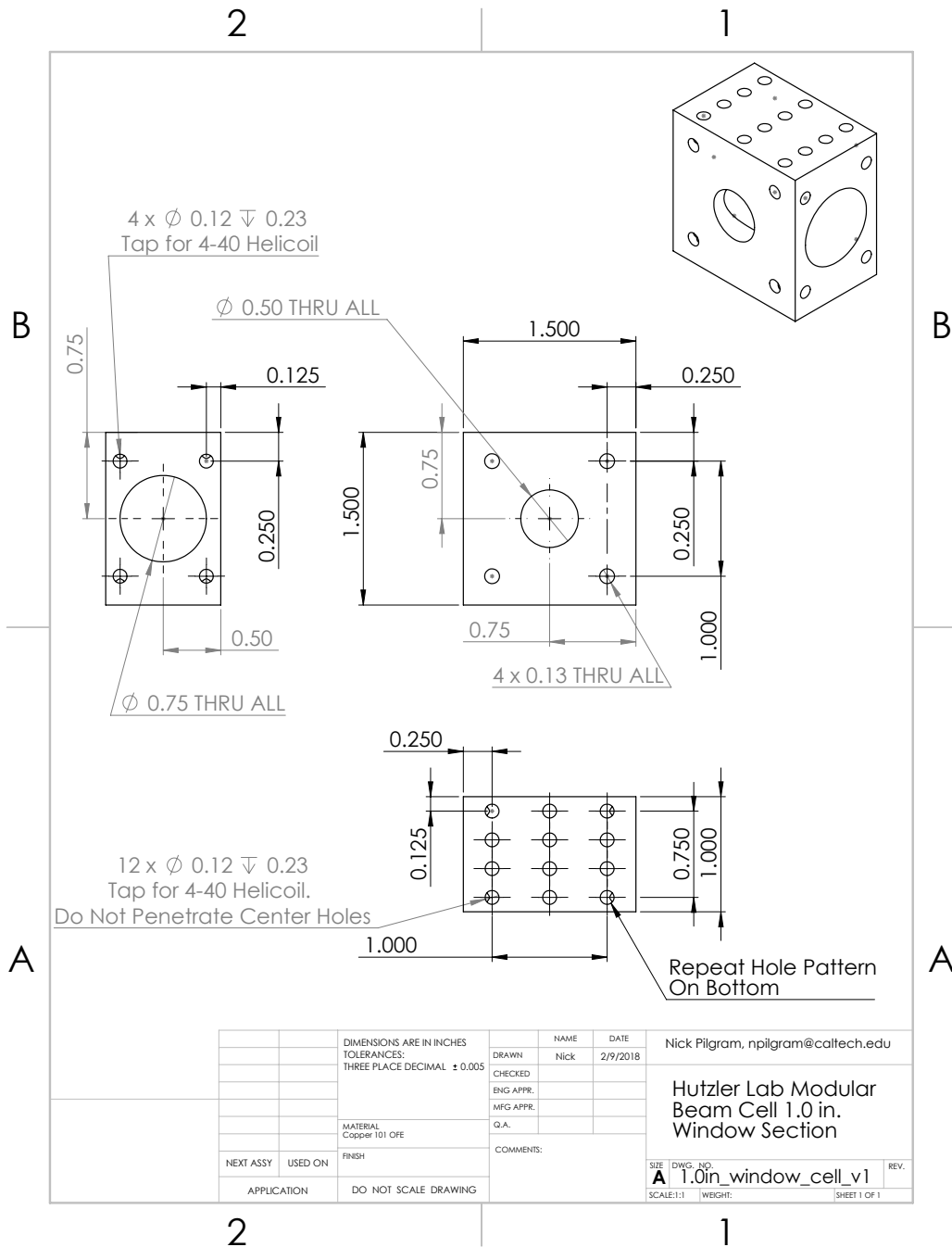


Figure B.9: 1.0-inch window cell piece.

Cell mounts and flanges

Drawings for the cell mounts used to mount and thermally anchor the cell to the 4 K top plate are below. Also below are drawings of a 1.0-inch snorkel and window flange. Window flanges for other size window cell pieces are scaled down versions of the one shown.

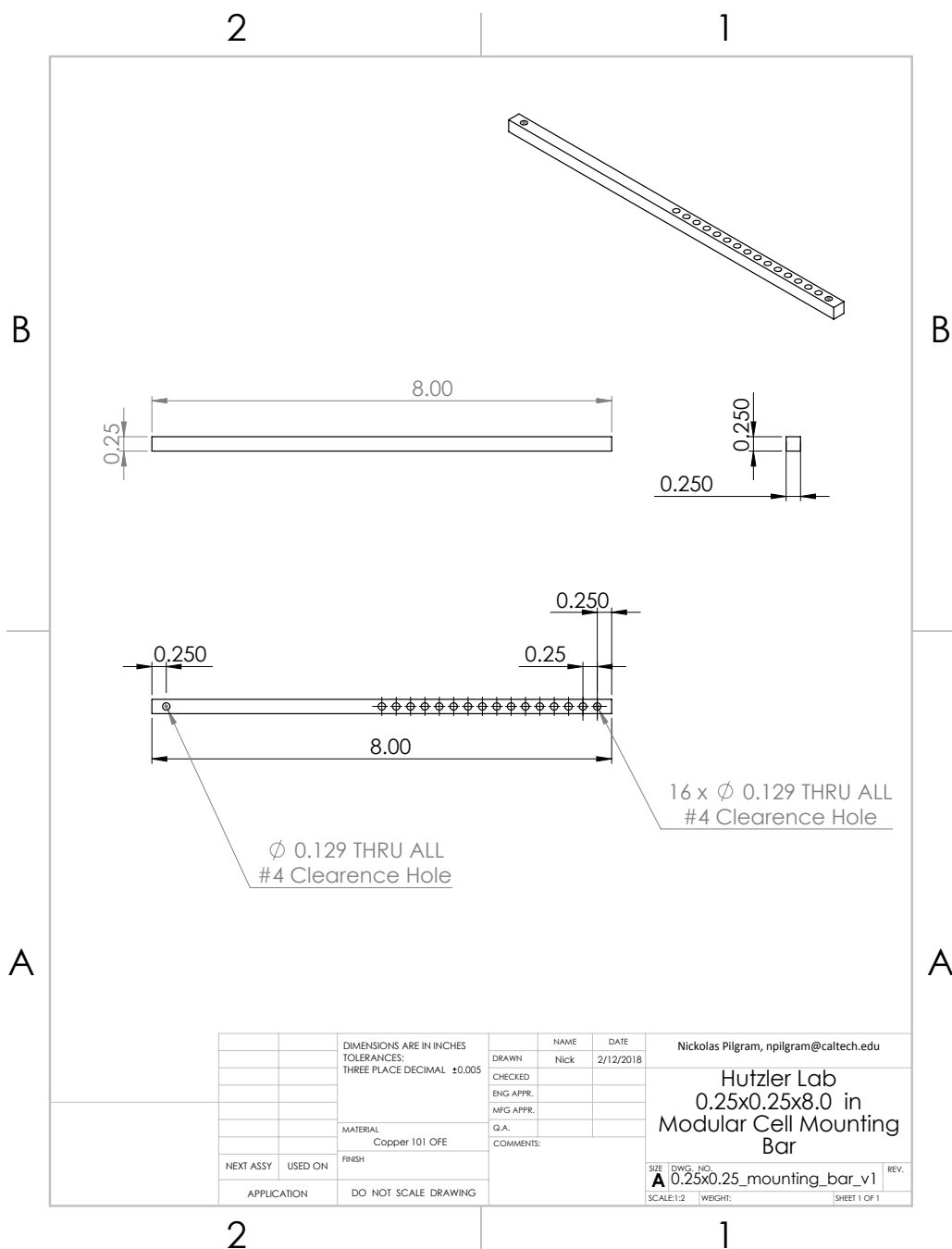


Figure B.11: 0.25-inch cell mounting bars. The pattern of through holes at the bottom are used to attach to the side of the cell.

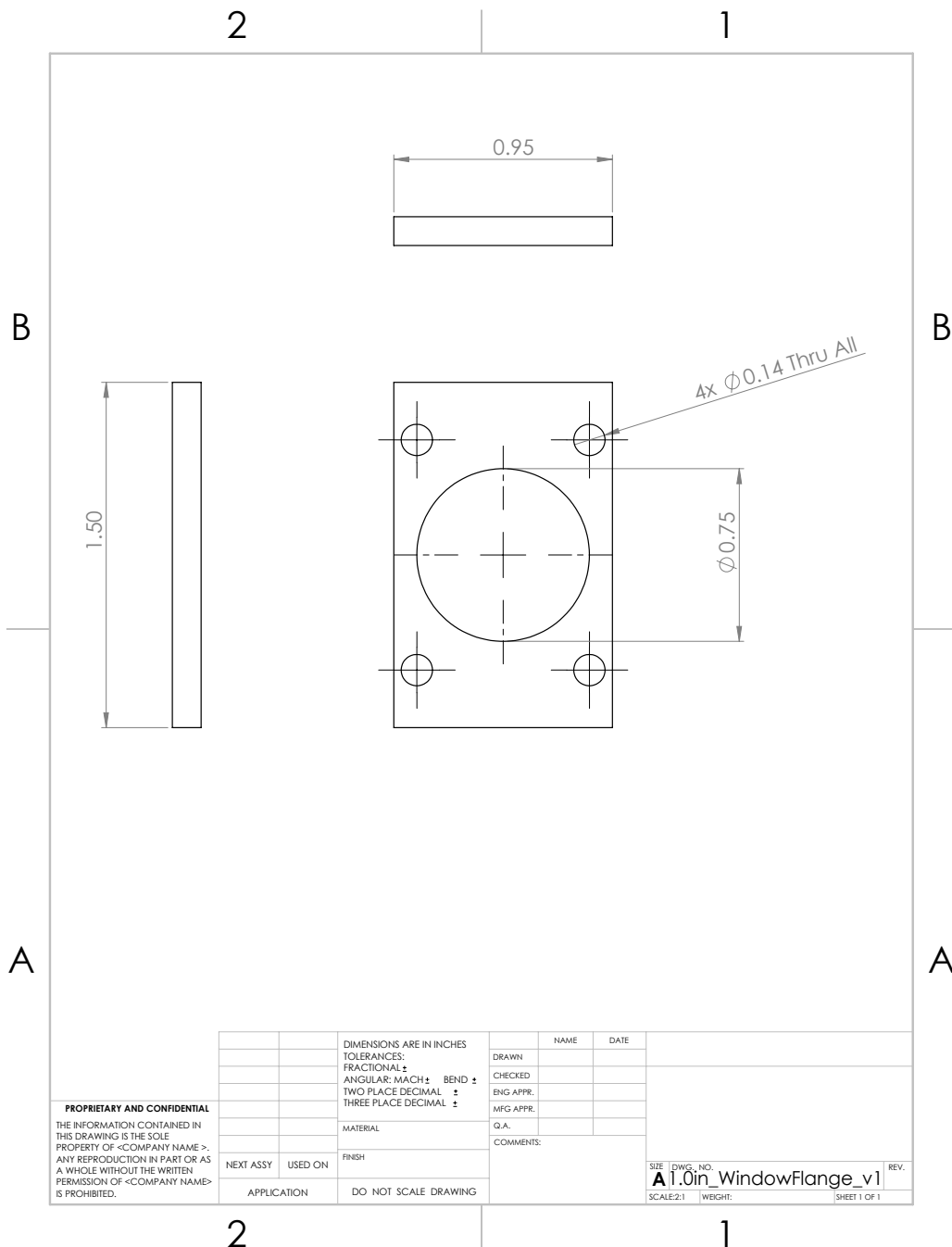


Figure B.12: 1.0-inch window flange. This is used to clamp a window to the the 1.0-inch window cell piece or to the end of the snorkel.

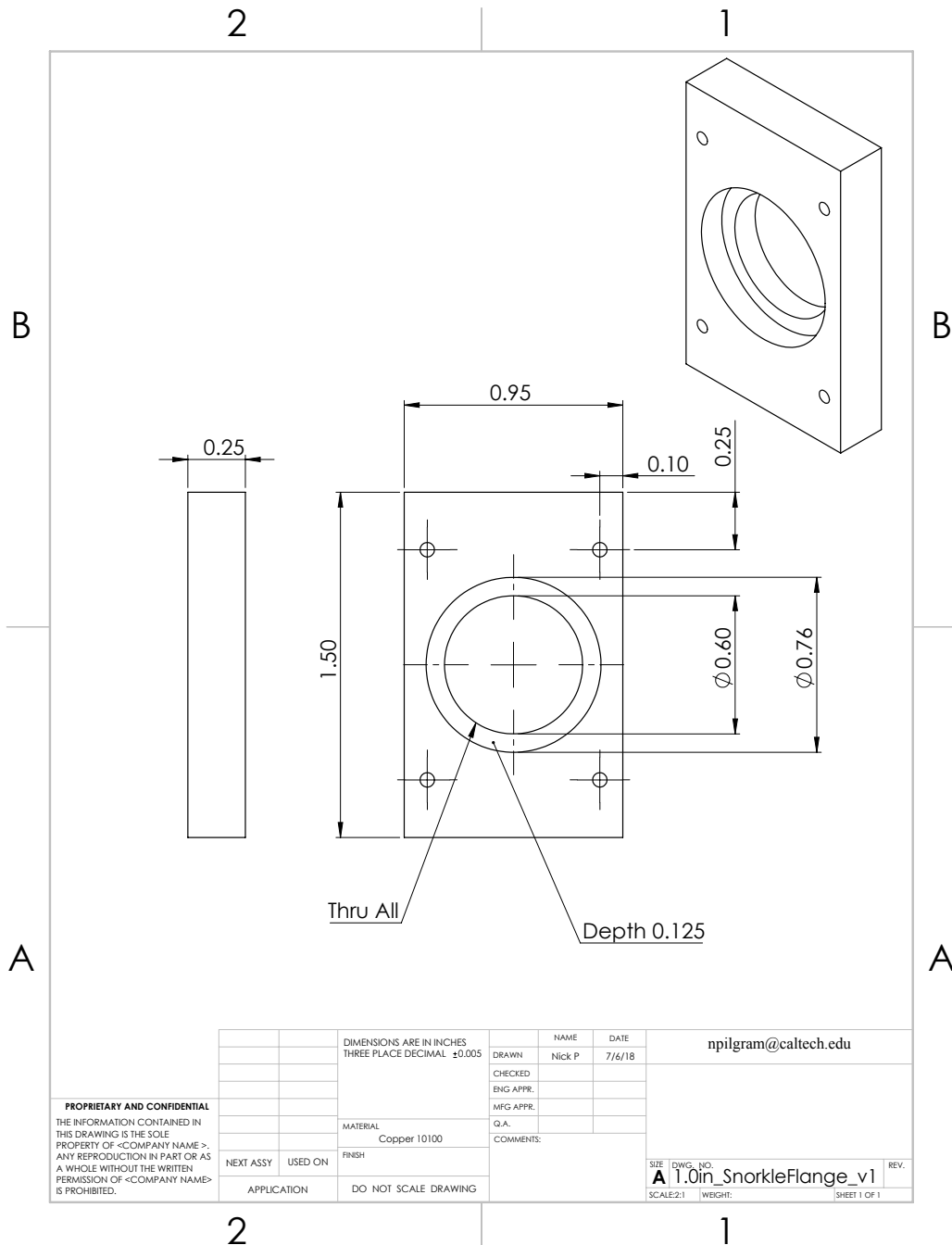


Figure B.13: 1.0-inch snorkel flange. The snorkel is made by brazing a 0.75-inch-OD Copper 101 tube in between two of these flanges. One side is then attached to the cell while the other has a window attached to it with a window flange.

B.2 50 K thermal shields

50K_TopPlate_PulseTubeHole_v3

Material: Aluminum 6061

Contact: Nick Pilgram

npilgram@caltech.edu

12/06/17

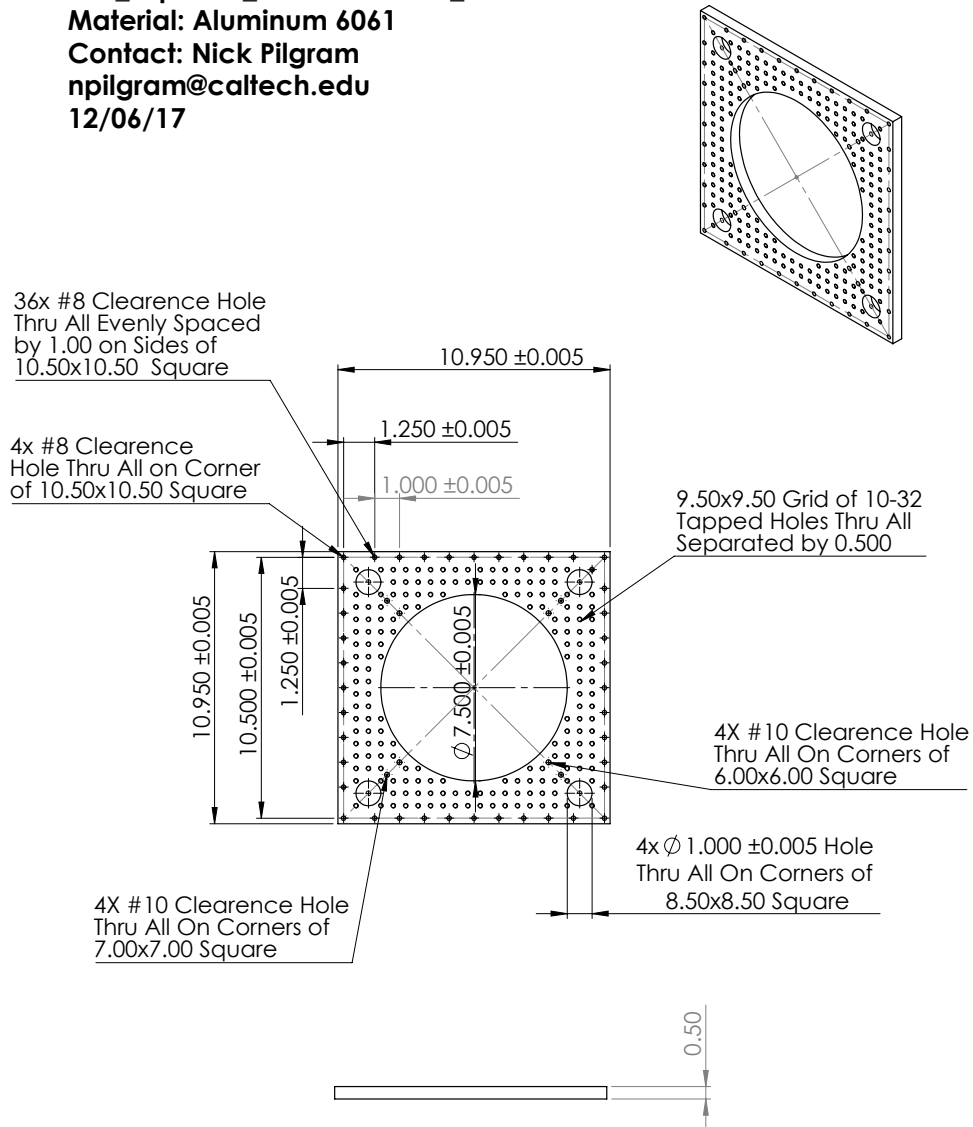


Figure B.14: 50 K top plate.

50K_BottomPlate_Blank_v3
 Material: Aluminum 6061
 Contact: Nick Pilgram
 npilgram@caltech.edu
 Updated: 12/13/17

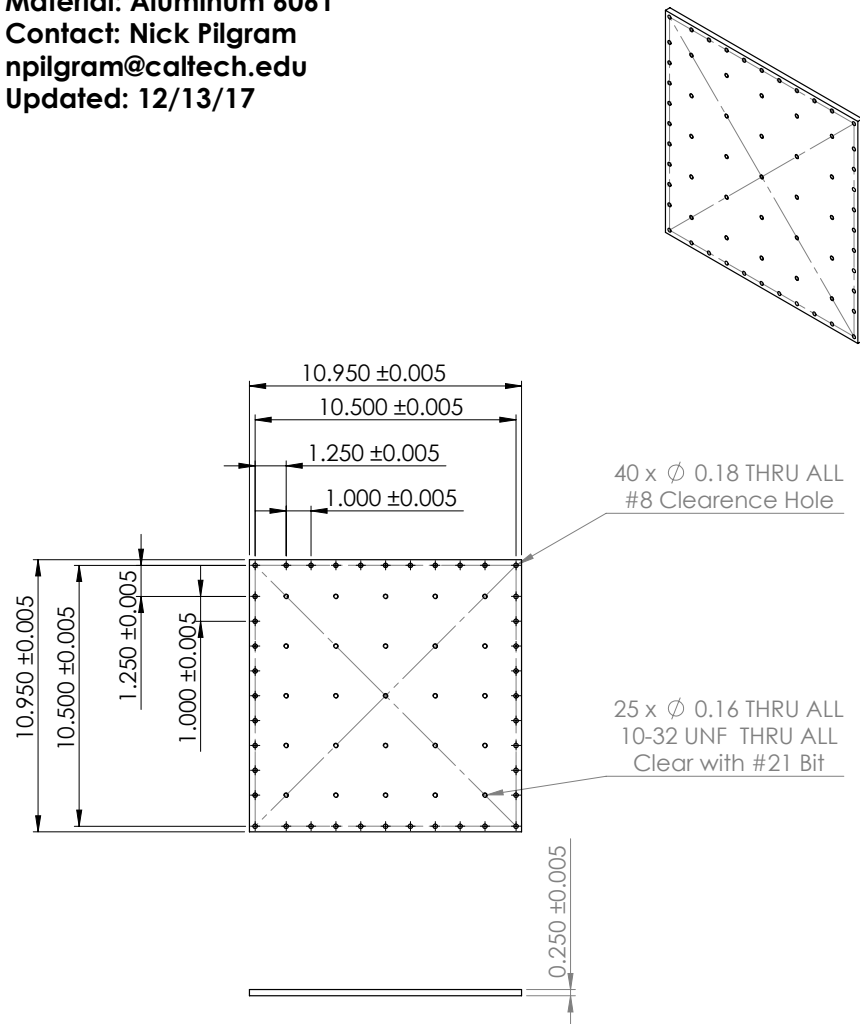


Figure B.15: 50 K bottom plate.

50K_SidePlate_Flange_v3
Material: Aluminum 6061
Contact: Nick Pilgram
npilgram@caltech.edu
Updated: 12/14/17

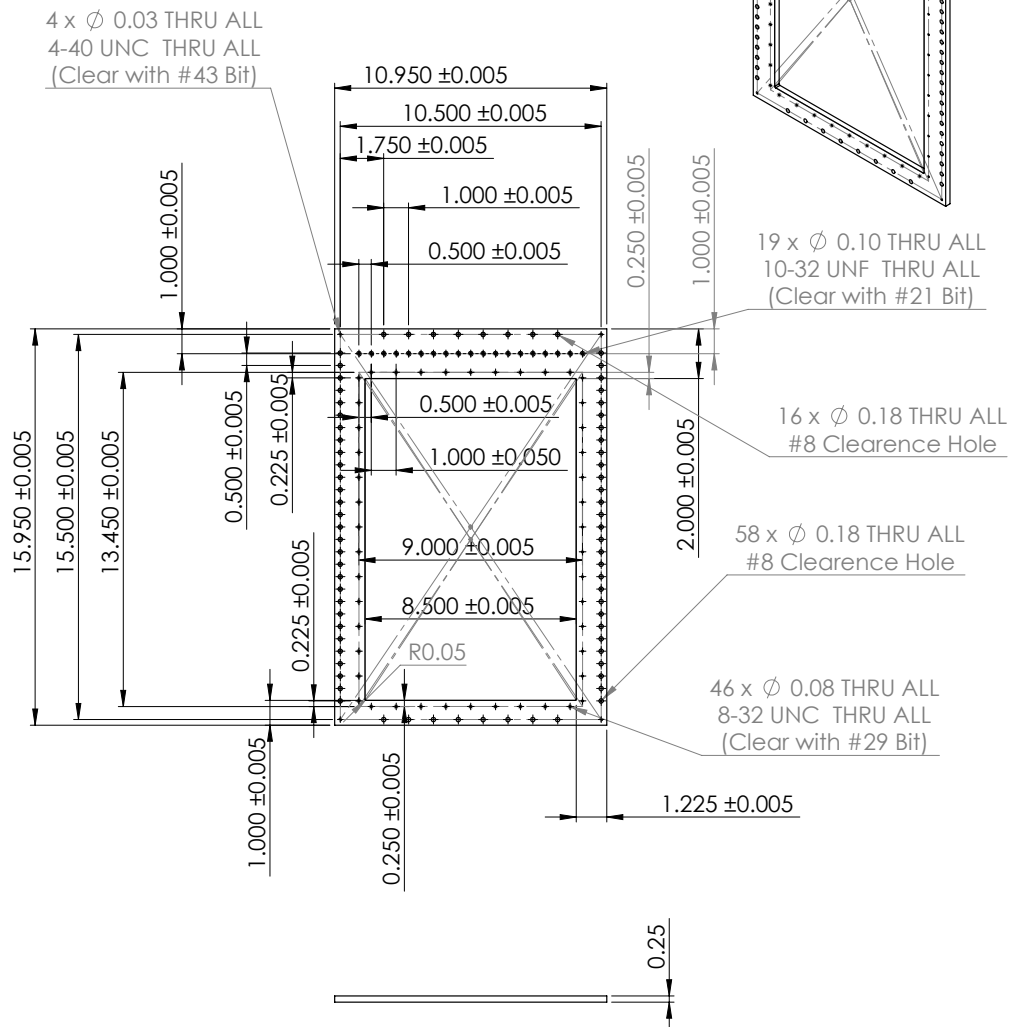


Figure B.16: 50 K side plate flange. As described in Ch. 3, 0.125-inch pockets around the edges of the flange were machined so that the thickness of the edges of the plate was only 0.125 inches. This allowed the plate to sit closer to the 50 K frame allowing the 300 K chamber to be dropped without removing the 50 K side plates.

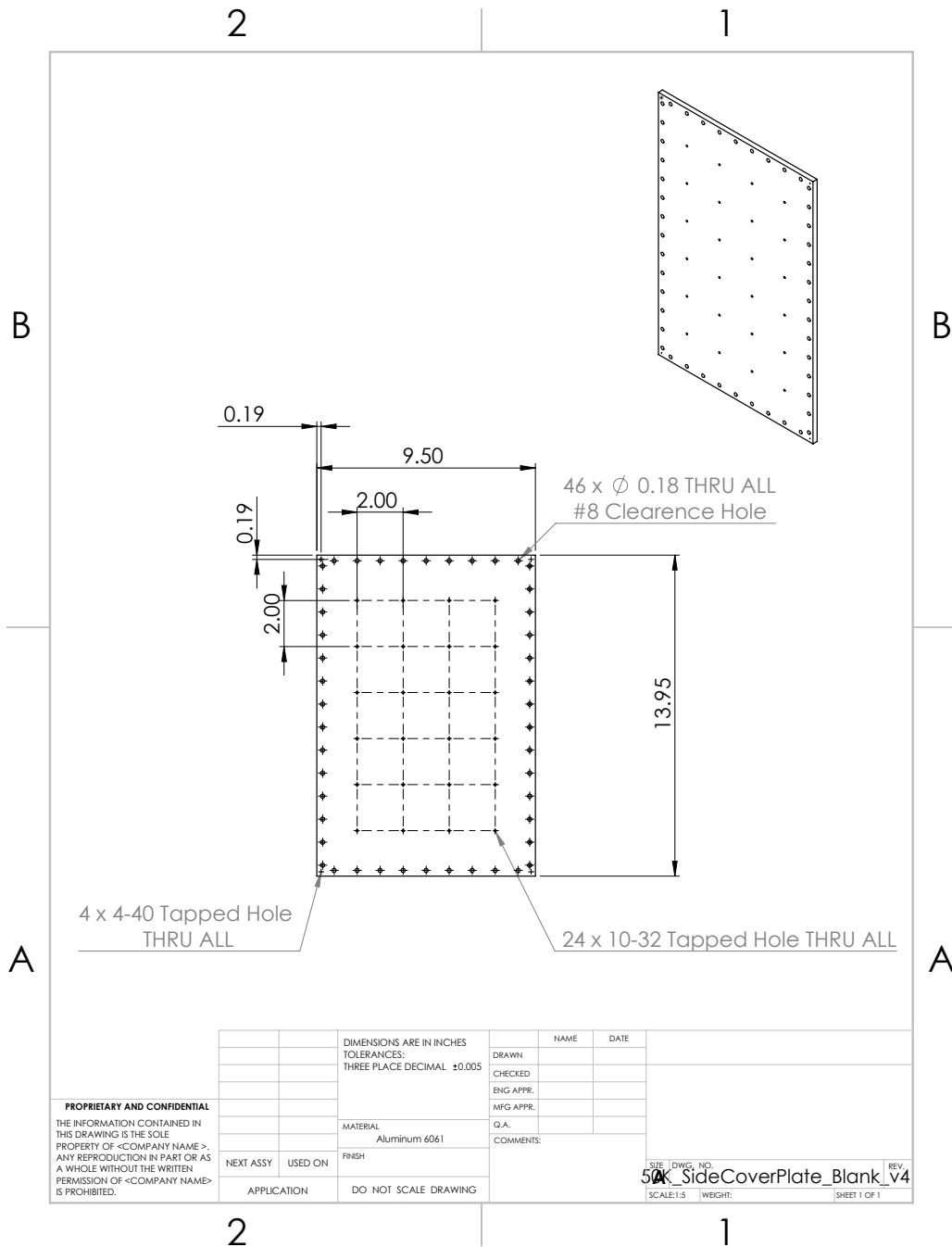


Figure B.17: Blank 50 K side cover plate.

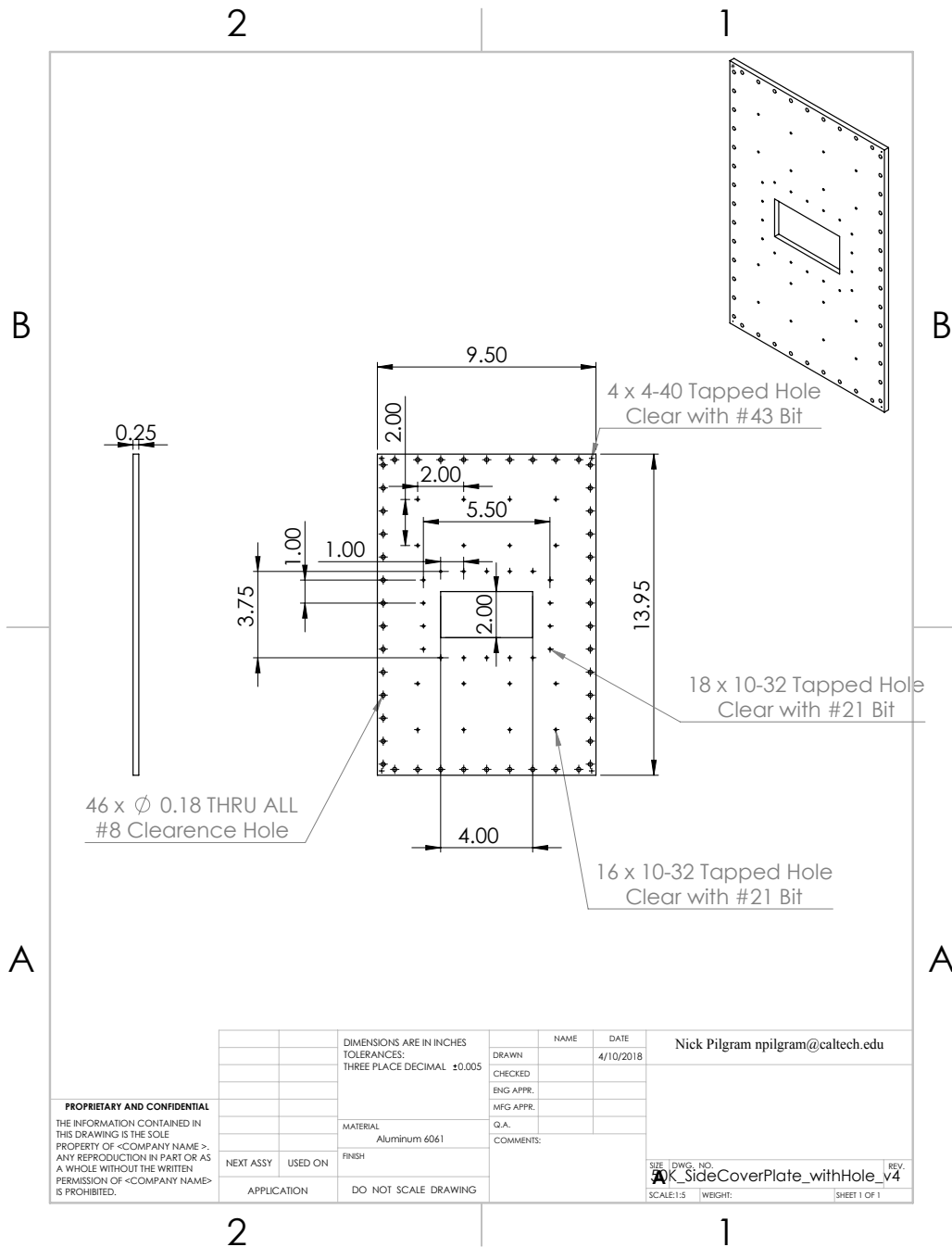


Figure B.18: 50 K side cover plate with hole for window.

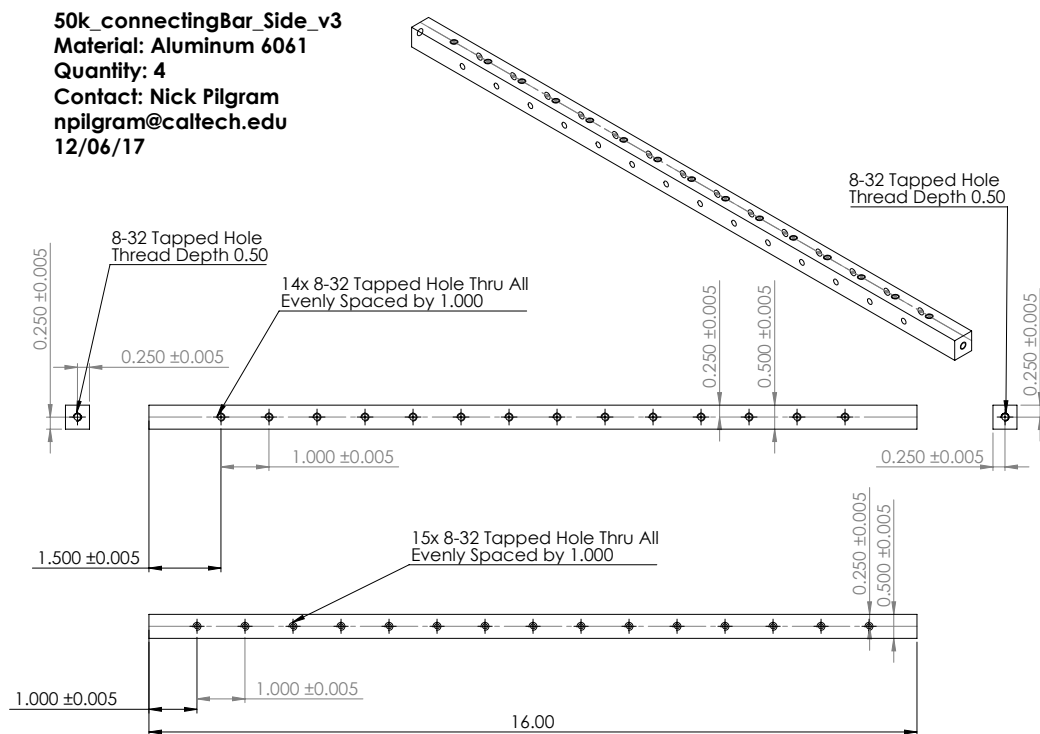


Figure B.19: 50 K vertical connecting bar.

50K_ConnectingBar_TopBottom_v3
Material: Aluminum 6061
Quantity: 8
Contact: Nick Pilgram
npilgram@caltech.edu
12/06/17

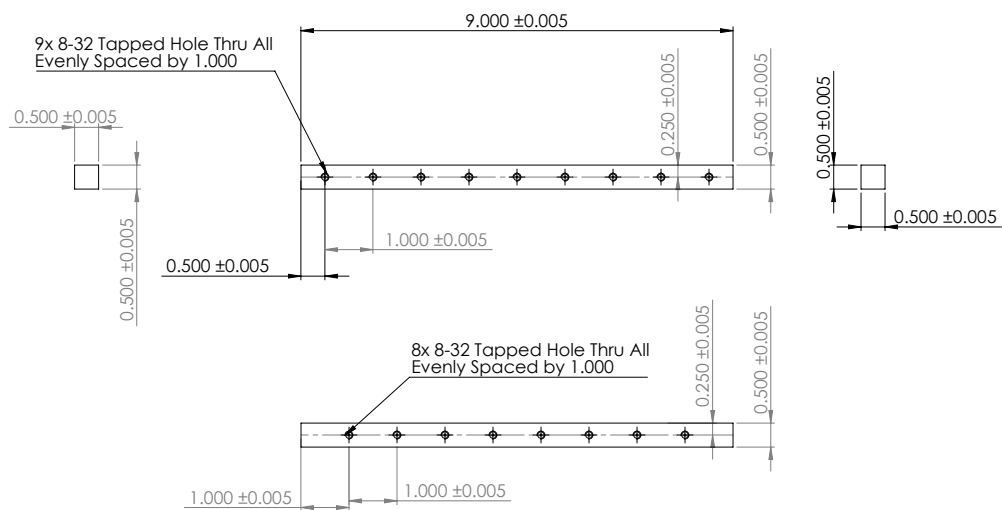
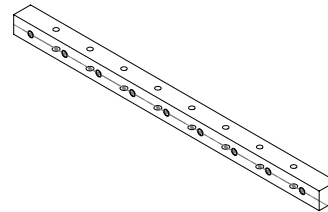


Figure B.20: 50 K horizontal connecting bar.

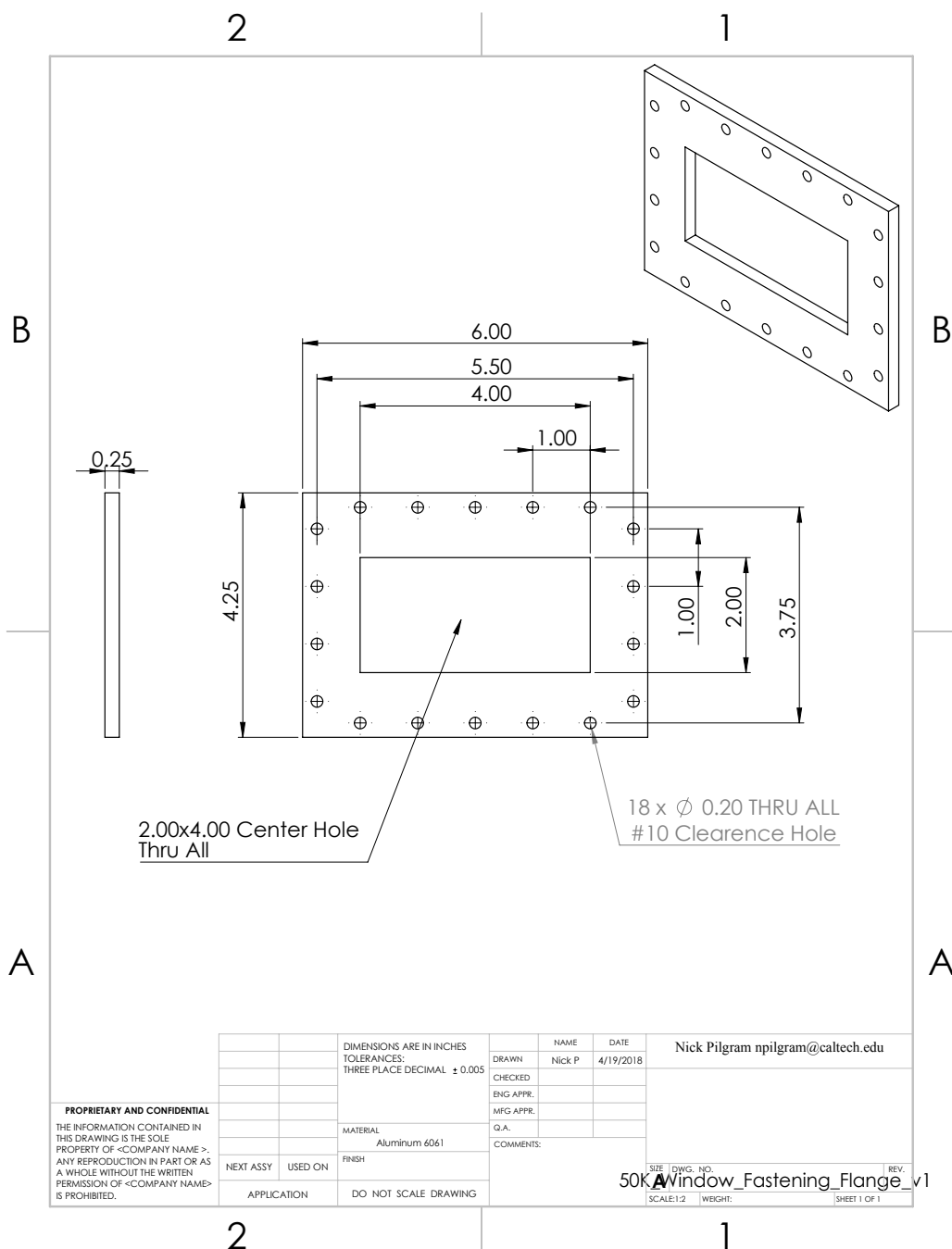


Figure B.21: 50 K window flange. This is used to attach a window the the 50 K side cover plate.

B.3 4 K thermal shields

4K_TopPlate_v3
Material: Copper 1010FE
Contact: Nick Pilgram
npilgram@caltech.edu
Updated: 12/12/17

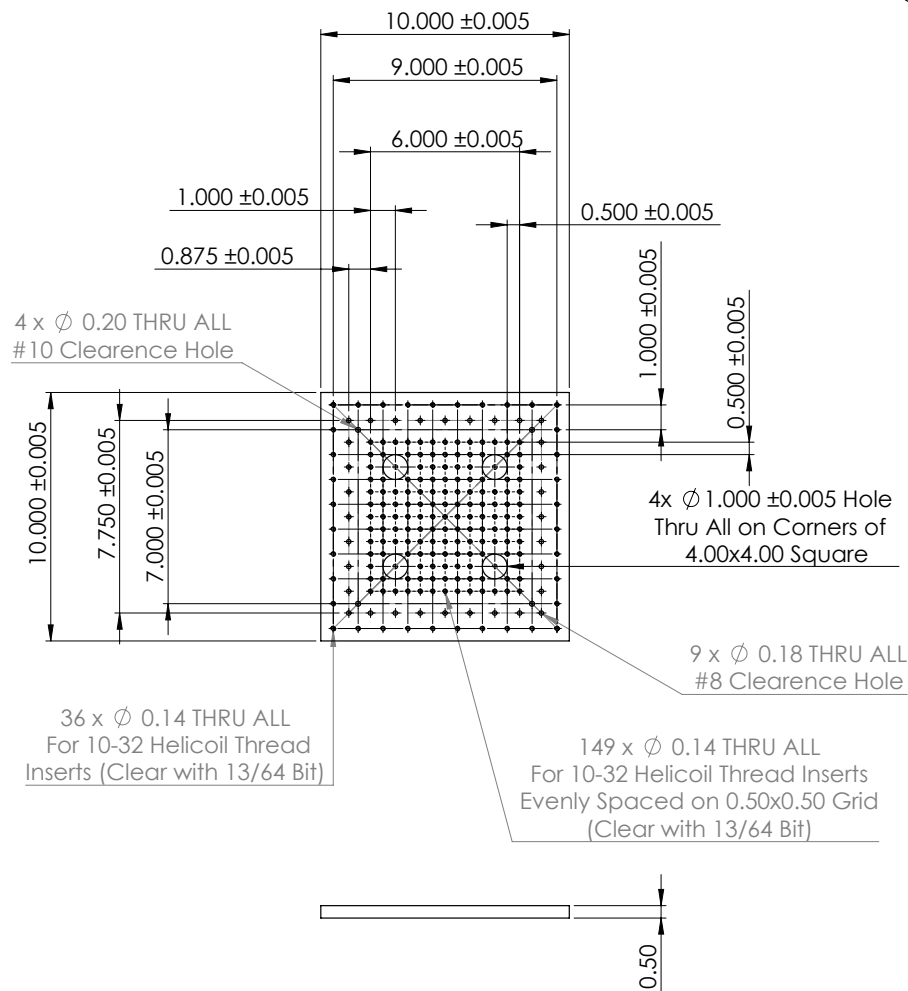
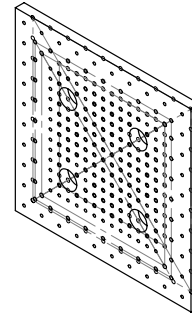


Figure B.22: 4 K top plate.

4K_BottomPlate_Blank_v2
Material: Copper 1010FE
Contact: Nick Pilgram
npilgram@caltech.edu
Updated: 3/20/18

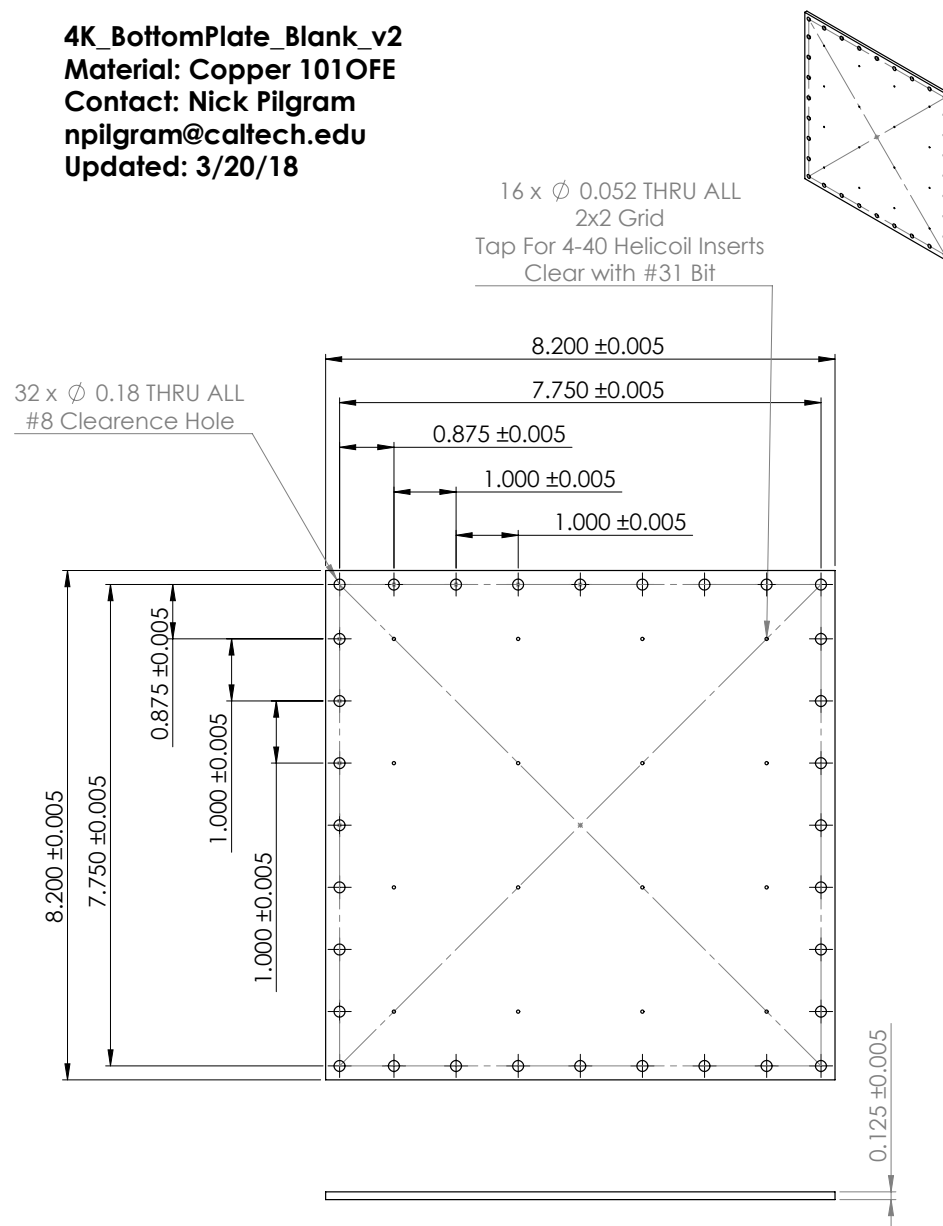


Figure B.23: 4 K bottom plate.

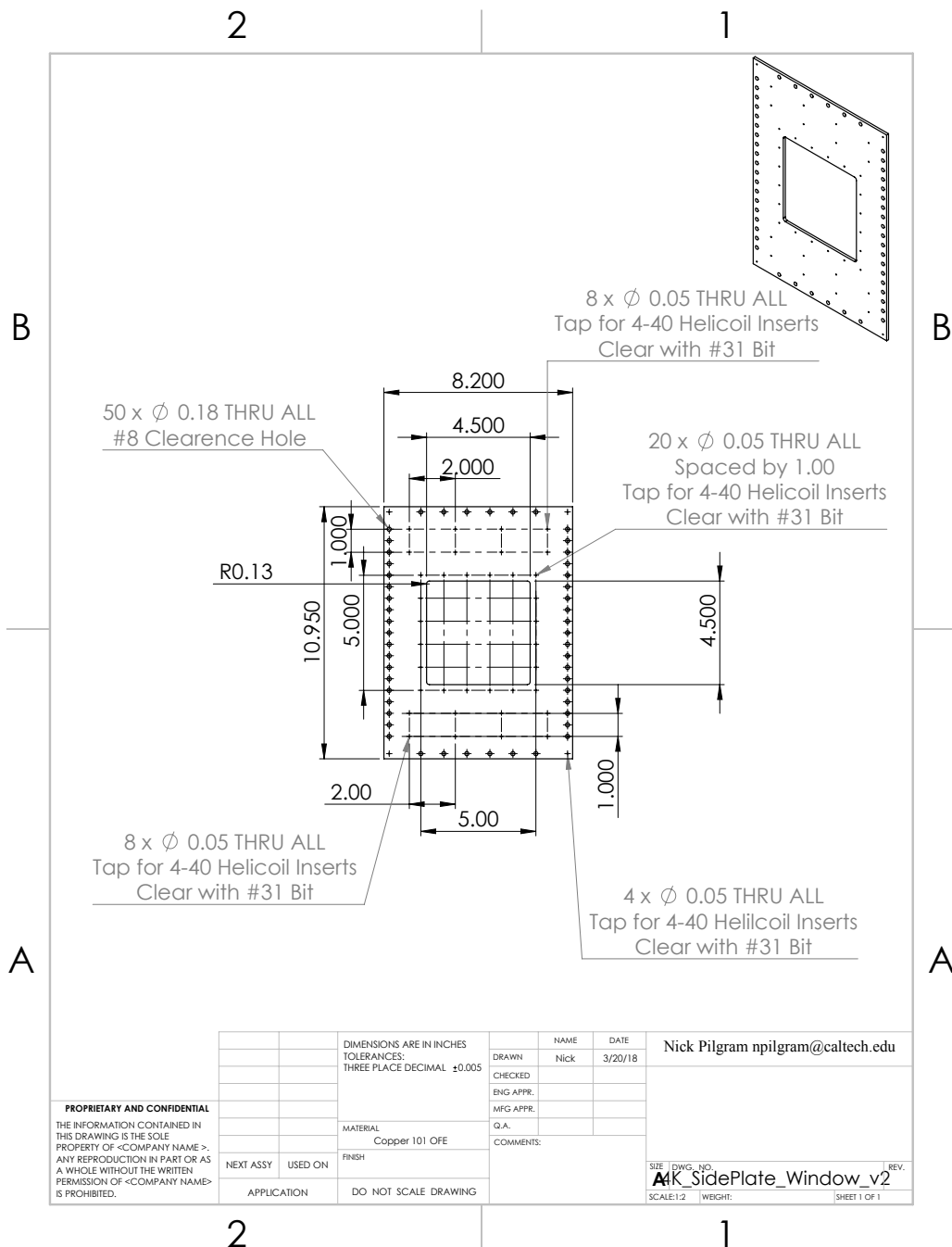


Figure B.24: 4 K side plate. The square hole in the center is covered by the 4 K side cover flange.

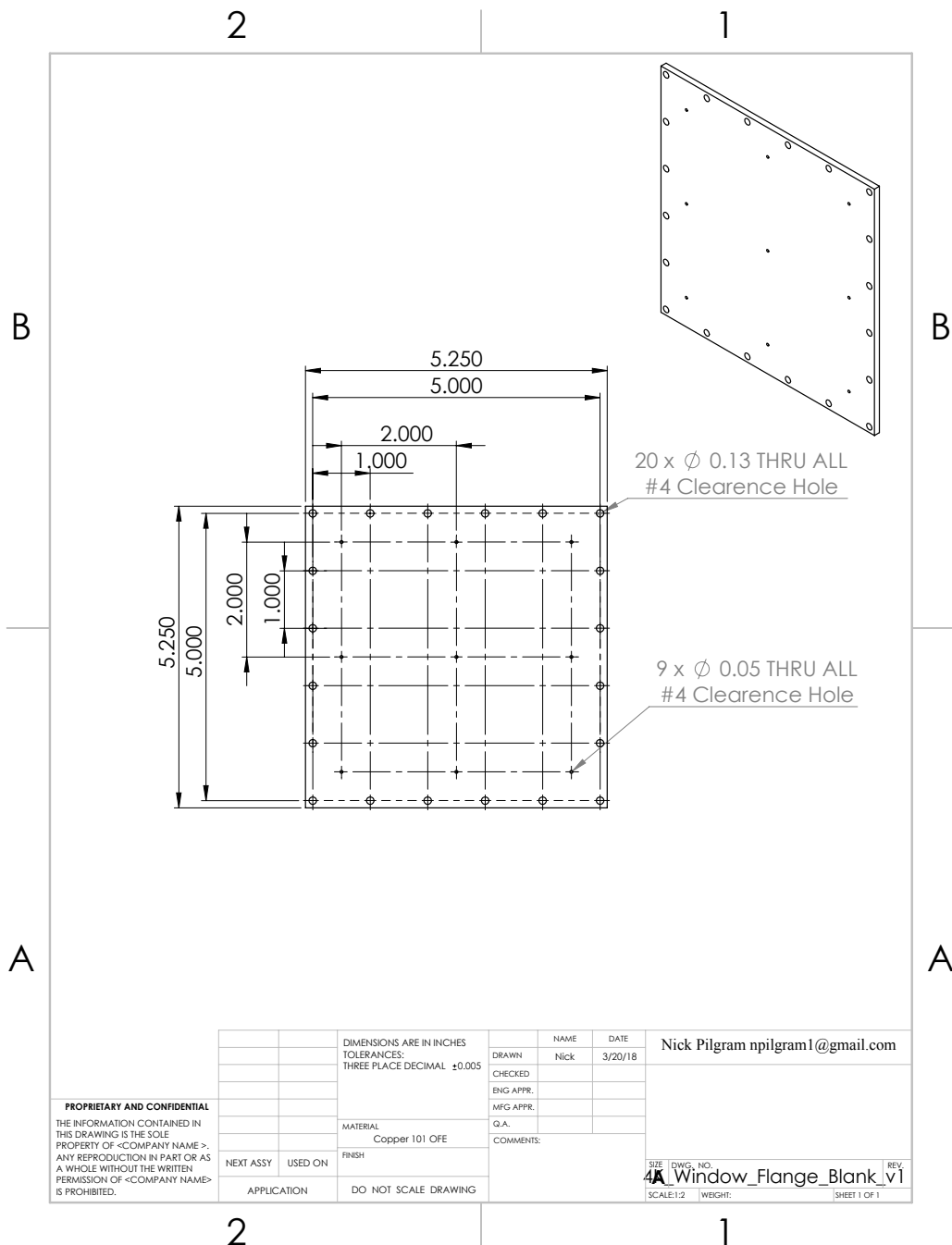


Figure B.25: Blank 4 K side cover flange. This flange is attached to 4 K side plate to cover the square hole.

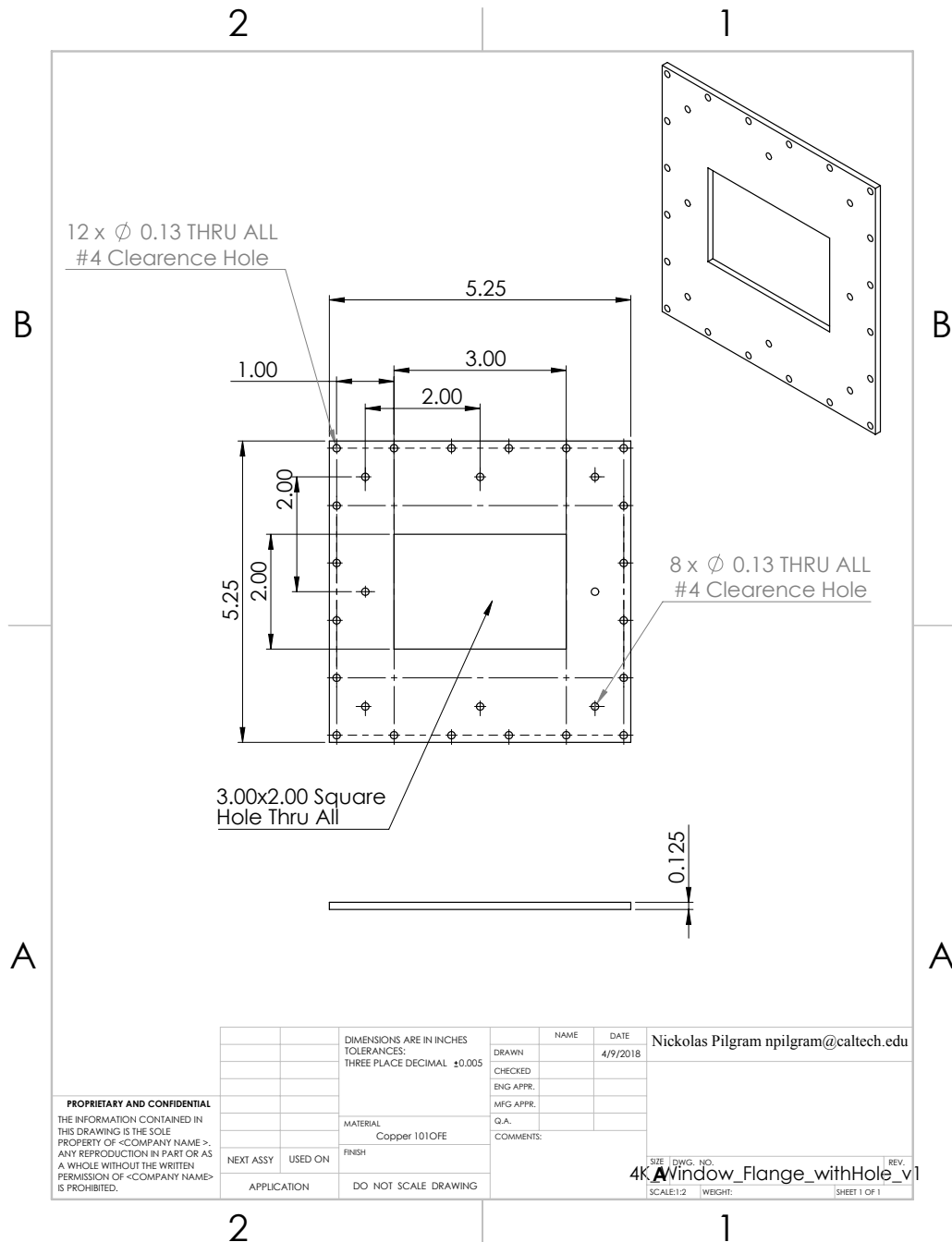


Figure B.26: 4 K side cover flange with window hole. This flange is attached to 4 K side plate to cover the square hole. The window hole provides optical access to the inside of the 4 K shields. It is left open and not covered by a window.

4K_ConnectingBar_Side_v1
Material: Copper 1010FE
Quantity: 4
Contact: Nick Pilgram
npilgram@caltech.edu
12/06/17

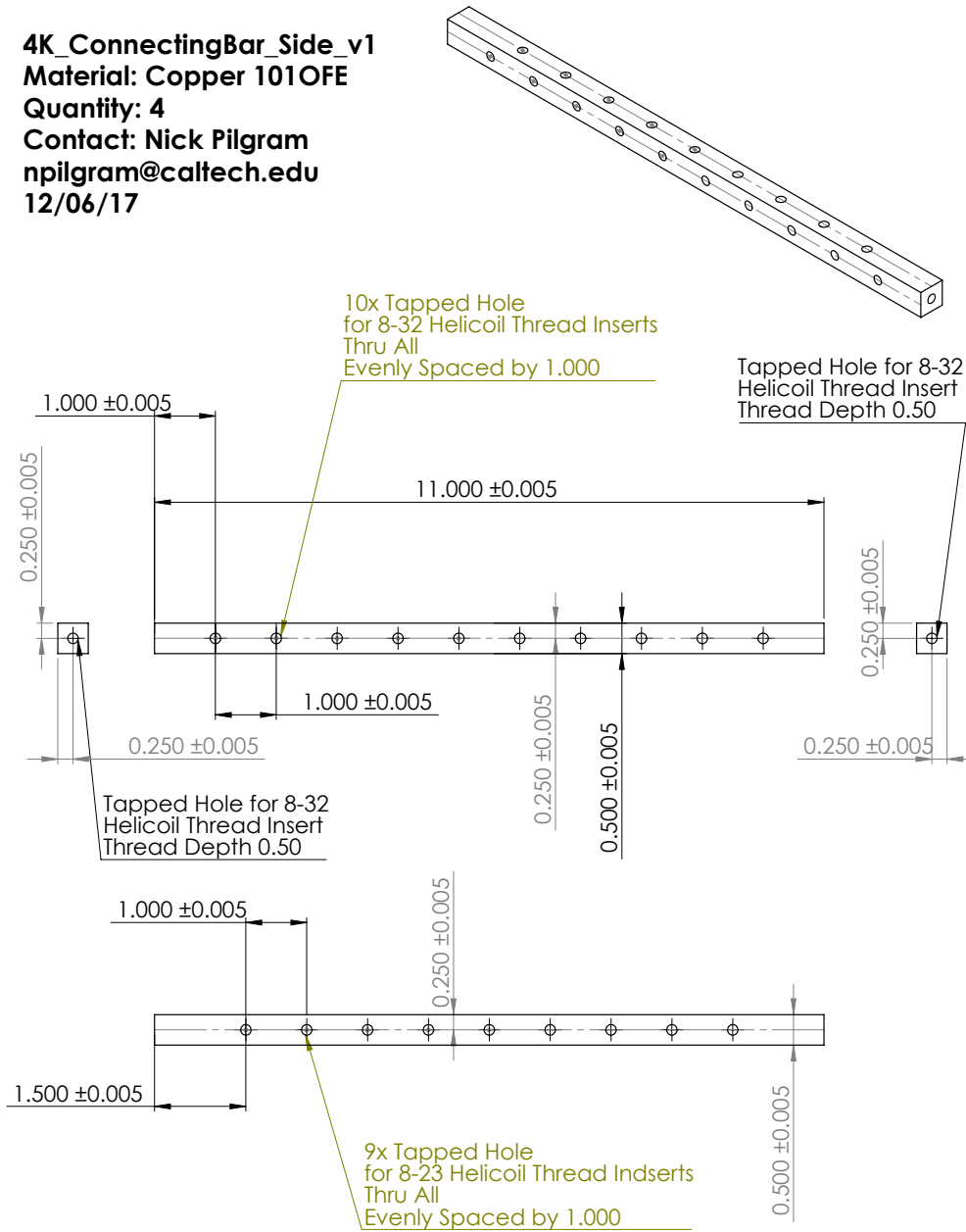


Figure B.27: 4 K vertical connecting bar.

4K_ConnectingBar_TopBottom_v2
Material: Copper 1010FE
Quantity: 8
Contact: Nick Pilgram
npilgram@caltech.edu
12/06/17

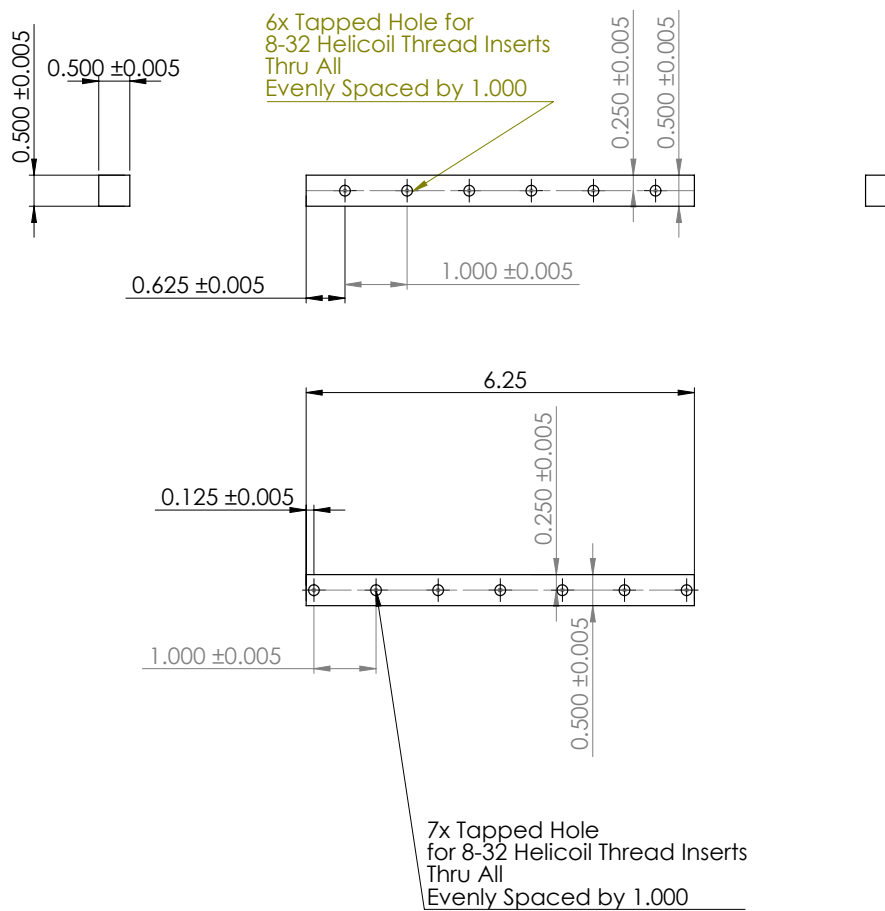
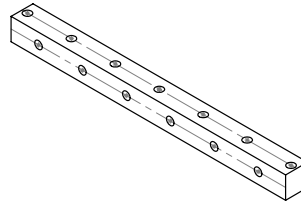


Figure B.28: 4 K horizontal connecting bar.

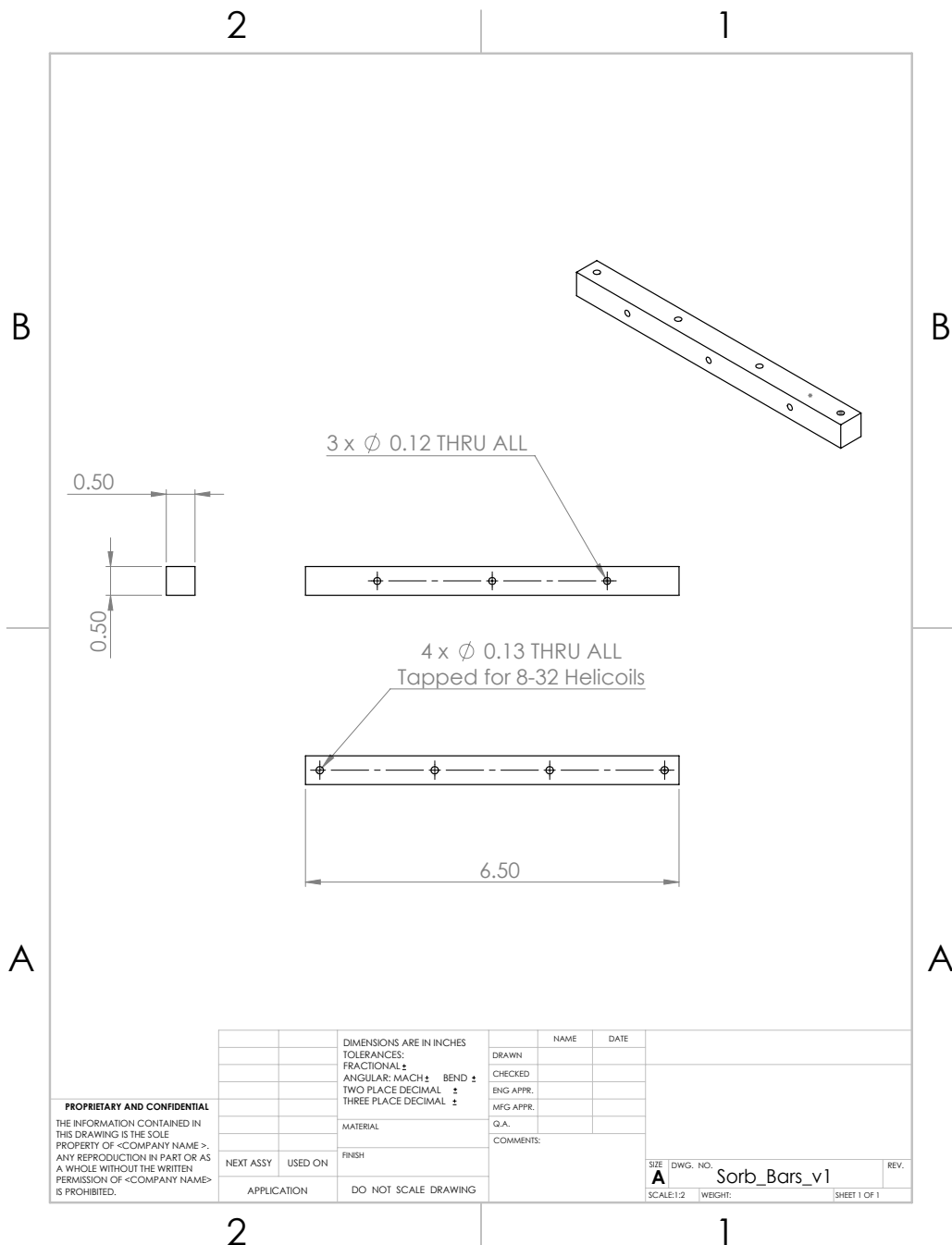


Figure B.29: Sorb bars. The through holes are used to attached to the inside of the 4 K bottom plate. The vertical sorb plates are attached to the side of these bars.

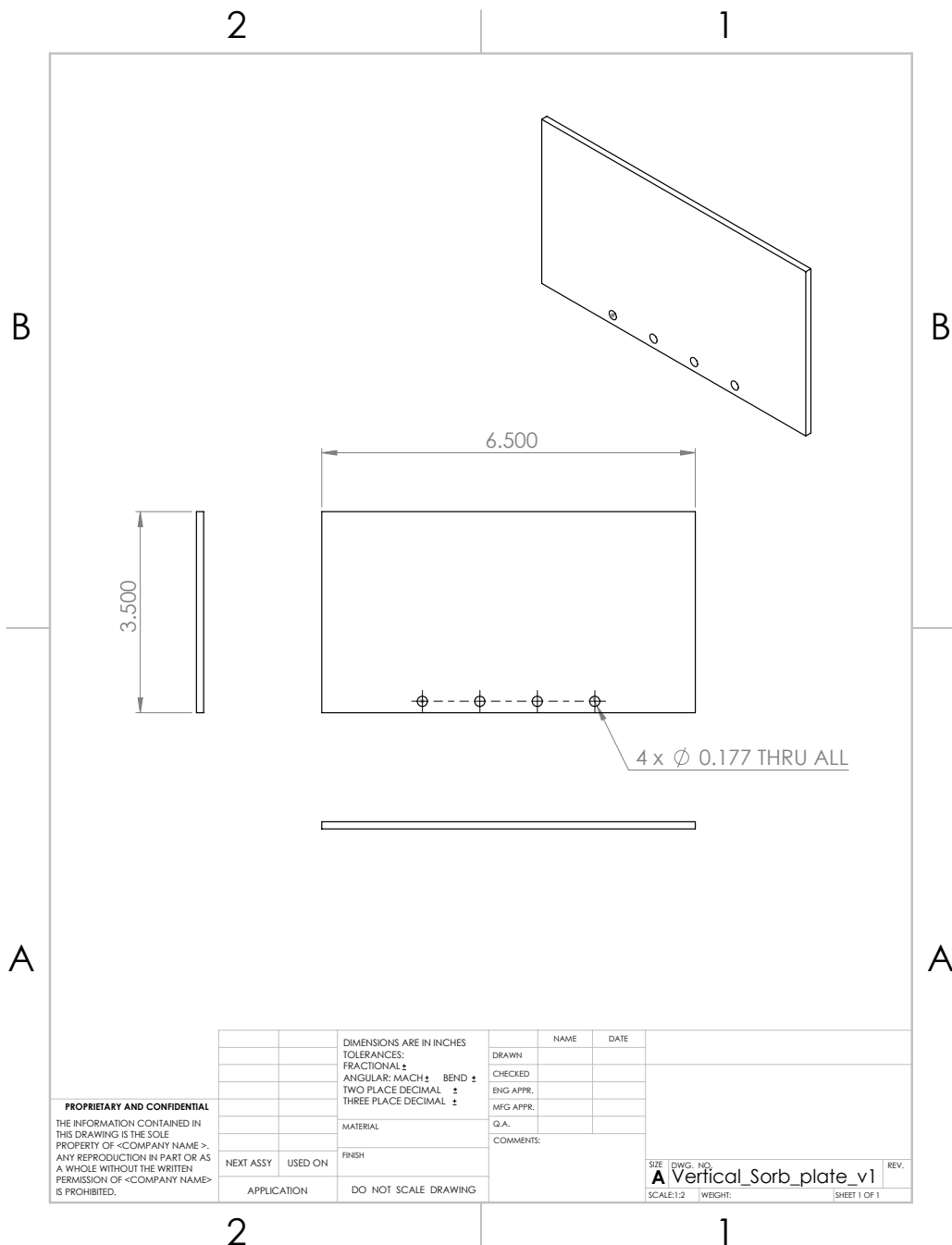


Figure B.30: Vertical sorb plates. Both sides of these plates are coated in activated charcoal for cryopumping.

B.4 Miscellaneous

The drawings for the custom nipple, octagon collar, and the components used to thermally connect to the pulse tube are below.

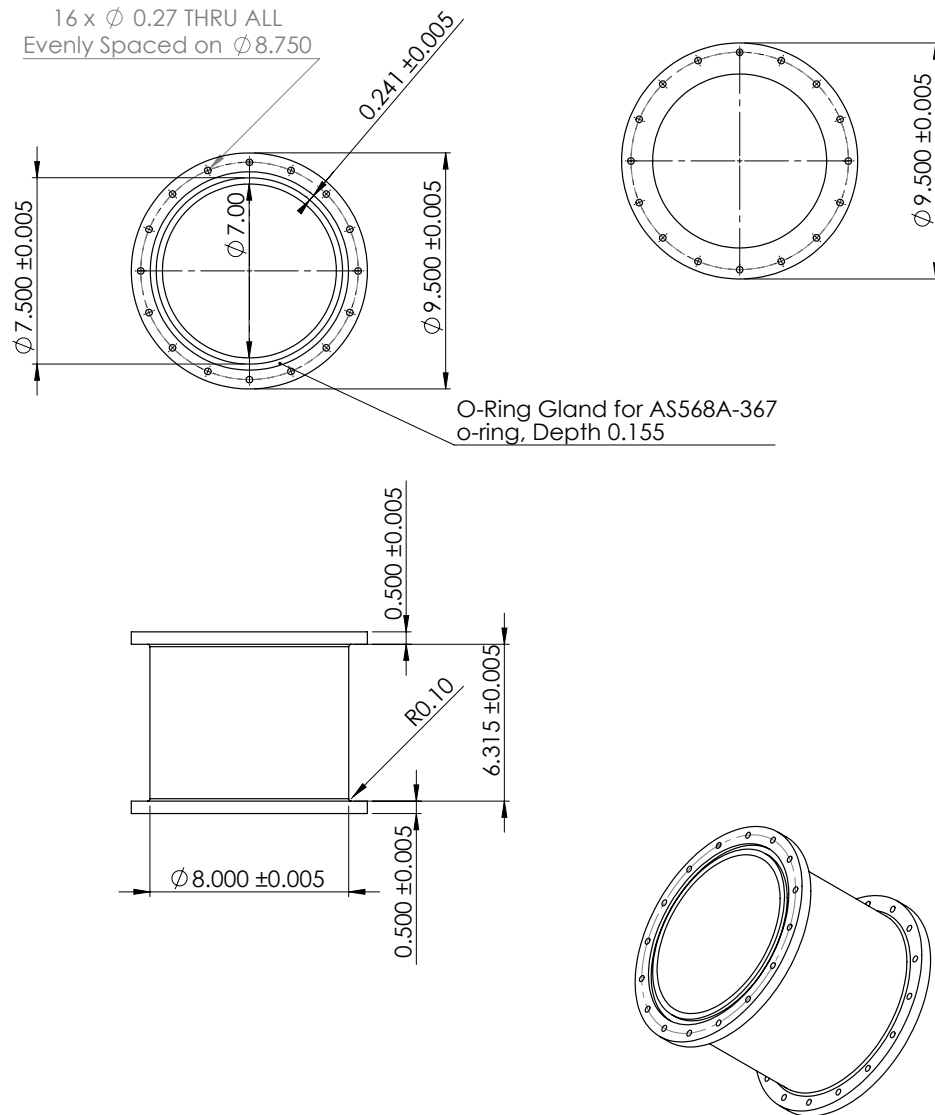


Figure B.31: Custom nipple used to connect the octagon collar and pulse tube to the top of the 300 K chamber.

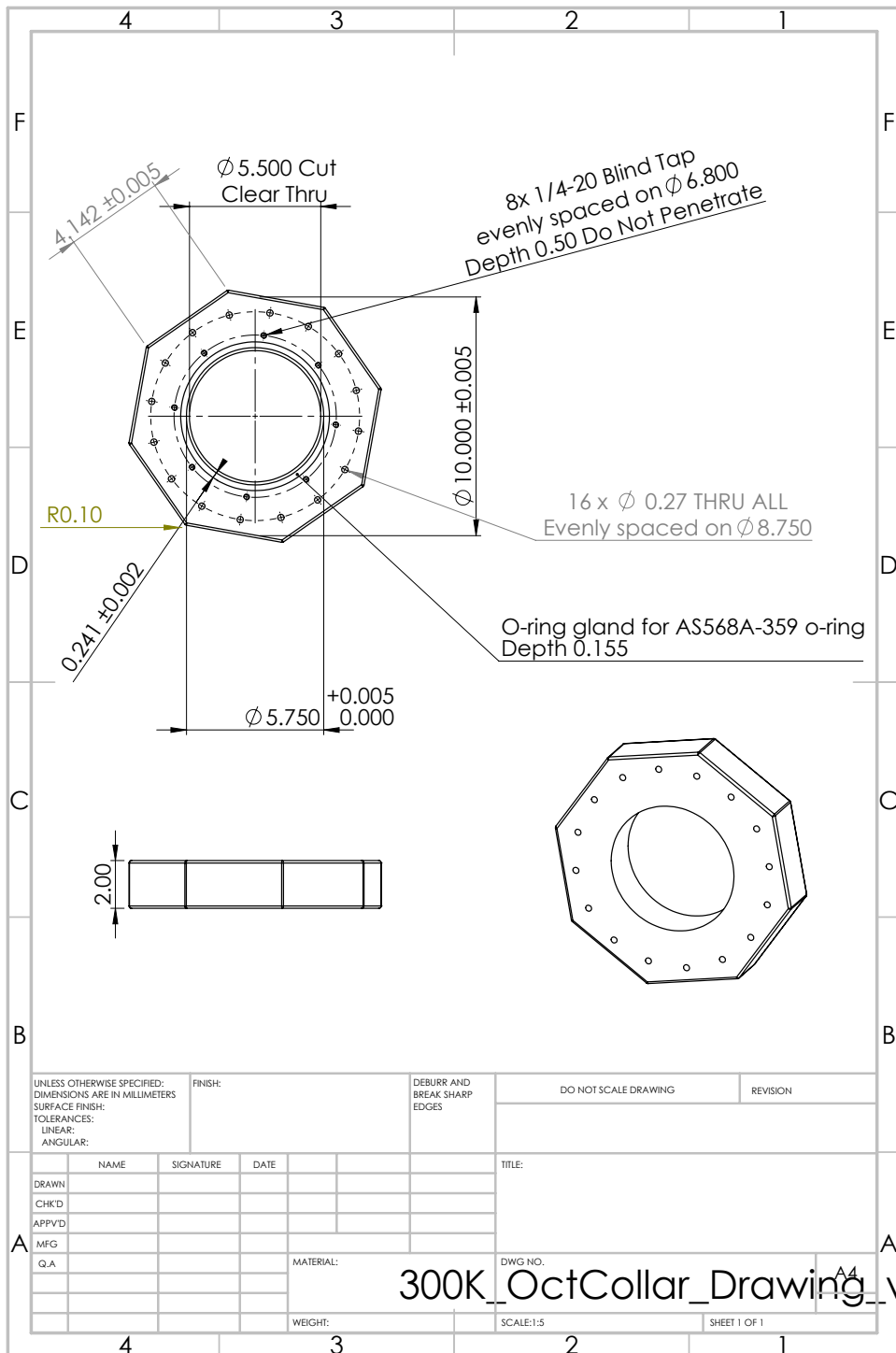


Figure B.32: Octagon collar.

50K_HexPlate_v1
Material: Copper 1010FE
Nick Pilgram
11/29/17

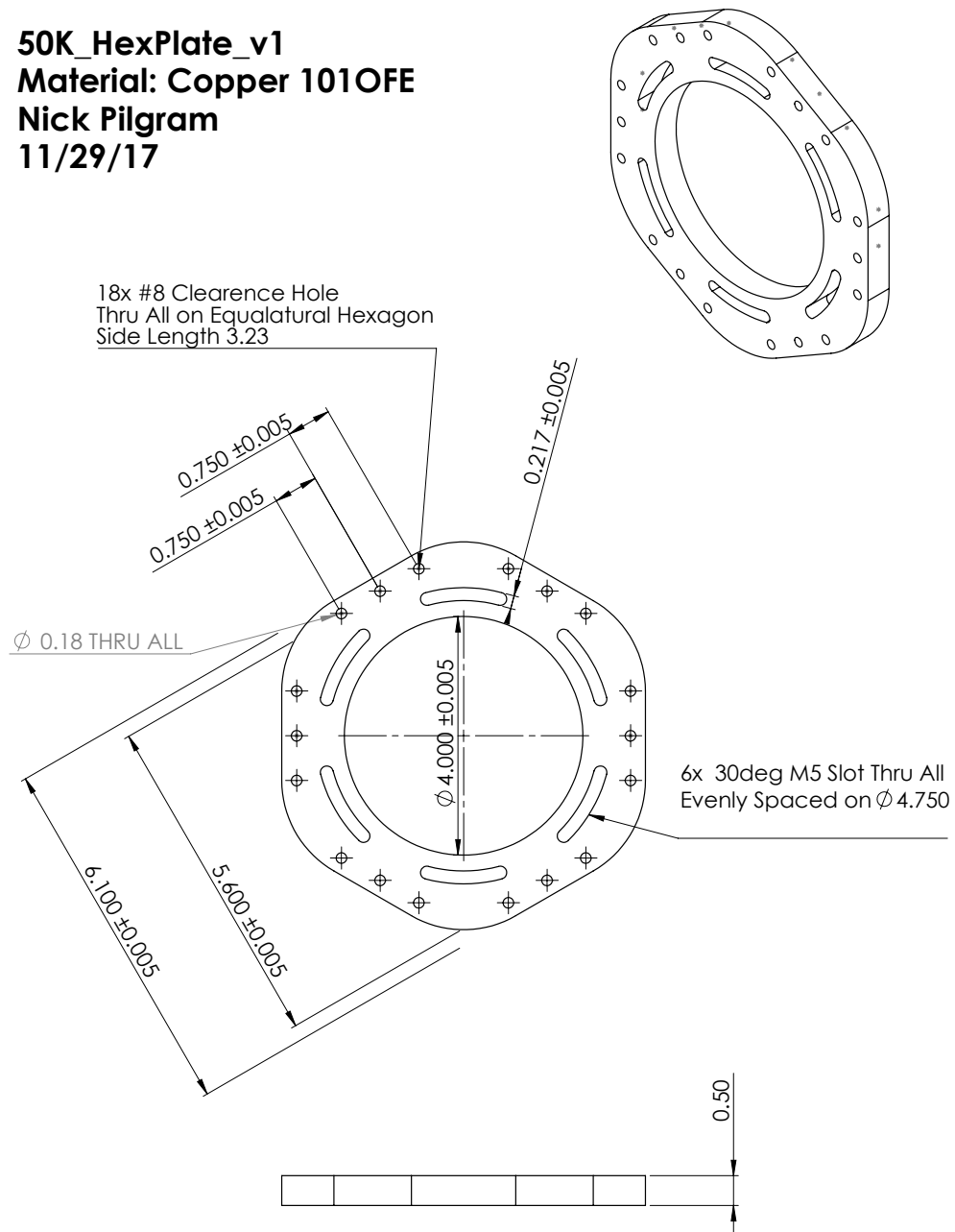


Figure B.33: 50 K hexagonal thermal plate. This plate is attached directly to the 50 K stage of the pulse tube.

50K_Collar_Side_v3
Material: Copper 1010FE
Contact: Nick Pilgram
npilgram@caltech.edu
Updated: 12/11/17
(All Dimensions in inches)

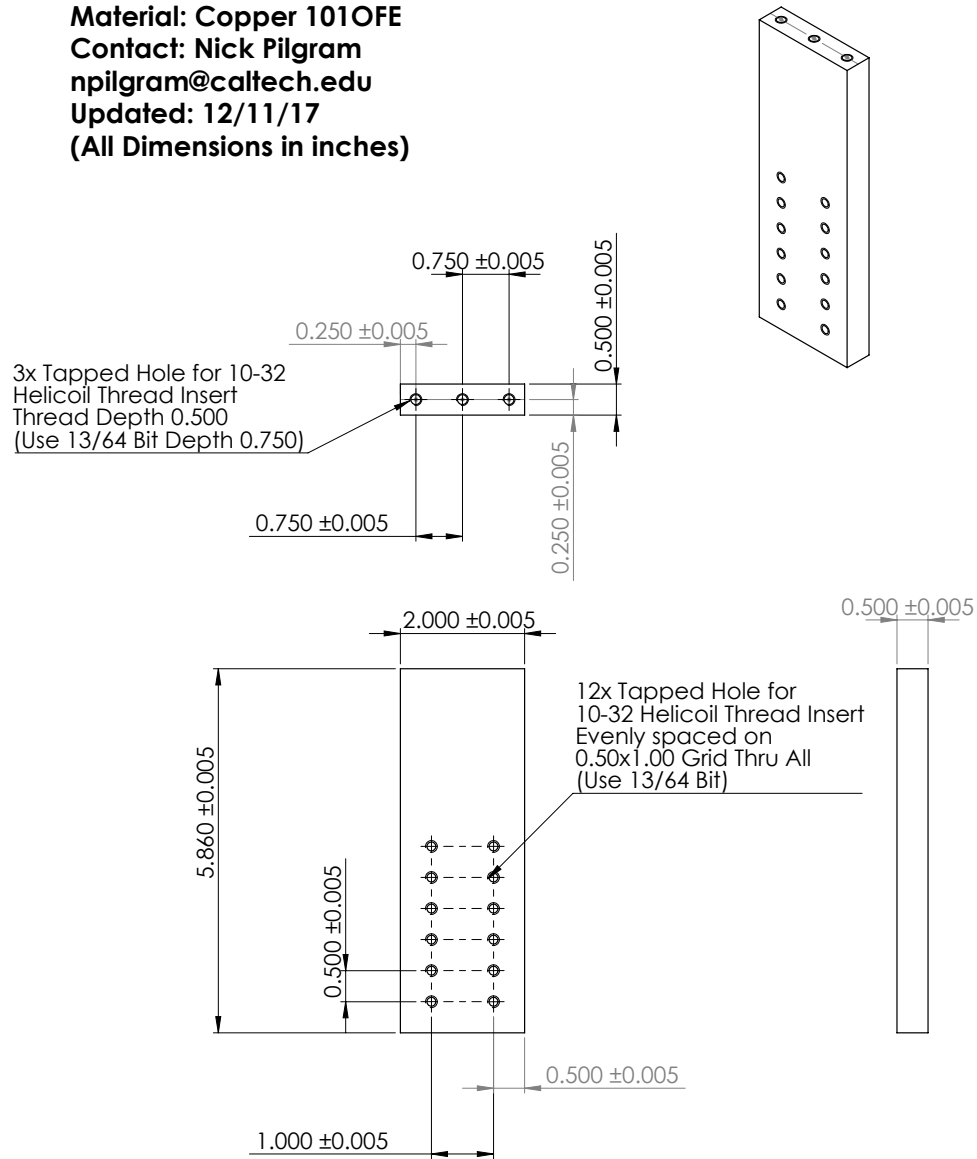


Figure B.34: 50 K extender bar. The top of this bar is attached to the 50 K hexagonal thermal plate.

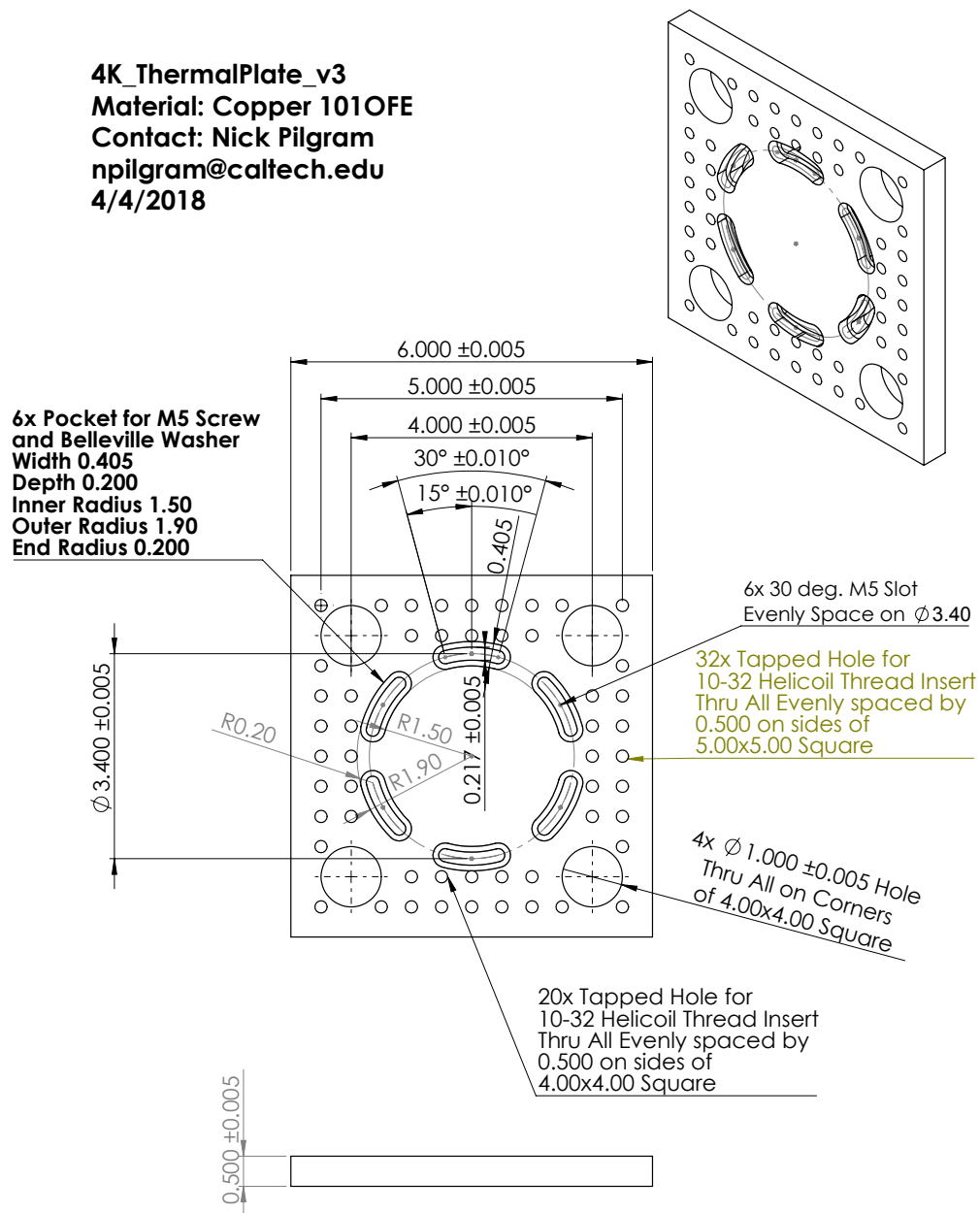


Figure B.35: 4 K thermal plate. This plate is attached directly to the 4 K stage of the pulse tube.

Bibliography

- ¹L. Canetti, M. Drewes, and M. Shaposhnikov, “Matter and antimatter in the universe”, *New Journal of Physics* **14**, 095012 (2012).
- ²A. D. Sakharov, “Violation of CP invariance, C asymmetry, and baryon asymmetry of the universe”, *Sov. Phys. Usp.* **34**, 392 (1991).
- ³A. Hocker and Z. Ligeti, “CP violation and the CKM matrix”, *Annual Review of Nuclear and Particle Science* **56**, 501–567 (2006).
- ⁴M. Dine and A. Kusenko, “Origin of the matter-antimatter asymmetry”, *Reviews of Modern Physics* **76**, 1–30 (2003).
- ⁵M. Gavela, P. Hernandez, J. Orloff, O. Péne, and C. Quimbay, “Standard model CP-violation and baryon asymmetry (II). Finite temperature”, *Nuclear Physics B* **430**, 382–426 (1994).
- ⁶C. S. Wu, E. Ambler, R. W. Hayward, D. D. Hoppes, and R. P. Hudson, “Experimental Test of Parity Conservation in Beta Decay”, *Physical Review* **105**, 1413–1415 (1957).
- ⁷J. P. Lees et al., “Observation of Time-Reversal Violation in the B^0 Meson System”, *Physical Review Letters* **109**, 211801 (2012).
- ⁸J. I. Friedman and V. L. Telegdi, “Nuclear Emulsion Evidence for Parity Nonconservation in the Decay Chain $\pi^+ \rightarrow \mu^+ \rightarrow e^+$ ”, *Physical Review* **106**, 1290–1293 (1957).
- ⁹I. B. Khriplovich and S. K. Lamoreaux, *CP Violation Without Strangeness* (Springer Berlin Heidelberg, Berlin, Heidelberg, 1997).
- ¹⁰M. Pospelov and A. Ritz, “Electric dipole moments as probes of new physics”, *Annals of Physics* **318**, 119–169 (2005).
- ¹¹J. Engel, M. J. Ramsey-Musolf, and U. van Kolck, “Electric Dipole Moments of Nucleons, Nuclei, and Atoms: The Standard Model and Beyond”, *Progress in Particle and Nuclear Physics* **71**, 21–74 (2013).
- ¹²T. Fukuyama, “Searching for New Physics Beyond the Standard Model In Electric Dipole Moment”, *International Journal of Modern Physics A* **27**, 1230015 (2012).
- ¹³J. L. Feng, “Naturalness and the Status of Supersymmetry”, *Annual Review of Nuclear and Particle Science* **63**, 351–382 (2013).
- ¹⁴M. Pospelov and I. Khriplovich, “Electric dipole moment of the W boson and the electron in the Kobayashi-Maskawa model”, *Soviet Journal of Nuclear Physics* **53**, 638–640 (1991).
- ¹⁵M. Pospelov and A. Ritz, “CKM benchmarks for electron electric dipole moment experiments”, *Physical Review D* **89**, 056006 (2014).

- ¹⁶Z. Lasner, “Order-of-magnitude-tighter bound on the electron electric dipole moment” (Yale University, 2019).
- ¹⁷R. Alarcon et al., “Electric dipole moments and the search for new physics”, arXiv [arXiv:2203.08103v2](https://arxiv.org/abs/2203.08103v2) (2022).
- ¹⁸J. Alexander et al., “The storage ring proton EDM experiment”, arXiv [arXiv:2205.00830](https://arxiv.org/abs/2205.00830) (2022).
- ¹⁹M. W. Ahmed et al., “A new cryogenic apparatus to search for the neutron electric dipole moment”, *Journal of Instrumentation* **14**, P11017–P11017 (2019).
- ²⁰N. J. Ayres et al., “The design of the n2EDM experiment: nEDM Collaboration”, *The European Physical Journal C* **81**, 512 (2021).
- ²¹T. M. Ito et al., “Performance of the upgraded ultracold neutron source at Los Alamos National Laboratory and its implication for a possible neutron electric dipole moment experiment”, *Physical Review C* **97**, 012501 (2018).
- ²²J. Martin, “Current status of neutron electric dipole moment experiments”, *Journal of Physics: Conference Series* **1643**, 012002 (2020).
- ²³D. Wurm et al., “The PanEDM neutron electric dipole moment experiment at the ILL”, *EPJ Web of Conferences* **219**, 02006 (2019).
- ²⁴V. V. Flambaum and J. S. M. Ginges, “Nuclear Schiff moment and time-invariance violation in atoms”, *Physical Review A* **65**, 032113 (2002).
- ²⁵M. Bishof, R. H. Parker, K. G. Bailey, J. P. Greene, R. J. Holt, M. R. Kalita, W. Korsch, N. D. Lemke, Z.-T. Lu, P. Mueller, T. P. O’Connor, J. T. Singh, and M. R. Dietrich, “Improved limit on the ²²⁵Ra electric dipole moment”, *Physical Review C* **94**, 025501 (2016).
- ²⁶N. Sachdeva, I. Fan, E. Babcock, M. Burghoff, T. E. Chupp, S. Degenkolb, P. Fierlinger, S. Haude, E. Kraegelloh, W. Kilian, S. Knappe-Grüneberg, F. Kuchler, T. Liu, M. Marino, J. Meinel, K. Rolfs, Z. Salhi, A. Schnabel, J. T. Singh, S. Stuibler, W. A. Terrano, L. Trahms, and J. Voigt, “New Limit on the Permanent Electric Dipole Moment of ¹²⁹Xe Using ³He Comagnetometry and SQUID Detection”, *Physical Review Letters* **123**, 143003 (2019).
- ²⁷F. Allmendinger, I. Engin, W. Heil, S. Karpuk, H.-J. Krause, B. Niederländer, A. Offenhäusser, M. Repetto, U. Schmidt, and S. Zimmer, “Measurement of the permanent electric dipole moment of the ¹²⁹Xe atom”, *Physical Review A* **100**, 022505 (2019).
- ²⁸E. R. Tardiff, E. T. Rand, G. C. Ball, T. E. Chupp, A. B. Garnsworthy, P. Garrett, M. E. Hayden, C. A. Kierans, W. Lorenzon, M. R. Pearson, C. Schaub, and C. E. Svensson, “The radon EDM apparatus”, *Hyperfine Interactions* **225**, 197–206 (2014).

- ²⁹O. Grasdijk, O. Timgren, J. Kastelic, T. Wright, S. Lamoreaux, D. Demille, K. Wenz, M. Aitken, T. Zelevinsky, T. Winick, and D. Kawall, “CeNTREX: A new search for time-reversal symmetry violation in the ^{205}Tl nucleus”, *Quantum Science and Technology* **6**, 044007 (2021).
- ³⁰R. F. Garcia Ruiz, R. Berger, J. Billowes, C. L. Binnersley, M. L. Bissell, A. A. Breier, A. J. Brinson, K. Chrysalidis, T. E. Cocolios, B. S. Cooper, K. T. Flanagan, T. F. Giesen, R. P. de Groote, S. Franchoo, F. P. Gustafsson, T. A. Isaev, Á. Koszorús, G. Neyens, H. A. Perrett, C. M. Ricketts, S. Rothe, L. Schweikhard, A. R. Vernon, K. D. A. Wendt, F. Wienholtz, S. G. Wilkins, and X. F. Yang, “Spectroscopy of short-lived radioactive molecules”, *Nature* **581**, 396–400 (2020).
- ³¹I. Khriplovich, “The limit on the proton electric dipole moment derived from atomic experiments.”, *Soviet Journal of Experimental and Theoretical Physics* **71**, 51–60 (1976).
- ³²V. Flambaum, “Spin hedgehog and collective magnetic quadrupole moments induced by parity and time invariance violating interaction”, *Physics Letters B* **320**, 211–215 (1994).
- ³³V. V. Flambaum, D. DeMille, and M. G. Kozlov, “Time-Reversal Symmetry Violation in Molecules Induced by Nuclear Magnetic Quadrupole Moments”, *Physical Review Letters* **113**, 103003 (2014).
- ³⁴S. A. Murthy, D. Krause, Z. L. Li, and L. R. Hunter, “New limits on the electron electric dipole moment from cesium”, *Physical Review Letters* **63**, 965–968 (1989).
- ³⁵L. I. Schiff, “Measurability of Nuclear Electric Dipole Moments”, *Physical Review* **132**, 2194–2200 (1963).
- ³⁶E. D. Commins, J. D. Jackson, and D. P. DeMille, “The electric dipole moment of the electron: An intuitive explanation for the evasion of Schiff’s theorem”, *American Journal of Physics* **75**, 532–536 (2007).
- ³⁷M. S. Safronova, D. Budker, D. DeMille, D. F. J. Kimball, A. Derevianko, and C. W. Clark, “Search for new physics with atoms and molecules”, *Reviews of Modern Physics* **90**, 025008 (2018).
- ³⁸P. Sandars, “The electric dipole moment of an atom”, *Physics Letters* **14**, 194–196 (1965).
- ³⁹N. R. Hutzler, “Polyatomic molecules as quantum sensors for fundamental physics”, *Quantum Science and Technology* **5**, 044011 (2020).
- ⁴⁰R. A. Ready, G. Arrowsmith-Kron, K. G. Bailey, D. Battaglia, M. Bishof, D. Coulter, M. R. Dietrich, R. Fang, B. Hanley, J. Huneau, S. Kennedy, P. Lalain, B. Loseth, K. McGee, P. Mueller, T. P. O’Connor, J. O’Kronley, A. Powers, T. Rabga, A. Sanchez, E. Schalk, D. Waldo, J. Wescott, and J. T. Singh, “Surface processing and discharge-conditioning of high voltage electrodes for the Ra EDM experiment”, *Nuclear Instruments and Methods in Physics Research Section A*:

- Accelerators, Spectrometers, Detectors and Associated Equipment **1014**, 165738 (2021).
- ⁴¹ACME Collaboration, “Improved limit on the electric dipole moment of the electron”, *Nature* **562**, 355–360 (2018).
- ⁴²W. B. Cairncross, D. N. Gresh, M. Grau, K. C. Cossel, T. S. Roussy, Y. Ni, Y. Zhou, J. Ye, and E. A. Cornell, “A precision measurement of the electron’s electric dipole moment using trapped molecular ions”, *Physical Review Letters* **119**, 153001 (2017).
- ⁴³N. J. Fitch, J. Lim, E. A. Hinds, B. E. Sauer, and M. R. Tarbutt, “Methods for measuring the electron’s electric dipole moment using ultracold YbF molecules”, *Quantum Science and Technology* **6**, 014006 (2021).
- ⁴⁴X. Wu, Z. Han, J. Chow, D. G. Ang, C. Meisenhelder, C. D. Panda, E. P. West, G. Gabrielse, J. M. Doyle, and D. DeMille, “The metastable $Q^3 \Delta_2$ state of ThO: a new resource for the ACME electron EDM search”, *New Journal of Physics* **22**, 023013 (2020).
- ⁴⁵Y. Zhou, Y. Shagam, W. B. Cairncross, K. B. Ng, T. S. Roussy, T. Grogan, K. Boyce, A. Vigil, M. Pettine, T. Zelevinsky, J. Ye, and E. A. Cornell, “Second-Scale Coherence Measured at the Quantum Projection Noise Limit with Hundreds of Molecular Ions”, *Physical Review Letters* **124**, 053201 (2020).
- ⁴⁶The NL-eEDM collaboration, P. Aggarwal, H. L. Bethlem, A. Borschevsky, M. Denis, K. Esajas, P. A. B. Haase, Y. Hao, S. Hoekstra, K. Jungmann, T. B. Meijknecht, M. C. Mooij, R. G. E. Timmermans, W. Ubachs, L. Willmann, and A. Zapara, “Measuring the electric dipole moment of the electron in BaF”, *The European Physical Journal D* **72**, 197 (2018).
- ⁴⁷A. C. Vutha, “A search for the electric dipole moment of the electron using thorium monoxide” (Yale University, 2011).
- ⁴⁸E. S. Shuman, J. F. Barry, and D. DeMille, “Laser cooling of a diatomic molecule”, *Nature* **467**, 820–823 (2010).
- ⁴⁹V. Zhelyazkova, A. Cournol, T. E. Wall, A. Matsushima, J. J. Hudson, E. A. Hinds, M. R. Tarbutt, and B. E. Sauer, “Laser cooling and slowing of CaF molecules”, *Physical Review A* **89**, 053416 (2014).
- ⁵⁰M. T. Hummon, M. Yeo, B. K. Stuhl, A. L. Collopy, Y. Xia, and J. Ye, “2D Magneto-Optical Trapping of Diatomic Molecules”, *Physical Review Letters* **110**, 143001 (2013).
- ⁵¹R. L. McNally, I. Kozyryev, S. Vazquez-Carson, K. Wenz, T. Wang, and T. Zelevinsky, “Optical cycling, radiative deflection and laser cooling of barium monohydride ($^{138}\text{Ba}^1\text{H}$)”, *New Journal of Physics* **22**, 083047 (2020).

- ⁵²J. Lim, J. R. Almond, M. A. Trigatzis, J. A. Devlin, N. J. Fitch, B. E. Sauer, M. R. Tarbutt, and E. A. Hinds, “Laser Cooled YbF Molecules for Measuring the Electron’s Electric Dipole Moment”, *Physical Review Letters* **120**, 123201 (2018).
- ⁵³I. Kozyryev, L. Baum, K. Matsuda, B. L. Augenbraun, L. Anderegg, A. P. Sedlack, and J. M. Doyle, “Sisyphus Laser Cooling of a Polyatomic Molecule”, *Physical Review Letters* **118**, 173201 (2017).
- ⁵⁴B. L. Augenbraun, Z. D. Lasner, A. Frenett, H. Sawaoka, C. Miller, T. C. Steimle, and J. M. Doyle, “Laser-cooled polyatomic molecules for improved electron electric dipole moment searches”, *New Journal of Physics* **22**, 022003 (2020).
- ⁵⁵L. Baum, N. B. Vilas, C. Hallas, B. L. Augenbraun, S. Raval, D. Mitra, and J. M. Doyle, “1D Magneto-Optical Trap of Polyatomic Molecules”, *Physical Review Letters* **124**, 133201 (2020).
- ⁵⁶D. Mitra, N. B. Vilas, C. Hallas, L. Anderegg, B. L. Augenbraun, L. Baum, C. Miller, S. Raval, and J. M. Doyle, “Direct laser cooling of a symmetric top molecule”, *Science* **369**, 1366–1369 (2020).
- ⁵⁷L. Anderegg, B. L. Augenbraun, E. Chae, B. Hemmerling, N. R. Hutzler, A. Ravi, A. Collopy, J. Ye, W. Ketterle, and J. M. Doyle, “Radio Frequency Magneto-Optical Trapping of CaF with High Density”, *Physical Review Letters* **119**, 103201 (2017).
- ⁵⁸S. Ding, Y. Wu, I. A. Finneran, J. J. Bureau, and J. Ye, “Sub-Doppler Cooling and Compressed Trapping of YO Molecules at μ K Temperatures”, *Physical Review X* **10**, 021049 (2020).
- ⁵⁹J. F. Barry, D. J. McCarron, E. B. Norrgard, M. H. Steinecker, and D. DeMille, “Magneto-optical trapping of a diatomic molecule”, *Nature* **512**, 286–289 (2014).
- ⁶⁰N. B. Vilas, C. Hallas, L. Anderegg, P. Robichaud, A. Winnicki, D. Mitra, and J. M. Doyle, “Magneto-optical trapping and sub-Doppler cooling of a polyatomic molecule”, *Nature* **606**, 70–74 (2022).
- ⁶¹L. Anderegg, L. W. Cheuk, Y. Bao, S. Burchesky, W. Ketterle, K.-K. Ni, and J. M. Doyle, “An optical tweezer array of ultracold molecules”, *Science* **365**, 1156–1158 (2019).
- ⁶²L. Caldwell, H. J. Williams, N. J. Fitch, J. Aldegunde, J. M. Hutson, B. E. Sauer, and M. R. Tarbutt, “Long Rotational Coherence Times of Molecules in a Magnetic Trap”, *Physical Review Letters* **124**, 063001 (2020).
- ⁶³T. K. Langin, V. Jorapur, Y. Zhu, Q. Wang, and D. DeMille, “Polarization Enhanced Deep Optical Dipole Trapping of Λ -Cooled Polar Molecules”, *Physical Review Letters* **127**, 163201 (2021).
- ⁶⁴Y. Lu, C. M. Holland, and L. W. Cheuk, “Molecular Laser Cooling in a Dynamically Tunable Repulsive Optical Trap”, *Physical Review Letters* **128**, 213201 (2022).

- ⁶⁵D. J. McCarron, M. H. Steinecker, Y. Zhu, and D. DeMille, “Magnetic Trapping of an Ultracold Gas of Polar Molecules”, *Physical Review Letters* **121**, 013202 (2018).
- ⁶⁶Y. Wu, J. J. Bureau, K. Mehling, J. Ye, and S. Ding, “High Phase-Space Density of Laser-Cooled Molecules in an Optical Lattice”, *Physical Review Letters* **127**, 263201 (2021).
- ⁶⁷I. Kozyryev and N. R. Hutzler, “Precision Measurement of Time-Reversal Symmetry Violation with Laser-Cooled Polyatomic Molecules”, *Physical Review Letters* **119**, 133002 (2017).
- ⁶⁸K. B. Ng, Y. Zhou, L. Cheng, N. Schlossberger, S. Y. Park, T. S. Roussy, L. Caldwell, Y. Shagam, A. J. Vigil, E. A. Cornell, and J. Ye, “Spectroscopy on the electron-electric-dipole-moment-sensitive states of ThF⁺”, *Physical Review A* **105**, 022823 (2022).
- ⁶⁹M. Denis, P. A. B. Haase, R. G. E. Timmermans, E. Eliav, N. R. Hutzler, and A. Borschevsky, “Enhancement factor for the electric dipole moment of the electron in the BaOH and YbOH molecules”, *Physical Review A* **99**, 042512 (2019).
- ⁷⁰M. Denis, Y. Hao, E. Eliav, N. R. Hutzler, M. K. Nayak, R. G. E. Timmermans, and A. Borschevsky, “Enhanced P,T-violating nuclear magnetic quadrupole moment effects in laser-coolable molecules”, *The Journal of Chemical Physics* **152**, 084303 (2020).
- ⁷¹I. Kozyryev, L. Baum, K. Matsuda, P. Olson, B. Hemmerling, and J. M. Doyle, “Collisional relaxation of vibrational states of SrOH with He at 2 K”, *New Journal of Physics* **17**, 045003 (2015).
- ⁷²E. B. Norrgard, D. S. Barker, S. Eckel, J. A. Fedchak, N. N. Klimov, and J. Scherschligt, “Nuclear-spin dependent parity violation in optically trapped polyatomic molecules”, *Communications Physics* **2**, 77 (2019).
- ⁷³W. Demtröder, *Molecular Physics: Theoretical Principles and Experimental Methods* (Weinheim: Wiley-VCH Verlag, 2003).
- ⁷⁴P. Bunker and P. Jensen, *Molecular symmetry and spectroscopy* (NRC Research Press, 2006).
- ⁷⁵T. Azumi and K. Matsuzaki, “What Does the Term “Vibronic Coupling” Mean?”, *Photochemistry and Photobiology* **25**, 315–326 (1977).
- ⁷⁶S. F. Rice, H. Martin, and R. W. Field, “The electronic structure of the calcium monohalides. A ligand field approach”, *The Journal of Chemical Physics* **82**, 5023–5034 (1985).
- ⁷⁷P. Carette and A. Hocquet, “Ligand field calculation of the lower electronic energy levels of the lanthanide monoxides”, *Journal of Molecular Spectroscopy* **131**, 301–324 (1988).

- ⁷⁸H. Schall, M. Dulick, and R. W. Field, “The electronic structure of LaF: A multiconfiguration ligand field calculation”, *The Journal of Chemical Physics* **87**, 2898–2912 (1987).
- ⁷⁹M. J. Dick, “Spectroscopy of selected calcium and strontium containing polyatomic molecules” (University of Waterloo, 2007).
- ⁸⁰P. M. Morse, “Diatomic Molecules According to the Wave Mechanics. II. Vibrational Levels”, *Physical Review* **34**, 57–64 (1929).
- ⁸¹P. F. Bernath, *Spectra of atoms and molecules*, 2nd ed (Oxford University Press, New York, 2005).
- ⁸²G. Herzberg, *Molecular Spectra and Molecular Structure Vol. 2: Infrared and Raman Spectra of Polyatomic Molecules* (New York: Van Nostrand, 1956).
- ⁸³W. Quapp and B. P. Winnewisser, “What you thought you already knew about the bending motion of triatomic molecules”, *Journal of Mathematical Chemistry* **14**, 259–285 (1993).
- ⁸⁴J. Brown, “The Renner-Teller Effect: The Effective Hamiltonian Approach”, in *Computational Molecular Spectroscopy* (John Wiley and Sons, LTD, 2000).
- ⁸⁵E. Hirota, *High-Resolution Spectroscopy of Transient Molecules*, red. by V. I. Goldanskii, R. Gomer, F. P. Schäfer, and J. P. Toennies, Vol. 40, Springer Series in Chemical Physics (Springer Berlin Heidelberg, Berlin, Heidelberg, 1985).
- ⁸⁶J. M. Brown and F. Jørgensen, “Vibronic Energy Levels of a Linear Triatomic Molecule in a Degenerate Electronic State: a Unified Treatment of the Renner-Teller Effect”, in *Advances in Chemical Physics*, edited by I. Prigogine and S. A. Rice (John Wiley & Sons, Inc., Hoboken, NJ, USA, Mar. 14, 2007), pp. 117–180.
- ⁸⁷J. M. Brown, “The rotational dependence of the Renner-Teller interaction: a new term in the effective Hamiltonian for linear triatomic molecules in Π electronic states”, *Molecular Physics* **101**, 3419–3426 (2003).
- ⁸⁸J. T. Hougen, “Rotational Energy Levels of a Linear Triatomic Molecule in a $^2 \Pi$ Electronic State”, *The Journal of Chemical Physics* **36**, 519–534 (1962).
- ⁸⁹J. Brown and A. Carrington, *Rotational spectroscopy of diatomic molecules* (Cambridge Univ. Press, 2003).
- ⁹⁰D. Gillett, “Transient Free Radicals Studied by Laser Magnetic Resonance Spectroscopy” (University of Oxford, 1994).
- ⁹¹B. L. Augenbraun, “Methods for Direct Laser Cooling of Polyatomic Molecules” (Harvard University, 2021).
- ⁹²J. M. Brown, I. Kopp, C. Malmberg, and B. Rydh, “An Analysis of Hyperfine Interactions in the Electronic Spectrum of AlF”, *Physica Scripta* **17**, 55–67 (1978).

- ⁹³S. Nakhate, T. C. Steimle, N. H. Pilgram, and N. R. Hutzler, “The pure rotational spectrum of YbOH”, *Chemical Physics Letters* **715**, 105–108 (2019).
- ⁹⁴J. A. J. Fitzpatrick, F. R. Manby, and C. M. Western, “The interpretation of molecular magnetic hyperfine interactions”, *The Journal of Chemical Physics* **122**, 084312 (2005).
- ⁹⁵C. Zhang, B. L. Augenbraun, Z. D. Lasner, N. B. Vilas, J. M. Doyle, and L. Cheng, “Accurate prediction and measurement of vibronic branching ratios for laser cooling linear polyatomic molecules”, *The Journal of Chemical Physics* **155**, 091101 (2021).
- ⁹⁶R. W. Field, *Spectra and dynamics of small molecules: Alexander von Humboldt lectures*, Lecture Notes in Physics 900 (Springer, Cham, 2015), 153 pp.
- ⁹⁷J. F. Barry, “Laser cooling and slowing of a diatomic molecule” (Yale University, 2013).
- ⁹⁸M. R. Tarbutt, “Laser cooling of molecules”, *Contemporary Physics* **59**, 356–376 (2018).
- ⁹⁹D. McCarron, “Laser cooling and trapping molecules”, *Journal of Physics B: Atomic, Molecular and Optical Physics* **51**, 212001 (2018).
- ¹⁰⁰B. K. Stuhl, B. C. Sawyer, D. Wang, and J. Ye, “Magneto-optical Trap for Polar Molecules”, *Physical Review Letters* **101**, 243002 (2008).
- ¹⁰¹S. Hofsässs, M. Doppelbauer, S. C. Wright, S. Kray, B. G. Sartakov, J. Pérez-Ríos, G. Meijer, and S. Truppe, “Optical cycling of AIF molecules”, *New Journal of Physics* **23**, 075001 (2021).
- ¹⁰²T. N. Lewis, C. Wang, J. R. Daniel, M. Dhital, C. J. Bardeen, and B. Hemmerling, “Optimizing pulsed-laser ablation production of AlCl molecules for laser cooling”, *Physical Chemistry Chemical Physics* **23**, 22785–22793 (2021).
- ¹⁰³J. C. Schnaubelt, J. C. Shaw, and D. J. McCarron, “Cold CH radicals for laser cooling and trapping”, arXiv **arXiv:2109.03953** (2021).
- ¹⁰⁴P. Yu, A. Lopez, W. A. Goddard III, and N. R. Hutzler, “Multivalent optical cycling centers in polyatomic molecules”, arXiv **arXiv:2205.11860** (2022).
- ¹⁰⁵T. C. Melville and J. A. Coxon, “The visible laser excitation spectrum of YbOH: The $A^2\Pi-X^2\Sigma^+$ ”, *The Journal of Chemical Physics* **115**, 6974–6978 (2001).
- ¹⁰⁶J. Coxon and C. Linton, “Re-analysis of the 000 – 000 and 000 – 100 bands in the $A^2\Pi_{1/2}-X^2\Sigma^+$ system of YbOH: Revised estimates of the ground state spin-rotation splitting parameters”, *Journal of Molecular Spectroscopy* **367**, 111242 (2020).
- ¹⁰⁷C. Zhang, B. L. Augenbraun, Z. D. Lasner, N. B. Vilas, J. M. Doyle, and L. Cheng, “Accurate prediction and measurement of vibronic branching ratios for laser cooling linear polyatomic molecules”, *The Journal of Chemical Physics* **155**, 091101 (2021).

- ¹⁰⁸N. R. Hutzler, H.-I. Lu, and J. M. Doyle, “The Buffer Gas Beam: An Intense, Cold, and Slow Source for Atoms and Molecules”, *Chemical Reviews* **112**, 4803–4827 (2012).
- ¹⁰⁹J. Doyle and W. Campbell, “Cooling, Trap Loading, and Beam Production Using a Cryogenic Helium Buffer Gas”, in *Cold Molecules*, edited by W. Stwalley, R. Krems, and B. Friedrich (CRC Press, June 25, 2009).
- ¹¹⁰J. F. Barry, E. S. Shuman, and D. DeMille, “A bright, slow cryogenic molecular beam source for free radicals”, *Physical Chemistry Chemical Physics* **13**, 18936 (2011).
- ¹¹¹H.-I. Lu, J. Rasmussen, M. J. Wright, D. Patterson, and J. M. Doyle, “A cold and slow molecular beam”, *Physical Chemistry Chemical Physics* **13**, 18986 (2011).
- ¹¹²S. Truppe, M. Hambach, S. M. Skoff, N. E. Bulleid, J. S. Bumby, R. J. Hendricks, E. A. Hinds, B. E. Sauer, and M. R. Tarbutt, “A buffer gas beam source for short, intense and slow molecular pulses”, *Journal of Modern Optics* **65**, 648–656 (2018).
- ¹¹³D. Patterson, E. Tsikata, and J. M. Doyle, “Cooling and collisions of large gas phase molecules”, *Physical Chemistry Chemical Physics* **12**, 9736 (2010).
- ¹¹⁴D. Patterson and J. M. Doyle, “Bright, guided molecular beam with hydrodynamic enhancement”, *The Journal of Chemical Physics* **126**, 154307 (2007).
- ¹¹⁵C. J. Foot, *Atomic physics*, Oxford Master Series in Physics 7. Atomic, Optical, and laser physics (Oxford University Press, Oxford ; New York, 2005), 331 pp.
- ¹¹⁶T. C. Steimle, C. Linton, E. T. Mengesha, X. Bai, and A. T. Le, “Field-free, Stark, and Zeeman spectroscopy of the $A^2\Pi_{1/2} - X^2\Sigma^+$ transition of ytterbium monohydroxide”, *Physical Review A* **100**, 052509 (2019).
- ¹¹⁷T. C. Steimle, R. Zhang, and M. C. Heaven, “The pure rotational spectrum of thorium monosulfide, ThS”, *Chemical Physics Letters* **639**, 304–306 (2015).
- ¹¹⁸F. Wang and T. C. Steimle, “Tungsten monocarbide, WC: Pure rotational spectrum and ^{13}C hyperfine interaction”, *The Journal of Chemical Physics* **136**, 044312 (2012).
- ¹¹⁹C. S. Dickinson, J. A. Coxon, N. R. Walker, and M. C. L. Gerry, “Fourier transform microwave spectroscopy of the $^2\Sigma^+$ ground states of YbX (X=F, Cl, Br): Characterization of hyperfine effects and determination of the molecular geometries”, *The Journal of Chemical Physics* **115**, 6979–6989 (2001).
- ¹²⁰J. Tandy, J.-G. Wang, and P. Bernath, “High-resolution laser spectroscopy of BaOH and BaOD: Anomalous spin-orbit coupling in the state”, *Journal of Molecular Spectroscopy* **255**, 63–67 (2009).
- ¹²¹T. C. Steimle, D. A. Fletcher, K. Y. Jung, and C. T. Scurlock, “A supersonic molecular beam optical Stark study of CaOH and SrOH”, *The Journal of Chemical Physics* **96**, 2556–2564 (1992).

- ¹²²J. Lim, J. R. Almond, M. Tarbutt, D. T. Nguyen, and T. C. Steimle, “The [557]- $X^2\Sigma^+$ and [561]- $X^2\Sigma^+$ bands of ytterbium fluoride, ^{174}YbF ”, *Journal of Molecular Spectroscopy* **338**, 81–90 (2017).
- ¹²³P. J. Domaille and T. C. Steimle, “Microwave Optical Double Resonance and Reanalysis of the $\text{CaF } A^2\Pi - X^2\Sigma$ Band System”, *Journal of Molecular Spectroscopy* **70**, 374–385 (1978).
- ¹²⁴B. E. Sauer, J. Wang, and E. A. Hinds, “Anomalous Spin-Rotation Coupling in the $X^2\Sigma^+$ State of YbF ”, *Physical Review Letters* **74**, 1554–1557 (1995).
- ¹²⁵R. F. Barrow and A. H. Chojnicki, “Analysis of the optical spectrum of gaseous ytterbium monofluoride”, *Journal of the Chemical Society, Faraday Transactions 2* **71**, 728 (1975).
- ¹²⁶A. Kramida, Y. Ralchenko, J. Reader, and N. A. T. (2021), *NIST Atomic Spectra Database (ver. 5.9)*, [Online].
- ¹²⁷E. B. Norrgard, D. S. Barker, S. Eckel, J. A. Fedchak, N. N. Klimov, and J. Scherschligt, “Nuclear-spin dependent parity violation in optically trapped polyatomic molecules”, *Communications Physics* **2**, 77 (2019).
- ¹²⁸A. Jadbabaie, N. H. Pilgram, J. Klos, S. Kotochigova, and N. R. Hutzler, “Enhanced molecular yield from a cryogenic buffer gas beam source via excited state chemistry”, *New Journal of Physics*, **10**. 1088/1367-2630/ab6eae (2020).
- ¹²⁹N. H. Pilgram, A. Jadbabaie, Y. Zeng, N. R. Hutzler, and T. C. Steimle, “Fine and hyperfine interactions in $^{171}\text{YbOH}$ and $^{173}\text{YbOH}$ ”, *The Journal of Chemical Physics* **154**, 244309 (2021).
- ¹³⁰T. Yang, A. Li, G. K. Chen, C. Xie, A. G. Suits, W. C. Campbell, H. Guo, and E. R. Hudson, “Optical Control of Reactions between Water and Laser-Cooled Be^+ Ions”, *The Journal of Physical Chemistry Letters* **9**, 3555–3560 (2018).
- ¹³¹A. G. Ureña and R. Vetter, “Dynamics of reactive collisions by optical methods”, *International Reviews in Physical Chemistry* **15**, 375–427 (1996).
- ¹³²W. Fernando, M. Douay, and P. Bernath, “Vibrational analysis of the $\tilde{A}^2\Pi - \tilde{X}^2\Sigma^+$ and $\tilde{A}'^2\Delta - \tilde{X}^2\Sigma^+$ transitions of baoh and baod”, *Journal of Molecular Spectroscopy* **144**, 344–351 (1990).
- ¹³³P. F. Bernath, “Gas-Phase Inorganic Chemistry: Monovalent Derivatives of Calcium and Strontium”, *Science* **254**, 665–670 (1991).
- ¹³⁴K. Pandey, A. K. Singh, P. V. K. Kumar, M. V. Suryanarayana, and V. Natarajan, “Isotope shifts and hyperfine structure in the 555.8-nm $^1\text{S}_0 \rightarrow ^3\text{P}_1$ line of Yb ”, *Physical Review A* **80**, 022518 (2009).
- ¹³⁵E. T. Mengesha, A. T. Le, T. C. Steimle, L. Cheng, C. Zhang, B. L. Augenbraun, Z. Lasner, and J. Doyle, “Branching Ratios, Radiative Lifetimes, and Transition Dipole Moments for YbOH ”, *The Journal of Physical Chemistry A* **124**, 3135–3148 (2020).

- ¹³⁶E. J. Salumbides, K. S. E. Eikema, W. Ubachs, U. Hollenstein, H. Knöckel, and E. Tiemann, “The hyperfine structure of $^{129}\text{I}_2$ and $^{127}\text{I }^{129}\text{I}$ in the B band system”, *Molecular Physics* **104**, 2641–2652 (2006).
- ¹³⁷P. E. Atkinson, J. S. Schelfhout, and J. J. McFerran, “Hyperfine constants and line separations for the $^1\text{S}_0 - ^3\text{P}_1$ intercombination line in neutral ytterbium with sub-Doppler resolution”, *Physical Review A* **100**, 042505 (2019).
- ¹³⁸N. Stone, “Table of nuclear magnetic dipole and electric quadrupole moments”, *Atomic Data and Nuclear Data Tables* **90**, 75–176 (2005).
- ¹³⁹H. Wang, A. T. Le, T. C. Steimle, E. A. C. Koskelo, G. Aufderheide, R. Mawhorter, and J.-U. Grabow, “Fine and hyperfine interaction in ^{173}YbF ”, *Physical Review A* **100**, 022516 (2019).
- ¹⁴⁰M. Barnes, A. J. Merer, and G. F. Metha, “Electronic transitions of cobalt carbide, CoC , near 750 nm: A good example of case ($b_{\beta S}$) hyperfine coupling”, *The Journal of Chemical Physics* **103**, 8360–8371 (1995).
- ¹⁴¹T. C. Steimle, T. Ma, and C. Linton, “The hyperfine interaction in the $A^2 \Pi_{1/2}$ and $X^2 \Sigma^+$ states of ytterbium monofluoride”, *The Journal of Chemical Physics* **127**, 234316 (2007).
- ¹⁴²Z. Glassman, R. Mawhorter, J.-U. Grabow, A. Le, and T. C. Steimle, “The hyperfine interaction in the odd isotope of ytterbium fluoride, ^{171}YbF ”, *Journal of Molecular Spectroscopy* **300**, 7–11 (2014).
- ¹⁴³T. C. Steimle, T. Ma, and C. Linton, “Erratum: “The hyperfine interaction in the $A^2 \Pi_{1/2}$ and $X^2 \Sigma^+$ states of ytterbium monofluoride” [J. Chem. Phys. 127, 234316 (2007)]”, *The Journal of Chemical Physics* **137**, 109901 (2012).
- ¹⁴⁴M. C. L. Gerry, A. J. Merer, U. Sassenberg, and T. C. Steimle, “The microwave spectrum of CuO , $X^2 \Pi$, measured with optical detection”, *The Journal of Chemical Physics* **86**, 4754–4761 (1987).
- ¹⁴⁵K. Gaul and R. Berger, “Ab initio study of parity and time-reversal violation in laser-coolable triatomic molecules”, *Physical Review A* **101**, 012508 (2020).
- ¹⁴⁶J. Liu, X. Zheng, A. Asthana, C. Zhang, and L. Cheng, “Analytic evaluation of energy first derivatives for spin-orbit coupled-cluster singles and doubles augmented with noniterative triples method: General formulation and an implementation for first-order properties”, *The Journal of Chemical Physics* **154**, 064110 (2021).
- ¹⁴⁷R. Blatt, H. Schnatz, and G. Werth, “Ultrahigh-Resolution Microwave Spectroscopy on Trapped $^{171}\text{Yb}^+$ Ions”, *Physical Review Letters* **48**, 1601–1603 (1982).
- ¹⁴⁸G. C. Bjorklund, “Frequency-modulation spectroscopy: a new method for measuring weak absorptions and dispersions”, *Optics Letters* **5**, 15 (1980).

- ¹⁴⁹N. C. Wong and J. L. Hall, “High-resolution measurement of water-vapor overtone absorption in the visible by frequency-modulation spectroscopy”, *Journal of the Optical Society of America B* **6**, 2300 (1989).
- ¹⁵⁰J. C. Bloch, R. W. Field, G. E. Hall, and T. J. Sears, “Time-resolved frequency modulation spectroscopy of photochemical transients”, *The Journal of Chemical Physics* **101**, 1717–1720 (1994).
- ¹⁵¹G. E. Hall and S. W. North, “Transient Laser Frequency Modulation Spectroscopy”, *Annual Review of Physical Chemistry* **51**, 243–274 (2000).
- ¹⁵²G. C. Bjorklund, M. D. Levenson, W. Lenth, and C. Ortiz, “Frequency modulation (FM) spectroscopy: Theory of lineshapes and signal-to-noise analysis”, *Applied Physics B Photophysics and Laser Chemistry* **32**, 145–152 (1983).
- ¹⁵³D. Forthomme, C. P. McRaven, T. J. Sears, and G. E. Hall, “Argon-Induced Pressure Broadening, Shifting, and Narrowing in the CN A ² Π-X ² Σ⁺ (1–0) Band”, *The Journal of Physical Chemistry A* **117**, 11837–11846 (2013).
- ¹⁵⁴A. G. Marshall and D. C. Roe, “Dispersion versus absorption: spectral line shape analysis for radiofrequency and microwave spectrometry”, *Analytical Chemistry* **50**, 756–763 (1978).
- ¹⁵⁵F. W. King, *Hilbert transforms*, Vol. 1, *Encyclopedia of Mathematics and Its Applications* 124-125 (Cambridge University Press, Cambridge [Eng.] ; New York, 2009).
- ¹⁵⁶F. W. King, *Hilbert transforms*, Vol. 2, *Encyclopedia of Mathematics and Its Applications* 124-125 (Cambridge University Press, Cambridge [Eng.] ; New York, 2009).
- ¹⁵⁷*Non-Linear Least-Squares Minimization and Curve-Fitting for Python — Non-Linear Least-Squares Minimization and Curve-Fitting for Python*, <https://lmfit.github.io/lmfit-py/> (visited on 06/23/2022).
- ¹⁵⁸C. Zhang, C. Zhang, L. Cheng, T. C. Steimle, and M. R. Tarbutt, “Inner-shell excitation in the YbF molecule and its impact on laser cooling”, *arXiv:2201.07871* (2022).